

# Design and Characterization of a Combined AFM-SICM Microscope



**Tyler Leslie Brian Enright**

Physics Department

McGill University, Montréal

April, 2020

*A thesis submitted in partial fulfillment of the  
requirements of the degree of  
Doctor of Philosophy*

©Tyler Enright, 2020

# *Abstract*

Electrochemical measurements on battery materials are important for experimental validation of the current theoretical models, and for methodical improvement of battery technologies. This requires simultaneous measurements of electrochemical and physical information to establish their correlation at the atomic scale, in-situ.

In this study, new dual Scanning Ionic Conductance Microscopy (SICM) and Atomic Force Microscopy (AFM) pipette probes were designed and created to fulfill these requirements. These probes were then tested on calibration materials to assess their capabilities.

To test their functionality as force probes the probes were oscillated via photothermal excitation at resonance frequencies in the range of 1-10 kHz. Approach curves were performed in deflection mode and tapping mode, and AFM topography images were performed on CD and DVD calibration samples in air and in liquid. An image of a carbon nanotube demonstrated the ultimate resolution of these probes and established their tip radius to be  $60 \pm 10$  nm. To verify the SICM capabilities, AFM-SICM approach curves were performed in deflection mode and tapping mode. A DVD surface was then imaged via SICM and AFM simultaneously. Correlation and cross-talk between all the data channels both verified the topographic measurement capabilities of SICM and demonstrated the systematic error inherent to the technique. To extract electrochemical information, a droplet approach was used to perform cyclic voltammetry at picoamp currents on a template-stripped gold surface. This functionality was then expanded upon through pointwise cyclic voltammetry scanning with AFM feedback on a gold surface. Finally, some preliminary tip-localized corrosion experiments were performed on gold.

This research demonstrates the viability of AFM-SICM pipette probes as a powerful and versatile tool in electrochemical scanning probe microscopy.



# *Résumé*

Les mesures électrochimiques sur les matériaux de batteries sont importantes pour la validation expérimentale des modèles théoriques actuels et pour l'amélioration informée des technologies de batteries. Cela nécessite la mesure électrochimiques et physiques simultanée pour établir leur corrélation in situ à l'échelle atomique. Dans cette étude, de nouvelles sondes de pipette pour la microscopie à conductance ionique à double balayage (SICM) et la microscopie à force atomique (AFM) ont été conçues et créées pour répondre à ces demandes. Ces sondes ont ensuite été testées sur des matériaux d'étalonnage pour évaluer leurs capacités. Pour tester leur fonctionnalité en tant que sondes de force, les sondes ont été oscillées via une excitation photothermique à des fréquences de résonance dans la plage de 1 à 10 kHz. Les courbes d'approche ont été effectuées en mode contact et en mode contact intermittent (tapping), et des images de topographie AFM ont été effectuées sur des échantillons d'étalonnage de CD et DVD dans l'air et dans un liquide. Une image d'un nanotube de carbone a démontré la résolution ultime de ces sondes et a établi leur rayon de pointe à  $60 \pm 10$  nm. Pour vérifier les capacités SICM, les courbes d'approche AFM-SICM ont été effectuées en mode contact et en mode tapping. Une surface DVD a ensuite été imagée via SICM et AFM simultanément. La corrélation et la diaphonie entre tous les canaux de données ont toutes deux vérifié les capacités de mesure topographique du SICM et démontré l'erreur systématique inhérente à la technique. Pour extraire des informations électrochimiques, une approche par gouttelettes a été utilisée pour effectuer une voltampérométrie cyclique aux courants de picocamp sur une surface modèle d'or dépouillée. Cette fonctionnalité a ensuite été étendue par balayage voltampérométrique cyclique ponctuel avec rétroaction AFM sur une surface en or. Enfin, quelques expériences préliminaires de corrosion localisée à la pointe ont été réalisées sur de l'or. Cette recherche démontre la viabilité des sondes de pipette AFM-SICM en tant qu'outil puissant et polyvalent en microscopie à sonde à balayage électrochimique.

# *Acknowledgements*

I would like to thank my supervisor Peter Grutter for his guidance throughout my University career. As a third-year undergraduate student, I went to ask for some clarification on an assignment. He turned that conversation towards my scientific interests and plans for my academic career and beyond. Three months later I was working in his lab, and 9 years after that I am submitting this Doctoral thesis. Your mentorship has allowed me to become the researcher I am today, and for that I am deeply thankful.

I would also like to thank Professor Yoichi Miyahara. Your vast knowledge and even greater patience were indispensable in this project. Our daily conversations not only accelerated the pace of my research but shaped my thinking about the experimental process. If I've learned to emulate any part of your approach, then I consider this PhD a success.

Thanks to Professor Janine Mauzeroll for all her expertise and friendly advice.

I would like to give a very big thank you to the whole Grutter research group and former members for their valuable input during many discussions, as well as for being my close friends. There are a few I would like to thank in particular. Thanks to Rasa for her friendship, especially during my construction banishment to the basement. Thanks to Andreas for his sunny attitude and expertise in AutoCAD. Thanks to Harrisonn, Connor, Maddy, and Ying for their support and encouragement through all the trials and tribulations that the research process can put you through. Thank you all.

Thanks to Robert Gagnon for all his help. He was always willing to hear out my wildest scientific ideas, eager to try out new creative solutions, and our interactions were some of the most fun parts of my research.

Thanks to my friends, in Montreal and abroad. The best part of attending McGill is having the opportunity to meet so many diverse and interesting people. I am thankful for all of your support.

Thank you to Emma for being there for me, and always saying what I needed to hear. You've steered me through the difficult times and been there for the best of times. Thank you.

Finally, thank you to my parents Ronald Enright and Caroline Green. You nurtured me academically from a young age, and you were there for me at every step of this journey.

# *Author Contributions*

All experiments were conducted in the laboratory of Professor Peter Grutter. All chapters of the thesis were written by Tyler Enright (TE) and edited by Peter Grutter.

**Chapter 1** consists of review and synthesis of literature relevant to the project.

**Chapter 2** demonstrates the design and creation of a combined AFM-SICM system by TE. Dr. Aleks Labuda built the electrochemical atomic force microscope (ECAFM) described and used in this project. Dr. Aaron Mascaro created a new signal box for the ECAFM. Dr. Andreas Spielhofer modified and created CAD drawings for the creation of AFM heads and sample holders. Dr. Yoichi Miyahara (YM) provided technical assistance in the reparation of the ECAFM and measurement apparatus.

**Chapter 3** demonstrates the force measurement characteristics of the SICM-AFM probes. All measurements were performed by TE. YM provided guidance in operating the AFM system.

**Chapter 4** demonstrates the current measurement capabilities of the SICM-AFM probes as performed by TE. All data analysis was performed by TE. YM provided guidance in operating the AFM system. Dr. Madeline Anthonisen provided assistance in operating the Asylum Research MFP 3D microscope to perform the experiments in “Destructive Sample Imaging – the Potential for Manipulating Surface” section.

**Chapter 5** is a summation of the work described in Chapter 3 and Chapter 4.

**Chapter 6** is an outlook on the future direction of this work.

# Contents

<b>Abstract</b>	<b>i</b>
<b>Résumé</b>	<b>ii</b>
<b>Acknowledgements</b>	<b>iii</b>
<b>Author Contributions</b>	<b>iv</b>
<b>1 Background and Theory</b>	<b>1</b>
1.1 Battery Materials . . . . .	1
1.1.1 Importance . . . . .	1
1.1.2 Lithium Ion Batteries . . . . .	2
1.1.3 Barriers to Battery Study . . . . .	7
1.2 Atomic Force Microscopy . . . . .	8
1.2.1 Contact Mode . . . . .	9
1.2.2 Tapping Mode . . . . .	9
1.2.3 Hopping Mode . . . . .	11
1.2.4 Force Spectroscopy . . . . .	11
1.3 Scanning Electrochemical Techniques . . . . .	12
1.3.1 Scanning Ion Conductance Microscopy . . . . .	12
1.3.1.1 Ion Current Rectification and Capacitance . . . . .	15
1.3.2 Scanning Electrochemical Cell Microscopy . . . . .	17
1.4 Combined AFM-SICM . . . . .	18
1.4.1 Introduction . . . . .	18
1.4.2 Implementations Found in Literature . . . . .	18
1.4.3 Challenges of Current Implementations . . . . .	23
<b>2 Experimental Methods and Instrumentation</b>	<b>26</b>

---

2.1	Introduction . . . . .	26
2.2	Scanning Probe Hardware . . . . .	29
2.3	Beam Deflection System . . . . .	31
2.4	Control Electronics and Data Acquisition System . . . . .	32
2.5	Combined SICM–AFM Probes . . . . .	38
2.5.1	Material choice for pulling pipettes . . . . .	39
2.5.2	Pipette Pulling Parameters . . . . .	41
2.5.3	Creating AFM Cantilevers from Pulled Pipettes . . . . .	44
2.5.4	Filling the SICM–AFM probe with electrolyte . . . . .	49
2.5.5	Probe actuation and deflection measurement . . . . .	50
2.5.6	Noise characterization of combined SICM–AFM probes . . . . .	53
2.6	Conclusion . . . . .	55
<b>3</b>	<b>Force Measurements</b>	<b>58</b>
3.1	Introduction . . . . .	58
3.2	Probe Force Sensing Characteristics . . . . .	59
3.3	AFM Scanning . . . . .	72
3.3.1	Scanning in Air . . . . .	73
3.3.2	Topography Scanning in Liquid . . . . .	82
3.4	Conclusion . . . . .	86
<b>4</b>	<b>Combined Electrochemical and Force Measurements</b>	<b>89</b>
4.1	Introduction . . . . .	89
4.2	Current Sensing Characteristics . . . . .	90
4.3	Dual AFM-SICM Measurements . . . . .	95
4.4	Electrochemical Droplet Measurements at a Point . . . . .	103
4.5	Electrochemical Droplet Measurements of a Surface . . . . .	120
4.6	Destructive Sample Imaging – the Potential for Manipulating Surfaces . . . . .	130
4.7	Conclusion . . . . .	135
<b>5</b>	<b>Conclusion</b>	<b>139</b>
<b>6</b>	<b>Outlook</b>	<b>146</b>
<b>A</b>	<b>Plasma Arc Circuit Diagram</b>	<b>151</b>
<b>B</b>	<b>GXSM Python Code</b>	<b>152</b>

---

B.1	Setting the General Vector Probe Variables for Hopping Mode Scan . . . .	153
B.2	Setting the General Vector Probe Variables for Tapping Mode Scan . . . .	155
B.3	Scanning Routine . . . . .	156
B.4	Line Scan . . . . .	157
B.5	Retraction Followed by Alternating Approach Steps and CV Measurements	158
B.6	Alternating Approach Steps and CV Measurements Retraction Followed by Retraction . . . . .	160
<b>C</b>	<b>Stiffness Test Protocol</b>	<b>162</b>
<b>D</b>	<b>Tungsten Electrode Protocol</b>	<b>164</b>
	<b>Bibliography</b>	<b>171</b>

# List of Figures

1.1	Shrinking-Core Model of Lithium Iron Phosphate . . . . .	3
1.2	Domino-Cascade Model of Lithium Iron Phosphate . . . . .	4
1.3	Phase Evolution of Lithium Iron Phosphate . . . . .	6
1.4	State-of-Charge Mapping Performed via Oxidation-State-Sensitive X-Ray Microscopy . . . . .	7
1.5	Topography and Phase Images of a Copolymer . . . . .	10
1.6	SICM Setups and Approach Curves . . . . .	13
1.7	Comparison of Noise Effects on SICM Measurements at 99% and 90% of Current Maximum . . . . .	14
1.8	Ion Rectification in Pipettes . . . . .	16
1.9	A Combined Scanning Ion Conductance and Shear Force Microscope . . . . .	19
1.10	A SICM/AFM Setup Where the Sample is Mounted on an AFM Cantilever . . . . .	20
1.11	A Combined Scanning Ion Conductance Microscope and Tapping-Mode Atomic Force Microscope . . . . .	21
1.12	FluidFM Probe Schematic . . . . .	22
1.13	SEM image of PeakForce SECM probe . . . . .	22
1.14	Imaging of Small Cellular Extensions via SICM and AFM . . . . .	24
2.1	Lateral Force Map of the Deposition and Desorption of CuCl on the Au(111) Surface . . . . .	27
2.2	The Electrochemical - Atomic Force Microscope built by Aleks Labuda . . . . .	29
2.3	Pipette Probe, AFM Head, and Compression Fitting . . . . .	30
2.4	Q Control Block Diagram . . . . .	34
2.5	Rigid Axopatch Connection . . . . .	35
2.6	Flexible Axopatch Connection . . . . .	35
2.7	Faraday Cage . . . . .	36
2.8	USB Microscope View of Tip and Sample . . . . .	37
2.9	Pipette Pulling Process . . . . .	41
2.10	Pipette Puller Components and Process . . . . .	42
2.11	Bent Probe Mounted in the EC-AFM Schematic . . . . .	44

---

2.12	Pipette Bending Apparatus . . . . .	45
2.13	SEM Image of Bend and Taper of a Pipette Probe . . . . .	47
2.14	SEM Image of Probe Apex . . . . .	47
2.15	Probe Tip Approached to Sample Surface . . . . .	48
2.16	Probe Tip Buckling as Force is Applied . . . . .	48
2.17	Capillary Tubes with and without a Filament . . . . .	48
2.18	Filling the Pipette Probes . . . . .	49
2.19	Forest of Peaks . . . . .	51
2.20	Probe Coating for Photothermal Excitation . . . . .	52
2.21	Pipette Probe Oscillation Amplitude Dependence on Laser Power . . . . .	54
2.22	Power Spectral Density of the Deflection Signal of a Pipette Cantilever . . . . .	54
2.23	Power Spectral Density of the Current Noise Measured by the Current Amplifier . . . . .	55
2.24	Deflection Drift Over Time . . . . .	56
2.25	Current Drift Over Time . . . . .	56
3.1	Pipette Stiffness Test . . . . .	60
3.2	Pipette Probe Stiffness Test . . . . .	61
3.3	Pipette Probe with Incorrect Bend Angle Bending Inappropriately . . . . .	62
3.4	Pipette Probe with Long Tip Bending Inappropriately . . . . .	63
3.5	Tip Instability Effects on a CD Stamper Tapping Mode AFM Scan . . . . .	64
3.6	Measurement of the Cantilever Transfer Function . . . . .	66
3.7	Measurement of the Empty Cantilever Transfer Function . . . . .	67
3.8	Measurement of the Filled Cantilever Transfer Function . . . . .	68
3.9	Transfer Function Measurement of a Cantilever Oscillated in Air . . . . .	70
3.10	Transfer Function Measurement of a Cantilever Oscillated in Electrolyte . . . . .	71
3.11	AFM Topography Scan of a CD Sample . . . . .	73
3.12	Line Profile Extracted From CD Sample Topography Scan . . . . .	74
3.13	Topography Scan of a DVD Sample . . . . .	75
3.14	Line Profile Extracted From DVD Sample Topography Scan . . . . .	76
3.15	Tip Convolution Effects in Pits . . . . .	77
3.16	Tip Convolution Effects on Bumps . . . . .	78
3.17	Topography Scan of a CD Stamper . . . . .	79
3.18	Line Profile Extracted From CD Stamper Topography Scan . . . . .	80
3.19	Topography Scan of a Carbon Nanotube Sample . . . . .	80
3.20	Line Profiles Extracted From CNT Topography Scan . . . . .	81
3.21	Tip Convolution of Small, High Aspect Ratio Sample Features . . . . .	82



---

3.22	Pipette Probe in a Liquid Bath . . . . .	83
3.23	Topography Scan of a DVD Sample Performed in Liquid . . . . .	84
4.1	AFM-SICM Deflection Approach Curve . . . . .	91
4.2	AFM-SICM Tapping Approach Curve . . . . .	92
4.3	AFM-SICM CD Stamper Scan . . . . .	96
4.4	Line Scans from AFM-SICM CD Stamper Scan Including a Defect . . . . .	97
4.5	Line Scans from AFM-SICM CD Stamper Scan Including Several Bumps . . . . .	97
4.6	Pairplot of AFM-SICM CD Stamper Scan . . . . .	98
4.7	SICM Ionic Resistance Considerations . . . . .	104
4.8	Current Voltammetry Time Trace Performed at a Point on a Gold Surface . . . . .	106
4.9	Cyclic Voltammogram of a Point on a Gold Surface . . . . .	106
4.10	Integrated Charge of Current Voltammogram Cycles of a Point on a Gold Surface . . . . .	107
4.11	Time Trace of Deflection and Z Position During CV Measurement of a Point on a Gold Surface . . . . .	107
4.12	Histogrammed Deflection Data During CV Measurement of a Point on a Gold Surface . . . . .	108
4.13	Tapping Mode Current Voltammetry Measurement . . . . .	109
4.14	Current Voltammogram in AFM Tapping Mode . . . . .	110
4.15	Integrated Charge of Current Voltammogram in AFM Tapping Mode . . . . .	111
4.16	Stepped AFM Approach and Cyclic Voltammetry . . . . .	112
4.17	Cyclic Voltammograms of Stepped AFM Approach . . . . .	112
4.18	Initial Cyclic Voltammograms of Droplet Measurement . . . . .	113
4.19	Time Trace of Current as Voltage is Ramped between 0 and 3 V . . . . .	114
4.20	Current Time Trace, Cyclic Voltammogram, Integrated Charge, and Deflection as Voltage is Ramped between 0 and 1 V . . . . .	115
4.21	Measurement Steps of SECCM Scan . . . . .	117
4.22	Path of Probe During SECCM Measurement . . . . .	118
4.23	Integrated Charge of an SECCM Scan of a Gold Surface . . . . .	121
4.24	Topography Scan Hysteresis . . . . .	122
4.25	Even Lines of an Integrated Charge of an SECCM Scan of a Gold Surface . . . . .	123
4.26	Odd Lines of An Integrated Charge of an SECCM Scan of a Gold Surface . . . . .	123
4.27	Odd Scan Lines of a SECCM Measurement on Gold . . . . .	124
4.28	Even Scan Lines of a SECCM Measurement on Gold . . . . .	125
4.29	Pairplot of SECCM Measurement of Gold Surface . . . . .	127

---

4.30 Topography and Integrated Current Channels of a SECCM Surface Scan of a Gold Sample . . . . .	128
4.31 Optical Image of Gold Delamination . . . . .	131
4.32 Optical Image of Surface Modifications Produced through Bias Routine .	132
4.33 Droplet Size as a Function of Pulse Duration . . . . .	133
4.34 Additional Measurements of Droplet Size as a Function of Pulse Duration	133
A.1 Plasma Arc Circuit . . . . .	151
C.1 Stiffness Test Apparatus . . . . .	163

# List of Tables

2.1 Properties of Various Commercially Available Capillaries . . . . .	40
--	----

# List of Equations

1.1 SICM Pipette Resistance . . . . .	12
1.2 SICM Access Path Resistance . . . . .	12
1.3 SICM Current as a Function of Tip Sample Distance . . . . .	12
1.4 Debye Length . . . . .	15
2.1 Spring Constant and Displacement Ratio Relation . . . . .	46
2.2 Spring Constant as Function of Length . . . . .	46
2.3 Second Moment of Inertia of a Cylindrical Cantilever . . . . .	46
2.4 Spring Constant of a Hollow Tube . . . . .	46
3.1 Experimental Stiffness Constant . . . . .	60
3.2 Resonance Frequency of a Rectangular Beam Cantilever . . . . .	68
3.3 Mass of Unfilled Pipette Probe . . . . .	69
3.4 Mass of Filled Pipette Probe . . . . .	69
3.5 Ratio of Filled to Unfilled Pipette Resonance Frequencies . . . . .	70
3.6 Characteristic Amplitude Settling Time . . . . .	77
3.7 Evaporation Rate per Hour . . . . .	85
3.8 Time for Liquid Bath to Evaporate . . . . .	85
4.1 Nernst Equation . . . . .	103
4.2 Maximum Bandwidth . . . . .	119

# Nomenclature

## Abbreviations

	<b>Meaning</b>
AC	Alternating Current
ADC	Analog-to-Digital Converter
AFM	Atomic Force Microscopy
CD	Compact Disc
CNT	Carbon Nanotube
CV	Current Voltammogram
DC	Direct Current
DVD	Digital Video Disc
EC-AFM	Electrochemical Atomic Force Microscope
GXSM	Gnome X Scanning Microscopy
LCO	$\text{LiCoO}_2$
LFP	$\text{LiFePO}_4$
NMC	$\text{LiNiMnCo}$
QRE	Quasi-reference Electrode
s/n	Signal-to-Noise Ratio
SECCM	Scanning Electrochemical Cell Microscopy
SECM	Scanning Electrochemical Microscopy
SEM	Scanning Electron Microscopy
SHE	Standard Hydrogen Electrode
SICM	Scanning Ion Conductance Microscopy
SLD	Super Luminescent Diode
SNOM	Scanning Near Field Optical Microscopy
SPM	Scanning Probe Microscopy
USB	Universal Serial Bus

## Constants

	<b>Meaning</b>	<b>Value</b>	<b>Units</b>
$\epsilon_0$	Vacuum permittivity	$8.854 \cdot 10^{-12}$	$F \cdot m^{-1}$
$e$	Euler's Constant	2.718	
$F$	Faraday constant	$9.65 \cdot 10^4$	$C \cdot mol^{-1}$
$g$	Gravity of Earth	9.81	$m \cdot s^{-2}$
$R$	Gas constant	8.3145	$J \cdot mol^{-1} \cdot K^{-1}$

**Variables**

	<b>Meaning</b>	<b>Units</b>
$\epsilon_r$	Relative permittivity	$F \cdot m^{-1}$
$\kappa$	Conductivity	$S \cdot m^{-1}$
$\lambda_D$	Debye Length	$m$
$\omega$	Frequency	Hz
$\rho$	Density	$kg \cdot m^{-3}$
$\tau$	Characteristic Settling Time	s
$A$	Area	$m^2$
$BW$	Bandwidth	Hz
$d$	Tip-Sample Distance	m
$E$	Young's Modulus	Pa
$E_{Ag/AgCl}^\circ$	Potential of the Ag/AgCl Electrode	V
$E_{QRE}$	Potential of the QRE	V
$g_s$	Mass of Water Evaporated per Second	$kg \cdot s^{-1}$
$H$	Height	m
$h$	Tip Length	m
$I$	Area Moment of Inertia	$m^4$
$I(d)$	Ionic Current	A
$I_s$	Ionic strength	$mol \cdot L^{-1}$
$k$	Spring Constant	N/m
$K_{sp}$	Solubility Product	
$l$	Length	m
$M$	Mass	kg
$R_{ac}$	Access Resistance	$\Omega$
$r_i$	Inner Tip Radius	m
$r_o$	Outer Tip Radius	m
$R_P$	Pipette Resistance	$\Omega$
$r_p$	Inner Radius of Pipette Base	m
$R_T$	Total Resistance	$\Omega$

---

$T$	Temperature	K
$t$	Thickness	m
$T_{evaporation}$	Time of Evaporation	s
$U$	Applied Potential	V
$v$	Velocity of Air	$\text{m} \cdot \text{s}^{-1}$
$w$	Width	m
$X$	Displacement	m
$x$	Air Humidity Ratio	$\text{kg} \cdot \text{kg}^{-1}$
$x_f$	Final Probe Position	m
$x_i$	Initial Probe Position	m
$x_s$	Saturated Air Humidity Ratio	$\text{kg} \cdot \text{kg}^{-1}$
$Q$	Quality Factor	

# Chapter 1

## Background and Theory

The aim of this Thesis is to develop a technique allowing the simultaneous determination of structure and properties on a nanometer length scale. The motivation for the development of this tool is the large number of interesting fundamental and applied questions that could be investigated in the field of batteries, catalytic systems or live cells.

In the following, I will outline in more detail why such a tool is needed by describing in detail an important current challenge in material science and engineering - batteries. This will illuminate some of the open questions that could be directly answered if one could characterize the structure and property of these materials at high spatial resolution with high sensitivity, thus motivating this thesis.

To facilitate discussion of this tool the chapter has been structured in four parts. The first discusses measurements and materials of interest to this new tool (1.1), the second describes principles of Atomic Force Microscopy used by this tool (1.2), the third explains Scanning Ionic Conductance Microscopy / Scanning Electrochemical Cell Microscopy principles used by this tool (1.3), and the fourth outlines other attempts at creating a similar combined system (1.4).

### 1.1 Battery Materials

#### 1.1.1 Importance

As of February 2020, all 197 members of the United Nations Framework Convention on Climate Change have signed on to the Paris Agreement [1]. As stated in Article 2, the



aim of this agreement is to decrease global warming by:

Holding the increase in the global average temperature to well below 21.5° C above pre-industrial levels and to pursue efforts to limit the temperature increase to 1.5° C above pre-industrial levels, recognizing that this would significantly reduce the risks and impacts of climate change. [2]

To accomplish this goal, Canada has committed to reducing its Green House Gas emissions to 70% of 2005 levels by 2030 [3]. Meeting this target requires substantial improvements to our energy creation, storage, and distribution systems [4]. Specifically, fossil fuel energy sources must be replaced by low emitting renewable energy sources such as wind and solar energy [5].

Use of renewable energy sources is impeded by the mismatch and unpredictability of energy creation and use. Weather conditions such as wind speed and cloud cover will determine when most energy is harvested, whereas users' schedules will dictate when the energy is used. Grid management is required to accommodate this volatility [6]. Through this system, energy can be stored at times of excess and used when demand increases. To do this, an efficient method of energy storage is required. Large scale battery management will be part of the arsenal of energy storage methods. To compete in large-scale energy storage these batteries must be improved in terms of their cost, life span, and performance [7].

Another venue to reduce green house gas emissions is to increase the market share of electric vehicles [8]; however, consumers need cars that match fossil fuel-based cars in terms of cost, speed, distance between refueling, and safety [9, 10]. Lithium ion batteries have been chosen by large manufacturers [11], and these batteries continue to see improvements in these measures of performance [12].

### 1.1.2 Lithium Ion Batteries

Batteries are chemical systems which store energy. Batteries which derive their energy from irreversible reactions are termed primary batteries, while those that use reversible processes are called secondary batteries [13]. Lithium ion batteries, such as LiNiMnCo(NMC), LiFePO<sub>4</sub> (LFP), and LiCoO<sub>2</sub> (LCO), are secondary batteries which rely on the reversible process of lithium intercalation [10]. These types of batteries are

tremendously important, highlighted by the Nobel Prize in Chemistry 2019 awarded jointly to John B. Goodenough, M. Stanley Whittingham and Akira Yoshino “for the development of lithium-ion batteries.” [14]

To charge a lithium ion battery, a potential is applied between the positive electrode (cathode) and the negative electrode (anode). Lithium ions from the cathode will deintercalate into an electrolyte, and then intercalate into the anode. If the applied potential is disconnected, the ions will stop moving and a potential difference between the anode and cathode persists. If a load is connected between the cathode and anode, the reaction will act in reverse, and a current will flow through the load [15].

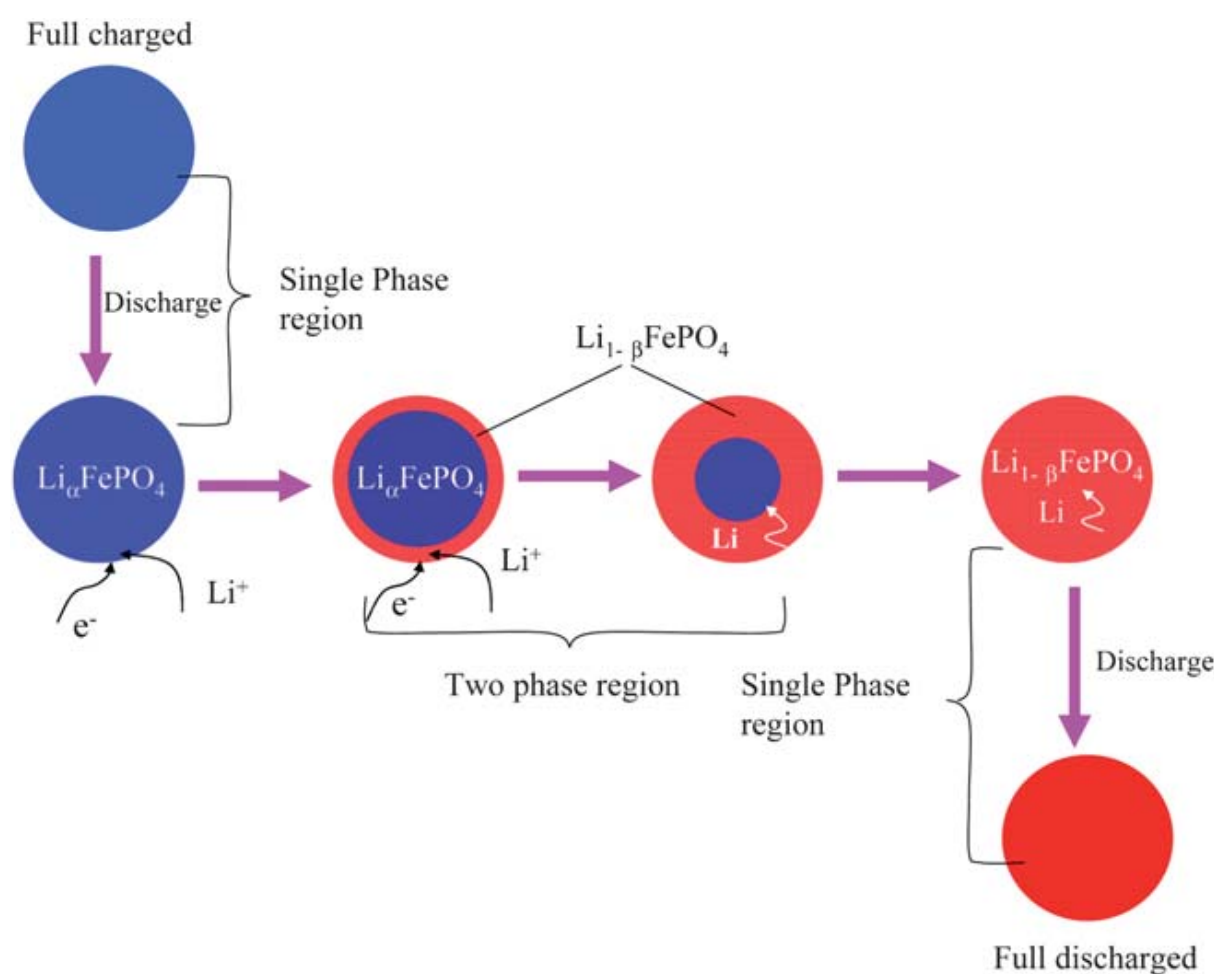


FIGURE 1.1: The shrinking-core model begins with a fully charged particle. As the particle begins to discharge, lithium will enter at the surface, and the entire particle’s composition will have a similar lithiation state. As discharging progresses the particle will separate into an outer lithium-rich shell and a lithium-poor core. Additional discharge will increase the size of the shell until the core disappears completely, and the entire particle is lithium-rich. The discharge continues until lithiation is maximised. Reprinted with permission from reference [15]. Copyright 2004 The Electrochemical Society.

While this process is simple, the efficiency and life time of this system is determined by many factors. In general, these can be broken down to the transit of the ions through the electrolyte [16], the travel of the ions through the solid electrolyte interphase (SEI) [17], and the transit of the ions through the bulk of the electrode materials [18].

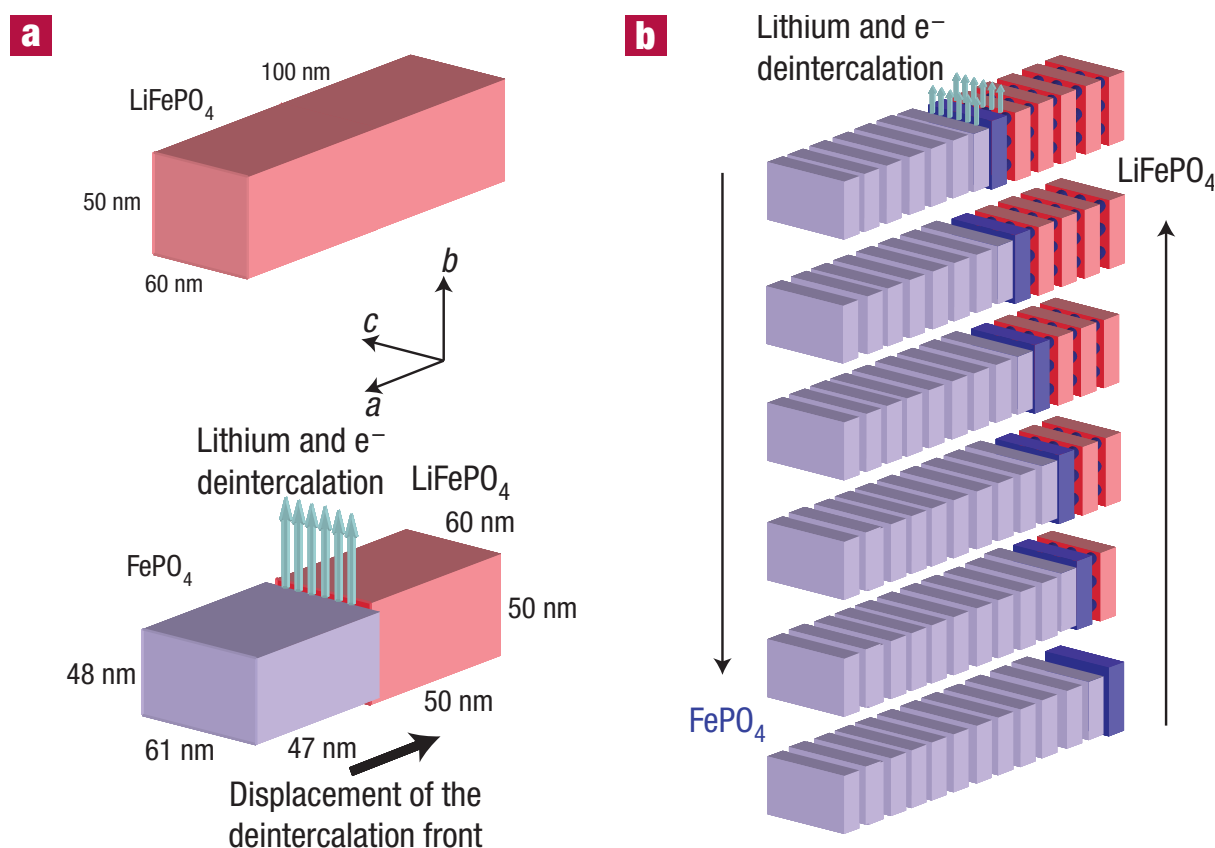


FIGURE 1.2: “Schematic view of the ‘domino-cascade’ mechanism for the lithium deintercalation/intercalation mechanism in a LiFePO<sub>4</sub> crystallite. Distances are not accurate because studied crystallites are rather isotropic. a, Scheme showing a view of the strains occurring during lithium deintercalation. b, Layered view of the lithium deintercalation/intercalation mechanism in a crystallite” Reprinted with permission from reference [19]. Copyright 2008 Nature Materials.

The Newman model is one of the most used frameworks which combines these effects [20]. According to Newman, intercalation can be described via a shrinking core model where transport results in a two-phase state of fully lithiated and fully delithiated regions. As shown in figure 1.1, the lithiated regions nucleate on the outer surface of the nanoparticles, and the material intercalates inwards.

The alternative ‘domino cascade model’ states that, as in the Newman model, particles exist as fully intercalated or fully deintercalated as shown in figure 1.2. Here there is no

shrinking core, but a phase boundary aligned with the  $\text{FePO}_4$  planes, moving perpendicular to the lithium flux [19].

While these models are the most used to study battery materials, experimental work on the underlying assumptions and abstractions are vital to improving the models. For example, there is no microstructural information needed beyond particle radius, electrode thickness, and electrode porosity. It assumes that the microstructure can be described as isotropic, homogeneous, one-dimensional porous material made up of monodisperse non-porous isotropic spherical particles that are small compared to the electrode thickness [15]. Such assumptions of uniformity cannot be assumed to be true.

The model's charge transfer step assumes a one step global process. However, the charge transfer step in a battery consists of the lithium de-solvating, transported through a surface electrolyte interface which not only consists of electrolyte and active material but of unintended products of side reactions as well, and then react with the electrode. To take the entire pathway as one step is to make a large simplifying assumption which ignores the geometries and chemical variation throughout the path of the lithium ions. Furthermore, these steps occur at an atomic level, and atomic inhomogeneities in the battery materials have been shown to exist. The geometry at this level is ignored in the model. The model's Butler-Volmer step describes how an electrode's electrical current depends on the electrode potential; it describes the electrical charge transfer. It is theorized to have a large part in degradation of the battery materials [22]. These cell degradation processes are poorly understood and defined. One suggestion has been that 'carbon retreat', relating to the carbon binder, has led to the loss of internal electrical conductivity witnessed experimentally [22]. This loss has also been explained by precipitation of thick films at the surface-electrolyte interphase [23], particle fracture [24], gas generation [25], and delamination of battery material from the current collector [26]. However, these issues are quite difficult to measure in-situ, so the chain of cause and effect is not quite clear, and atomic reasons for these issues lack a basis that can be strongly integrated into current theory. Even the domino-cascade model which was thought to have displaced the shrinking-core model has been proven inaccurate. Ramana's study [20] has shown through use of x-ray and electron microscopy that dependent on the synthesis technique used to create the lithium iron phosphate sample, the phase boundaries will take on different shapes. Simply, both delithiated and lithiated states may exist within one particle. This leads to much different dynamics, the result being a lithiation scheme which is shown visually in figure 1.3 [21]. This has been validated by other studies, but these studies use different synthesis processes which may affect the lithiation process [27].

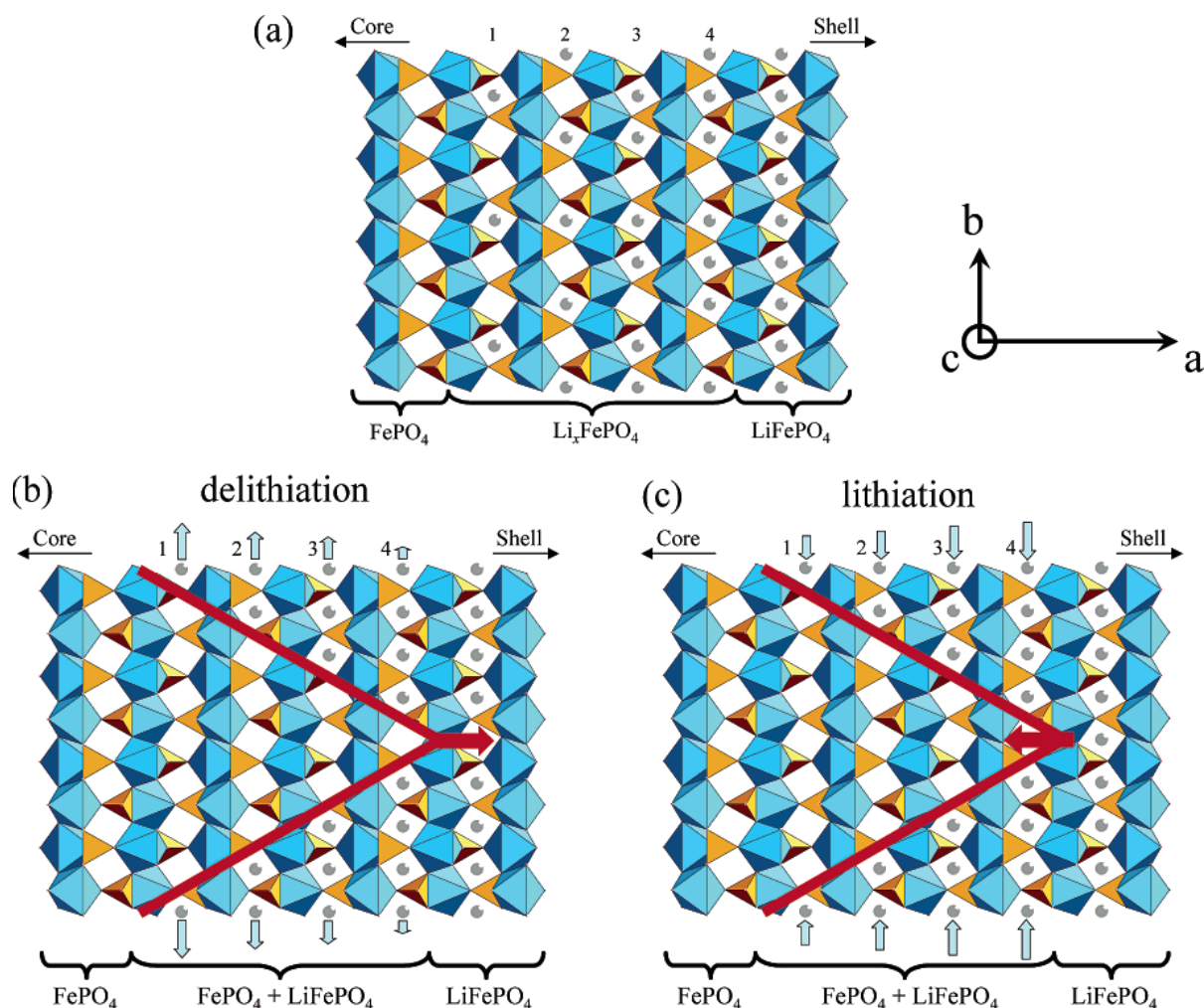


FIGURE 1.3: “Schematic views of the interfacial region between LiFePO<sub>4</sub> and FePO<sub>4</sub> phases. (a) Hypothesis of a disordered Li<sub>x</sub>FePO<sub>4</sub> phase with a gradient of Li content between FePO<sub>4</sub> and LiFePO<sub>4</sub> end members; (b) front phase evolution during delithiation; (c) front phase evolution during lithiation. Small vertical arrows indicate the movement of (Li<sup>+</sup>, e<sup>-</sup>) pairs, the longest ones symbolizing an energetically favored extraction/insertion from/into the channels. The large red arrows indicate the direction in which the interfacial region is moving.” Reprinted with permission from reference [21]. Copyright 2006 Chemistry of Materials.

While current theory explains some electrochemical quantities, many details at an atomic level are missing to describe the fundamental interactions within batteries. These fundamental processes are crucial to understanding degradation processes as well as the general process of lithium intercalation and may only be completely described by a versatile tool which directly observes lithiation in situ.

### 1.1.3 Barriers to Battery Study

To validate and improve the existing theoretical framework related to batteries, more experimental work must be done. This work must be done in situ as capacity loss and kinetics will allow lithium ions to change position after charging or discharging events. Therefore, studies that require two systems to charge and examine the battery will risk viewing a sample that is not indicative of an actual step of the charging process. Also, due to questions raised about the steps of the actual process of ionic transport of lithium, it is crucial to see the development of the charged battery step from fully delithiated to fully lithiated and the reverse at small charge increments. To achieve this, the battery material must be measured continuously through the charging process. This requires a fully integrated electrochemical cell and must deal with the individual constraints of the observing system.

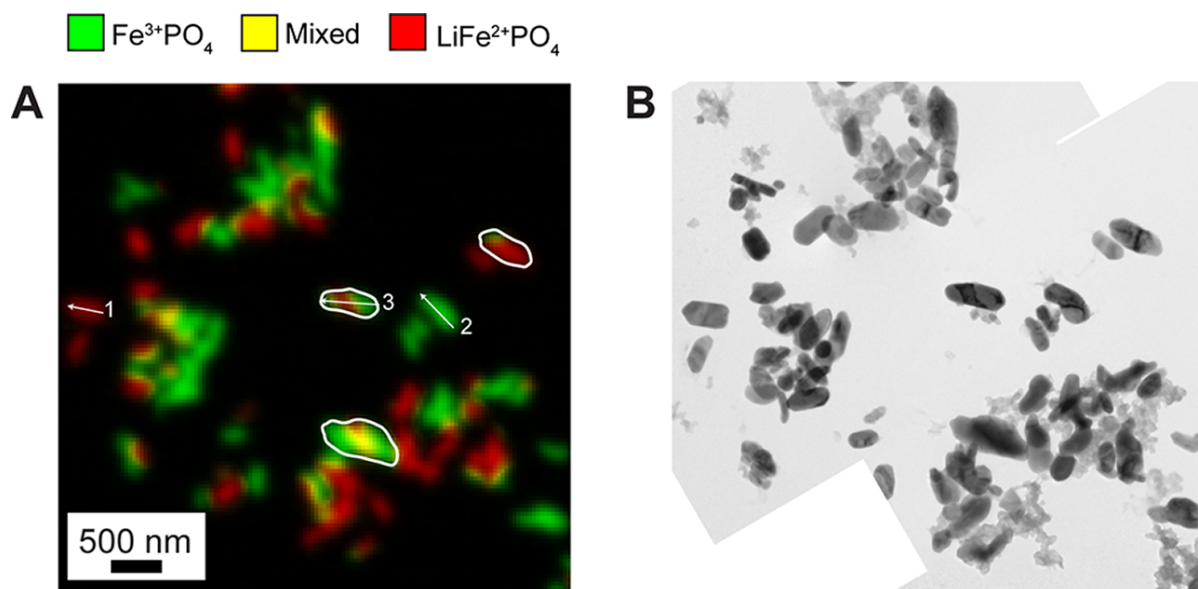


FIGURE 1.4: “(A) State-of-charge mapping and (B) morphology of lithium iron phosphate electrode powder dispersed by sonication. Outlined in white are particles in which two phases coexist within the same particle.” The image was taken using oxidation-state-sensitive X-ray microscopy. Reprinted with permission from reference [27]. Copyright 2013 Nano Letters.

A suitable technique must also have comparable resolution and sample sizes to compare with ex-situ measurements. In-situ oxidation state sensitive X-ray microscopy may be performed to take clear images of the charging states of nanoparticles as seen in figure 1.4, the length scale of these measurements has a resolution of approximately 40 nm [27]. At this resolution the charge state of particles may be depicted, but the atomic features are missing.



This study has been used to disprove the domino-cascade model by demonstrating that charging times are not negligible in comparison to nucleation time scales, as supported by the fact that approximately 2% of the particles are in a mixed charge state. However, with greater resolution it is hoped that the ionic pathways and the resultant charged areas within these particles may be viewed. To perform such an experiment would also mean selectively charging the electrode material. To see charge pathways at an atomic scale local charging is necessary to determine the path of ions in their entirety, from application to voltage bias to lithiation of specific areas of the battery materials. This is a crucial step in determining the evolution of ‘hot spots’, areas which attract higher ionic charges for unknown reasons [28].

Indeed, there are a plethora of experimental data performed at scales which must necessarily ignore nanometer scale features due to their characteristic resolutions. Many details of battery operation and aging at this length scale are poorly understood [29]. The development of lithium batteries, and batteries in general, can be improved and expedited by characterizing material distances at this length scale, in situ, across several measurement simultaneously.

## 1.2 Atomic Force Microscopy

Atomic force microscopy is a versatile scanning probe method in which a silicon cantilever with a sharp tip is used to measure forces through optical detection of its deflection [30]. Most commonly, the probe is raster scanned across a surface to create a topographic image through force detection. From this essential scheme, conditions may be changed to accommodate a wide range of measurements. By changing some experimental parameters properties as diverse as topography, friction, contact potential difference, conductance, and dopant profiles can be mapped over surfaces [31, 32]. The resolution of these measurements can be on the atomic scale, but the same principles are used to create microscopes which measure millimetres in range [33]. Additionally, these measurements can be performed in vacuum, air, and liquid at temperatures ranging from millikelvin to over 750° Celsius [34, 35]. This type of microscopy provides a powerful platform for studying a wide range of materials. In the following section the modes used are depicted.

### 1.2.1 Contact Mode

In contact mode the tip of the silicon cantilever is brought into repulsive contact with a sample surface [30]. When the probe meets the surface, this force will deflect the probe. The optical detection system will record this change in deflection and thus probe the tip-sample forces.

To use this to measure surfaces, the probe is raster scanned over a sample. As the probe moves over the sample, the deflection should change due to the topography. However, an electronic feedback system adjusts the height of the probe to maintain a constant deflection. These height adjustments of the probe can be displayed as a (constant force) topography image of the surface.

This type of imaging is the most basic AFM mode, and the easiest to use; however, it can result in the damage of soft samples. In repulsive contact, a force is applied between the sharp tip and the sample. If this force is large enough it can destroy parts of the sample (or tip). To prevent this, low stiffness cantilevers and small deflections (i.e. small forces) are used.

### 1.2.2 Tapping Mode

In tapping mode, the cantilever is oscillated, most commonly through piezo actuation [30]. The instantaneous deflection of the cantilever is measured by the optical deflection system. A lock-in amplifier is used to measure the amplitude of this oscillation. The probe is approached to the sample surface until the oscillation amplitude of the probe begins to decrease. This reduction in amplitude occurs as the probe makes intermittent contact with the surface (i.e. when ‘tapping’ the surface). Just as in the contact mode case, the probe is raster scanned over the surface, and the tip-sample position is controlled with a feedback circuit to maintain a consistent amplitude. Similarly, this measurement will produce an image of the sample topography by raster-scanning the sample. However, since the probe is only in intermittent contact with the surface, the force applied to the sample can be less than in the contact mode [36]. Lateral forces are strongly reduced as the tip lifts off the surface after every tap. The magnitude of the normal force during the ‘tap’ is a function of the operator selected oscillation amplitude reduction. In general, this leads to less damage to the sample or tip. Aside from the amplitude measurement, the lock-in amplifier also yields a phase difference measurement. This is the phase difference between the signal used to excite the probe via the actuation piezo, and the oscillatory signal of



the probe's position. Phase data indicates the presence of dissipation forces, which may be attributed to viscoelasticity, adhesion, friction, and topometric changes such as slope [37]. Although many forces contribute to the phase image, valuable information may be extracted from the data such as that seen in figure 1.5 [38]. In this image the two phases of a co-polymer can not be distinguished via the tapping mode AFM, but the phase signal clearly defines the position of the two phases. In this manner, phase imaging can be used as a method of qualitatively differentiating the constituents of features with identical topography, whether it be different materials or different crystallographic orientations.

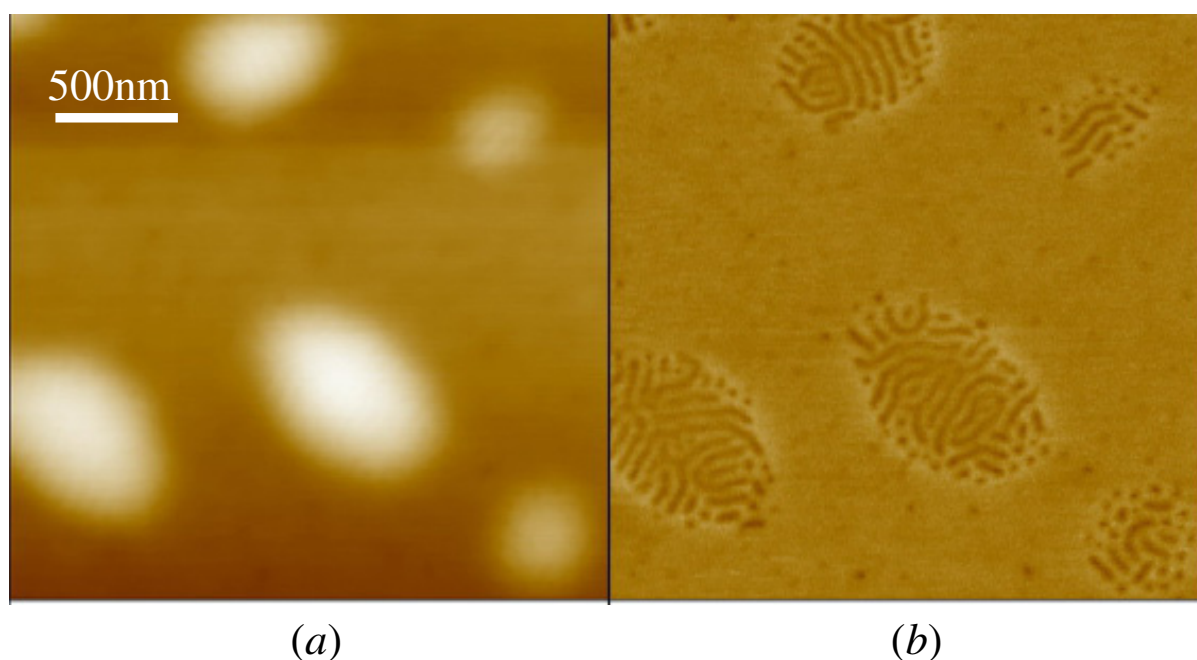


FIGURE 1.5: “Topography and phase images of a copolymer treated by solvent annealing. The height scale is 10 nm and the phase angle scale is  $20^\circ$ . (a) Topography image, (b) phase image.” Reprinted with permission from reference [38]. Copyright 2008 Measurement Science and Technology.

Using tapping mode in liquid can be challenging. Since the cantilever must oscillate within the liquid, hydrodynamics act dissipatively, and will decrease the Quality factor ( $Q$ ) of the resonance peak. This reduction of the  $Q$  factor is usually unwanted in experimental conditions as it means the sensitivity to changes in force is reduced. In addition, many resonance peaks are often observed in liquids (‘forest of peaks’ [39]) due to the excitation of various hydrodynamic resonances with the actuation piezo.

### 1.2.3 Hopping Mode

Hopping mode is a variation of both contact and tapping. It is generally used to scan very rough surfaces, where the feedback will not be able to retract the probe fast enough to prevent the probe from crashing into the surface when scanning. It is also used for soft and adhesive surfaces which may be damaged easily by lateral forces [40]. Hopping mode avoids these problems by moving the probe far away from the surface before lateral motion. In this mode, measurement (such as the contact force or oscillation amplitude reduction) are performed near the surface at one point, the probe is retracted to a safe distance, the probe moves laterally to the next position in the grid of measurements, the probe is approached again, and another measurement is performed. In this type of measurement, the tip is protected because it is not laterally dragged across the surface so there is less force applied to the tip during movements of the tip. The added steps of approach and retraction for each point will increase the time required to scan the sample.

### 1.2.4 Force Spectroscopy

In force spectroscopy, a cantilever approaches and retracts from a sample at a single point [41]. During this measurement the deflection or oscillation amplitude or frequency of the cantilever is recorded, which can be converted to a force. In this way the force can be plotted as a function of vertical position. This is called a ‘force curve’ or ‘force-distance curve’. Using this as a basis, many types of measurements can be performed. It can be used to test mechanical properties such as elastic moduli or yield strength. If a bias is applied between the tip and surface, we can see the effects of electrostatics. In bias spectroscopy, the tip can remain at a fixed position relative to the sample, and the potential difference between tip and sample can be ramped, which may elicit a force response. In time spectroscopy, the force is simply monitored over a set time to see if the system changes over that period.

This single point spectroscopy can then be integrated into a hopping mode type system where this spectroscopy can be performed at an array of points on the sample surface [42].

## 1.3 Scanning Electrochemical Techniques

### 1.3.1 Scanning Ion Conductance Microscopy

Scanning ion conductance microscopy (SICM) is a scanning probe method which measures ionic resistance [43]. In this method, the probe is a glass pipette filled with electrolyte and an electrode. It operates in a bath of liquid which also covers the sample surface. A potential is applied between the electrode in the probe and an electrode in the bath of electrolyte, which drives an ionic current. The magnitude of this current will be determined by the ionic resistance between the two electrodes. Far from the sample surface, the resistance will be determined by the electrolyte concentration and the resistance of the pipette. As the tip is approached to an ionically insulating sample surface the ionic resistance will increase as the pathway the ions may follow is restricted. The resistance can be modelled mathematically:

$$R_p = \frac{h}{\kappa \cdot \pi \cdot r_p \cdot r_i} \quad (1.1)$$

$$R_{ac} \approx \frac{3 \ln\left(\frac{r_o}{r_i}\right)}{2 \cdot \kappa \cdot \pi \cdot d} \quad (1.2)$$

$$\begin{aligned} I(d) &= \frac{U}{R_T} \\ &= \frac{U}{R_p + R_{ac}} \\ &\approx \frac{U}{R_p} \left( 1 + \frac{3 \ln\left(\frac{r_o}{r_i}\right) \cdot r_p \cdot r_i}{2 \cdot h \cdot d} \right)^{-1} \end{aligned} \quad (1.3)$$

The total resistance ( $R_T$ ) may be modeled as two resistors in series where  $R_p$  is the probe resistance caused by the ionic path needing to pass through the small (nm) opening of the pipette, and the access path resistance ( $R_{ac}$ ) which is determined by the space between probe and sample that allows the ionic charge to pass [43] while a potential is applied ( $U$ ). The pipette resistance is calculated through the geometric parameters of inner tip

radius ( $r_i$ ), the inner radius of the tip base ( $r_p$ ), the outer radius of the tip opening ( $r_o$ ), the tip length ( $h$ ), the conductivity of the electrolyte in the pipette ( $\kappa$ ). As the probe is approached to the surface, the distance between tip and sample ( $d$ ) will decrease, leading to a change in the access resistance and ionic current ( $I(d)$ ) as seen in figure 1.6a and figure 1.6b. It should be noted that this assumes that the pipette is perpendicular to the sample surface. In practice, this may not be true. An accurate description requires a geometrical model of the separation between the probe apex and sample surface.

This tip-sample distance dependent current can then be used to create a distance feedback mechanism. In practice, the probe is approached to the surface until there is a reduction (usually 1%) in the current [44]. Then the probe is scanned over the surface, and the vertical position of the probe is changed to maintain a consistent ionic current. The position of the probe over this scan will be recorded as a topographic image.

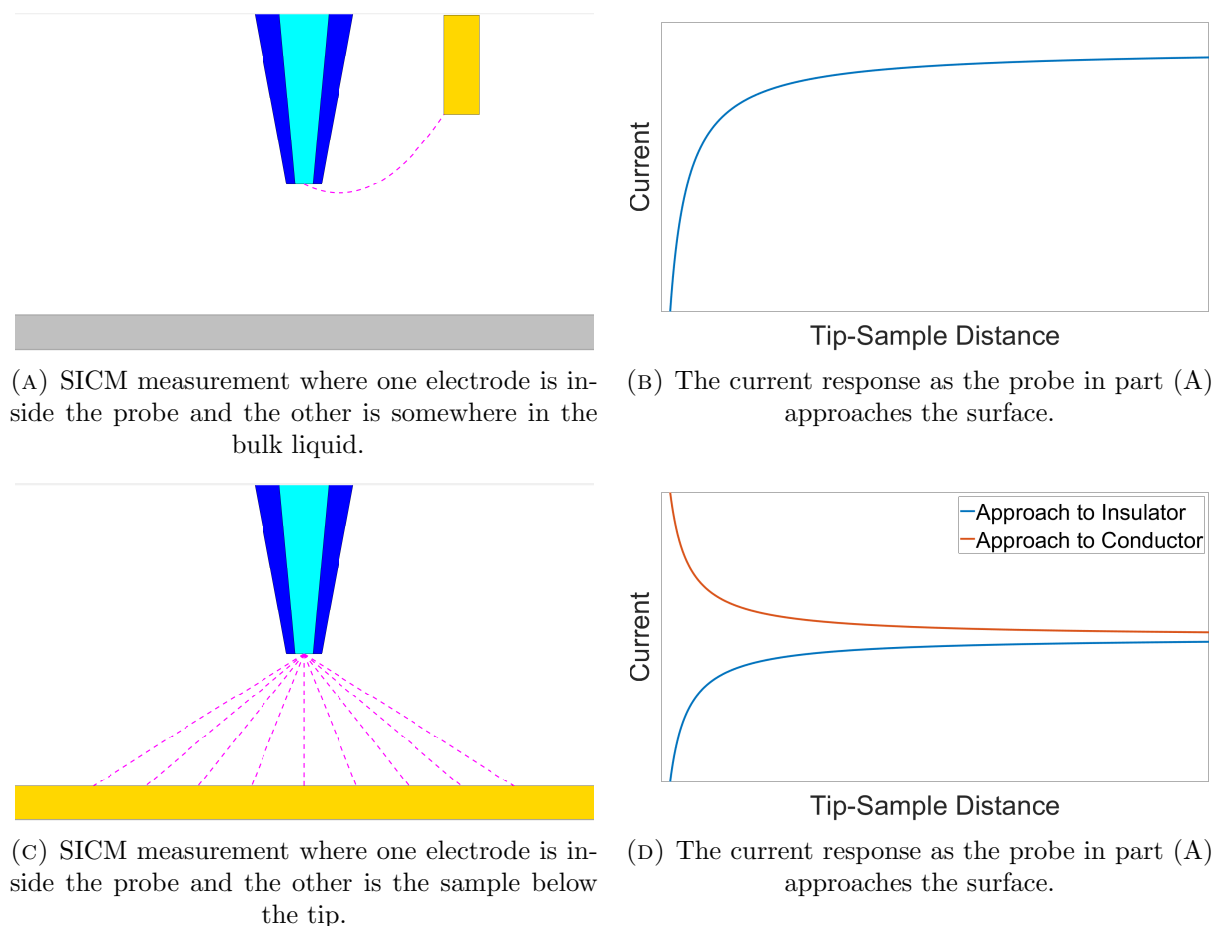


FIGURE 1.6

In another version of this technique, the electrode in the bath is removed, and potential is applied between the electrode in the probe and the sample [45], as seen in figure 1.6c and figure 1.6d. In this configuration, the sample is at least partially ionically conductive.

The same feedback system as previously explained will function for this system; however, when the probe scans over areas of sample conductivity, the measured ionic current will increase. Under certain experimental parameters this may result in insulating areas having a negative sloping current with respect to changes in probe height above the sample and conducting areas having positive slopes. This cannot be used as a topography feedback system, as the feedback conditions required to stably scan an insulator area will cause a crash of the probe over the conducting area. If the sample is flat, the probe can be scanned over the sample at a constant height relative to the sample, without active feedback. In this way, the conductivity of the sample may be mapped.

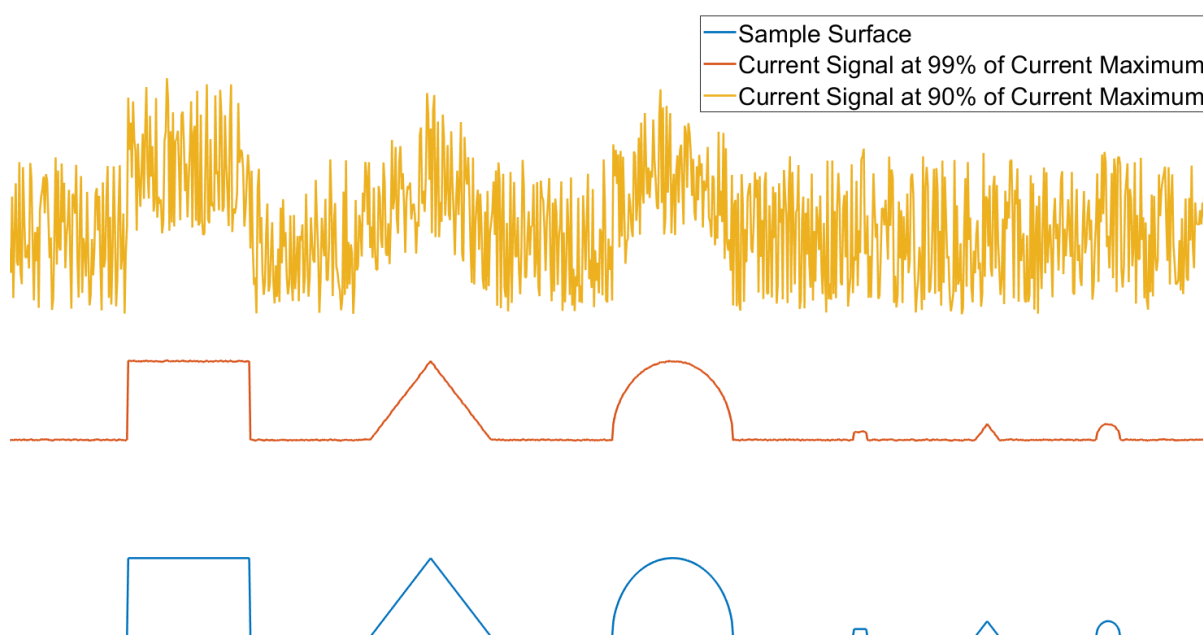


FIGURE 1.7: The blue line shows a sample surface, while the yellow and orange curves show the topography information recorded if the probe is scanned 99% of the current maximum, and 90% of the current maximum with a noise level of 0.1% of the current maximum. Since the current-distance curves is quite flat at the 99% mark, this noise will have a large effect on the measured topography. At 90% the curve is much steeper, so a small distance adjustment will offset the instantaneous noise.

If this sample has topographic features, things become even more difficult. Without active feedback, there is a risk that the probe may crash into raised topographic features. If the probe does not crash, the information is difficult to interpret because a smaller distance between probe and sample may be misinterpreted as an area of higher conductivity, and vice versa. If a very high current resolution, and consequently topographic resolution is required, then approaching the surface to maintain a constant distance from a sample which is thought to be an area of lower height but is actually an area of lower conductivity will cause a crash of the tip. That is why this technique has typically been used for biological samples where the resolution isn't as important. Biological systems studied

using this method are usually quite sensitive, so the non-invasive, low energy, non-contact, micrometer resolution of this technique is more than adequate. However, for higher resolution on surface with non-negligible roughness, other techniques are required for vertical height detection.

### 1.3.1.1 Ion Current Rectification and Capacitance

While the ohmic model of resistance in SICM fits experimental data well, especially in high concentration electrolyte environments, a growing body of evidence is developing which examines electrical double layer or Debye Layer (DL) and its effect on the measured current [46].

The Debye layer refers to the structure that forms at the surface of an object exposed to a fluid [47]. When a conductor is in contact with an electrolyte two layers will form, the Helmholtz layer closest to the interface, and a diffuse charge layer. This is the origin of charging current or capacitance in SICM/SECCM measurements. The Debye length (the thickness of the DL) in an electrolyte at low potentials is:

$$\lambda_D = \sqrt{\frac{R \cdot T \cdot \epsilon_r \cdot \epsilon_0}{2 \cdot 10^3 \cdot F^2 \cdot I_s}} \quad (1.4)$$

Where  $\lambda_D$  is the Debye length (m),  $R$  is the gas constant ( $8.3145 J \cdot mol^{-1} \cdot K^{-1}$  [48]),  $T$  is temperature (K),  $\epsilon$  is relative permittivity ( $F \cdot m^{-1}$ ),  $\epsilon_0$  is vacuum permittivity ( $8.854 \cdot 10^{-12} F \cdot m^{-1}$ ),  $F$  is Faraday's constant ( $9.65 \cdot 10^4 C \cdot mol^{-1}$  [49]), and  $I_s$  is the ionic strength (mol/L) [50]. The ionic strength of a solution is a summation of concentration of the ionic species, weighted by their charge. Therefore, the Debye length will depend on the nature and concentration of the electrolyte.

It has been shown that this Debye layer can lead to some distortions of the approach curve and ion rectification during linear voltage sweeps [51]. The glass (or quartz) pipettes are insulators with trapped negative charges. If the Debye length at this interface is approximately equal or larger than the diameter of the tip opening, then this can impede the flow of ions. Positively charged ions will be able to pass through the tip opening, but negative ions will be impeded or blocked at tip opening. If the voltage is swept linearly ion current will be rectified as shown in figure 1.8[51].

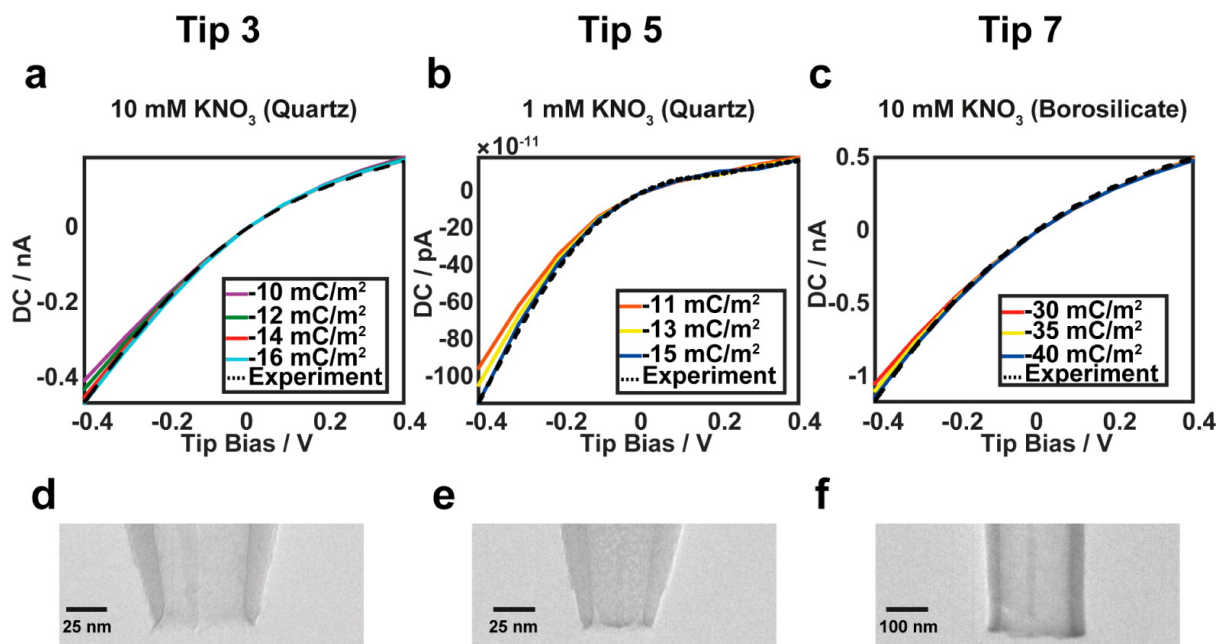


FIGURE 1.8: "I-V characteristics of quartz nanopipettes at low ionic strength reveal ion current rectification in 10 mM KNO<sub>3</sub> (a), which is seen more strongly as the ionic strength decreases further to 1 mM KNO<sub>3</sub> (b). Larger borosilicate nanopipettes also exhibit ion current rectification, and a correspondingly larger nanopipette surface charge is required to match the experimental response. The noise level for these experiments was 3 pA (peak-to-peak). Corresponding TEM images for each tip are shown (d-f). Note that the surface charge on the nanopipette is the only variable in the simulation to fit to the experimental data. The simulation results for different charges are shown as the colored lines." Reprinted with permission from [51]. Copyright 2020 American Chemical Society.

The Debye layer phenomenon will occur at any charged interface, including the sample surface. There have been recent developments in charge mapping [46, 52, 53]. In these measurements, the Debye layer thickness will correlate with the spatially distributed surface charges. When the probe tip passes through the Debye layer of these surface features the ionic current will be rectified according to the electrochemical details and charge at the interface. Although this can yield new information about surfaces in electrolytes, it can also make other measurements more challenging. Take for example biological samples. Typically, biological systems can only live within very specific electrolyte and pH conditions. If the electrolyte concentration is too dilute, then the DL will be large, and will vary according to small changes in ionic strength and surface charge. If SICM is used to measure topography this could lead to crashes when passing from a positively charged surface feature to a negatively charged feature. A distance regulation technique that is not reliant on ion current measurements can allow these measurements to proceed reliably, and in doing so yield new information.

### 1.3.2 Scanning Electrochemical Cell Microscopy

Scanning Electrochemical Cell Microscopy (SECCM) is another pipette probe-based technique [54]. In this technique, a pipette filled with electrolyte and an electrode is approached to a dry surface. When the probe meets the sample surface, the liquid at the end of the probe tip will contact the surface and a droplet will form on the surface. A potential is applied between the electrode in the probe and the sample surface. This will drive an ionic current. Since the ions require the electrolyte to move to the surface, electrochemical reactions will therefore be confined to the area of the surface defined by the footprint of the droplet. In this way, an electrochemical cell is defined. Within this electrochemical cell cyclic voltammetry may be performed. By employing a hopping mode approach, this technique can be used to create a topographic map of voltammetric curves.

It should be noted that the current measured by this technique relies on droplet concentration, droplet footprint, and sample composition. Heuristically, if there is a current between the probe and sample, they must be in proximity to each other. However, this technique is completely unable to disentangle these factors, meaning topography and surface decomposition cannot be separated directly from the ionic current signal. To deal with this, the probes are oscillated vertically, which means the tip sample distance will be oscillated, and ionic current signal will oscillate [38]. This is essentially a derivative of the current approach curve. This derivative is then used as the distance regulation mechanism, as it is insensitive to DC changes in this curve. While this will prevent crashing the tip due to sudden increases in the DC current, this derivative of the approach curve is still a product of the DC curve and will therefore be subject to the same contributing factors. That is to say, the technique may be used to measure topography, but the error on this measurement will be large and difficult to quantify.

While there are significant challenges in using this technique, a tremendous amount of research has been done recently to address these problems and push electrochemical scanning probe techniques farther [43, 55–61]. As these systems have recently been commercialized [62–64], scanning probe electrochemical measurements will continue to grow in importance.



## 1.4 Combined AFM-SICM

### 1.4.1 Introduction

SICM and SECCM proffer the ability to extract interesting electrochemical information from materials. It is clear that the topographic feedback that these techniques employ not only lack precision and potentially conflate chemical activity with topography/structure, they also contribute to considerable error in their electrochemical measurements. To solve this difficulty, these techniques can be combined with the distance regulation mechanisms of atomic force microscopy. Topography is characterized by a surface of constant force (or oscillation amplitude, depending on the AFM operation mode), while simultaneously performing the electrochemical or ionic conductance measurements at a well-defined distance from the topographic surface. Various mechanisms have been proposed and carried out to accomplishing this.

### 1.4.2 Implementations Found in Literature

The most common combined system is shear force detection, as seen in figure 1.9 [65]. In shear force detection SICM systems the probe is perpendicular to the sample surface, and the tip is oscillated parallel to the sample surface via piezo actuation. The probe's oscillation amplitude is detected optically, and the magnitude of this oscillation is used as feedback mechanism. In contrast, in tapping mode AFM the probe oscillated perpendicular to the surface. The difference means that shear force detection will measure shear forces, and these forces can damage probes, clog probes, and damage samples. Additionally, as the probe oscillates, the tip remains close to the surface, and the measured force response will be a measure of the force felt through the entire oscillation cycle. Therefore, the lateral resolution of the technique will rely on the amplitude of oscillation, so large oscillation amplitudes will result in lower resolution via lateral force averaging. A commercial implementation of this combination is the Park Systems Park NX 10 SICM module [66]. The system is generally run with a 1-2% decrease in current to avoid crashes. Additionally, the force feedback does not yield possible AFM information such as phase contrast.

Another method is to simply have a system where the SICM and AFM probes and sensing systems (referred to as the head) may be interchanged [67]. This allows for both measurements on the same sample so both scans can be compared on one region.

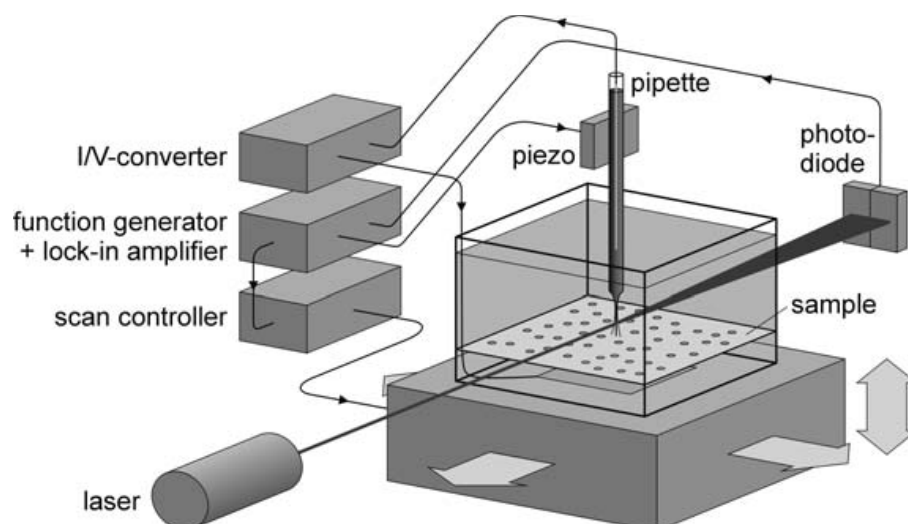


FIGURE 1.9: “Schematic illustration of the setup of a combined scanning ion conductance and shear force microscope. The lateral oscillatory motion of the probe’s tapered end is induced by a piezo element to which the micropipette is attached. By focusing a laser beam on the tapered probe and detecting the diffracted light with a segmented photodiode the mechanical oscillation is converted into an electrical signal. This is analyzed by means of a lock-in amplifier whose reference channel is synchronized with the driving signal of the dither piezo. The amplitude of the probe’s oscillation serves as the input signal of a feedback loop. The latter controls the vertical position of the scanner in such a way that a constant, predefined oscillation amplitude is maintained during xy-scanning. As a consequence, the SICM probe precisely follows the sample topography. Simultaneously, the local ion current owing between the electrodes in the micropipette and under the porous sample is recorded. Thus, possible variations in the local ion conductivity can be analyzed along with the surface topography.” Reprinted with permission from reference [65]. Copyright 2006 Springer.

This system can take accurate images of identical 80 micrometer regions, with lateral resolution on the order of microns. In this situation, piezo-electric drift will not have a large effect. However, if a higher resolution image on a smaller scale is performed then drift will mean that the tip holder on the second scan will be displaced a non-negligible amount. Depending on the drift on this system, this could lead to entirely different scan area. Also, the mechanism of switching tips needs to employ new techniques in order to ensure that a change in probe from AFM cantilever to SICM pipette does not lead to a large displacement. If the sample is actively changing through these experiments, then having to switch between the two tips will mean a loss of time-resolved data compared to a system which could continuously take data using both scanning methods. Also, the SICM method must still make use of shear force methods since the topography may have drifted or changed between scans so a prior AFM scan cannot be taken as completely accurate.

Another method pictured in figure 1.10 relies on performing SICM measurements on a

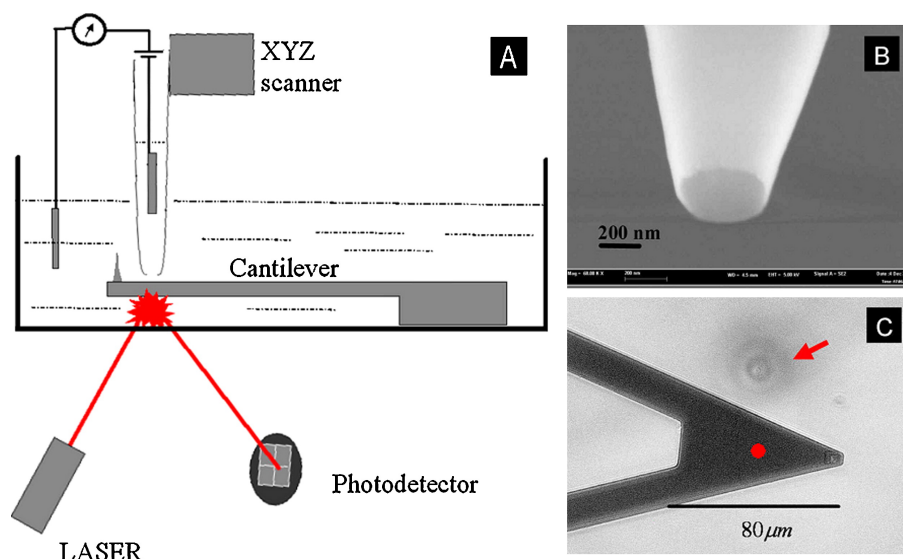


FIGURE 1.10: “(A) A SICM/AFM setup where the sample is mounted on an AFM cantilever. As the SICM probe scans over the sample the cantilever oscillation will change, providing topography information. (B) The SICM probe tip apex. (C) An inverted optical microscope image of a triangular cantilever next to a SICM pipette (indicated by arrow). The pipette is displaced from its measurement position.” Reprinted with permission from reference [68]. Copyright 2006 Neuroscience Research.

cantilever sample stage [68]. The SICM probe is held stationary over an AFM cantilever which holds a sample. The cantilever scans underneath the probe, tracing out a two-dimensional grid in reference to the SICM probe. The pipette performs ionic current measurements, while topography can be extracted via optical detection of the cantilever’s oscillation.

A major challenge to this method is fitting the sample on a  $100\ \mu\text{m}$  long cantilever, which requires microfabrication. Alternatively, a larger cantilever could be fabricated to accommodate larger samples. Larger cantilevers have a lower frequency, which slows down scanning and increases susceptibility to environmental noise (building vibrations, acoustic noise, etc.).

Figure 1.11 depicts a bent AFM-SICM probe which can perform both functions simultaneously, without the samples restrictions of the previous setup. In this system, a pipette is bent and used as both AFM probe via optical beam deflection, and as an SICM probe. Such a system was used on a synthetic membrane [69] and abalone nacre [70], proving that these probes could function. However, their absence from the literature thereafter highlights the challenge of producing viable probes. The tips of the probe are  $100\ \mu\text{m}$  long, so the entirety of the probe must enter the liquid, which elicits the “forest of peaks”

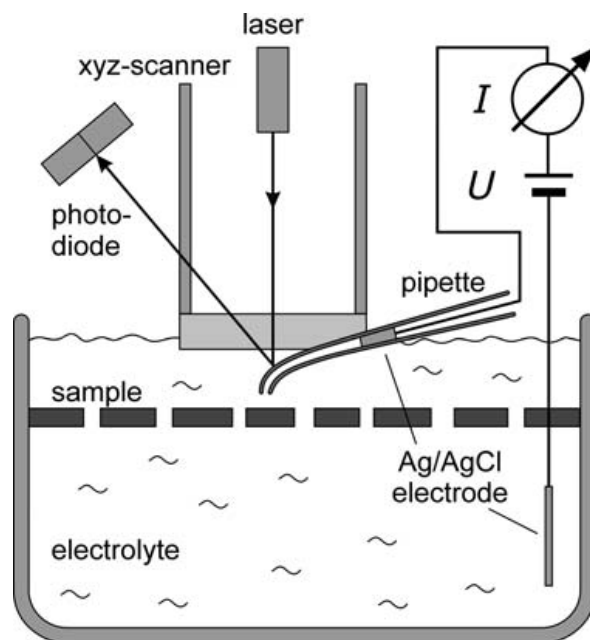


FIGURE 1.11: “Combined scanning ion conductance microscope and tapping-mode atomic force microscope. A bent nanopipette is used as both an ion conductance probe and an atomic force microscope cantilever. Tapping mode operation enables topographic imaging of soft samples. The tip-sample distance is thereby kept constant by mechanically vibrating the pipette and using feedback to keep the vibration amplitude constant. The vibration amplitude of the cantilever is detected with nanometer precision using the optical beam deflection method. The pipette is coated with a layer of gold (thickness  $\approx 30$  nm) to increase its reflectivity. Simultaneously to the topography, the ion current through the pipette is recorded, thereby generating complementary images of topography and local ion conductance.” Reprinted with permission from reference [65]. Copyright 2006 Springer.

problem. Additionally, a large reflector cannot be used in this scenario, as liquid damping would prevent oscillation of the probe. Without a large reflector, the amount of light reflected by the probe is small, contributing to a decreased signal to noise ratio. In terms of their signal, their resonance frequencies were stated to be between 50 kHz and 100 kHz, but their stiffness constants are not listed. Increases in stiffness require increased amounts of oscillation energy to attain sufficient oscillation amplitudes. Increase in oscillation energy applied by the piezo shaker can exacerbate the “forest of peaks” difficulties common to AFM scanning in liquid.

FluidFM probes manufactured by Nano-surf rely on hollow AFM cantilevers [71]. They operate as AFM cantilevers, with fluid channel that opens at the tip apex as shown in figure 1.12. This permits AFM force measurements with concurrent electrochemical measurements. This combination has allowed for surface charge measurements due to the force feedback accuracy in low electrolyte concentrations, which provide a challenge for

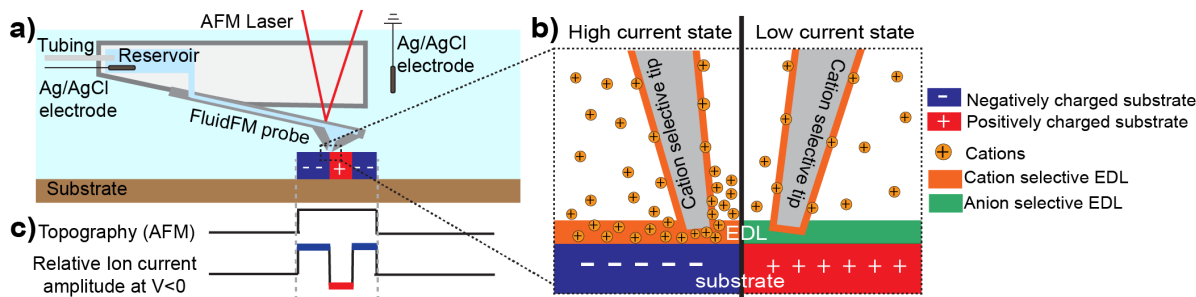


FIGURE 1.12: "Principle of surface charge mapping with the FluidFM. a) Schematic representation of the FluidFM probe operating over a charged feature on the substrate. b) Illustration of the surface-induced rectification phenomenon occurring in the negatively charged and negatively biased nanopipette probe over a negatively charged (left) and a positively charged (right) substrate. c) Schematic line scan profiles depicting the AFM topography and ion current recorded in a configuration depicted in (a) with a negatively biased cantilever probe." Reprinted with permission from reference [71]. Copyright 2020 American Chemical Society.

electrochemical feedback systems[71]. However, the tip opening is 300 nm, which limits the resolution. Additionally, as these probes must incorporate an interior channel, their dimensions exceed those of AFM cantilevers [72]. This exacerbates the "forest of peaks" phenomenon, and therefore measurements are performed in AFM contact feedback mode. This can lead to wear on tips, which will degrade the resolution further. Additionally, micro-channel cantilevers have well-documented difficulties with filling and leakage which can make them experimentally challenging to operate [73]. FIB must be used to create the hole at the apex, which will imbed charged ions in the material. While this is advertised as a feature of the probes for charge mapping [71], the embedded charge may cause increased electrochemical resistance, thereby decreasing signal to noise.

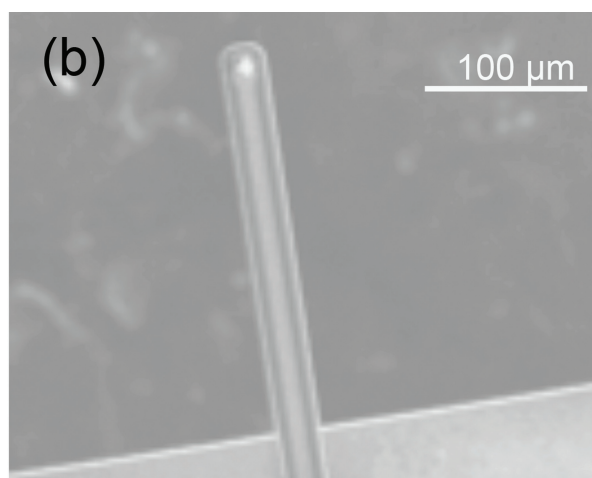


FIGURE 1.13: "SEM image of the probe cantilever showing the Pt conductive path with a width of 15 μm." Reprinted with permission from reference [74].

The Bruker Peakforce Scanning Electrochemical microscope employs a metal patterned silicon nitride cantilever to perform SECM measurements as seen in figure 1.13 [74]. The probes may be scanned at a normal AFM scan rate, however their quoted 100 nm peakforce tapping amplitude reveals that the probes must be oscillated at extremely large amplitudes to overcome the signal to noise issues of operating in liquid. Such amplitudes can result in tip damage. Additionally, while the tip apex is 50 nm in diameter, the probe diameter widens quickly after the first 200 nm. This will effectively distort topography images with steps of larger than 200 nm. There has also been some evidence of pinholes in their coatings [73], which may effect the geometry of the measurements, and increase the error on quantitative measurements.

### 1.4.3 Challenges of Current Implementations

The goal of this project is to create a probe that may perform simultaneous force measurements and electrochemical measurements to facilitate direct comparison between these channels of information. The value of this approach is demonstrated in the following examples, and shown in figure 1.14.

The figure shows images taken via a sequence of images of SICM, AFM, and SICM again [75]. By employing both measurements key information can be derived. Here, AFM scans show much thinner fibroblasts than SICM scans. By repeating the measurements, it was seen that after an AFM contact mode scan the SICM scan sees the fibroblasts as thicker than that shown in the AFM measurement, but not as thick as in the initial SICM measurement. This leads to two conclusions. The first is that the SICM sees the fibroblasts as larger features due to their ionic characteristics because the pre and post AFM scans show smaller fibroblasts. Second is that the AFM measurements harm the fibroblasts. Successive SICM scans show little difference in the form of the fibroblasts, but after the AFM scan they have changed considerably. These successive measurements give a lot of information about the system, although the necessary change of tips between measurements introduces systematic errors that put the results of this study in question.

By performing simultaneous SICM and AFM on lithium-ion battery materials, one could potentially see the changes that the SICM measurements make on the topographic information.

Crystallographic shifts will occur when the sample is lithiated, which should be seen through measurement of topography. To see such differences both techniques are required,



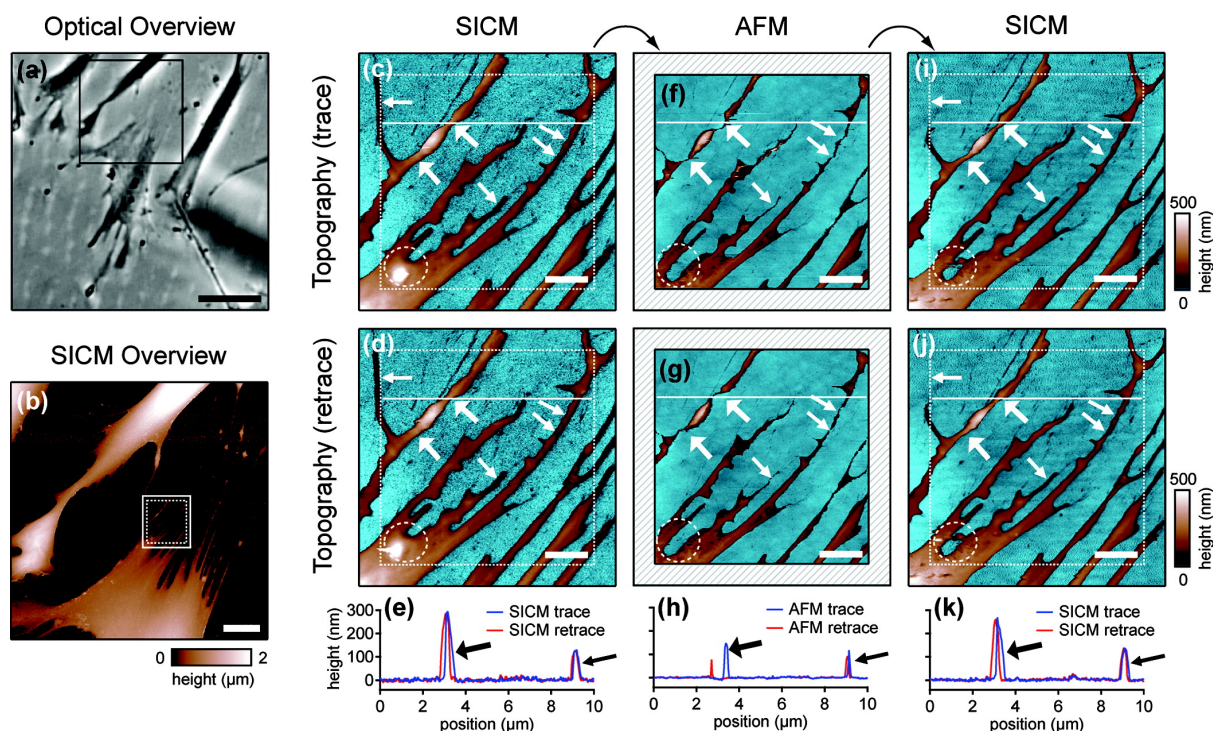


FIGURE 1.14: “Imaging of small cellular extensions. (a) Optical phase contrast overview image of fixed fibroblast cells. (b) SICM overview image of the boxed region in (a). The following SICM-AFM-SICM image sequence was acquired in the boxed region, where the SICM scan area (solid box) was slightly larger than the AFM scan area (dotted box). (c, d) Fibroblast extensions were imaged by using SICM first. Both the (c) “trace” image (where the probe moved from left to right) and the simultaneously recorded (d) “retrace” image (where the probe moved from right to left) are shown. (e) Respective height profiles along the horizontal lines in (c) and (d). (f, g) In the subsequent AFM images the features appear significantly lower and narrower (diagonal arrows). Weakly attached sections are shifted laterally by the AFM tip (thick arrows). These observations are also apparent in the respective height profiles (h). (i, j) SICM images and (k) height profiles recorded after the AFM images. The weakly attached sections appear stable again (thick arrows). However, one extension (horizontal thin arrow) is missing, suggesting that it was removed during AFM imaging. Furthermore, another extension (dashed circle) might have been permanently damaged by AFM imaging. Scale bars:  $40\ \mu\text{m}$  (a),  $10\ \mu\text{m}$  (b), and  $2\ \mu\text{m}$  (c, d, f, g, i, j).” Reprinted with permission from reference [75]. Copyright 2011 Langmuir.

but crystallographic shifts mean this sample area would be tremendously difficult to find again if one had to switch between the AFM system and SICM system as the identifying features would change between scans.

Shear force has been extensively used as a distance control mechanism, however the lateral averaging is not optimal for high resolution AFM measurements. Shear force measurements can also pose risk to samples, as force is applied to surfaces, resulting in more damage than tapping mode measurements. These shear force measurements are

also used simply as a distance control protocol, therefore neglecting some of the power functionality of AFM imaging such as phase contrast imaging and force spectroscopy.

The probes that do perform AFM and electrochemical measurements simultaneously (FluidFM and Bruker) do suffer from their bulky size and use of piezo-actuation. The 'forest of peaks' brought on by the liquid environment is challenging to overcome. In FluidFM this results in measurements being performed in contact mode, where surfaces may be damaged and there is no phase information. In Bruker's implementation the free oscillation amplitude is 100 nm, which indicates there is a large amount of force on the tip apex, which could lead to damage of sample and tip. This demonstrates the need for a probe that can be oscillated in liquid, and that can be used with photothermal oscillation to avoid any difficulties with the "forest of peaks".

To reiterate, the goal of this project is to create a probe that may perform simultaneous force measurements and electrochemical measurements to facilitate direct comparison between these channels of information. In particular, AFM tapping mode (topography and phase) and SICM/SECCM measurements need to occur simultaneously to all for the correlation of structure with electrochemical properties.

Chapter 2 discusses the design and fabrication of probes to address the objective of combined force and electrochemical measurements. Chapter 3 demonstrates the probes use force measurement sensors. Chapter 4 demonstrates the probes electrochemical abilities, and highlights some measurements where force measurements and electrochemical measurements are performed simultaneously. Chapter 5 reflects on the results of Chapters 3 and 4. Chapter 6 discusses the opportunities and challenges that these probes present for the future of scanning probe microscopy.



# Chapter 2

## Experimental Methods and Instrumentation

### 2.1 Introduction

This chapter describes general aspects of the AFM instrumentation used (2.2, 2.3, 2.4). In section 2.5, solutions to one of the major challenges facing SICM and AFM - fabricating a probe suitable for simultaneous SICM/SECM and AFM measurements—are presented. The process for fabricating SICM probes, by pulling and bending suitable glass capillaries, generating SICM pipettes with small (down to 100 nm) apertures and suitable spring constants to serve as AFM cantilevers, is then described (2.5.1, 2.5.2, 2.5.3). A process of filling probes with electrolyte solution without air bubbles that would inhibit SICM/SECM operation is then described (section 2.5.4). Finally, it is shown that these SICM probes can be used as AFM sensors via oscillation via light as an actuation mechanism (2.5.5). The advantages of this method when operating in liquids are discussed.

The microscope developed in this study is inspired by the combined AFM-SICM microscope shown in figure 1.14. The key characteristics of the AFM-SICM system developed in this thesis can be described in terms of mechanical stability, cantilevered probes, optomechanical oscillation, and high sensitivity, multi-channel data acquisition.

The basis of mechanical stability in this system was an existing highly mechanical stable electrochemical atomic force microscope (EC-AFM), originally created by Labuda [77, 78]. Labuda demonstrated that this microscope can perform atomic scale imaging in solution with silicon cantilevers, as in figure 2.1, proving the high stability of this microscope. In

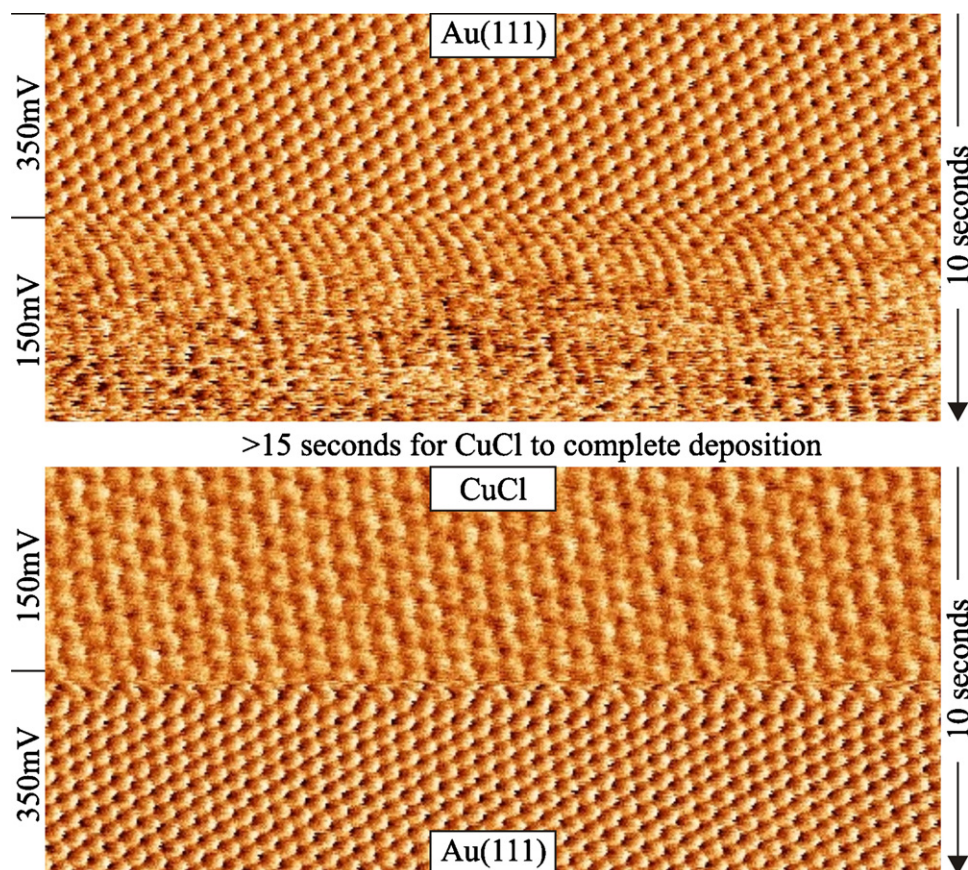


FIGURE 2.1: “Lateral force map of the deposition and desorption of CuCl on the Au(111) surface in 0.1 M  $\text{HClO}_4$  + 1.5 mM  $\text{Cu}(\text{ClO}_4)_2$  +  $10^{-5}$  M HCl (normal load 2.0 nN, scanning at 25 lines/s). The switching of the sample potential (vs Ag/AgCl) is indicated on the left. Lattice spacings: CuCl 3.67 Å and Au(111) 2.88 Å. Average friction for CuCl covered and Au(111) surfaces:  $f_{Cu} = 100$  pN,  $\sigma_{Cu} = 20$  pN;  $f_{Au} = 240$  pN,  $\sigma_{Au} = 30$  pN.” This image demonstrates the high resolution capabilities of the EC-AFM microscope used in this Thesis. Reprinted with permission from reference [76].

Copyright 2010 Review of Scientific Instruments.

this project, the common silicon AFM cantilever was replaced with a pipette cantilever and the mechanical stability of this new system was confirmed through measurements on carbon nanotubes (see section 3.3.1). To do this, the ‘forest of peaks’ [39] problem and actuation problems had to be dealt with systematically.

The probe design consisted of a borosilicate pipette, bent to resemble the geometry of typical silicon cantilevers. Bent probes can be approached to a surface that is perpendicular to the motion of the pipette, and this surface is also perpendicular to the incoming detection laser. This contrasts with the shear force detection mechanism more commonly used in SICM systems. As detailed in section 1.4 shear force motion can lead to damage to both tip and samples, as well as lateral force averaging. In contrast to the bent pipette probe used by Hersam [70], our probe design include longer tips to limit Quality factor

damping in liquid and the ‘forest of peaks’ problem. Longer, thinner probes result in less stiff probes which can be oscillated more easily.

The method in which the probes are oscillated can also ameliorate these issues. Commonly used piezo acoustic oscillators not only excite the resonance frequency of the cantilever but will indiscriminately excite other mechanical resonances within the AFM. When AFM is performed in liquids, the resonance peak of the cantilever suffers a reduction in quality factor and amplitude. Therefore, the unwanted mechanical resonances are relatively larger, and the ‘forest of peaks’ problem appears. To avoid this difficulty, photothermal actuation may be used to oscillate the probe. In this case the actuator is a light source shone on the cantilever, thereby heating the probe. Modulating the intensity of the light source causes an oscillatory heating. In turn, this creates a periodic mechanical strain which oscillates the cantilever. By using photothermal actuation, only the resonance peaks of the probe itself are excited. This method is still challenging, as these probes are much larger than commercial silicon cantilevers and are transparent to the wavelength of the light source used herein. These are workable challenges, however, as described more fully in section.

Finally, the success of this system relies on its acquisition system and low noise design for highly accurate results. The GXSM controller used has 8 16 bit 100 kHz ADC input data channels and outputs (see Chapter 2) to control the scanning routines of the sample positioning piezo. The combination of low current amplifiers and careful electronic shielding allows for measurements on the range of 10s of fA to mA with 1 MHz maximum bandwidth [79] in the current channel, and nN force sensitivity. This combination of features demonstrates a powerful and unique tool built to perform difficult and important material measurements.

The probes described in were designed and created by the author. Dr. Aleks Labuda built the electrochemical atomic force microscope (ECAFM) described and used in this project. Dr. Aaron Mascaro created a new signal box for the ECAFM. Dr. Andreas Spielhofer modified and created CAD drawings for the creation of AFM heads and sample holders. Dr. Yoichi Miyahara provided technical assistance in the reparation of the ECAFM and measurement apparatus.

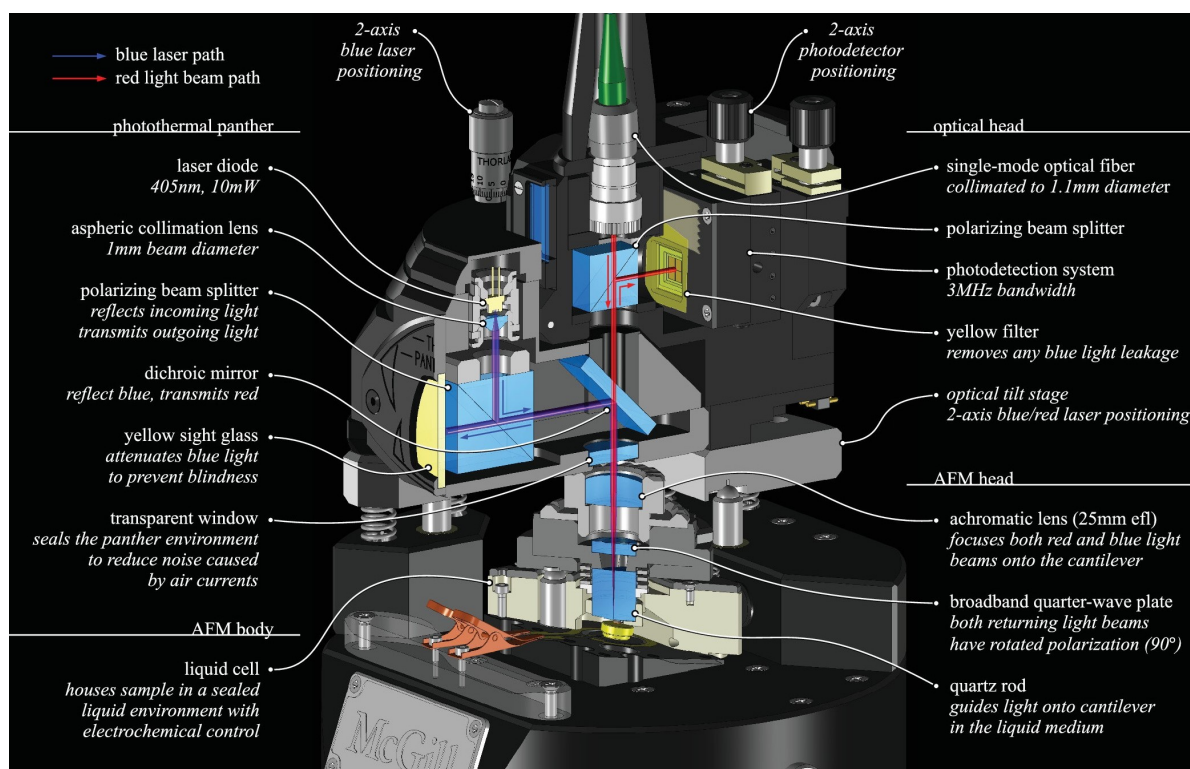


FIGURE 2.2: A schematic of the Electrochemical - Atomic Force Microscope built by Aleks Labuda. Reprinted with permission from reference [77]. Copyright 2008 Review of Scientific Instruments.

## 2.2 Scanning Probe Hardware

The goal of this project was to perform spatially resolved electrochemical measurements with force feedback. An existing highly stable electrochemical atomic force microscope (EC-AFM), originally created by Alex Labuda [77], was adapted by replacing the common silicon AFM cantilever with a new type of probe made from a pipette (see section 2.5) and adapting the microscope to allow small electrical currents to be measured. Figure 2.2 depicts the components of the EC-AFM microscope and figure 2.3 portrays how the pipette probe fits in the microscope in reference to the AFM head.

This AFM, which was built and used to perform measurements in electrochemical conditions, has many properties that allowed for easy adoption of AFM-SICM probes (e.g. its electrochemical cell, photothermal excitation, easy access to the sample stage, and lack of “black box” components). The AFM is also very stable in terms of drift and frequency noise, as demonstrated in figures 2.22 and 2.24 of 2.5.6. This is crucial given that the pipette probes used are susceptible to mechanical noise due to their low frequency (1-20 kHz, see 3.2).

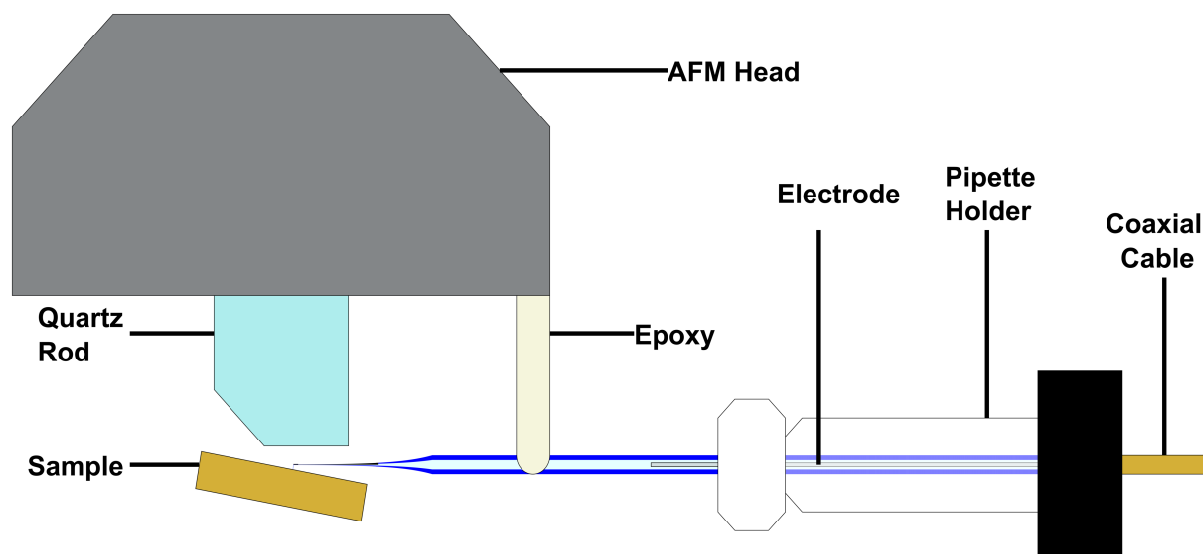


FIGURE 2.3: The pipette probes were attached to the AFM head, which can be seen in figure 2.2. Further details of the probe geometry can be seen in figure 2.11.

The microscope's built-in electrochemical cell was not used, despite its potential utility in establishing an electrochemical environment, because the long capillary ends of the probes prevented its use. Specially-made Teflon protectors made by Labuda [77] were, however, effective at protecting the piezo from electrolyte.

This easy access allowed the preamplifier head stage and other current measuring devices to be attached close to the probe from the side, thus minimizing electronic pick-up noise. These combined SICM–AFM probes are approximately 5 cm long, which is notable, given that most AFMs do not have clearance for such a long probe. Note that a  $10^\circ$  tilt exists between the sample and cantilever to maintain clearance between the tip holder and sample. The sample is tilted, rather than the probe, which facilitated the machining process by keeping all the optical components in one axis.

The optical deflection sensing system needed to measure the deflection (and thus force) acting on the AFM cantilever which presented a major challenge in the use of this microscope. The beam deflection system is compatible and works well with silicon (Si) cantilevers. The position of the Si cantilevers must be more exactly regulated than the pipette probes because their reflective surface areas are smaller (e.g. MLCT, Bruker [80]). Given this challenge, as well as the fact that Si cantilevers are identical in size, a holder was specifically designed for ease of positioning in the microscope. Si cantilevers can be remounted efficiently as they are held on the AFM head by a plastic clamp and an



alignment chip. Pipette probe cantilevers are much more difficult to align because they are individually hand crafted and thus have a substantial variability in geometry. The variability in geometry pertains to the position and angle of the reflector. The reflector was glued to the probe, and during the curing of the glue the position of the reflector could settle 500  $\mu\text{m}$  away from the set position, and the angle of the reflector could deviate from parallel by up to 5 degrees.

The various relevant AFM components are described in more detail in 2.3 and 2.4.

## 2.3 Beam Deflection System

A common method of tracking the AFM probe is to reflect a light source off of the cantilever to a photodetector which records the position of the cantilever by changes in the position of the reflection off of the probe [81]. The optical pathways of the AFM system used in the present study are shown in the above schematic [77]. A super luminescent diode or SLD provides a red light-source with short coherence [82]. This light first passes through a polarization-maintaining optical fiber to the AFM. The light then passes through a polarizing beam splitter which polarizes the light, through a dichroic mirror which has no effect on the beam, and through a quarter waveplate which rotates the polarization by  $45^\circ$ , after which it arrives at the probe. The light is then reflected into the microscope. The light returns through the quarter waveplate where the polarization is rotated by a further  $45^\circ$ , arrives at the beam splitter, and is reflected to the photodetector board where the position of the light beam is measured. The photodetector board consists of 4 quadrants. Each quadrant of the photodetector produces a voltage in relation to the intensity of the light which is incident on that section. The sum of the four signals indicates how much light is being reflected onto the board in total and is the first signal to be maximised. Summing the two top signals and subtracting the two bottom signals gives the AFM deflection signal, whereas the sum of the two signals on the right, minus the two signals on the left yields the lateral signal. The AFM signal is used to measure the force perpendicular to the AFM probe tip, whereas the lateral signal is used to measure the torsion of the tip resulting from lateral forces. To maximise sensitivity, the SUM value is maximised, and both the sum and lateral signals are minimized. Satisfying these conditions results in maximum amount of detected light, and the maximum intensity will be close to the center of the photodetector. At this position, if the probe is deflected vertically or laterally and the amount of light changing position from one quadrant to another is maximized. These conditions ensure maximum sensitivity to applied forces.

Lasers can be used as the light source for the beam deflection system, although their coherence length can cause spurious interferences [83] leading to noise in deflection sensing. The signal is very sensitive to position changes of the probe, with the full distribution going from maximum to minimum amplitude over a quarter of the wavelength of the laser light [84]. With a laser source of 650 nm, this would correspond to 162.5 nm from minimum to maximum. This is an interferometry signal, and while it could be used as a very sensitive measurement of probe position, it increases noise in the four-quadrant deflection measurement technique. Rather than simply measuring the movement of the light over the surface of the photodiode, the intensity of the light is constantly changing. It is difficult to separate the two effects in real time. To avoid these problems, a superluminescent diode is used [82]. These diodes can be of a similar intensity to lasers with minimal angular dispersion, preventing the light from spreading out over the course of the optics. Due to their much shorter coherence length the back reflections do not result in interference. <sup>1</sup>

## 2.4 Control Electronics and Data Acquisition System

We used a Soft dB digital electronics and open source SPM GXSM control and data acquisition software (MK2-A810, Soft dB, [85]). This controller has 8 16 bit 100 kHz ADC input data channels and outputs to control the scanning routines of the sample positioning piezo. It controls a coarse adjustment motor which will bring the pipette down to the sample, and applies a bias which can be used to control the voltage of the electrode in SICM measurements.

The GXSM hardware and software allowed for a great deal of freedom in measurement technique. The software provides the scanning routines and point spectroscopy capabilities of most AFM software. The Python scripting feature allows for open-ended creation of measurement routines. By specifying vectors of spatial movement, time, bias, and sampling values, any scan possible can be created. Automating different testing procedures saved an immense amount of time (see Appendix B).

---

<sup>1</sup>Our SLD broke at one point, and during this time we did try to use the interferometry signal to track the position of the probe. We observed a lot of mode hopping, even after controlling the temperature of the laser. Our assumption is that reflections of the laser light were directed back into the laser which caused the mode hopping. While this method could be very useful in tracking these probes, we required more equipment to eliminate this problem, and we returned to the SLD approach.

To scan the sample, a high scanning voltage needs to be applied to the piezo. The high voltage amplifier receives a signal from the SPM controller and amplifies the signal, which is then applied to the piezo which controls the position of the sample stage. Labuda [77] used a 120 V high voltage amplifier (AFM CU, Omicron [86]); however, this was switched to a 400 V amplifier (HVAMP-400-3, Nanonis [87]) to achieve a larger range.<sup>2</sup>

The typical settling time scale of a damped harmonic oscillator is given by  $Q/f$ , where  $Q$  is proportional to the inverse damping of the oscillator. Due to the low ratio of  $Q$  factor to resonance frequency of the AFM-SICM probes,  $Q$  control was used to reduce the  $Q$  factor and scan faster without ringing.  $Q$  control refers to a method by which the electronically measured resonance response of a cantilever can be modified to achieve more advantageous resonance characteristics, such as  $Q$  enhancement for increased sensitivity, and  $Q$  reduction for shorter settling times in tapping mode [88]. It is important to note that this does not change the geometry or fundamental resonance characteristics of the probe, rather, this is an electronic modification of the effective  $Q$  factor. To do this, a function generator supplies the input oscillatory signal to the blue laser (DL-LS5042, Sanyo [77]) as in figure 2.4. The blue laser shines on the probe which causes it to oscillate. The probe position is then measured by the photodetector and this probe position signal is amplified and phase shifted. That signal is then added to the original oscillatory input signal which then goes to the blue laser, thus completing the loop. In this case, a  $270^\circ$  phase shift was used to maintain the same resonance frequency while decreasing the effective  $Q$  factor [89].

SICM requires measurement of a very small current, on the order of picoamps to nanoamps. At these current levels, electronic noise in the lab can dominate the signal unless the measurement is engineered to reduce the noise. Coaxial cables and small separations between the measurement and the measuring device are thus critical. We used two different current amplifiers:

The SR570 amplifier has a very low noise at currents on the order of pA (SR570, Stanford Research Systems [79]). It also had a large dynamic range of amplification settings and can measure mA currents. This was convenient as testing the probes would require doing current measurements in a bath of electrolyte where the current is on the order of nA per volt applied, whereas the droplet measurements were on the order of pA. This amplifier does not have a preamplifier head that can be brought close to the probes, so shielded cables were important to eliminate excess noise.

---

<sup>2</sup>Piezo tubes will depolarize or short circuit via dielectric breakdown if the voltage is too high. Increasing the voltage range must be done judiciously.



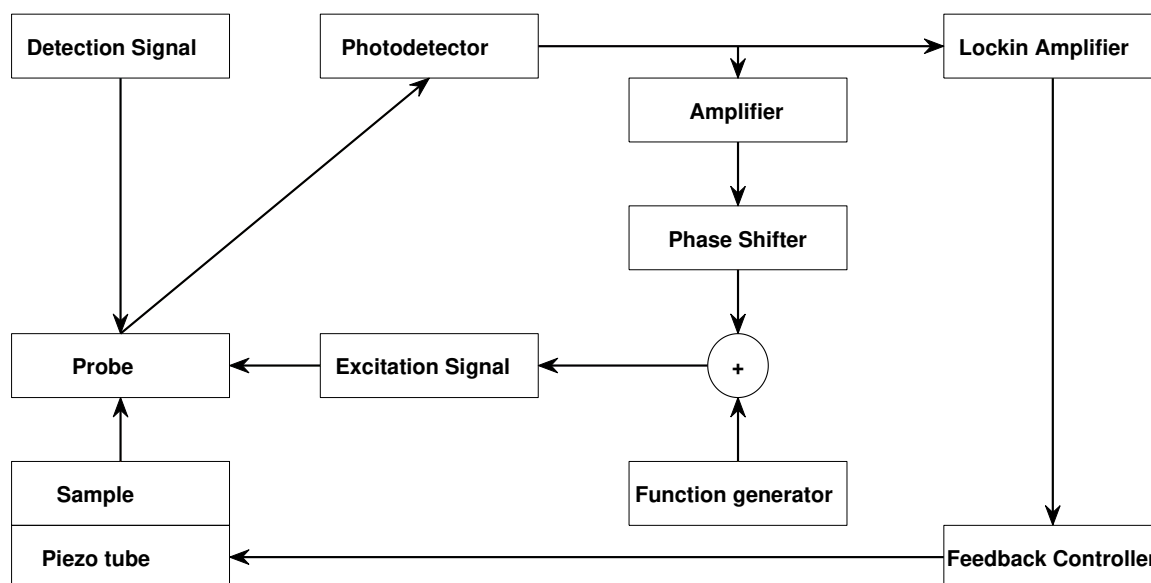


FIGURE 2.4: The Q control circuit can be used to reduce the effective Quality factor of the probe’s resonance peak. A function generator creates an oscillatory signal at the probe’s frequency. This is used as the excitation signal to oscillate the probe. The movement of the probe is detected by the photodetector via the detection signal. This detected signal is amplified, phase shifted by  $270^\circ$  and added to the function generator signal to be used as the excitation signal. The signal as the photodetector also goes to the lockin amplifier which measures the amplitude of the signal. This amplitude value is used by the feedback controller to control the piezo tube, and maintain the probe-sample distance.

The Axopatch 200B is specifically for low-noise low current electrophysiological patch clamp measurements (Axopatch 200B, Axon Instruments [90]). It is thus specifically designed to accommodate pipettes, and importantly has a separate preamplifier head designed to be used with pipettes. The Axopatch is designed to reduce the artifacts caused by the capacitance and resistance of pipettes (see section 1.3.1), so it compensates through an offset resistance and capacitance control. Small pipette diameters like the pipettes used here have significant capacitance (on the order of pF), and we made use of this feature. Grounding of the Axopatch is more complicated than that of the SR570. Defining the ground needs to be done carefully, as stray voltages will result in currents that saturate the 20 nA range of the controller.

In most SICM and electrophysiology systems the pipette is mechanically fixed at one point. In electrophysiology, where patch clamp amplifiers are commonly used [91], the pipette is held by a compression fitting which also holds an electrode in the pipette. In this AFM-SICM probe setup, however, it is always necessary to keep the probe in a fixed



FIGURE 2.5: The pipette holder is rigidly tightened to the preamplifier in the original configuration.



FIGURE 2.6: The coaxial cable connection replaces the rigid connection

position relative to the AFM head. Probes must be rigidly affixed to the AFM head, otherwise deflection sensing and positioning relative to the sample will be compromised. Extending from the point where the probe is glued is approximately 5cm of capillary tubing which leads to the probe (see figure 2.3). The Axopatch 200B system was used initially by placing and finger tightening a compression fitting (1-HL-U, Axon Instruments [92]) on the capillary tube end of the probe. This compression fitting was then screwed into the preamplifier headstage of the patch clamp amplifier as seen in figure 2.5. To avoid applying stress on the fragile glass tubing between the fixed glue point and the compression tubing, the mounted pipette probe with attached compression fitting was placed and held in the AFM microscope. The preamplifier headstage was held in a vice to prevent its movement. Then the preamplifier and vice were slowly and carefully moved to the compression fitting electrode until the electrode was inserted into the preamplifier. At this point, any small movement of the vice, preamplifier, and AFM head would break the probe. Due to this condition, the probe was approached to the surface before this process could occur, which increased the possibility of accidents, as a bit of stress to the end of the probe can result in the displacement of the probe tip which can easily crash into the sample surface and break the probe. This process resulted in many broken probes.

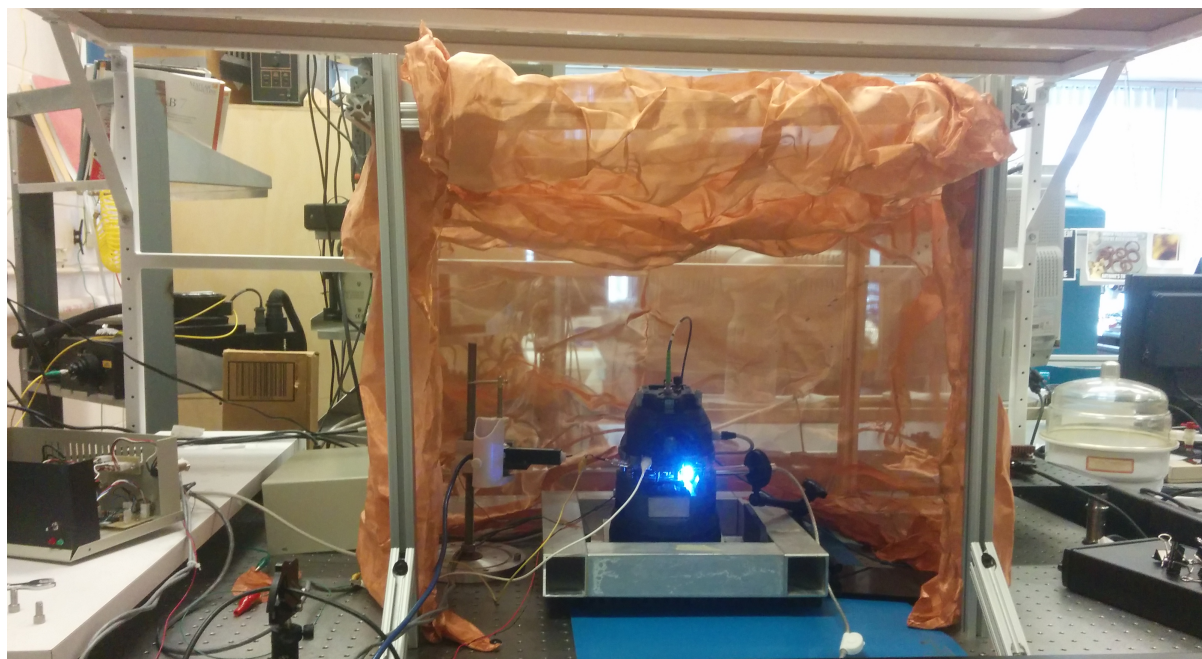


FIGURE 2.7: The first version of the Faraday cage consisted of a copper mesh held by a metal frame.

This fragile, brittle connection was remedied by using a short piece of thin, coaxial cabling as strain relief to make a short connection between the compression fitting and the preamplifier head, as seen in figure 2.6. This meant that there was minimal force applied between the preamplifier head and the probe end. Also, the coaxial cable was grounded properly, and resulted in no increase in noise. The preamplifier head stage exists so that the small measured signals produced at the electrodes are contaminated by as little noise as possible before being amplified. Elongating the distance between the electrodes and the preamplifier stage could create additional noise. Unshielded cable contributes a large amount of noise proportional to the length of the wire; however, this effect was noticed when shielding was used.

The signals that need to be measured by the SICM technique are on the order of hundreds of fA. Because of this, the noise of the system had to be reduced as much as possible to make this small current visible. This was accomplished via a Faraday cage. Initially, a large cage structure with copper mesh drapes was used, which is shown in figure 2.7.

This accommodated the preamplifier head stage within the Faraday cage; however, AFM oscillation noise from air currents prevented the pipette probes from being oscillated with an amplitude on the order of 10 nm. The Faraday cage did little to reduce this noise. A

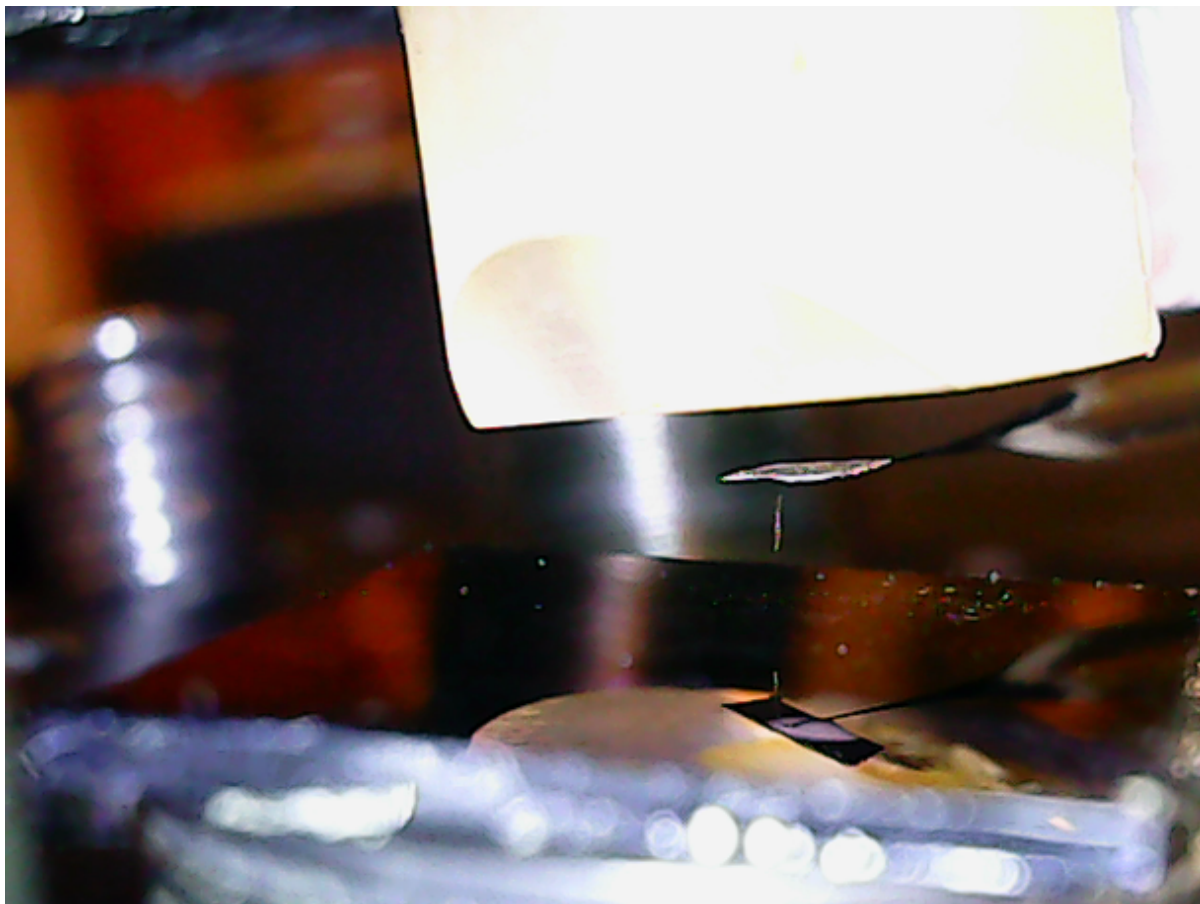


FIGURE 2.8: This image was taken via USB microscope. This viewpoint allowed for fast approaches to the sample surface.

large amount of noise-dampening foam would be required to dampen noise in the system given the cage's size.

While technically possible, the foam would be unwieldy when trying to access the microscope, rendering this solution impractical. Because of this, a Faraday cage box previously created by Labuda [77] was used. This wooden box is lined with aluminum foil and sound dampening foam. The fit is tight, so the preamplifier headstage will not fit inside with the microscope. Because of this, the coaxial connection between the pipette probe and headstage was elongate to 10 cm. Noise was not impacted by this elongation because of the grounding of the cable.

Carefully approaching a fragile probe from macroscopic distances down to nm with scanning probe presented a major challenge. Without being able to observe the position of the probe with respect to the surface, it is easy to over-approach and crash the probe,



resulting in damage. One way to address this is to point a USB microscope (B005 Digital Microscope [93]) at the sample and probe. The view from this USB microscope is shown in figure 2.8. The probe is quickly approached to the surface of the sample until the gap between the tip apex and the reflection of the tip apex cannot be resolved, at which point automatic approach is used, which is much slower, but also much safer. The routine for approaching is to set an approach condition relative to the free oscillation amplitude of the probe, the rationale being that a surface close to an oscillating probe will lead to significant force gradients. These force gradients will change the probe resonance frequency, which manifests itself as a reduced probe oscillation amplitude even before repulsively crashing/touching the surface. This allows the approach to stop at small tip-sample interactions. The GXSM program is thus instructed to approach the sample until the oscillation amplitude of the probe is 90% of the initial free oscillation amplitude. To do this, the sample piezo extends upwards towards the probe tip. If the oscillation reduction condition is not met over the 10  $\mu\text{m}$  extension of the piezo, then the piezo is retracted downwards, away from the probe. Then a voltage is applied to the coarse approach motor which will move the probe downwards by 5  $\mu\text{m}$  towards the surface. This process is repeated until the probe and sample meet, as defined by the free oscillation amplitude reduction condition.

Once engaged (i.e. close to the surface), GXSM is used to scan the surface in several modes. Alternatively, the deflection signal as well as the simultaneously acquired current signal can be used to perform noise characterization of the system.

## 2.5 Combined SICM–AFM Probes

A new type of probe with specific traits was required to perform the proposed combined AFM-SICM measurements because the probe needed to be able to perform AFM measurements as well as SICM measurements.

Hollow probes are required for performing SICM measurements so that electrolyte and an electrode can be placed inside, allowing an ionic current to be passed through the tip of the probe. To optimise the SICM probe, the tip of the probe must be as small as possible, as the size of the hole at the tip controls the resolution of the technique. Small, long, tapered tips increase the resistance of the probe to the ionic current (see section 1.3.1), so the measured signal decreases.

To optimise AFM resolution, the radius of the tip apex must be minimized. Dimensions of the probe geometry must be chosen to attain a reasonably small cantilever spring constant (to maximize force sensitivity), high resonance frequency (to minimize noise and maximize the potential AFM measurement speed), and allow it to be driven to oscillations and the motion of this oscillation must be detectable.

To produce probes with all of these capabilities requires rigorous optimisation, as well as compromises. The following section describes the choices made, how the probes were fabricated, how they were filled with electrolyte, and their performance as AFM sensors. One of the most surprising results of the current project was that these pulled pipette probes can be made to oscillate at a substantial amplitude just using light. This facilitates many operational aspects of using pulled pipettes as AFM sensors.

### 2.5.1 Material choice for pulling pipettes

To create the probes, pipettes were selected as a starting material. The decision was made not to use microfabrication. Given the paucity of results in the literature and discussions with vendors, it was decided that such systems are not reliable at this time and have limited flexibility at great expense. Based on experience with pulling and bending optical fibers for Scanning Near Field Optical Microscopy applications and microbottle resonators [94], it was decided that the potential of pulled capillary tubes as combined force and SICM/SECM sensors would be investigated. These sensors are created by heating and pulling apart capillary tubes in a commercial pipette puller (typically used in electrophysiology). This technique is advantageous because all processing can be done in the lab, guaranteeing ultimate control and flexibility.

Table 2.1 provides a summary of the properties of various commercially available capillaries.

The pipette puller that we have in our lab is the Sutter P-87. This version of the puller is incapable of producing enough heat to reach the softening temperature of the quartz glass (Heraeus HSQ300, Sutter Instrument Company [98]). Even if we were to buy the P-2000 puller, the probes must be bent after this. This would require a CO<sub>2</sub> laser, or some comparably expensive system to heat and bend the probe. For these reasons, quartz was not considered for our situation. The difference between the main types of glass comes down to the properties of softening temperature, dielectric constant, and cost. For

<b>Glass Type</b>	Borosilicate (Corning 7740)	Aluminosilicate (Schott 8252)	Quartz (Heraeus HSQ300)
<b>Annealing temperature (degrees C)</b>	560	725	1220
<b>Softening temperature (degrees C)</b>	821	935	1770
<b>Dielectric constant</b>	4.6	6.1	3.81
<b>Cost per capillary (for filamented, 100-50-10) (USD)</b>	0.24	1.91	1.45

TABLE 2.1: Properties of various commercially available capillaries. [95][96][97] Product code 100-50-10 refers to an outer diameter of 1.00 mm, inner diameter of 0.50 mm, and length of 10 cm [98].

our application we did not initially anticipate that dielectric noise, which would favour quartz, to play a major role.

Aluminosilicate (Schott 8252, Sutter Instrument Company [98]) has a higher softening temperature than borosilicate; however, both may be pulled by the P-87 pipette puller. Aluminosilicate capillaries are 7 times the price of the borosilicate glass, which is not prohibitive. Aluminosilicate glass’s dielectric constant is significantly higher than borosilicate. This difference leads to larger capacitance in the electrochemical system, which is undesirable. Furthermore, borosilicate pipettes are more commonly used in existing literature, and more varieties are produced by the supplier. Due to these factors, borosilicate was chosen for this work.

Borosilicate capillaries (Corning 7740, Sutter Instrument Company [98]) can be purchased with a variety of inner and outer diameters. When deciding on which to use, the Sutter Pipette Cookbook was consulted, which states: “To achieve higher resistances and smaller tips, use thick-walled glass and a trough filament” [99]. This guideline was followed given that the current project required the smallest apertures/tips possible. Borosilicate glass retains the inner diameter to outer diameter ratio as it is heated and pulled [98]. As the pipette is pulled and heated, the glass separates into two pipettes when the “bridge” of softened glass between them has become too thin to support the mechanical strain (see figure 2.9). For the same glass cross-sectional area at the tip the hole of the thick-walled glass will thus be smaller. This means that smaller outer diameters (relevant for AFM resolution) can be achieved with thin-walled pipettes, but smaller inner diameters (relevant for SICM resolution) can be achieved with thick-walled pipettes.

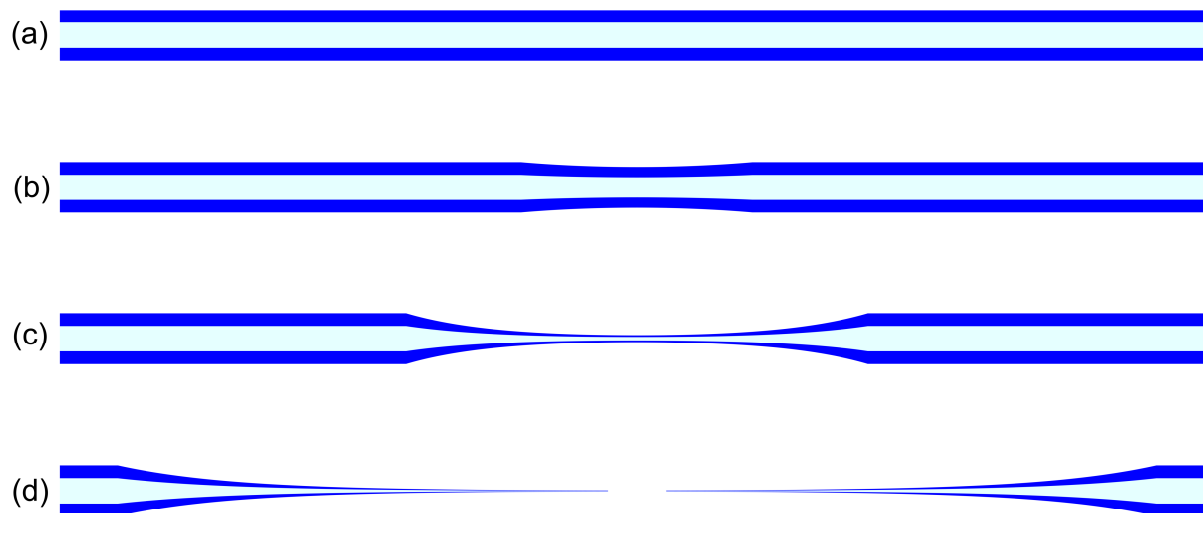


FIGURE 2.9: As the pipette is pulled and heated, the glass separates into two pipettes when the “bridge” of softened glass between them has become too thin to support the mechanical strain. We can see this in the four illustrations of the pulling process. (a) The first capillary is shown before being manipulated, (b) the second has started to melt, (c) the third has melted and is being pulled apart, and (d) the fourth shows the completion of the process.

Assuming the ratio of outer diameter to inner diameter is kept constant, different diameters of capillaries are available. The Sutter Cookbook also advises smaller diameter capillaries to make pipettes with smaller tips [99]. This is to accommodate different sizes of electrodes. A silver wire electrode of  $250\ \mu\text{m}$  diameter (99.99% purity, World Precision Instruments [100]) was used so that the electrode could still be inserted into the smallest diameter pipette. The electrode was chlorided by immersing the silver wire in bleach (Clorox, [101]) for an hour [102].

## 2.5.2 Pipette Pulling Parameters

Pipettes were pulled using the Sutter P-87. By controlling several parameters, a variety of pipette geometries can be created using the P-87. The parameters generally control the taper length and tip size. These parameters are coupled, but there are some combinations of parameters to, for example, maximize the opening angle while minimizing the tip radius.

The Sutter P-87 allows several parameters to be selected:

1. Heat

The first step of the pull process is the heating of the capillary. The heat value is



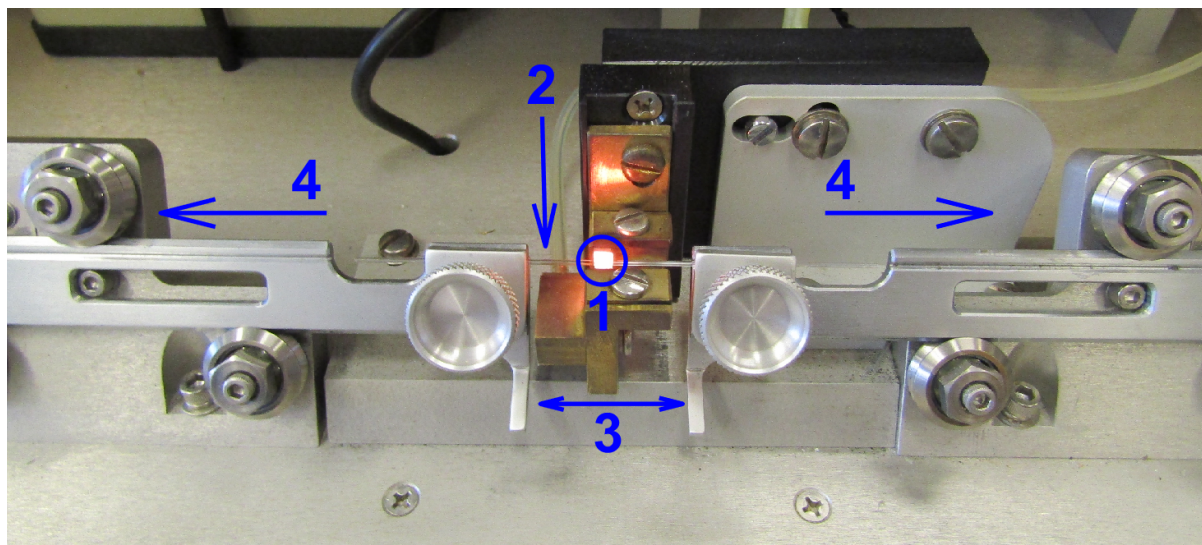


FIGURE 2.10: The pipette pulling process begins once a capillary tube has been loaded. The (1) platinum filament produces heat which softens the capillary tube locally. A gravitational weight from a weight within the puller pulls the capillary apart. When the capillary is (3) elongating at a sufficient velocity, the puller (4) quickly pulls the capillary apart into two separate pipettes.

related to the current passed through the platinum filament. This causes an increase in temperature due to resistive heating. This current to heat conversion creates reproducible pipettes, but variations can occur if the relation between current and heat is modified. As seen in figure 2.10, the heating occurs in a fixed, repeatable geometry. If the filament is deformed, it will heat the capillaries in a different configuration, with different results. Furthermore, humidity or temperature in the room can change the rate of heat dissipation of the filament. To address this, the ramp test is implemented in the controls of the P-87. This program pulls a capillary while the heat value is ramped from 0 to a value at which the probe softens. As soon as the probe softens, the puller senses that the capillary has become elongated and the routine stops. This ramp test value is used as a benchmark for any further pipette creation. This can be seen in any literature referencing programs made using these pullers. Heat values are quoted as “+Value”, for example “+15”, meaning that the desired value is “ramp value + 15”. Higher heat values produce longer and smaller tips.

## 2. Velocity

Once the puller has heated the capillary to the point of softening, the gravitational force applied by the plunger in the pipette puller begins to elongate the capillary, and the heated area begins to thin. As this elongation occurs the puller measures the

movement. Once this movement reaches a speed given by the Velocity parameter, the pull process is initiated. Larger velocity values result in sharp pipettes.

### 3. Pull

Once the puller has hit the Velocity threshold value, the Pull procedure is initiated. The force acting upon the capillary here comes from a plunger in the pipette puller, and a solenoid. When the pull value is 0, this means that only the gravitational force of the plunger is applied to the capillary. Non-zero values are related to the amount of current applied to pull a solenoid, which in turn pulls the capillary. Larger pull values lead to sharper and longer pipettes.

### 4. Pressure

While the pull is occurring, the capillary is simultaneously actively cooled by a stream of air aimed at the heated area of the capillary. A pressure value of 500 produces a stream of air of 2 psi. A higher-pressure value increases the cooling rate, which produces shorter tips.

### 5. Time

The time value is multiplied by 0.5 ms to get the actual time that the pipette puller applies the air flow and pulls the capillary. It begins counting down as soon as the velocity tripoint has been reached. This time is usually related to the type of filament and type of capillaries that are being pulled. For box filaments and thick-walled glass, which were used in the present study, greater Time values are required.

### 6. Loops

A loop refers to one cycle of the heat-pull process. In more complicated pipette pulling routines, small Velocity and Time values can be used to progressively elongate the tapered area without separating the capillary into two pipettes. These programs can iterate many times to slowly create very long pipettes. These elongation steps may be followed by a final hard pull of a high pull value to produce a small tip.

After many experiments the following optimized parameters were selected:

Capillaries BF-100-50-10 [98] (Product code BF100-50-10 refers to borosilicate capillaries with filaments and outer diameters of 1.00 mm, inner diameters of 0.50 mm, and lengths of 10 cm)

Heat Ramp +15

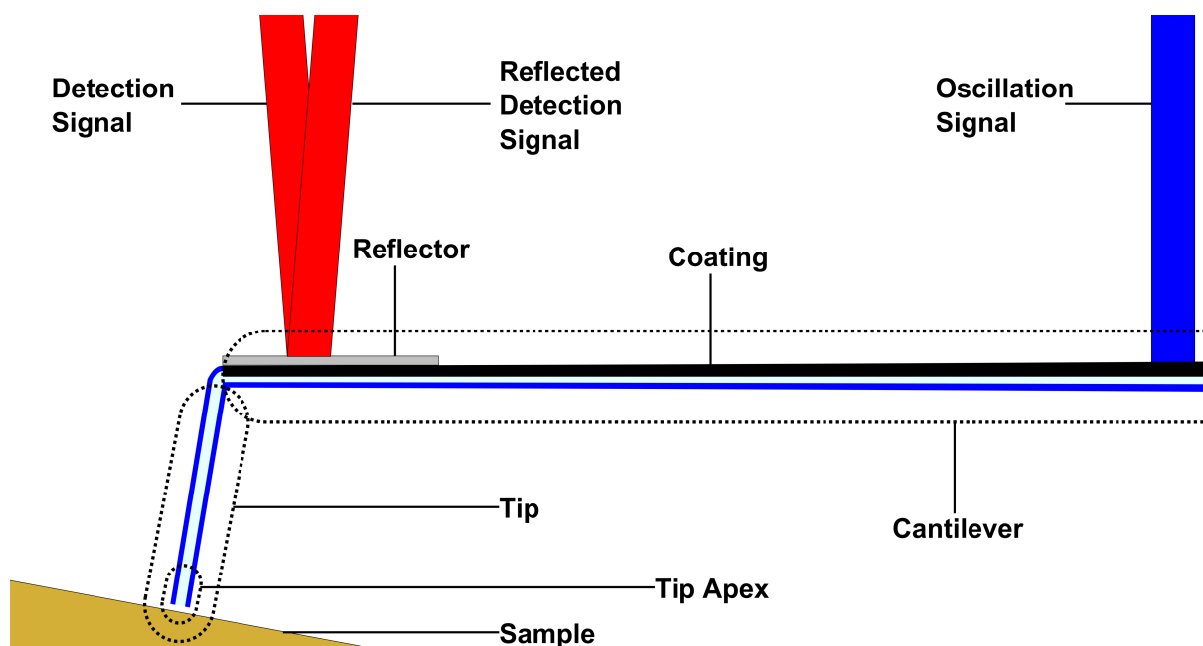


FIGURE 2.11: A schematic of a bent probe mounted in the EC-AFM. The blue line shows the oscillation light source which oscillates the pipette probe. The motion of the probe through a detection signal mirrored off the reflector to the photodiode.

Pull 5

Velocity 80

Time 170

Pressure 300

These parameters produced pipettes with sub 100 nm holes at the tip and tapers of several millimetres with a 100% yield success rate, as long as the filament was not damaged. The length of the taper is important for the next step—the bending process to define the AFM tip and cantilever. If the taper is too short then the probe is impossible to bend without damaging the tip.

### 2.5.3 Creating AFM Cantilevers from Pulled Pipettes

To use these pipettes as AFM probes in our Electrochemical AFM they must be bent to resemble the geometry of typical silicon cantilevers (see figure 2.3). Bent probes can be approached to a surface that is perpendicular to the motion of the pipette, and this surface is also perpendicular to the incoming detection laser as shown in figure 2.11.

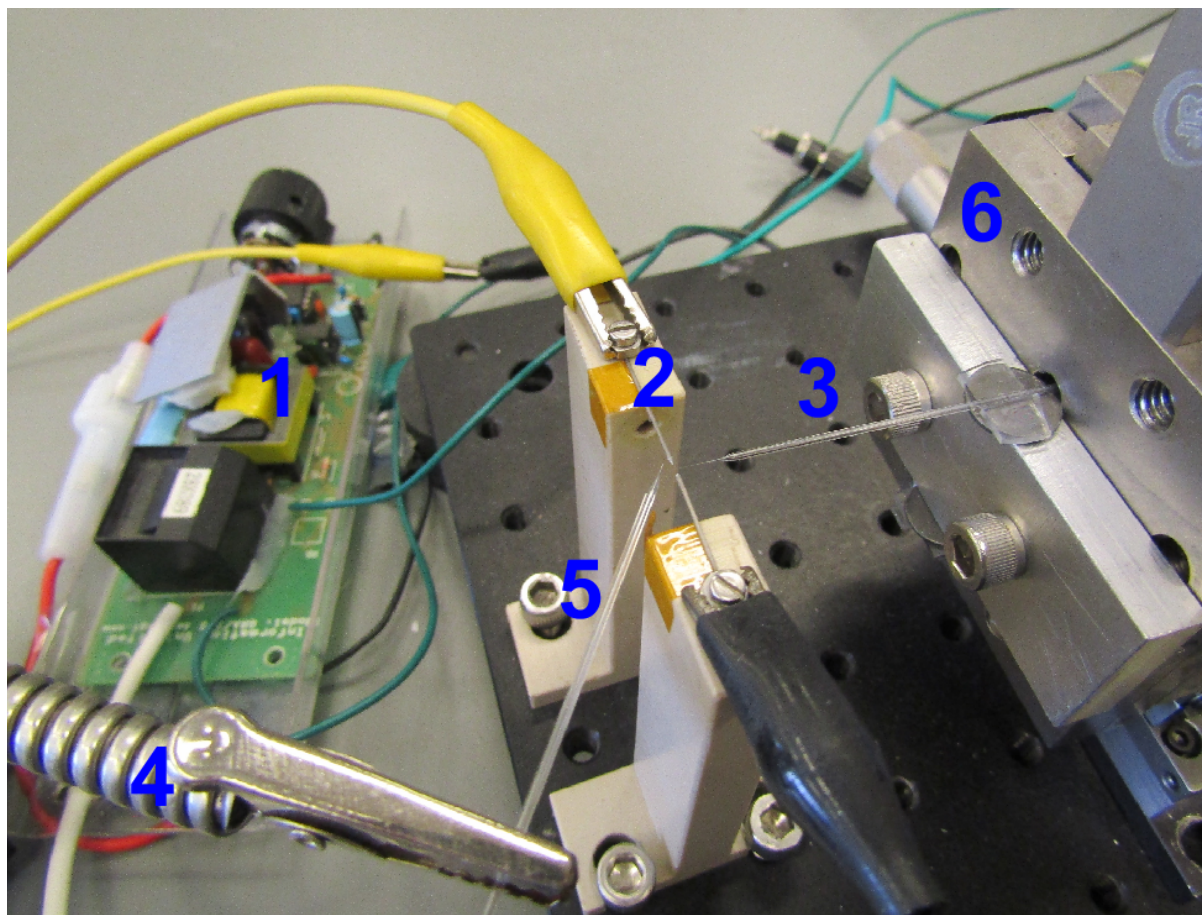


FIGURE 2.12: This apparatus was used to bend pipettes. The (1) high voltage circuit (see Appendix A) was connected to the (2) electrodes to create a localised plasma arc. The (3) pipette was mounted on a (6) micromanipulator (MB-PP2 Coarse Manipulator, Narishige [104] and GN2, Thorlabs [105]) and was brought into the plasma arc. A second (4) micromanipulator (462-XYZ-M ULTRAlign, Newport [106]) held another (5) pipette which was used to apply a force to the end of the first (3) pipette. By softening and applying force, the pipette was bent into the desired geometry.

To perform the bending process, the pipette is locally softened, force is applied, and it is bent in a controlled manner. Dielectric breakdown of air between two sharp tungsten electrodes (see Appendix D) was used to locally apply heat to soften the pipette pulled as described above. Similar setups of plasma discharge in air were used to fuse aluminosilicate or borosilicate optical fibers.

To achieve this, two electrodes separated by a few millimetres (see figure 2.12), and a large voltage (7500 kV [103]) was applied between them. Dielectric breakdown will occur at high enough fields, appearing as a plasma arc occurring between the electrodes. This heats the pipette and forces were controllably applied to the pipette to bend the glass while it is soft.



To create suitable force sensors, we must consider the probe geometry. The tip and cantilever (figure 2.11) can be considered as two springs in series. The deflection of the cantilever (and thus measured AFM signal) associated with a force between tip and sample can be reduced by the ratio of:

$$\frac{X_1}{X_2} = \frac{k_2}{k_1} \quad (2.1)$$

Where  $X$  is displacement (m), and  $k$  is the spring constant of springs 1 and 2 (N/m). The spring constant of these springs are:

$$k = \frac{3EI}{l^3} \quad (2.2)$$

Where  $E$  is elastic modulus (Pa),  $l$  is length (m), and  $I$  is the area moment of inertia ( $\text{m}^4$ ). The pipette is tapered, so it is some type of hollow, truncated cone with a nonlinear dependence of diameter on length. However, for an approximation of stiffness on short length scales (where  $r_o \ll L$  and  $\frac{dr_o}{dL} = \text{Constant}$ ) we can consider it to approximately be a hollow cylinder. The second moment of inertia for a cantilever deflected along the length axis is:

$$I_x = \frac{\pi (r_o^4 - r_i^4)}{64} \quad (2.3)$$

Where  $r_o$  is the outer radius (m) and  $r_i$  is the inner radius (m). The spring constant for a hollow tube is:

$$k = \frac{3\pi E (r_o^4 - r_i^4)}{64L^3} \quad (2.4)$$

From formula 2.4, we see that the sensitivity of the probe increases as the tip spring constant increases and the cantilever spring constant decreases. Stiffness increases as the length becomes shorter, and the radius becomes larger. The tip must be as short as possible to increase sensitivity. The radius will necessarily increase from tip to cantilever, but if the taper is more gradual then this has less of an effect on the stiffness.

Accomplishing this through the bending process requires control over the position of the pipette, the arc power, and force applied to the tip. By using a micromanipulator, the

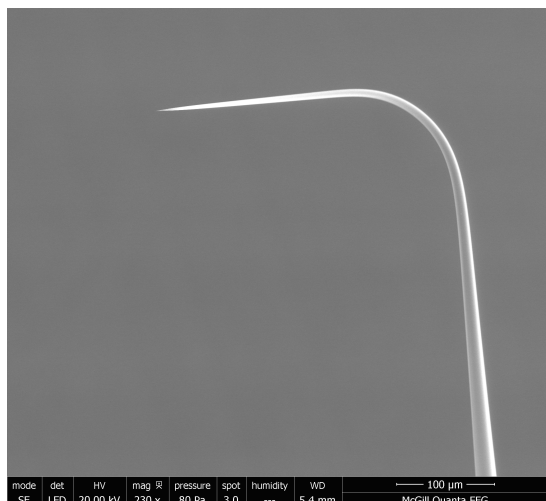


FIGURE 2.13: An SEM image demonstrating the bend and taper of the probe

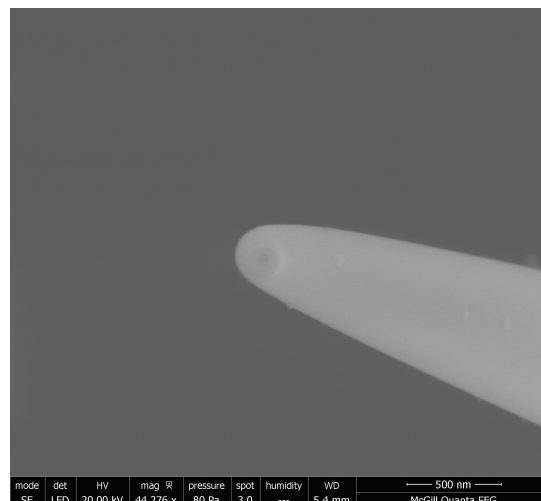


FIGURE 2.14: Higher magnification of the same tip. The tip hole is less than 100 nm in diameter.

probe can be reliably positioned in reference to the plasma arc, and thereby control the length of the tip and the angle of the bend. Arc power is controlled by a variable resistor (see Appendix A) so that the glass was softened enough to slowly and controllably bend without closing the channel odd within the pipette off. Force is applied near the tip apex during the bending to better control the direction of the bending. The force is applied by another pipette and controlled by another micromanipulator. The resultant pipette cantilevers are shown in figures 2.13 and 2.14.

Functional probes were made using these techniques, with measured spring constants in the range of 20-80 N/m. In silicon cantilevers, stiffness constants range from 0.01 N/m (MLCT, Bruker [80]) to 200 N/m (MPP-13100-W, Bruker [107]) depending on the intended use of the probe. In batch fabricated silicon cantilevers, microfabrication techniques lead to cantilevers of consistent spring constants within small tolerances. The difficulty in making cantilevers of uniform spring constant can be traced to their individual fabrication by hand and the lack of automation of these techniques. This led to phenomena such as buckling instabilities as seen in figures 2.15 and 2.16. When this occurs, the tip bends, but the cantilever moves much less. Probes with tip instabilities tended to be longer; thus, shortening the tips reduced the frequency of this occurrence.

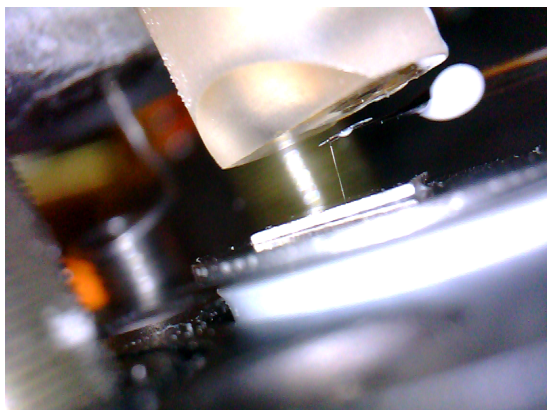


FIGURE 2.15: The probe tip meets the surface of a sample. No force is applied.

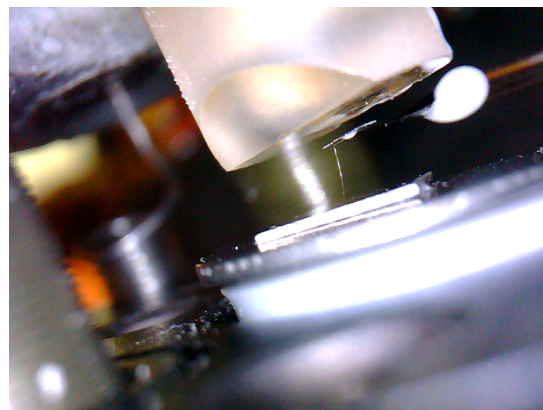


FIGURE 2.16: The probe tip bends outwards, but the reflector does not deflect.

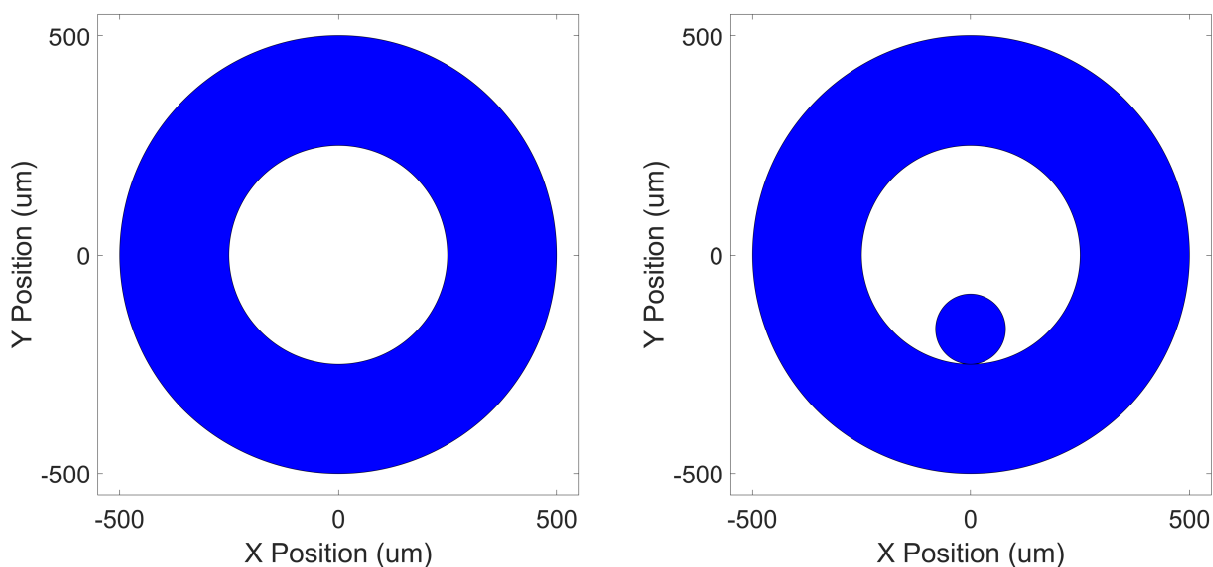


FIGURE 2.17: The figure to the left shows the geometry of a capillary tube without a filament, and figure to the right shows a capillary tube with a filament. Both have an outside diameter of 1mm and inside diameter of 0.5mm. With the inclusion of the 160μm diameter filament, the inside perimeter increase by a third of the original inside perimeter.

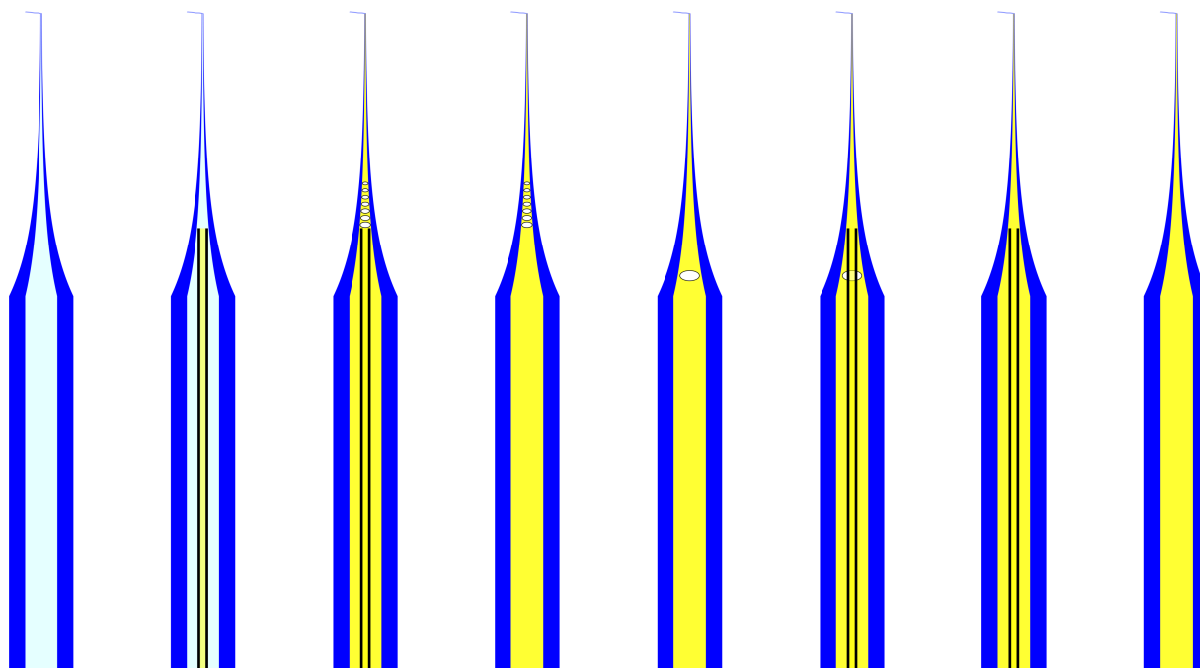


FIGURE 2.18: The first pipette is initially unfilled. A pipette filler is inserted, then liquid from the pipette filler is pumped into the probe resulting in the illustrated bubbles. The pipette filler is removed, and the bubbles remain. Then the pipette is placed in a vacuum chamber, and the bubbles reorganize. The pipette is removed from the vacuum chamber, the pipette filler is inserted, and more liquid is pumped into the probe. This removes the remaining bubbles and the pipette filler is removed.

### 2.5.4 Filling the SICM–AFM probe with electrolyte

Filling pipettes with liquid while avoiding air bubbles presented a major challenge during the present study. This was achieved using capillary forces, which depend on surface energy and area. By including a filament in the pipette, the surface area was increased substantially. Typically, the filament is a  $160\ \mu\text{m}$  thin rod of glass which is annealed to the inside surface of the capillary tubes [99]. This is crucial for filling the probe as the resistance of pipettes can be high enough that applying large amounts of mechanical pressure are not enough to fill these pipettes.

By taking a cross section of the pipette (shown in figure 2.17), it becomes obvious that by adding the filament the area which is filled by electrolyte will decrease slightly while the perimeter of this inner cavity will be increased substantially. This ratio is critical, as the capillary force between electrolyte and glass will only occur at the interfaces between the two. The higher the ratio of glass surface area to volume per unit length, the higher the amount of force per volume of electrolyte. For pipettes, tips of under  $1\ \mu\text{m}$  filaments are required to prevent air bubbles from becoming trapped in the pipette. [108]. It should



be noted that the filament is also made of borosilicate, meaning that the ratio of filament diameter to inner diameter of the pipette remains the same, which will have a negligible effect on the ionic resistance of the pipette.

The pipettes were difficult to fill with electrolyte <sup>3</sup> due to their long tapers and small diameters. The method that was found to work best was using a pipette filler combined with the use of the vacuum chamber as illustrated in figure 2.18. The pipette filler is a 10 cm long, 164  $\mu\text{m}$  in diameter, flexible syringe (MF34G-5, World Precision Instruments [114]). This can be inserted into a pipette up until the its diameter prevents it from being inserted. The pipette is then overfilled with electrolyte. After this process, some bubbles will remain in the tip of the pipette, past where the filler can access. The probe is then placed into a vacuum chamber (F42025-0000, Bel-Art [115]) and suctioned. The air bubbles move from the thinnest portion of the pipette tip and after a few minutes stop moving at section of the probe with a larger diameter. The probe is then removed from the chamber, and the pipette filler is reinserted into the pipette. Once the bubbles have shifted to a higher diameter area, the pipette filler flushes them out easily. In this way, the probes can be filled reliably within 10 minutes.

### 2.5.5 Probe actuation and deflection measurement

The two requirements of these bent probes for force sensing are actuation and deflection measurement. Deflection of the probe is required for optical beam deflection methods to be used to track forces felt by the tip. Actuation allows for the use of tapping mode, which is the least destructive method for the fragile tip openings and provides phase information which gives us some material properties in addition to topography. Furthermore, there is a well-known so-called ‘forest of peaks’ problem.

Most AFM measurements use piezo-actuation, where a voltage signal-controlled actuator mechanically oscillates the AFM cantilever. However, the piezo-actuator has its own frequency transfer function, as does the AFM itself. These mechanical modes will show up in a frequency sweep of the cantilever. In air and vacuum this will occur [117], but in general the effect is minimal. Measurements in fluid exhibit spurious frequency peaks can be an impediment to identifying the cantilever’s resonance frequency peak. In fluid, the

---

<sup>3</sup>Two electrolytes were used in this project. The first was 0.4 M NaCl ( $\geq 99.5\%$  purity, Sigma Aldrich [109]) in water (water of  $> 18\text{M}\Omega\text{cm}$  after filtration through a Millipore Milli-Q Reference Water Purification System, Fisher Scientific [110]). The second was 0.002M ferrocene methanol (97%, Sigma-Aldrich [111]) and 1M sodium perchlorate ( $\geq 98.0\%$ , Sigma Aldrich [112]) in propylene carbonate (99.7%, Sigma-Aldrich [113]).

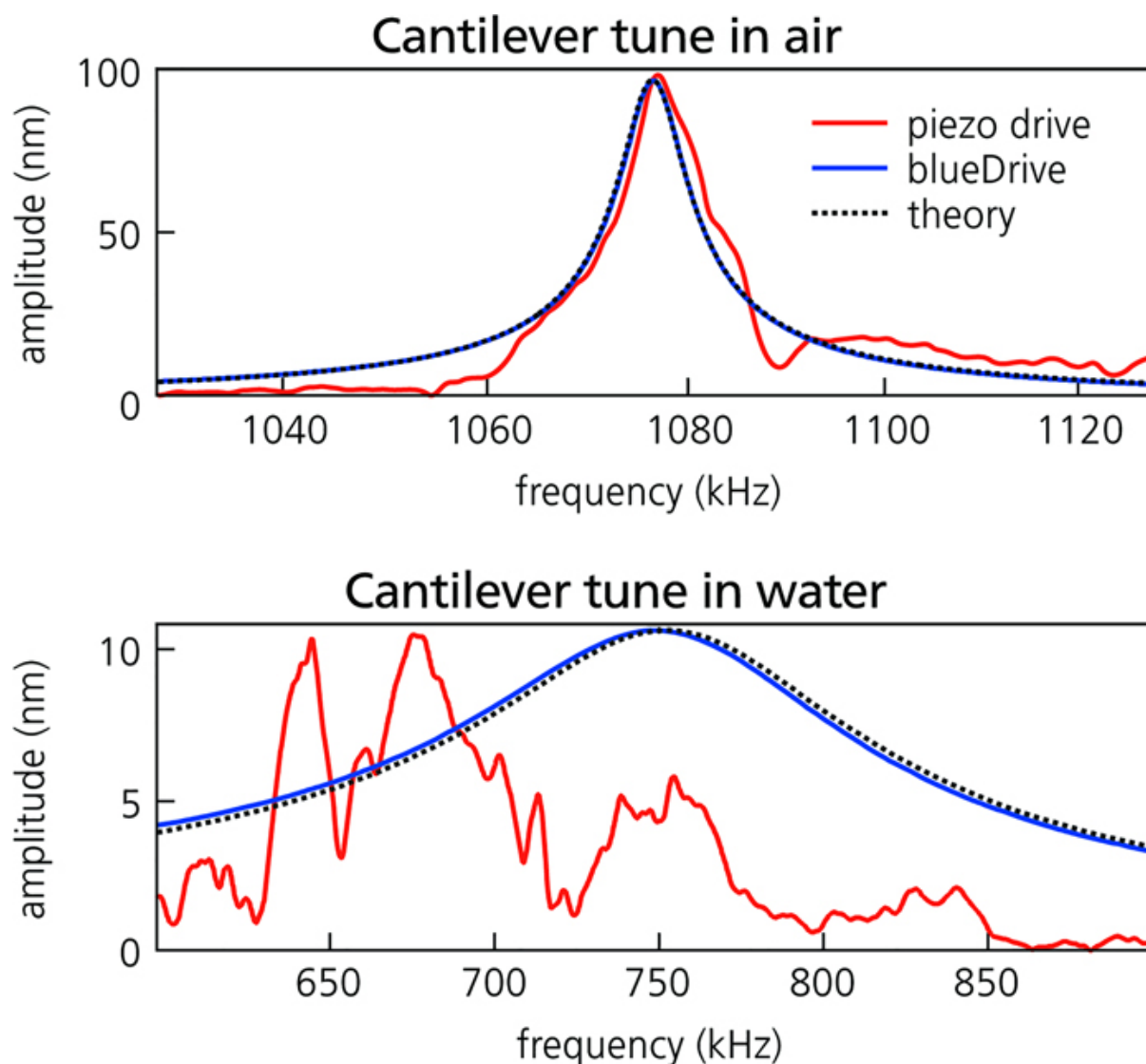


FIGURE 2.19: "Spectra or "tunes" of cantilever response amplitude versus frequency for the same cantilever actuated by piezoelectric excitation (red curves) and blueDrive photothermal excitation (blue curves) in air (top) and in water (bottom). The black dashed lines represent the response predicted by simple harmonic oscillator theory. Results are shown for a small, gold-coated, arrow-shaped cantilever used for high-speed imaging. Acquired on the Cypher ES." [116]

driving efficiency of the cantilever and the  $Q$  factor of the resonance peak are reduced due to viscous drag and clamping losses [118]. In contrast, the mechanical resonances of the AFM couple to the liquid and excites hydrodynamic modes of the surrounding fluid [119]. This produces the "forest of peaks" as shown in figure 2.19 [116] where identification of the resonance peak is difficult. Additionally, the mechanical coupling will change with temperature and time, shifting the forest of peaks [116]. This shifting will change the measured cantilever frequency spectrum and increase uncertainty on quantitative force measurements.

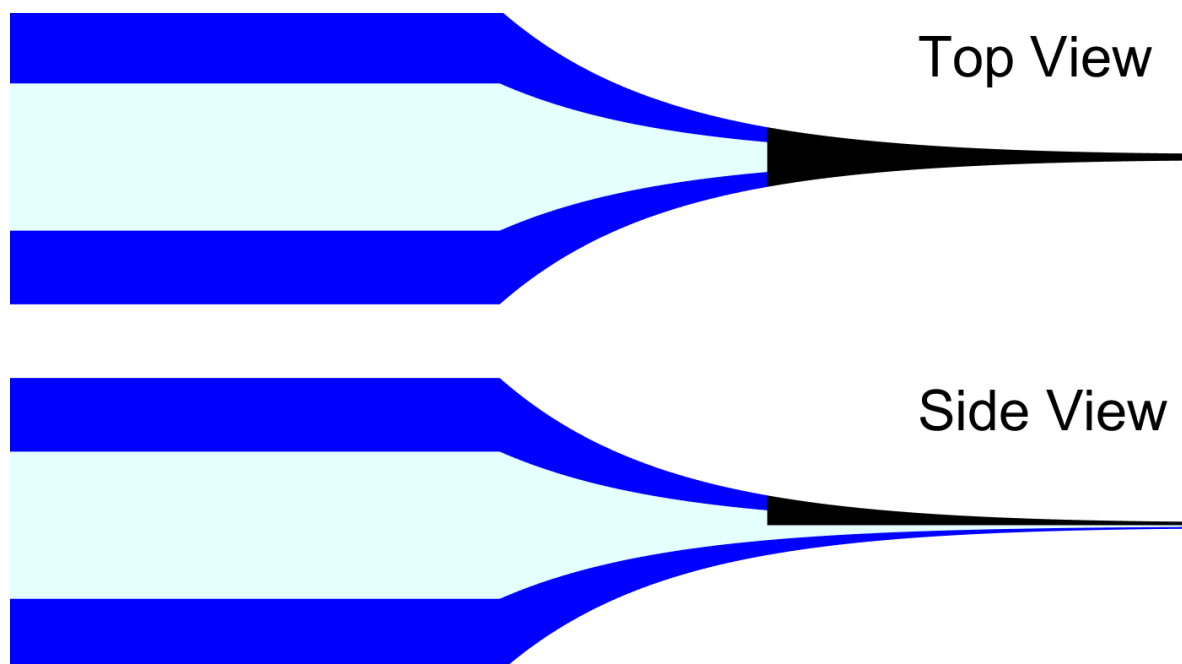


FIGURE 2.20: The probes were coated with marker to permit photothermal excitation. The geometry of the the coating is shown in two pipette probes, rotated to different positions.

In contrast, the photothermal excitation transfer function is time and temperature stable and does not couple mechanical oscillations of the AFM to the cantilever REF. This leads to the experimental observation that the forest of peaks is not present in photothermally driven AFM systems, as shown in figure 2.19. Therefore, photothermally driven AFM measurements are more quantitatively accurate.

To accurately record deflection, the probes must be able to reflect the detection laser. Typical silicon AFM cantilevers have a flat surface off of which light can be reflected for optical detection (e.g. MLCT, Bruker [80]). Pipettes are curved so that light will be spread out and only a small fraction of the light will be reflected to the photodiode board which detects the position of the cantilever. To fix this we can attach a flat, reflective piece of material to the probes for better reflection.

We used Schott 10  $\mu\text{m}$  glass (D263 Thin Glass, Schott [120]), and evaporated 100 nm of aluminum onto it to create a reflective, flat surface. By hand, the large sheets of glass were cut into reflectors that could be mounted to the probe with epoxy [121]. The size of the reflectors varied but were approximately 500  $\mu\text{m}$  x 250  $\mu\text{m}$ . With this reflector in place, the probes had more signal than a typical AFM cantilever because the reflectors were larger than those of a typical cantilever. To accommodate the optics of our AFM the reflector had to be affixed to an angular tolerance of  $3^\circ$ . Also, the placement and

amount of glue would change the stiffness of the probe slightly, so this process had to be performed precisely.

Surprisingly, these macroscopic probes can be actuated by photothermal excitation. In photothermal actuation, the intensity of a driving laser is modulated to create a periodic heating at the resonance frequency of the probe. This creates a periodic strain in time, which results in a periodic oscillation of the pipette. Typically, to use photothermal excitation, we need to use a small oscillator because its low mass means that the heat capacity of the probe will be low, which in turn means that the driving efficiency will thus be greater. Furthermore, to drive the cantilevers at high frequency (100 kHz for commercial Si cantilevers), the probes must be able to thermalize rapidly. Immersion in liquid ensures that this condition is fulfilled.

In the case of the pipette probe, the pipettes are originally transparent. They were coated with black marker (see figure 2.20) so the conversion of light to heat and strain is more efficient. This technique worked well, despite the pipettes being so much larger than typical AFM cantilevers. With the blue laser's power of up to 8 mW, probes were oscillated at frequencies between 1 kHz and 16 kHz with oscillation amplitudes of over 1  $\mu\text{m}$ . The relation between laser oscillation power and peak amplitude is shown in figure 2.21.

### 2.5.6 Noise characterization of combined SICM–AFM probes

To examine the deflection noise of the probes in our system, the thermal spectrum of the probes was recorded while they were mounted in the microscope. The results are shown below in figure 2.22.

In this thermal spectrum, the blue laser is off, so the probe is not externally driven. In this spectrum, the thermally driven resonance peak is at 6733 Hz. Several other peaks are also apparent, many of which are attributable to 60Hz ground loop noise in the electronics and higher harmonics of this frequency.

The frequency spectrum of SICM current measurement system output was also recorded. In these measurements, the SICM probe was mounted in the microscope, with the silver chloride electrode in the probe, and another electrode in a bath of electrolyte on the sample stage. The results are shown in figure 2.23. The wire referred to in the figure is the coaxial connection between the Ag/AgCl electrode and the current amplifier.

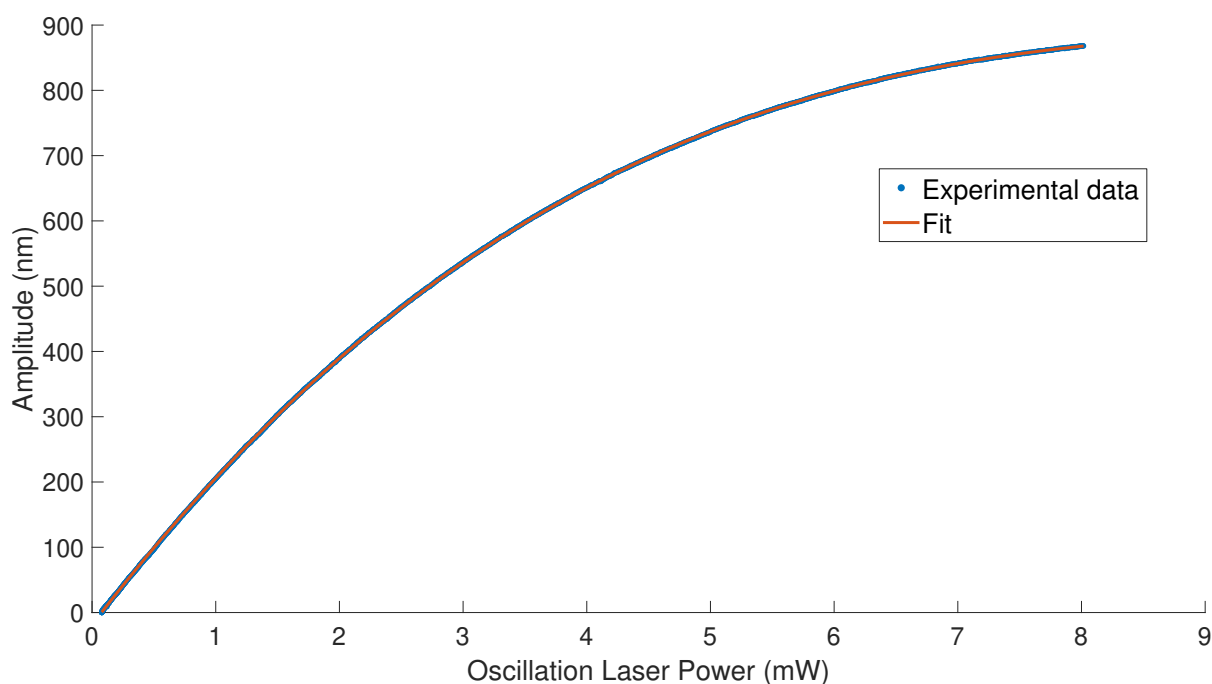


FIGURE 2.21: As the oscillation laser power of the blue laser increases, the amplitude of the probe at resonance will increase. The data is fit to a third degree polynomial ( $A = (0.699 \pm 2)P^3 + (-22.54 \pm 0.03)P^2 + (246.3 \pm \pm 1)P + (-18.59 \pm 0.7)$  where  $A$  is amplitude and  $P$  is power). The error on each point was determined to 0.6 nm but is not shown.

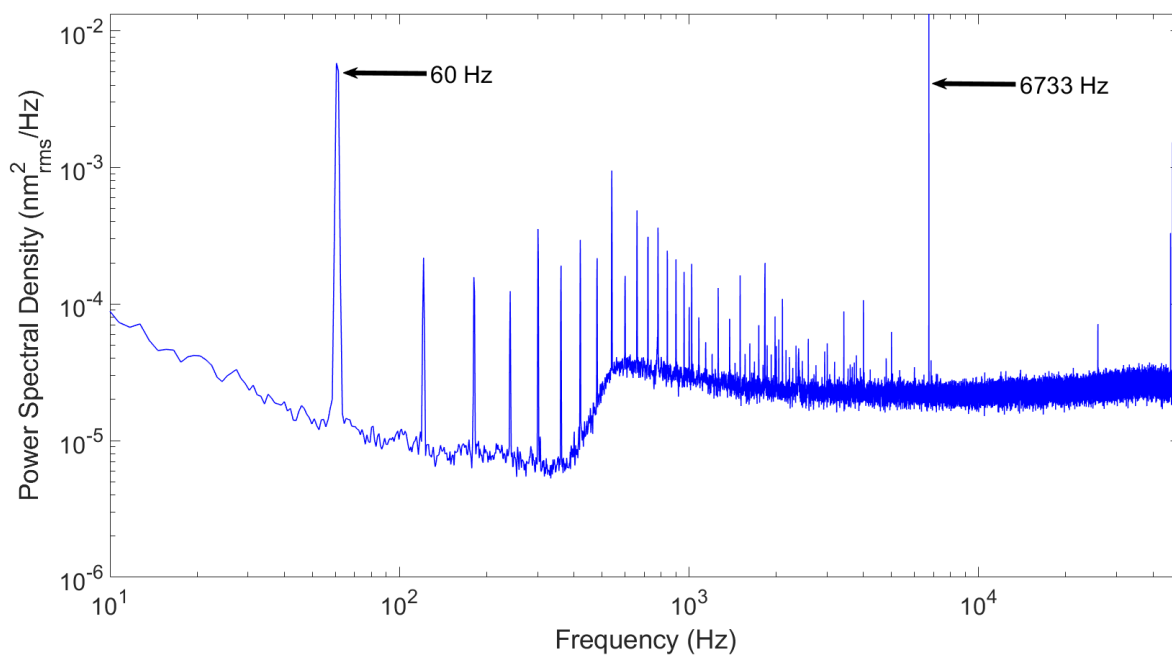


FIGURE 2.22: Power spectral density of the deflection signal of a pipette cantilever. The resonance frequency is 6733 Hz and there is noise peak at 60 Hz.

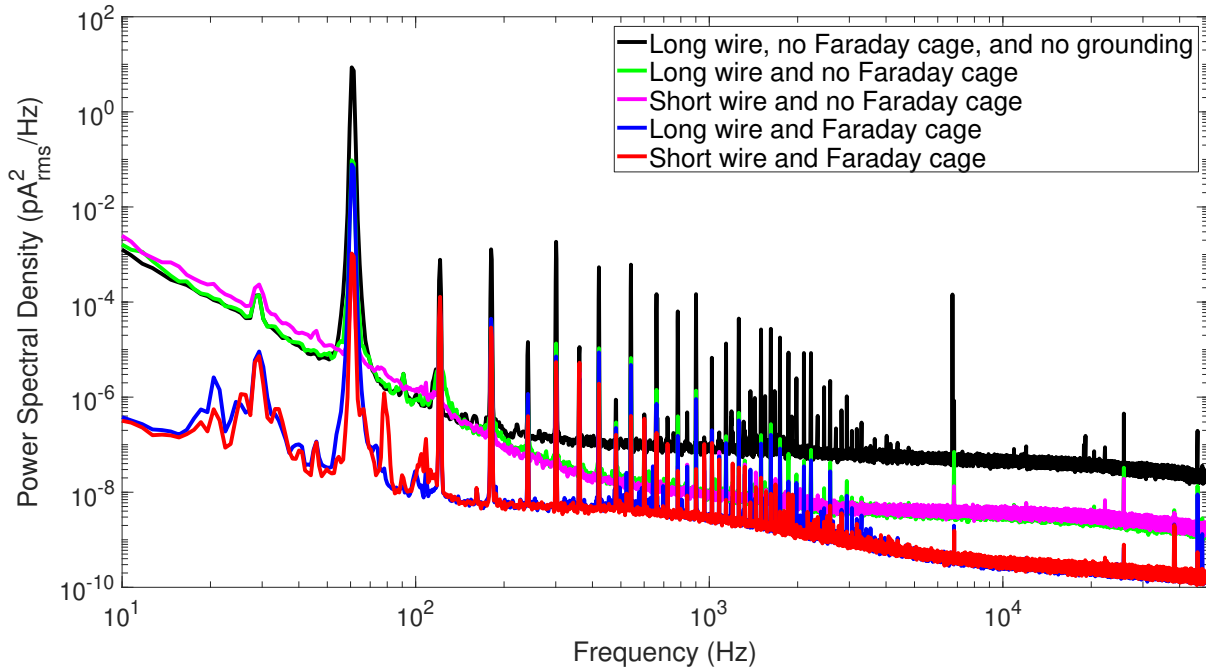


FIGURE 2.23: Power spectral density of the current noise measured by the current amplifier. Ground loop problem are seen by the 60 and 120 Hz noise peaks.

These measurements demonstrate that by using a shorter wire and performing the measurement within a Faraday cage, the current noise drops by over an order of magnitude. Some ground loop noise is also visible as a 60Hz peak, as well as the harmonics of this frequency.

To measure the drift of these signals, the deflection and current signals were then recorded for a time span of 20 minutes.

The total range of the deflection over this time span is 14.4 nm, or 0.7 nm/minute as seen in figure 2.24.

In the current channel, the drift is smaller than the noise as seen in figure 2.25.

## 2.6 Conclusion

The key characteristics of the AFM-SICM system developed in this thesis can be described in terms of mechanical stability, cantilevered probes, optomechanical oscillation, and high sensitivity, multi-channel data acquisition.

While the cantilevered probe design is inspired by the combined AFM-SICM microscope shown in figure 1.14, this version differs in important aspects. The probe tip is very

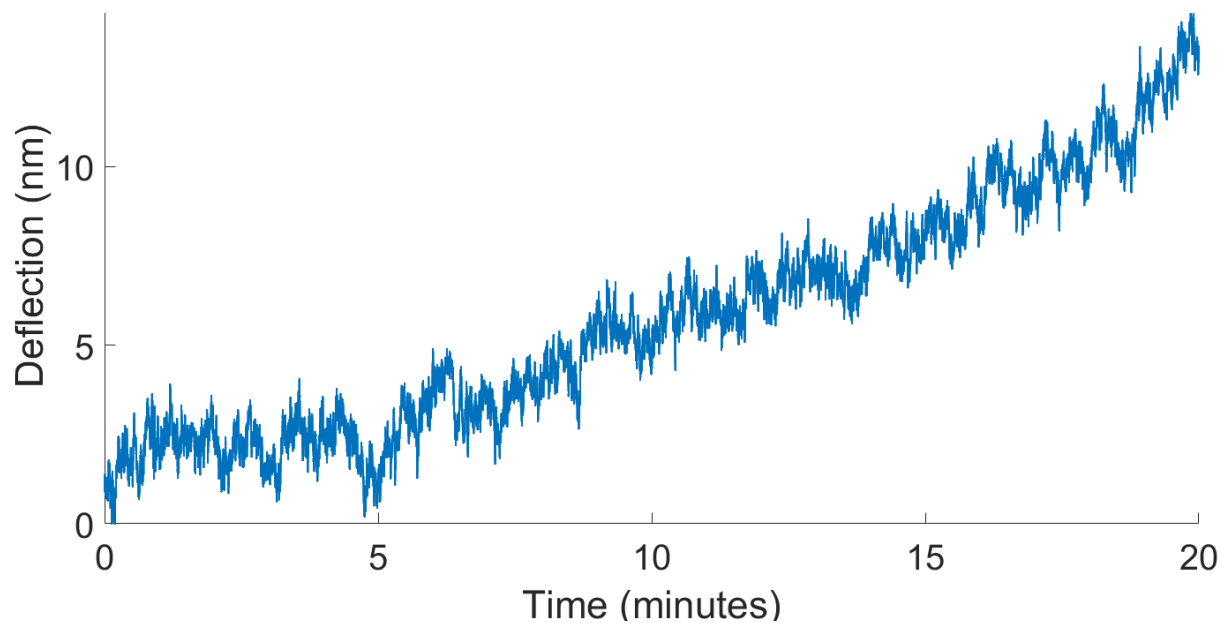


FIGURE 2.24: The deflection signal is recorded as a function of time.

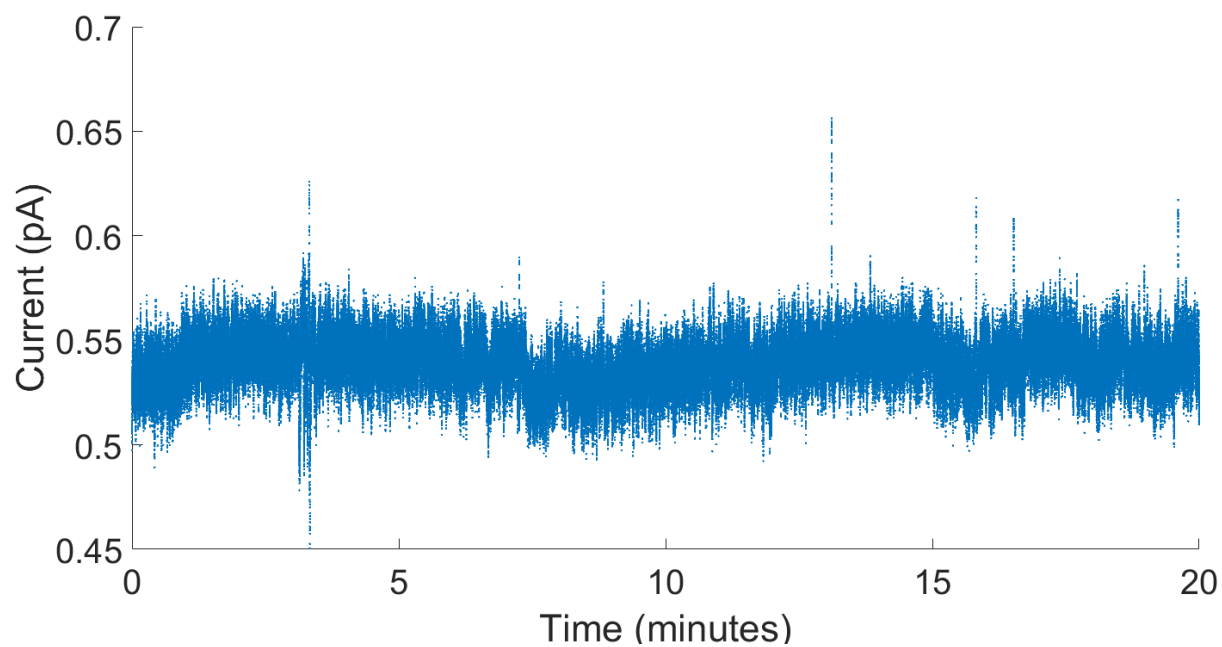


FIGURE 2.25: The current signal is recorded as a function of time.

long, allowing the probe reflector to stand outside the fluid environment while the tip can simultaneously interact with an immersed sample surface. As the reflector being immersed drastically reduces the driving efficiency and Q factor of such probes, this is a significant improvement. Additionally, these long, these probes have low stiffness constants, and can be excited more efficiently. More importantly, these massive probes are equipped to be oscillated thermally. By replacing the piezo-actuation that is used in nearly every other system, the "forest of peaks" problem is eliminated. This offers a huge improvement to signal-to-noise ratio and allows for high resolution force measurements in a fluid environment.

To complement this, the probes are used within a highly mechanically stable EC-AFM. Additionally, the system the probes have been integrated into is have a low noise design for highly accurate results, as demonstrated by the noise measurements. By leveraging the acquisition system, up to 8 data channels may be recorded simultaneously. In comparison to distance regulated shear-force system, this allows for phase imaging and the more accurate tapping mode force measurements. Commercial systems that combine AFM and electrochemical measurements in one probe (Bruker, Nano-surf), can also acquire these channels. However, due to their mechanical properties, contact mode or large tapping amplitudes must be used which may damage sample surface.

To understand the full effect of these improvements the probes' mechanical properties and their relation to AFM performance must be characterised fully.



# Chapter 3

## Force Measurements

### 3.1 Introduction

The results presented here were performed as the probes were developed. The process for testing these probes is well-defined, but the process of engineering the probes requires refinement of their properties over the course of use. Initially the resonance properties were tested (3.2), and they were used to perform AFM scans (3.3) without any liquid electrolyte involved. Once this was done, they were used for electrochemical measurements (4). Through the course of these measurements the properties of the probes were changed in ways that impeded or prevented their use as AFM cantilevers to facilitate electrochemical measurements (for example, elongating the probe tip to ensure the pipette tip apex was not melted shut). This meant that the initial AFM resonance measurements had to be conducted again with additional testing constraints (3.2). A detailed account of each of these iterations is beyond the scope of this thesis; however, it should be noted that even after successful AFM scans, and after thousands of electrochemical measurements had been performed, the properties of the probes were further refined. The creation and use of these probes was an iterative process of testing and improvement. Each completed measurement was designed to provide new information and understanding about the challenge at hand. Every solution to probe design that was employed would yield additional difficulties. Because of this, creating the probes became a game of balancing attributes to find a happy medium that would satisfy all the requirements for functioning probe. The goal of the project was to simply improve the probes in one aspect while not ruining their other capabilities.

To achieve combined AFM and electrochemical measurements the probes had to progress through a series of tests and answer a set of key questions. In terms of the force measurements those steps are:

1. Can the probes perform AFM force measurements? This requires a demonstration of force control at a single point and resonance curves to show that the probes are capable of basic AFM functions (3.2).
2. Can the probes be used to image a surface using AFM? This is necessary to examine how the geometry of the tips may affect the topography images (3.3).

These measurements and their analysis of this chapter were performed by the author. Yoichi Miyahara provided guidance in operating the AFM system.

## 3.2 Probe Force Sensing Characteristics

To perform atomic force microscopy with a probe, certain conditions of stiffness and resonance must be fulfilled.

Commercial AFM cantilevers are sold as soft if their stiffness constant (also described as force constant or spring constant) is less than 1 N/m, and stiff if they are more than 40 N/m [122]. Each AFM operational mode needs different cantilever stiffnesses. Soft cantilevers are typically used in contact mode measurements as they allow for less force to be applied to the sample for the same deflection signal. This means that for the smallest detectable deflection signal these cantilevers will apply less force to a sample. This is important as larger forces will potentially lead to damage of the tip and the sample.

Stiff cantilevers are typically used for tapping mode and non-contact measurements, as higher stiffnesses are related to higher resonance frequencies [123], meaning that these probes can be scanned faster. Higher stiffness is also important if a probe ‘snap-in’ [124] is to be avoided – this happens when the tip-sample force gradient is larger than the force constant of the cantilever. Tapping-mode is also important when lateral shear forces need to be avoided, allowing soft samples (particularly biological ones) to be non-destructively imaged [125]. Additionally, higher resonance frequencies are less susceptible to low frequency noise, thus allowing a more stable force control of the probe [126].

For the initial testing of the pipette cantilevers, these force constants served as a good reference. A stiffness constant between 1 N/m to 100 N/m was used, and once this condition was met the resonance frequency was maximised.

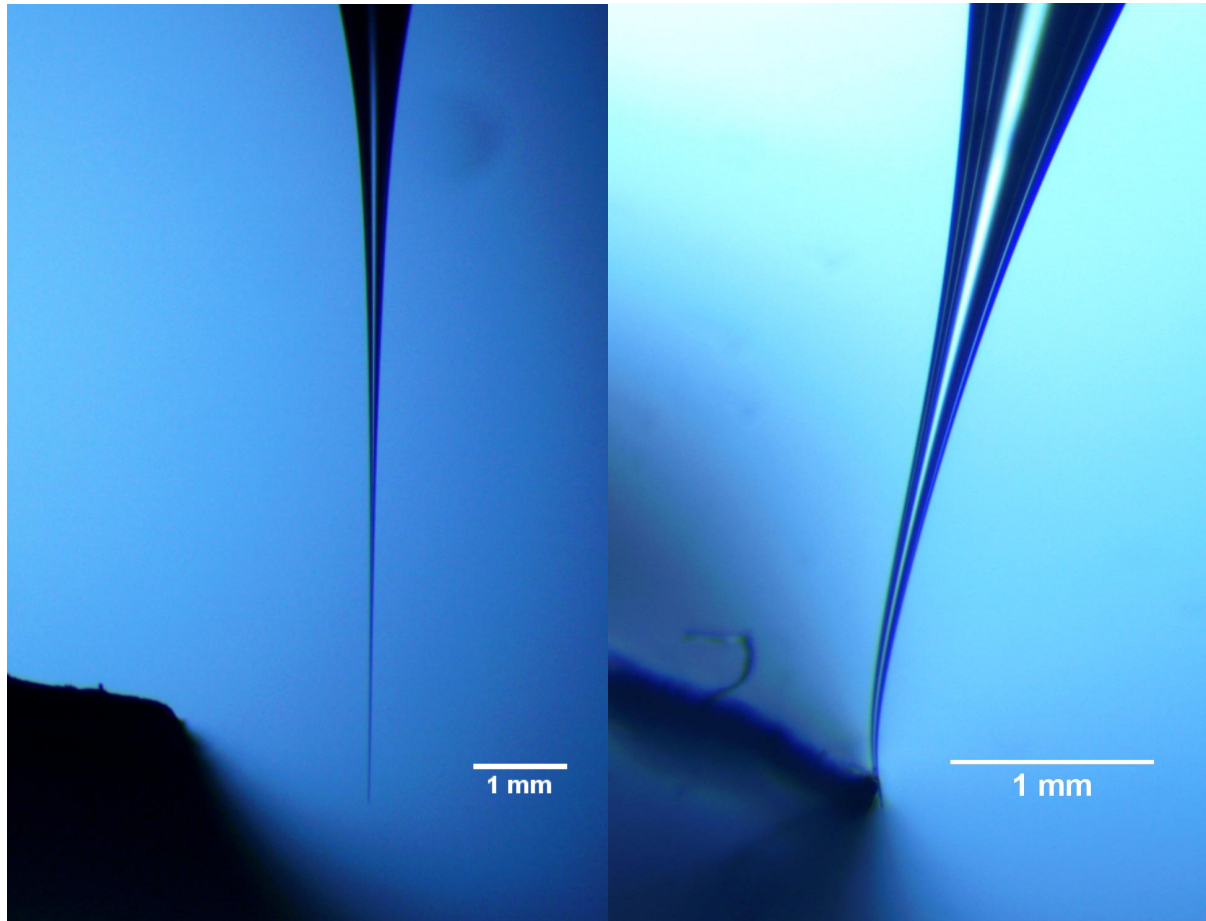


FIGURE 3.1: The pipette is shown before and after contacting a razor blade. After contact, it bends due to the repulsive tip-sample forces.

The stiffness constant of the probes was determined as described in Appendix C and is shown in figure 3.1. First and foremost, pipettes with low stiffness constants needed to be pulled to accommodate the AFM cantilever geometries. A recipe for long, thin pipettes was chosen from the Sutter cookbook, and gradually changed the parameters of the pulling procedure to make different varieties of pipettes with different stiffness constants.

The stiffness of the probes was calculated using the following formula:

$$k = \frac{M \cdot g}{x_i - x_f} \quad (3.1)$$

Where  $k$  is the stiffness constant,  $M$  is mass recorded by the scale,  $g$  is the gravity of Earth,  $x_i$  is the initial probe position, and  $x_f$  is the final probe position.

By iteratively changing the pipette pulling parameters (see section 2.5) and bending parameters (distance between tip apex and bend) and testing the stiffness of the probes in this way, probes were reliably created with stiffness constants of 1-100 N/m.

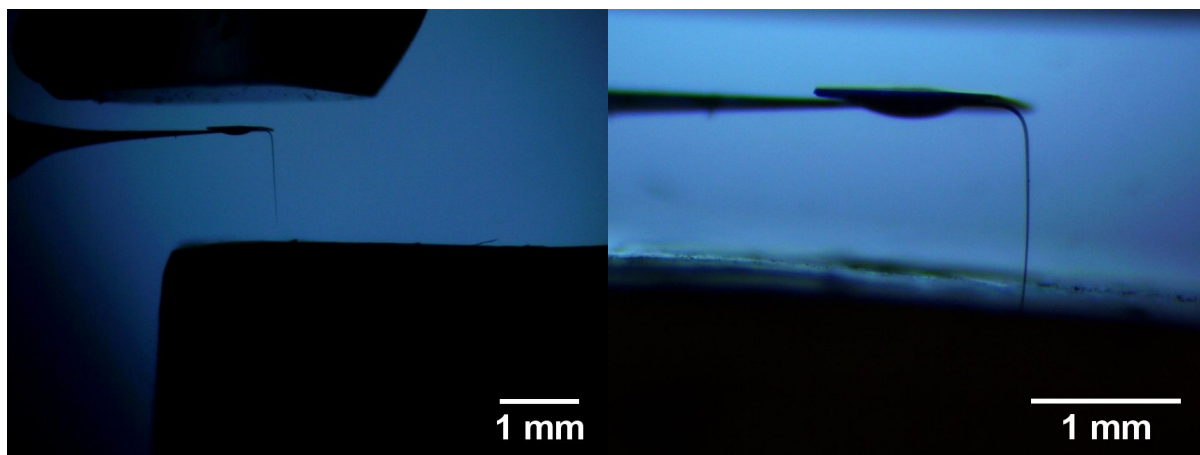
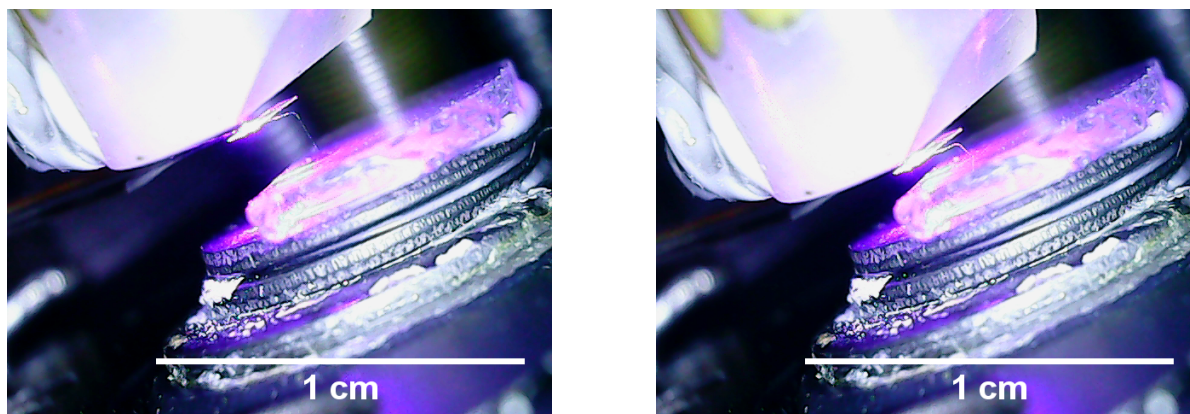


FIGURE 3.2: A mounted pipette probe was brought into contact with the stiffness measurement device.

Measuring the stiffness of these pipettes involved significant errors, as applying force at different positions on the pipette would yield different stiffness constants. From the images in figure 3.1 we can see that the conical shape of the pipette means that the pipette will continuously increase in diameter from the tip of the pipette to the shank. As the diameter increases, the pipette becomes stiffer. The more important stiffness testing occurs after the pipettes are manipulated into their permanently bent form. Once the probes are bent, force can be applied to the tip in the same direction that occurs during actual AFM measurements (see figure 3.2). It should be noted that this stiffness constant measurement can damage the tips of the probes. During these tests, force was applied directly at the apex of the tip of the probe, as this is where force is applied during an AFM scan. However, the resolution of the micrometer screw used for moving the probe was about  $1\ \mu\text{m}$ .  $1\ \mu\text{m}$  deflections of a probe with a stiffness constant of 100 N/m means a force of 0.1 mN applied to a glass tip of 100 nm in diameter. If we consider the hole of the pipette to be 50 nm in diameter then the area of the tip apex is  $2.45 \cdot 10^4\ \text{nm}^2$ . If we apply 0.1 mN to this area, a pressure of 4 GPa is applied. If the force is not uniformly applied to the tip apex (if there is a protrusion at the tip apex), then the pressure can be even higher over a smaller area. The theoretical yield strength of glasses is 17 GPa and the practical strength is quoted as 70 MPa [127] due to imperfections in the glass [128]; we would thus expect that the tip apex is damaged. To prevent this, two stiffness

measurements were conducted: one at the tip of the probe and another at the bend of the probe, where the reflector was eventually placed. These values were generally close, with a much higher variability in the stiffness constant measured at the bend of the probe because applying force at the bend of the probe can happen in many different places, which will test for different stiffnesses. Once a suitable probe recipe was established, the probes were only tested at the bend for stiffness. This would provide a non-destructive measurement to verify that the probe was of the approximately correct stiffness.



(A) The probe apex is close to the sample surface, but has not made contact with the sample surface.

(B) The probe apex made contact with the sample surface, the probe tip bends outwards, and the reflector is not deflected.

FIGURE 3.3: The pipette was bent to an incorrect angle, so the tip bends while the cantilever does not move appreciably.

Through these stiffness measurements, it was found that probes of 80 N/m were the best for tapping mode AFM measurements. Probes with larger stiffness constants could damage the sample surfaces due to the large applied forces. Smaller stiffness constants were difficult to attain as this would require the probes to be bent closer to the tip. Lower spring constants were sometimes caused by probes not being bent to the correct  $10.5^\circ$  angle, resulting in the tip of the probe bending rather than the cantilever being deflected, as in figure 3.3. Similarly, a small spring constant can indicate a probe with a very long tip. These tips would have instabilities as shown in figure 3.4, meaning that the probe would buckle upon meeting the surface. The reason for this is easy to understand. Think of two springs in series – the tip spring and the cantilever spring. We need to ensure that the effective tip spring is stiff, so that the observable deflection is by the cantilever only. The tip spring constant is small if the forces are not applied parallel to its axis (hence the need for a precise angle) or if it is too long (Euler buckling instability).

Figure 3.4 shows the probes bending outward and the tip being forced outward along the surface of the sample. This improper bending essentially leads to probes for which



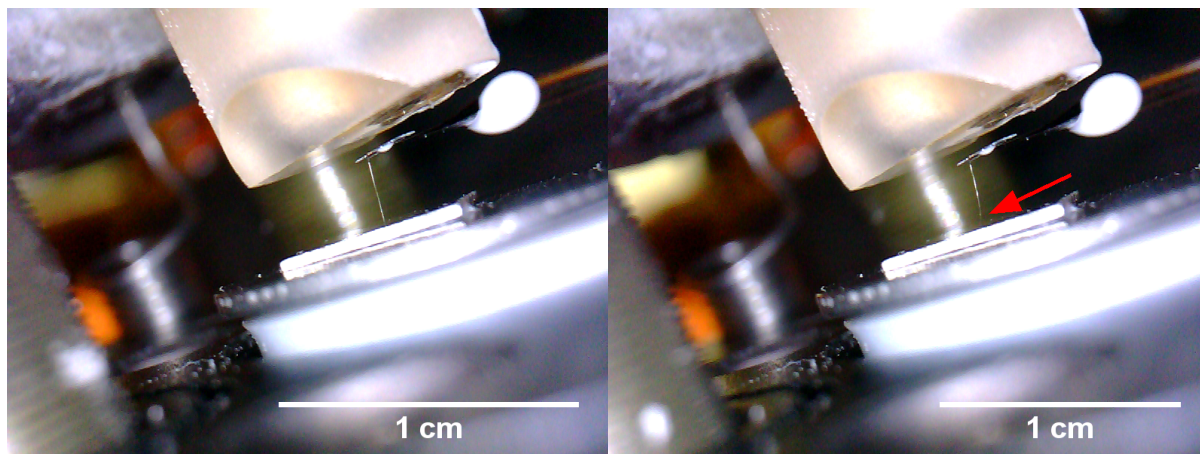


FIGURE 3.4: A long probe was approached to the surface sample, which lead to the probe tip deflecting outwards. The red arrow indicates where the probe was deflected outwards.

the force applied at the tip of the probe is not collinear with the tip; the tip axis is not perpendicular to the sample surface plane and the reflector. This happens because this mechanical bending mode is much less stiff than the compression mode in which the tip moves perpendicularly to the surface and deflects the reflector. Tips of this variety cannot be used for AFM measurements as the deflection of the reflector does not accurately indicate the force on the probe.

The probe depicted in figure 3.4 shows the phenomenon very clearly. Some probes were more difficult to diagnose and problems could only be identified once the probe was used for scanning, as shown in figure 3.5. In these cases, the AFM scan would function correctly for the first few lines of a scan. Suddenly, the tapping amplitude of the probe would increase, and the AFM feedback would move the probe micrometers closer to the sample to no avail. If the scan was left to continue, the probe would sometimes reengage the sample surface and feedback normally. What can be seen in figure 3.4 is the tip bending to a different geometry due to the force applied to the tip (Euler buckling instability).

This absence of tip bending can also be diagnosed when the tip approaches the surface. In operating an AFM, either a setpoint amplitude (in tapping mode) or setpoint deflection (in contact mode) is chosen. The AFM tip approaches the surface until this setpoint is reached. To check if the probe has this bending instability, the setpoint can be reduced so that the probe will approach the sample further. Since the stiffness of these probes has been tested, and the piezo has been calibrated, the distance the probe should deflect

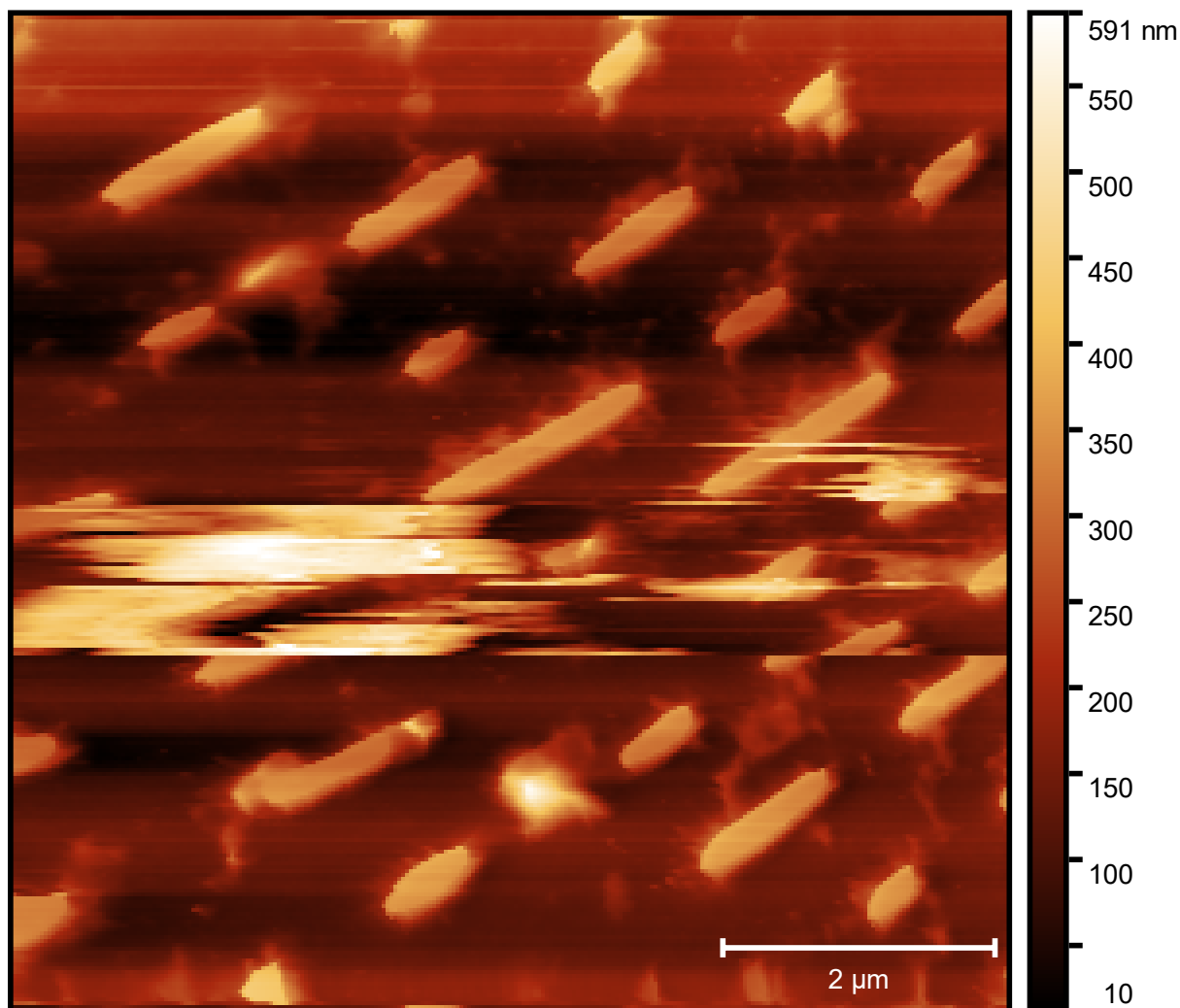


FIGURE 3.5: A topography scan of a CD stamper performed in tapping mode. The irregularities and streaks are the result of tip instabilities.

can be calculated. If the approach is much longer than expected, or the probe is not able to find the setpoint at all, this could indicate three things:

1. A bending irregularity (i.e., the tip is too soft or not at the right angle).
2. A false approach. Typical false approaches occur when the detection laser is not reflecting properly off the cantilever. For example, because the reflector is dirty, or the reflected laser spot is not properly centered on the photodetector. In these cases, small displacements of the detection laser can lead to large signal changes that will reduce the amplitude or deflection signal. They may change the signals to the point that the signals reach the setpoint value, so it looks like the probe has met the desired setpoint through a force interaction. In this microscope, the coarse approach of the sample to the surface relies on the turning of three screws by a

central motor. If these screws descend unequally, this can change the position of the cantilever in relation to the deflection laser beam, which can cause this false approach signal.

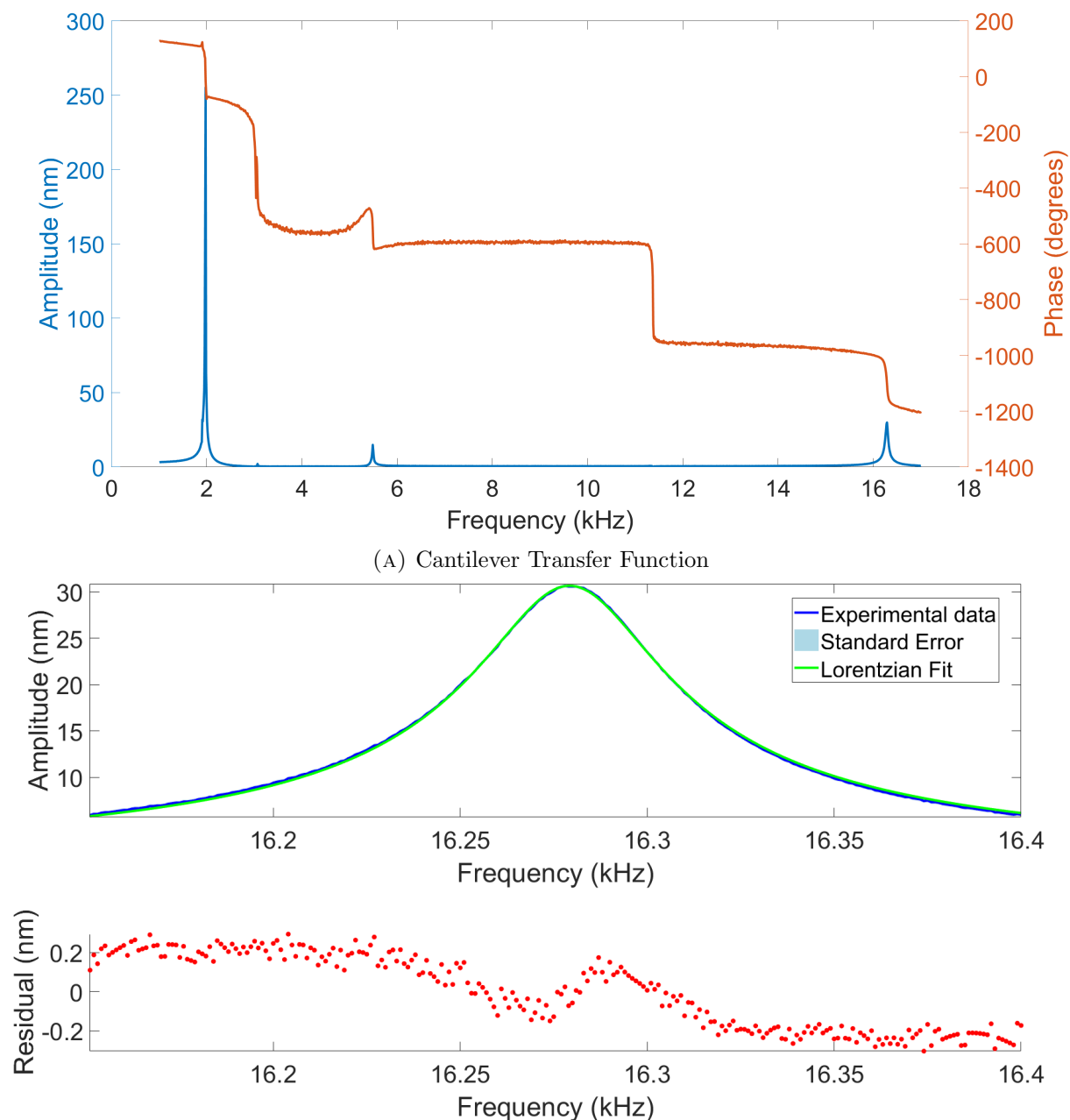
3. As described above, the pressure due to the applied force can exceed the yield stress of the material and lead to crack formation, in some cases even leading to a complete breaking off the tip apex. These breaks leave behind a larger tip to sample separation, which also resembles a false approach.

The USB microscope used to take the above images was crucial in disentangling these problems. In figures 3.3 and 3.4, the probe can be seen touching down on the surface, then bending outwards before any reduction of tapping amplitude is measured. This clearly demonstrates the bending mode that caused the false approach. In passing it is noted that the USB microscope was very useful in detecting other ‘wrong’ approaches, such as broken electrical connections to the photodetector or the controller, which can result in conditions that would look like a false approach.

To perform tapping mode measurements, a relevant property of these probes is their resonance characteristics. Commercial silicon cantilevers are generally beams with dimensions on the order of 100  $\mu\text{m}$  long, 30  $\mu\text{m}$  wide, and 4  $\mu\text{m}$  thick (e.g. MLCT, Bruker [80]). The pipette cantilever is a truncated cylindrical cone with a tip on the order of 100 nm in outer diameter and 50 nm inner diameter and a base that is 1 mm in outer diameter and 0.5 mm in outer diameter. The tip of the probe is 250  $\mu\text{m}$  long, and while it is difficult to define the length of the probe, it is on the order of millimeters. The dimensions differ by an order of magnitude in length, so a large discrepancy in resonance frequencies was expected.

Piezoexcitation (also known as acoustic excitation) of cantilever oscillations is often inefficient and, particularly in liquids, has the well-known ‘forest of peaks’ problem (see section 2.5.5). This is a result of non-linear coupling between different mechanical modes of the cantilever and possibly other mechanical components of the microscope [129]. The result is that exciting the cantilever leads to many resonances which are difficult to identify. To solve this problem, photothermal excitation [77] was used, which allows for a clean frequency spectrum to be measured, as only the end of the cantilever is driven with minimal excitation of other modes. It is also well known that photothermal excitation leads to a very stable and drift free excitation of cantilever oscillations. This is important in obtaining sufficient s/n on small currents for high spatial resolution measurements.





(B) A peak from Figure (A) showing a Lorentzian fit of the experimentally determined resonance peak, with its associated residual.

FIGURE 3.6: The oscillation amplitude response of a pipette cantilever as the excitation frequency was swept while in air. The experimentally obtained amplitude and phase data is shown, and a subplot of the 16 kHz resonance peaks is shown. (Resonance frequency =  $16279.21 \pm 0.05$  Hz, Q factor =  $328 \pm 5$ , Spring constant =  $77 \pm 1$  N/m).

The laser power is  $1.2 \pm 0.1$  mW

Photothermal excitation was thus useful and key in the development of these cantilevers. It should be noted that, surprisingly, it was found that photothermal excitation of the macroscopic cantilevers used in this project is possible. Early attempts at oscillating

probes led to very small oscillation amplitudes that could easily have been overlooked if piezo excitation had been used, since the initial amplitudes of these peaks were on the order of system vibrations (a forest of peaks outside of liquid). Figure 3.6 shows a photothermal driven measurement of the cantilever transfer function with a resonance frequency of around 2 kHz. Note the very clean (i.e. high s/n) phase and frequency response. Also, a phase shift of  $360^\circ$  can be seen at 11.3 kHz, where a small feature in the amplitude can also be seen. This small feature may be two small neighbouring peaks, or it could be an artifact of the laser detection. Regardless, if 16 kHz peak is used, this area of the transfer function can be avoided completely. Because the 16 kHz peak has sufficient amplitude for the purposes of the current project, and a higher frequency peak allows for faster scanning, this peak was chosen for tapping mode scanning.

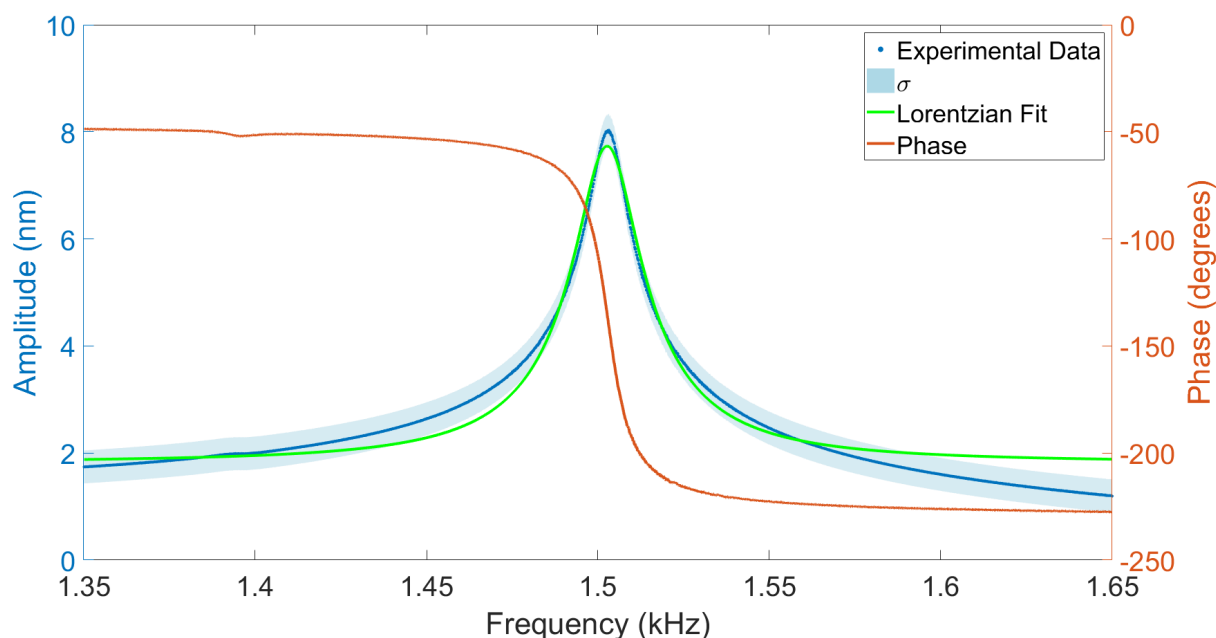


FIGURE 3.7: A measurement of the empty cantilever transfer function. The experimentally obtained amplitude and phase data is shown, and a subplot of the 16kHz resonance peaks is shown. (Resonance frequency =  $15026.0 \pm 0.1$  Hz, Q factor =  $147 \pm 4$ , Spring constant =  $70 \pm 1$  N/m).

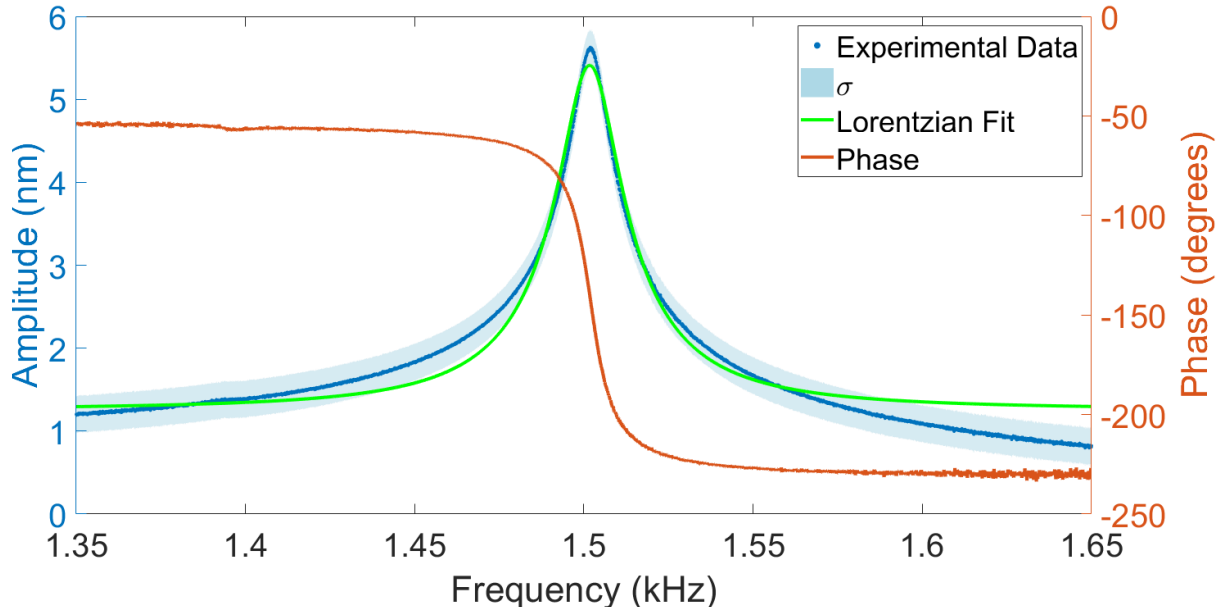


FIGURE 3.8: The cantilever from the previous measurement is filled with aqueous 0.4 M NaCl electrolyte, and the transfer function is measured again. The experimentally obtained amplitude and phase data is shown, and a subplot of the 16kHz resonance peaks is shown. (Resonance frequency =  $1501.8 \pm 0.1$  Hz, Q factor =  $152 \pm 4$ , Spring constant =  $70 \pm 1$  N/m)

Once probes with adequate stiffness and resonance characteristics were fabricated, the effect of filling the cantilevers with electrolyte needed to be established. The probes must be filled to create an electrochemically conductive pathway in the probe suitable for SICM measurements. To test this, transfer function measurements were performed with probes before and after filling them with an aqueous 0.4 M NaCl electrolyte (NaCl of  $\geq 99.5\%$  purity, Sigma Aldrich [130]). The results are shown in figures 3.7 and 3.8. The data show some small deviations from the fit; however, this was not an impediment to any measurements.

As can be seen from these curves, the resonance frequency changes very little once it is filled with liquid. The changes in resonance frequency due to the probe being filled with liquid can be estimated. For rectangular beam cantilevers, frequency follows the relation

$$\omega = 1.029 \frac{t}{l^2} \left( \frac{E}{\rho} \right)^{\frac{1}{2}} \quad (3.2)$$

Where  $\omega$  is frequency,  $t$  is thickness,  $l$  is length,  $E$  is Young's Modulus and  $\rho$  is density [131]. Resonance frequency will scale with the inverse square root of density if all other

dimensions do not change. To compare density before and after it is filled with liquid, consider the added masses of the reflector and liquid to be uniformly distributed, and to have no effect on the geometry. Then, one only needs to consider the change of the mass of the probe when it is filled with electrolyte.

Before the probe is filled:

$$\begin{aligned}
 M_{probe} &= M_{pipette} + M_{reflector} \\
 &= \pi \cdot \rho_{borosilicate} \cdot (r_o^2 - r_i^2) \cdot l_p + \rho_{glass} \cdot w_r \cdot l_r \cdot t_r \\
 &= \pi \cdot 2.23 \text{ g/cm}^3 \cdot ((20 \text{ }\mu\text{m})^2 - (10 \text{ }\mu\text{m})^2) \cdot (500 \text{ }\mu\text{m}) \\
 &\quad + 2.51 \text{ g/cm}^3 \cdot (500 \text{ }\mu\text{m}) \cdot (250 \text{ }\mu\text{m}) \cdot (50 \text{ }\mu\text{m}) \\
 &= 1.67 \cdot 10^{-5} \text{ g}
 \end{aligned} \tag{3.3}$$

Where  $M_{probe}$  is the mass of the probe (kg),  $M_{pipette}$  is the mass of the pipette (kg),  $M_{reflector}$  is the mass of the reflector (kg),  $\rho_{borosilicate}$  is the density of the pipette borosilicate ( $\text{kg}\cdot\text{m}^{-3}$ ) [132],  $l_p$  is the length of the pipette,  $\rho_{glass}$  is the density of the reflector's constituent D263 glass [133] ( $\text{kg}\cdot\text{m}^{-3}$ ),  $w_r$  is the width of the reflector (m),  $l_r$  is the length of the reflector (m), and  $t_r$  is the thickness of the reflector (m).

When the pipette is filled with electrolyte:

$$\begin{aligned}
 M_{filledprobe} &= M_{probe} + M_{liquid} \\
 &= \text{mass of probe} + \pi \cdot \rho_{water} \cdot r_i^2 \cdot l_p \\
 &= 1.67 \cdot 10^{-5} \text{ g} + \pi \cdot 9.97 \cdot 10^{-1} \text{ g/cm}^3 \cdot (10 \text{ }\mu\text{m})^2 \cdot (500 \text{ }\mu\text{m}) \\
 &= 1.69 \cdot 10^{-5} \text{ g}
 \end{aligned} \tag{3.4}$$

Where  $M_{filledprobe}$  is the mass of the probe when it is filled with electrolyte (kg),  $M_{liquid}$  is the mass of the electrolyte in the probe (kg), and  $\rho_{water}$  is the density of water ( $\text{kg}\cdot\text{m}^{-3}$ ).

If frequencies of the filled and unfilled pipette are compared:

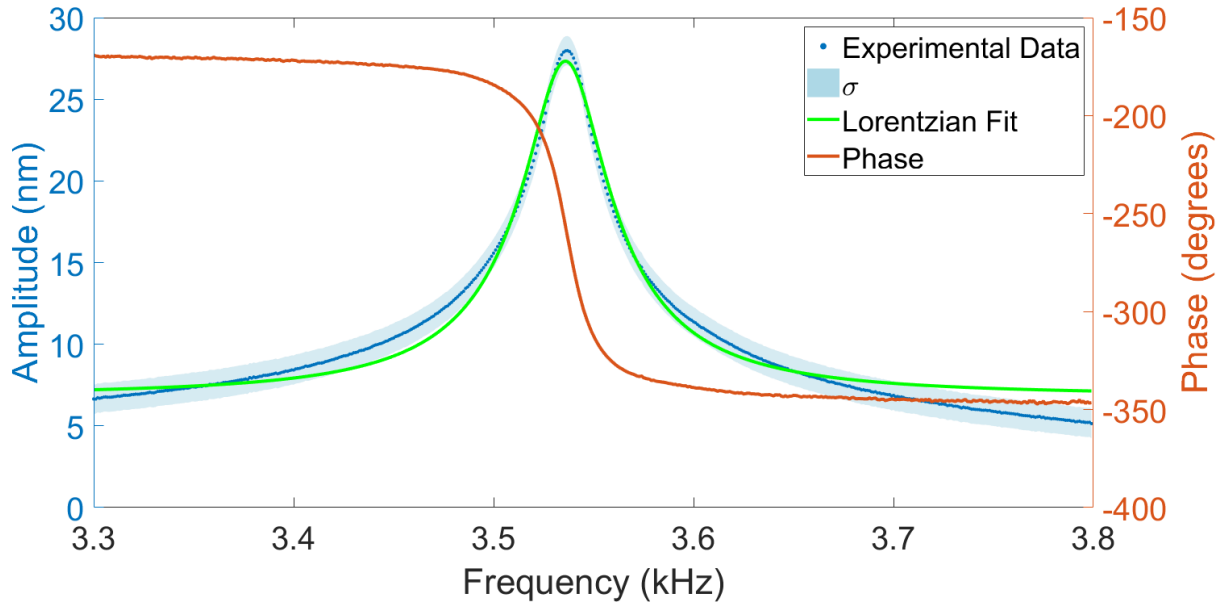


FIGURE 3.9: The transfer function of a pipette cantilever outside of the liquid, in air. (Resonance frequency =  $3536.0 \pm 0.2$  Hz, Q factor =  $79 \pm 5$ , Spring constant =  $80 \pm 1$  N/m)

$$\begin{aligned}
 \frac{\omega_{filled}}{\omega_{unfilled}} &= \frac{\rho_{filled}^{-1/2}}{\rho_{unfilled}^{-1/2}} \\
 &= \frac{M_{filledprobe}^{-1/2}}{M_{probe}^{-1/2}} \\
 &= 0.99
 \end{aligned} \tag{3.5}$$

Where  $\omega_{filled}$  is frequency of the probe when it is filled (Hz),  $\omega_{unfilled}$  is the frequency of the probe when it is unfilled (Hz),  $\rho_{filled}$  is density of the filled probe ( $\text{kg}\cdot\text{m}^{-3}$ ), and  $\rho_{unfilled}$  is the density of the unfilled pipette ( $\text{kg}\cdot\text{m}^{-3}$ ).

From this estimation we can see that the largest contribution to the mass of the probe is the large and massive reflector. The mass added by filling the probe is small in comparison, so the change in frequency is small.

To complete some of the other proposed measurements the probes must be able to perform AFM topography in liquid. The transfer function measurements in air and liquid are shown in figures 3.9 and 3.10.

As can be seen from the resonance curves of figure 3.9 and figure 3.10, entering electrolyte does not change the resonance frequency substantially. The amplitude is reduced by entering the electrolyte and will continue to decrease due to drag as the probe descends

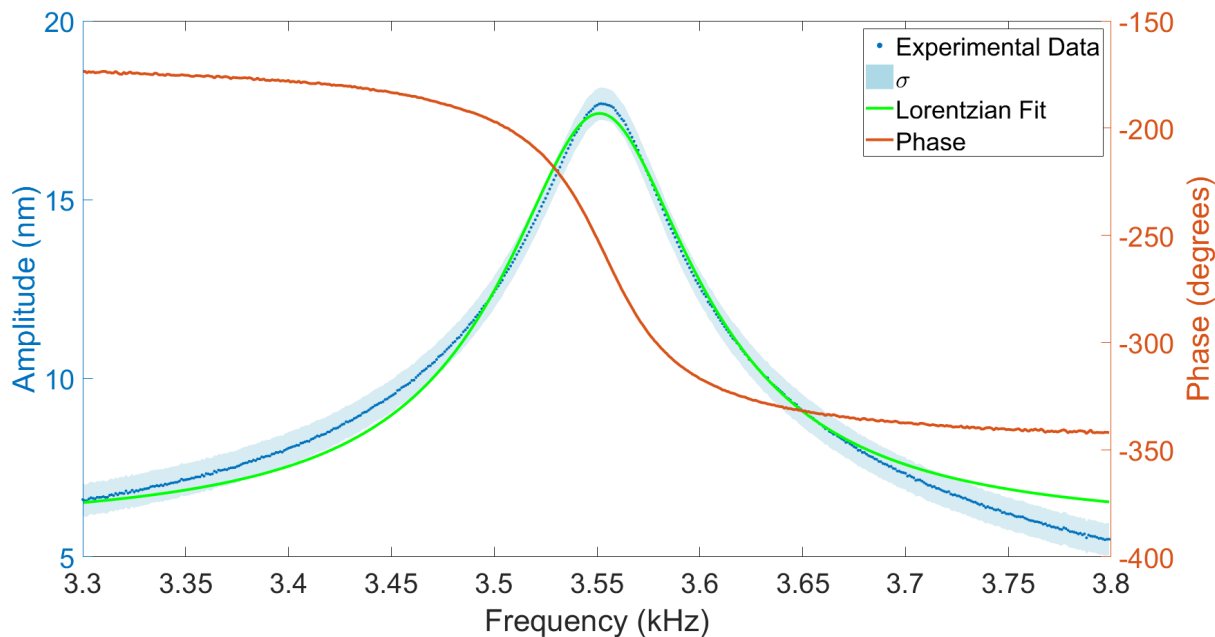


FIGURE 3.10: The transfer function of a pipette cantilever in aqueous 0.4 M NaCl electrolyte. (Resonance frequency =  $3551.3 \pm 0.4$  Hz, Q factor =  $33 \pm 2$ , Spring constant =  $80 \pm 1$  N/m)

farther into the electrolyte. Most hydrodynamic modeling in AFM assumes that the entire cantilever is immersed in electrolyte, which is not applicable here, so estimating the frequency shift from theory would require additional study [94].

Performing AFM topography images in liquids presents challenges even when using commercial cantilevers. The damping from the liquid reduces the driving efficiency of the cantilever and reduces the Q factor substantially. The pipette cantilevers experience a less severe decrease in Q factor, from  $79 \pm 5$  in figure 3.9 to  $33 \pm 2$  in figure 3.10, because only the tip of the probe is long enough that the reflector of the probe is not submerged. This is beneficial for AFM topography scanning. Longer tips allow the probes to scan in thicker layers of liquid; immersing the reflector in liquid completely dampens any oscillations, and longer tips allow the probe to descend further into the liquid without this happening. It is possible to operate these long tip cantilevers, and scans with tips of up to 1mm were successfully performed during this project (see figure 3.11). However, long tips are not as stiff, which can lead to the aforementioned buckling issues. Their bending angle has a smaller tolerance, and their operation requires special attention to avoid accidental over-approaches where the probe is bent by the surface with minimal deflection at the cantilever. Also, longer tips mean more drag through the liquid, requiring larger excitation forces. By shortening the tip length, the liquid layer thickness is decreased. The tips are stiffer, the cantilever is less stiff, and this ratio of stiffnesses results in better

sensitivity at the reflector.

In summation, hollow borosilicate force sensors were created, which can perform AFM deflection and tapping mode measurements. The fact that this was possible, and specifically that it was done with photothermal actuation is remarkable. The size of these probes is enormous compared to commercial silicon cantilevers, and one might assume that this discrepancy would result in large stiffness constants and an inability to oscillate the pipettes using only an optical drive. On the contrary, the versatility of the pipette puller allows for a great deal of control over the physical dimensions of these cantilevers, which facilitates identification of useful tip geometries. This allowed for the creation of functional force sensors with stiffness constants of 80 N/m, and resonance frequencies in the range of kHz. Through use of photothermal oscillation, oscillation amplitudes of over 1  $\mu\text{m}$  can be attained, which is more than enough amplitude for tapping mode measurements.

### 3.3 AFM Scanning

With the cantilever properties established in 3.2, AFM topographic surface scans were then performed. While the fundamental probe properties show that these measurements may be possible, more information is required to determine whether the force measurement is enough for the proposed dual measurements. Geometric features of the probe such as the shape of the tip apex may affect the fidelity of the measurement, meaning that model surfaces needed to be examined to elucidate these effects.

To do this, surfaces that had large, repetitive, easy to find features were examined. The large, repetitive features are important as a coarse sample positioning system is not available in the EC AFM, making it difficult to find small features at a specific sample location. The first measurements were conducted with a DVD sample and a CD sample to examine how the probe scanned holes. Then a CD stamper sample was measured to determine how the probe scanned protrusions. A carbon nanotube sample was then used to test of the ultimate resolution of the technique due to its small feature size.

High resolution scanning in air is an important step in testing the probes, yet SICM-AFM measurements require force feedback in a fluid environment which presents additional challenges (e.g. 'forest of peaks'). A DVD samples was scanned in liquid to determine whether force feedback continued to work.

### 3.3.1 Scanning in Air

The first samples attempted was a CD (figure 3.11).

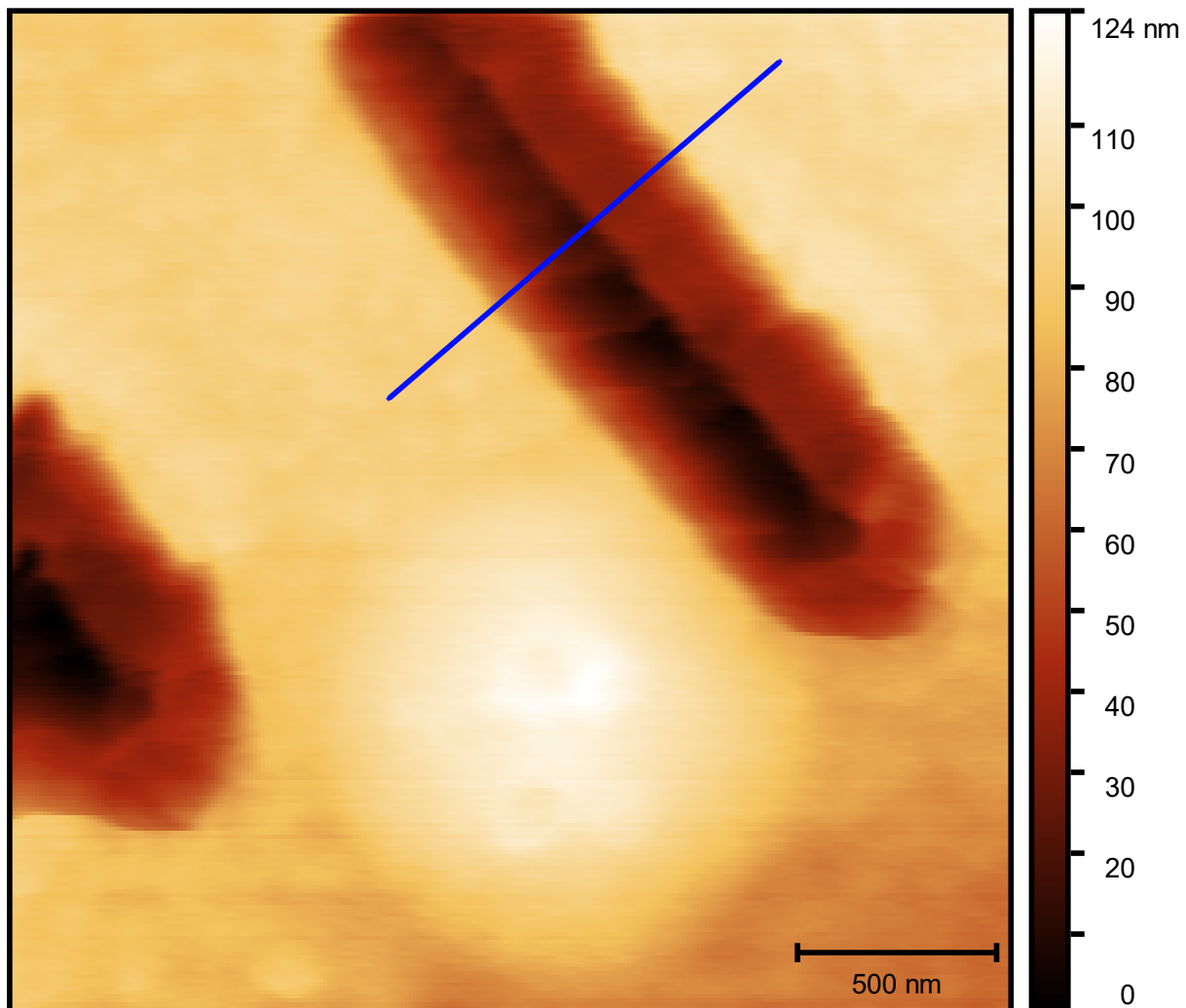


FIGURE 3.11: The surface of a commercial CD sample. The width of the pits is 600 nm with a depth of 130 nm; the pitch is 1.6  $\mu\text{m}$ .



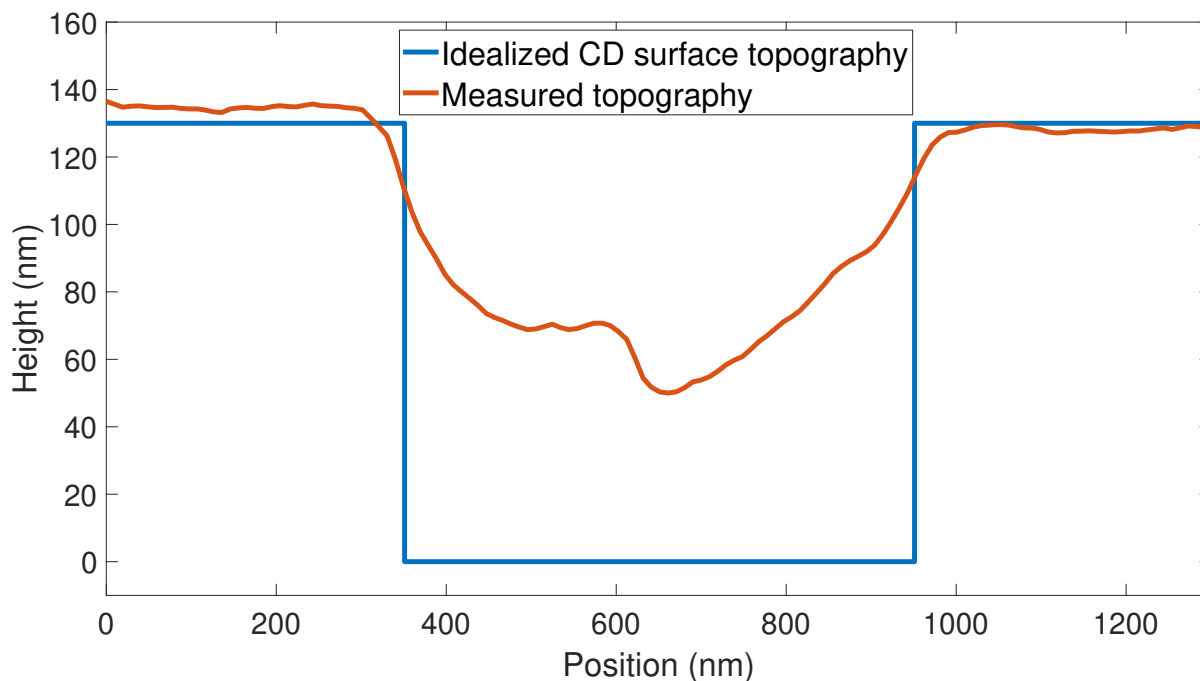


FIGURE 3.12: A line profile extracted from the location of the blue line in the topography scan of figure 3.11.

In this CD sample, sloped walls can be seen in the pits, which can be attributed to the slope of the tip. A gradual slope of the pit can also be seen in figure 3.12, descending until it ascends on the other side. To follow the surface the tip apex should be where the force is applied to the probe, but as the tip apex enters the hole, other parts of the probe begin to interact with the sample. Therefore, the image is not a representation of the force felt at the apex of the probe, but rather the force felt by the entire tip. This phenomenon is common in AFM measurements, and is classified as a tip artifact [134] (a similar phenomenon is observed in SICM measurements [135]). To remedy this, smaller tip apexes were required.

After switching to a new probe, the DVD sample in figure 3.13 was measured.

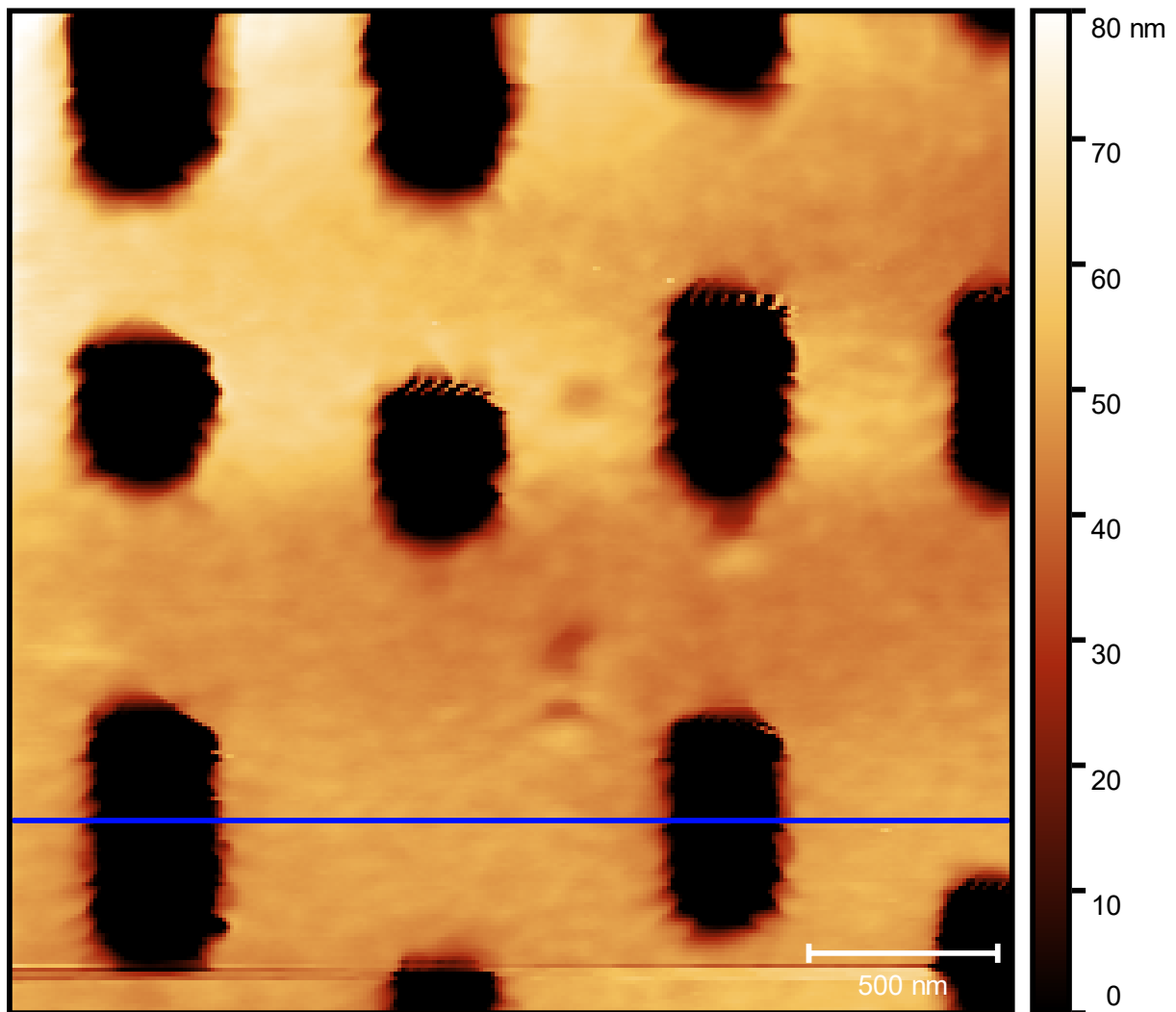


FIGURE 3.13: The surface of a commercial DVD sample. The pits are 320 nm in width and 108 nm deep, the pitch is 740 nm.

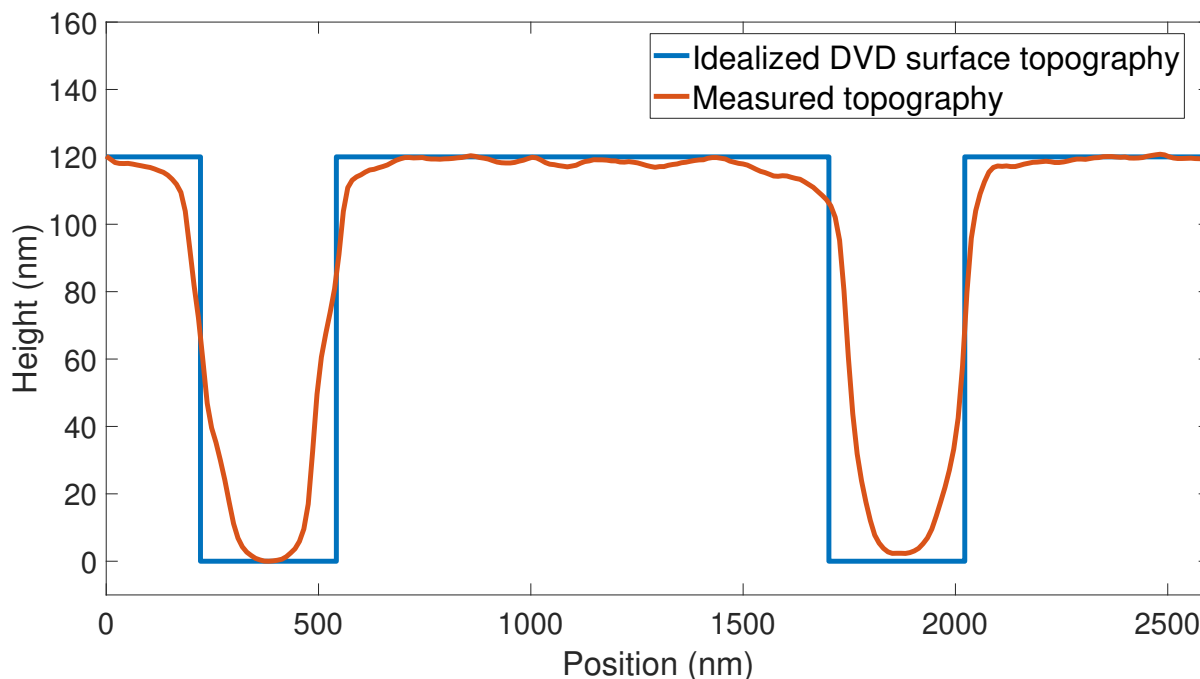


FIGURE 3.14: A line profile extracted from the location of the blue line in the topography scan of figure 3.13.

In this DVD sample, the pits appear simply as holes, with very sharp descent into 320 nm-wide pits. This more closely shows what the pits should look like, in contrast to the CD image. As demonstrated in figure 3.14, the tip followed the surface properly and descended into the pit. It shows a flat topography at the bottom of the pit. From this, one can conclude that the tip is less than 100 nm in radius.

If the tip had a higher aspect ratio (i.e., was ‘sharper’), then we would expect the tip to follow the sample the entire time as is illustrated in figure 3.15. Figure 3.16 also demonstrates the importance of alignment of these probes. As the probe tip begins to deviate from being perpendicular to the surface then the tip will become asymmetric. One side of the probe will have a very low aspect ratio, leading to unwanted interactions and artifacts when scanning high aspect ratio features on the surfaces. Specifically, when the aspect ratio of sample features is greater than that of the tip, this is expected to occur. It should be noted that the features of this sample are very high, and in scans of flatter samples we may simply not see these artifacts since the tip apex will always be closer to the surface than the rest of the probe. Regardless, this measurement led to a more exact tip mounting system.

An important aspect of the experiments of section 3.3 was that even on these large sample scales, the feedback on the probes works properly and follows the topography accurately.

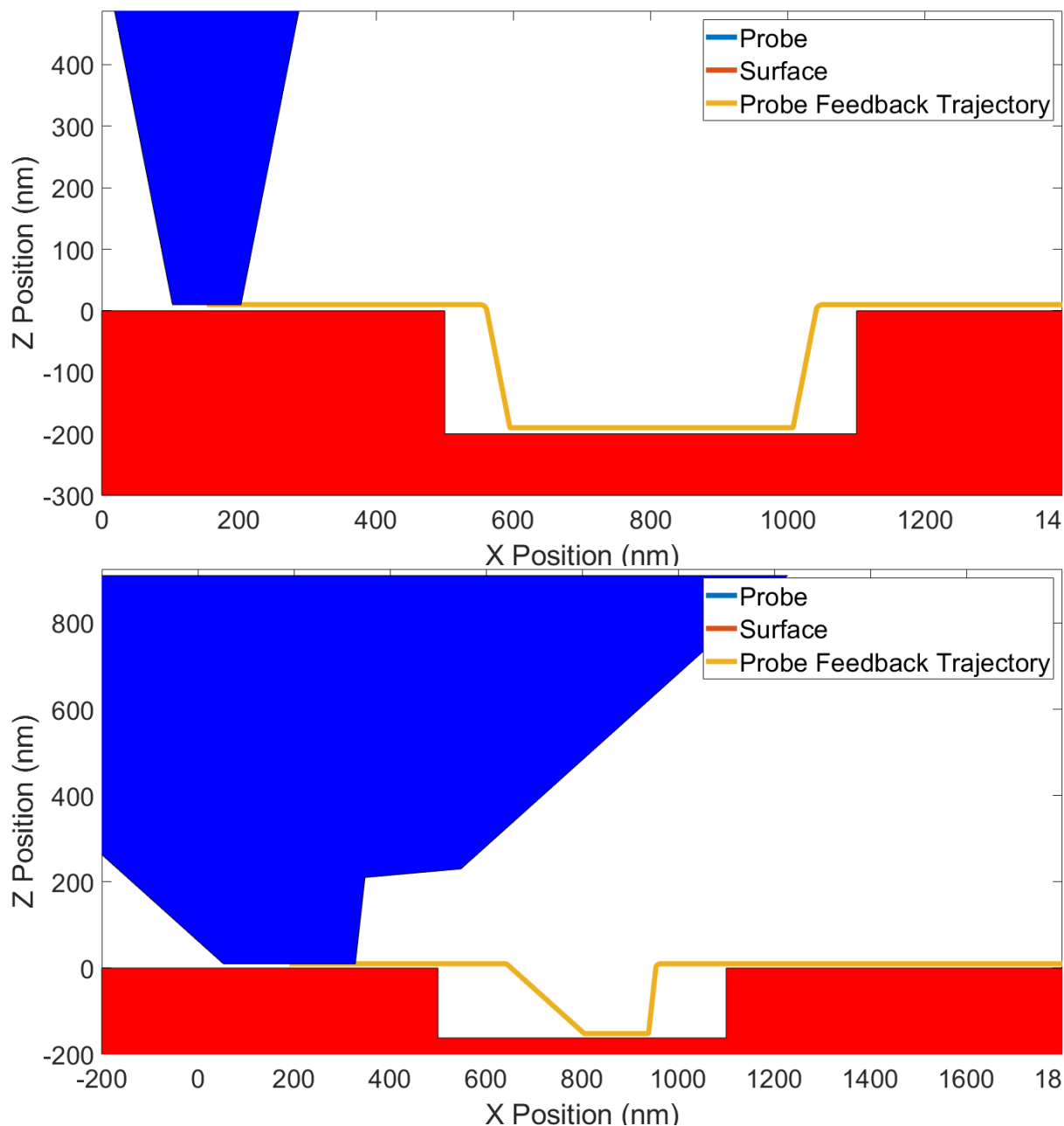


FIGURE 3.15: Depending on the geometry of the tip, convolution effects can be observed. To see an accurate image of the surface, the tip apex must be the part of the probe which is closest to the sample. This is not always true, as shown in these fat tips and high aspect ratio sample features. Depending on the shape of the tip, the CD pits will be recorded differently.

Note that the Q factor of these probes is very high with respect to their low resonance frequency, which limits their scan speed. The characteristic amplitude settling time is:

$$\tau = \frac{Q}{\omega} \quad (3.6)$$

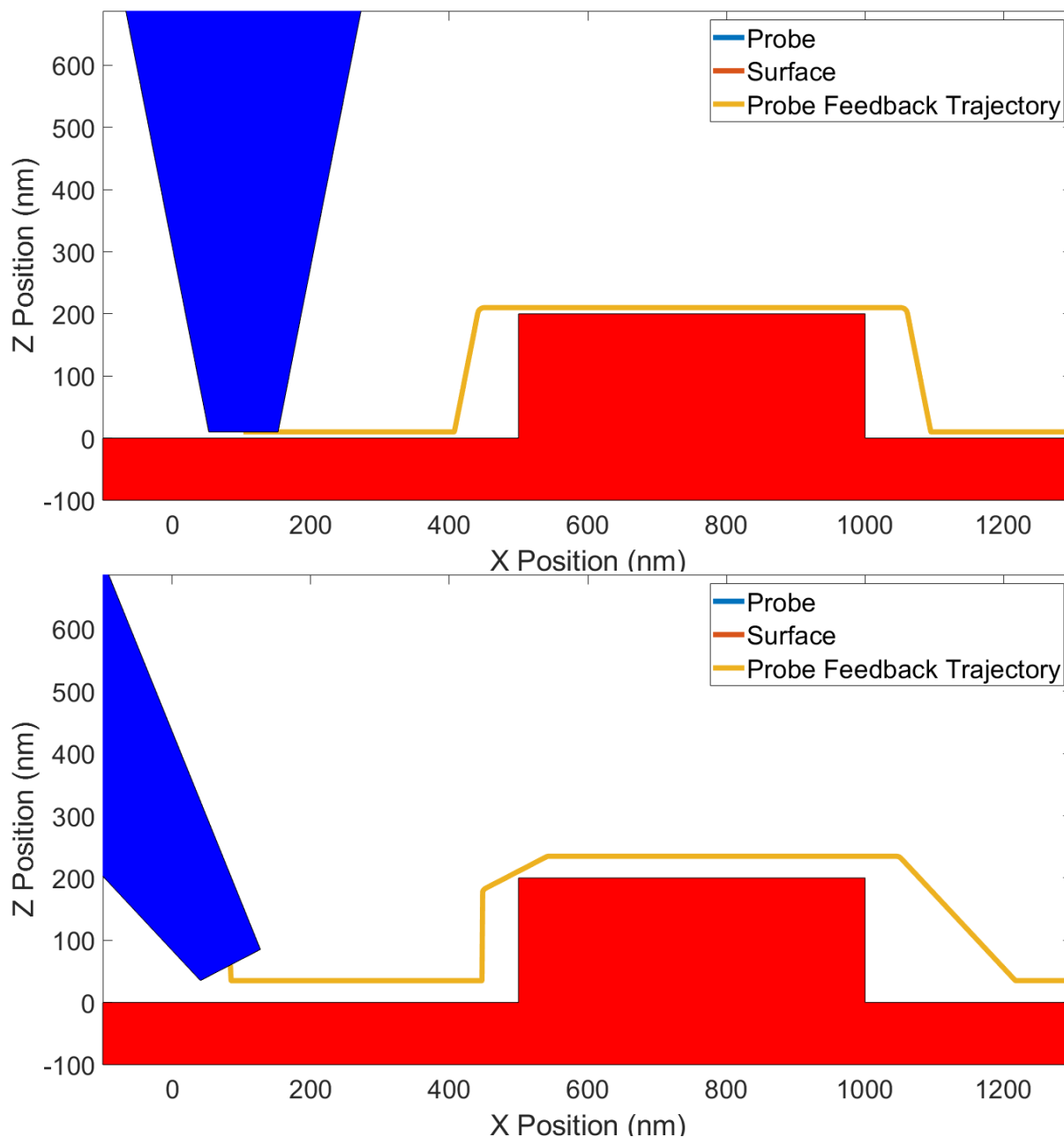


FIGURE 3.16: A tip which deviates from being perpendicular to the surface will cause artifacts, which are most evident at high aspect ratio regions of the scan.

Where  $Q$  is the  $Q$  factor ( $\sim 16\text{kHz}$ ), and  $\omega$  is the frequency ( $\sim 300$ ). It takes time  $\tau$  for a step in the amplitude to settle down by a factor of  $e^{-1}$ . For 10% topography tracking error (which is about  $e^{-2}$ ) one needs to wait 2 (or better even 3) settling times  $\tau$ . One needs to spend at least 2-3 characteristic times per data point (0.1 s). When scanning, slow microscope drift due to thermo-mechanical instabilities or creep can be an issue. Drift or other artifacts characteristic of slow scans was not seen in this sample. This validates the stability of the microscope. Also, to speed up these scans either a higher

harmonic, or Q control (see figure 2.4) can be used to decrease the settling time and increase scan speeds.

The third sample scanned was a CD stamper (figure 3.17) where the topographic features are hills instead of pits on a flat surface.

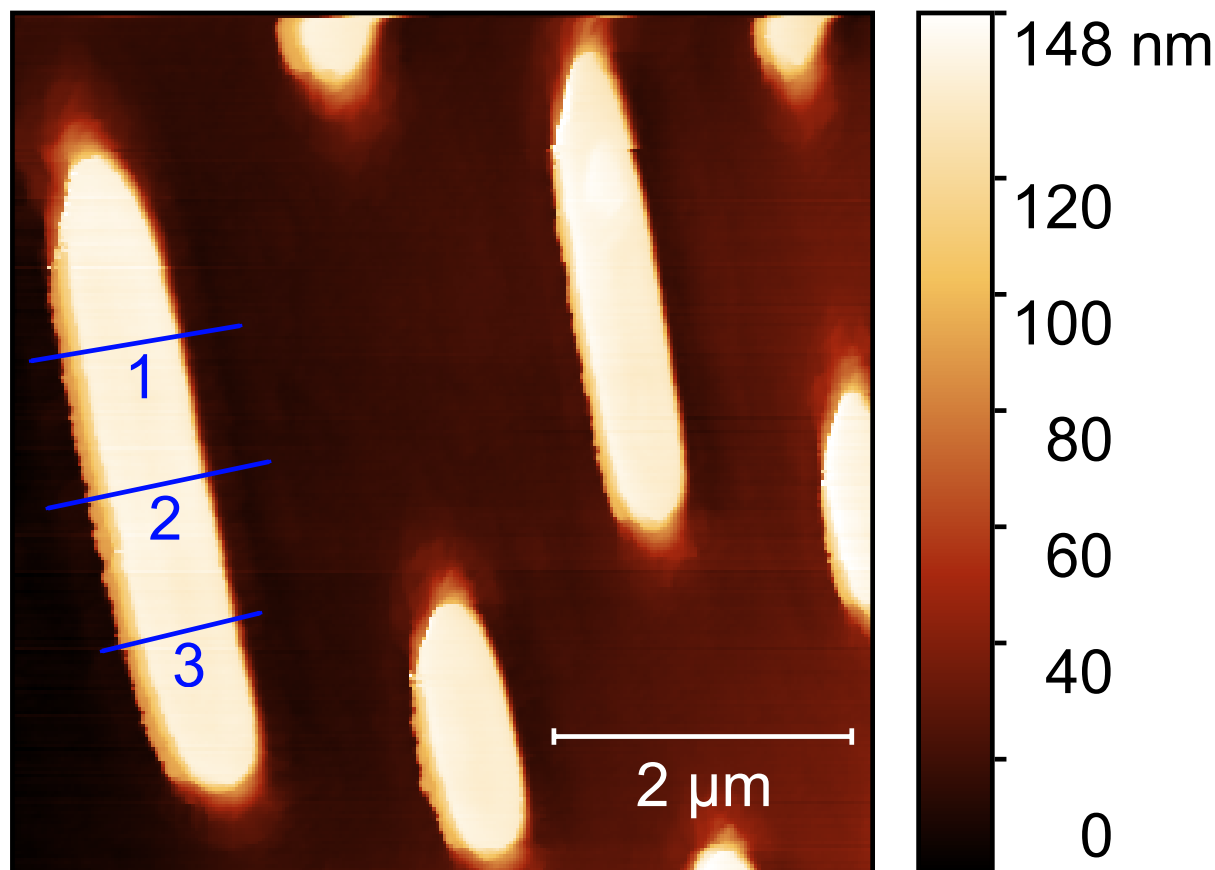


FIGURE 3.17: A topography scan of a CD stamper performed in tapping mode. The numbered lines correspond to the line scans in the following image.

In figure 3.17 a flat background is scanned, with 600 nm wide, 130 nm high protrusions separated by 1.6 μm. Crisp boundaries and very flat surfaces are observed, demonstrating a good feedback with the surface. The aspect ratio phenomenon (as seen in figure 3.19) can be seen in this measurement as well in figure 3.17. The walls of the CD stamper protrusions should be very steep. In the CD stamper image, a very sharp topographic change can be seen on the right side of each protrusion. On the left of the protrusions, the tip passes over the edge, finds a step, then finds the surface again. This is a case of the probe being angled such that force is felt by the probe above the tip apex during the step between protrusion and the rest of the sample. From the line scan shown in figure 3.18, we can make some inferences about the probe. If the probe apex measures a 130 nm protrusion, then the intermediate step is measured at 100 nm, then imaging of the

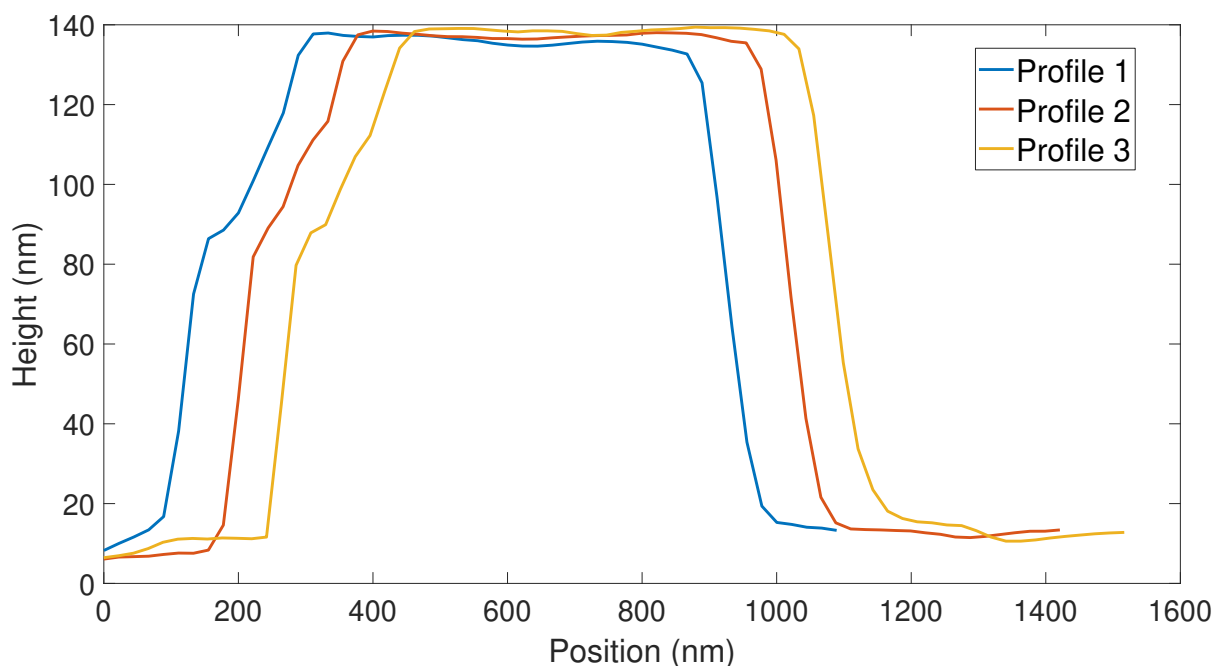


FIGURE 3.18: Line scans from the topographic image of a CD stamper of 3.17. We can see an asymmetry between the right and left side of the protrusion.

protrusion is being carried out with a part of the tip which is 150 nm further up the probe. The intermediate step width elucidates the separation between the tip apex and this point in the lateral direction, around 300 nm. These measurements demonstrated that the limit on accurate slope measurements is around 150 nm over a lateral distance of 300 nm. This is a very steep slope, but by making the perpendicular alignment of the tip to the sample better, some of this effect can be removed.

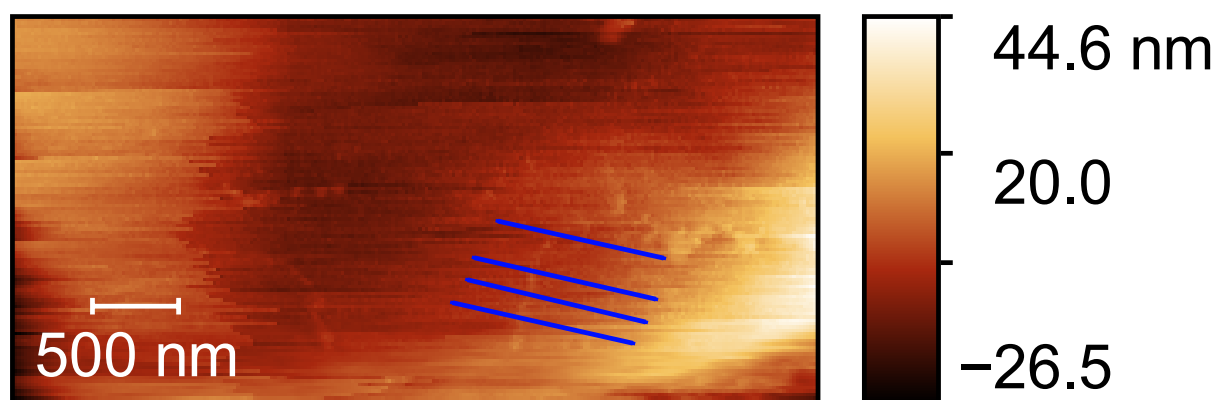


FIGURE 3.19: A topographic scan of carbon nanotubes (CNT) on a template stripped gold surface. The lines pass through a CNT which appears as a light white line. The lines are numbered vertically, from 1 to 4, and their profiles are shown in figure 3.20

As a demonstration of the resolution limit that can be achieved with these probes, a sample of carbon nanotubes on a template stripped gold surface [136] was scanned as



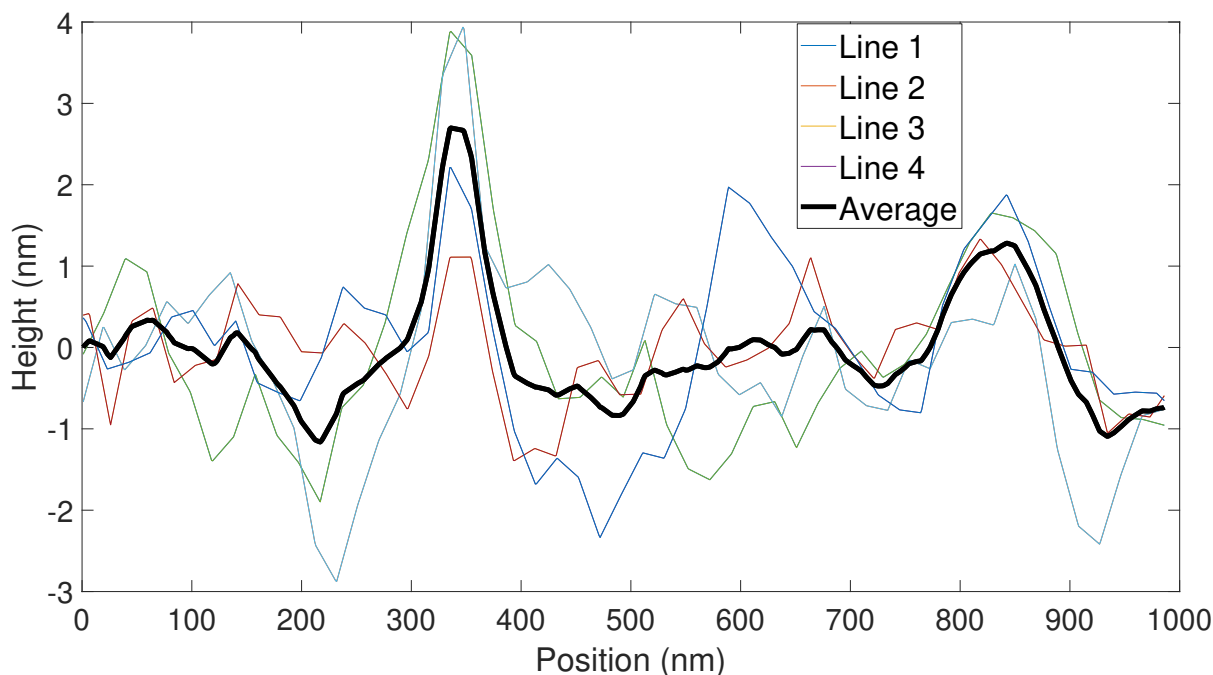


FIGURE 3.20: The numbered lines of the scan depicted in figure 3.19 correspond to this topographic information. The black line is an average of the other lines. From the full width half maximum of the CNT feature we calculate that the diameter of the tip is  $60 \pm 10$  nm.

seen in 3.19. The white line in the topographic image is the carbon nanotubes. The line profiles extracted from the image and presented in figure 3.20 show that this carbon nanotube is approximately 4nm high. The recorded full width half maximum of the nanotube is  $60 \pm 10$  nanometers. This width can be attributed to the fact that the probe tip is wider than carbon nanotube. Therefore, the width of this feature will indicate the width of the probe tip itself. Figure 3.21 demonstrates an example of a tip scanning a feature which is smaller than the tip, and the resulting topography line scan.

These experiments in air demonstrate that the probes developed can image with  $\sim 100$  nm lateral and  $\sim 1$ -2 nm height resolution. The measurement also clearly demonstrated tip-sample convolution artifacts well-known in AFM of rough surfaces [137–140].

This result confirms that a pipette probe can be used for feedback. However, the probes must operate in a fluid environment to perform SICM measurements which presents additional challenges as described by the 'forest of peaks' phenomenon. The previous frequency sweeps indicate that the 'forest of peaks' problem should not significantly affect the quality of the measurements, but this must be confirmed by a full scan in a fluid environment.

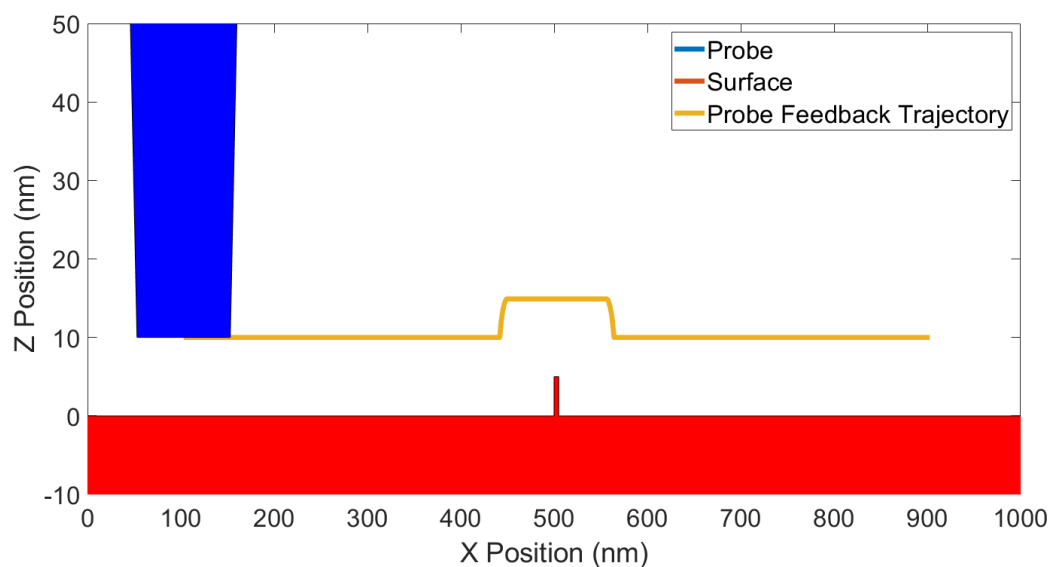


FIGURE 3.21: In this simulation, the probe was scanned over a small feature with the approximate dimensions of a carbon nanotube. Although the carbon nanotube appears in the topography image, the exact shape that is recorded is dependent on the tip apex shape.

### 3.3.2 Topography Scanning in Liquid

In this section, AFM measurements were performed in liquid based on the information gleaned from observations made during the AFM topography scans in air in 3.3.1. This is crucial given that the aim of this technique is to correlate simultaneous AFM measurements with electrochemical measurements, which requires the tip to be in fluidic contact with the sample.

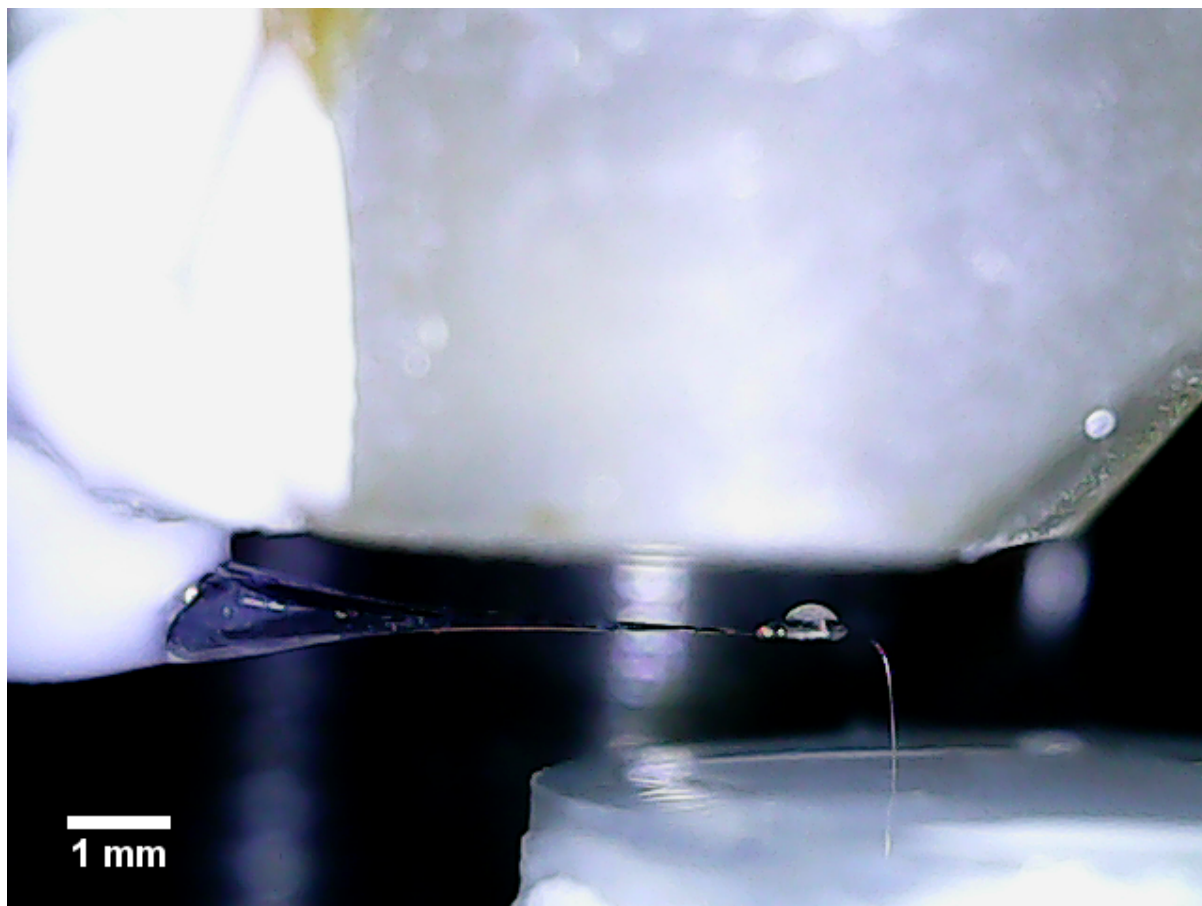


FIGURE 3.22: A probe descending into a liquid bath, to a DVD sample surface. That measurement is shown in figure 3.23

In comparison to the previous DVD measurement (see figure 3.13), the signal to noise ratio is substantially lower in figure 3.23, so the image appears to be blurrier. This was partially due to liquid dampening the tapping amplitude. To reduce the dampening, the probes tip length was changed and the reflector was experimented with to increase the free oscillation amplitude.

Another persistent challenge was the evaporation of the aqueous 0.4 M NaCl electrolyte. The tip of the probe must be immersed partially in the electrolyte, so the tip apex can reach the sample and image as seen in figure 3.22. However, the reflector of the probe must not be immersed. The reflector acts as a large paddle in the liquid, meaning that oscillating the probe with a detectable amplitude requires a very large excitation amplitude to overcome the hydrodynamic drag. With the excitation laser power used in this microscope, it was not possible to detect the amplitude of the probe when the reflector was immersed in liquid.

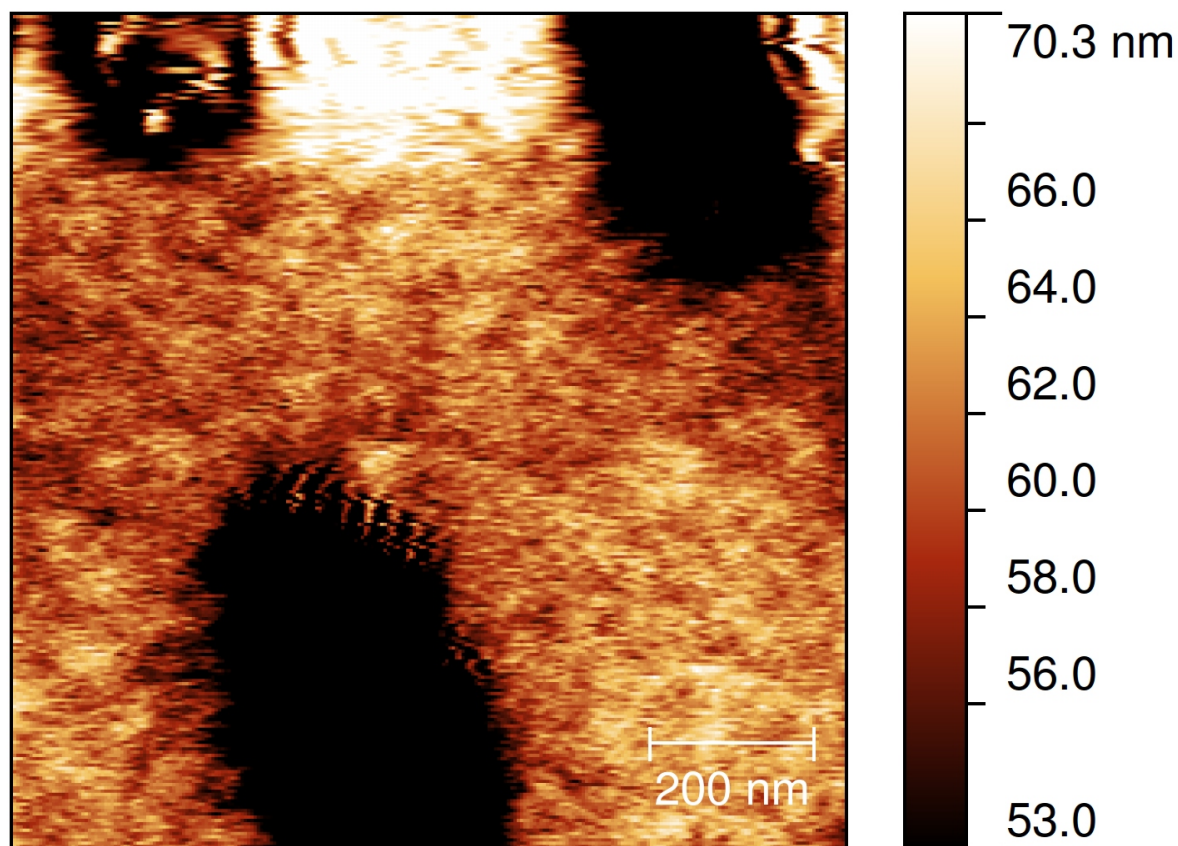


FIGURE 3.23: A topographic scan of a DVD sample in performed in a bath of water.

This means that the tip was only partially immersed in liquid. Also, depending on how much of the tip is in the liquid, the probe will feel different amounts of drag. If the level of the liquid recedes during measurement, the force on the tip will change.

Reference electrodes like AgCl work well in aqueous solutions, so an aqueous 0.4 M NaCl electrolyte (NaCl of  $\geq 99.5\%$  purity, Sigma Aldrich [130]) was used during initial measurements. As the tip approached the surface, the tapping amplitude reduced as the tip descended further into the electrolyte. The tip eventually reached the surface, adjust the optics and begin scanning. During the scan, water would evaporate, the length of the tip immersed in liquid would become shorter, and amplitude was affected. The rate of evaporation was variable because conditions such as humidity (which depended on ambient conditions) and temperature (which depended on ambient conditions and the heat from the incident detection laser and excitation laser intensity) would be different on each run. Furthermore, the thickness of the liquid layer was dictated by the length of the tip. Generally, once a scan began, it took one hour for the water to completely evaporate.

For an estimate of the evaporation rate per hour:

$$g_s = (25 + 19v)A(x_s - x) \quad (3.7)$$

Where  $g_s$  is the mass of water evaporated per second (kg/s),  $v$  is the velocity of the air above water surface (m/s),  $A$  is the water surface area (m<sup>2</sup>),  $x_s$  is the maximum humidity ratio of saturated air at the same temperature as the water surface (kg/kg), and  $x$  is the humidity ratio of air (kg/kg) [141].

To find the time required for the liquid bath to evaporate, the mass of water is divided by the rate of evaporation.

$$\begin{aligned} T_{evaporation} &= \frac{M_{water}}{g_s} \\ &= \frac{\rho_{water} \cdot H \cdot A}{(25 + 19v)A(x_s - x)} \\ &= \frac{\rho_{water} \cdot H}{(25 + 19v)(x_s - x)} \end{aligned} \quad (3.8)$$

Where  $H$  is the height of the liquid and  $\rho_{water}$  is the density of water. The velocity of the air is 0 m/s because the bath is protected from air currents in the isolation box, at 25° Celsius the maximum humidity ratio of saturated air is 0.019826 kg of water / kg of Air [142], and the humidity level in the building where the measurements were conducted, is about 50%.

If the tip is assumed to be fully immersed, then 500  $\mu\text{m}$  of liquid must evaporate to expose the surface. Evaluating with these values we attain a value of 2 hours. Each value may vary slightly, and approaching the tip to the sample is not instantaneous, meaning that the observed evaporation time of 1 hour is reasonable.

This slow evaporation lead to a slow drift towards the surface as the tip was scanned. By post-processing the images, much of this drift was removed. Also, the faster the scan happens, the less time there was for evaporation to occur. The thickness of the water layer still limits the total time of the measurement, and this is limited by the probe tip length. If the reflector touches the electrolyte it will cease to oscillate due to the drag of this large reflector through liquid. Also, longer tips lead to tip instabilities as discussed in section 3.2, so the tip needed to be kept short.

Another way to deal with the evaporation is by changing the evaporation rate. If the AFM is operated in high humidity conditions, then the evaporation rate is reduced. This is done in other SICM labs by placing sponges of water around the microscope, thereby increasing the humidity around the microscope. However, this can lead to corrosion of the microscope, which can impede its function. Also, condensation of liquid in the microscope could lead to short circuits. Short circuiting of the piezo can lead to the piezo cracking, which takes substantial time and resources to fix. Given the potential risks posed to the microscope, this method was not attempted.

Another method is to use an electrolyte with a very low vapor pressure, which is why the electrolyte was eventually switched to propylene carbonate (this includes all measurements from 4.4 until the end of the thesis, excluding figure 4.31).

### 3.4 Conclusion

To assess the results of this Chapter, the initial questions must be considered. The first question posed whether the probes can perform basic AFM functionalities. The resonance curves and approach curves in air and fluid confirmed that the probes function as AFM force sensors. Through this measurements it was demonstrated that as these pipette probes are massive compared to commercial silicon cantilevers, they are impossible to oscillate optically when they are completely immersed by liquid. However, the long tip of these probes allows the tip apex to reach the sample surface without immersing the reflector. Having only the tip immersed in liquid drastically reduces the viscous damping, and the reduction in Q factor is small. Additionally, piezoelectric actuation in liquid can introduce the “forest of peaks” problem (see section 2.5.5). This problem was completely avoided using photothermal actuation. This combination of long-tipped probes and photothermal excitation provides an opportunity for faster, higher signal-to-noise tapping mode AFM measurements in liquid.

The second question posed was whether the probes can be used image a surface. These images demonstrate that it is possible to perform topographic scans on multiple sample surfaces, with sample feature sizes ranging from the >100 nm tall hills on CD stampers to 2 nm tall carbon nanotubes. This is crucial, as the strength of the proposed technique is its ability to disentangle topographic information from electrochemical variations. Although the geometry of the tip apex can introduce some uncertainty to the topographic images, these effects are predictable and could be eliminated by tip characterization and




deconvolution of the topography images. High aspect ratio features will show some distortion, but the  $>100$  nm features of CD and DVD samples are quite large, and many interesting samples do not have features of this size. Meanwhile, the carbon nanotube sample demonstrates that the probes are sensitive enough to image and characterize extremely small features. While the tip size will limit the lateral resolution of this technique, the resolution of the probes is more than sufficient for many interesting samples.

These measurements can also be adjudicated through the lens of some other electrochemical SPM results. Korchev's study on proteins of the plasma membrane of boar spermatozoa with SICM used a 13 nm inner diameter quartz pipette tip to attain high resolution SICM images [143]. This diameter will determine the resolution of the technique, so the measured feature sizes on the order of 10 nm. However, the distribution of protein widths histogram shows two peaks at between 10 and 20 nm and another between 30 and 40 nm. This could be indicative of tip artifacts, the first peak being at the diameter of the tip openings, and the second at the diameter of the tip apex. However, delineation of this effect is not possible as there is only the one channel of information. In a further study [144] the method of AC-SICM is used to attain a more reliable feedback signal that is not affected by ionic changes or tip blockages. While this acknowledges the challenge of tip artifacts that were observed in the study on proteins, AC-SICM is operated far from the surface to avoid crashes, and therefore current changes are relatively small in comparison to the bulk current. Additionally, a piezo must oscillate the probe, which exacerbates the positional noise of the probe (especially due to the "forest of peaks" 2.5.5). This results in a noisier SICM topography system. To compensate for this, the data is "splined" to remove "spikes" which is equivalent to post-measurement low-pass spatial filtering which can create artifacts of its own. Together, this demonstrates the tremendous challenge in achieving high spatial resolution measurements, and the necessity of multiple data channels to delineate the phenomena at play. Although the quoted resolution of this purely SICM system was higher than the resolution on the CNTs in this study, the challenge of tip artifacts can play a large role that may only be unraveled through a combination of techniques. Additionally, the probes of this study could be modified to obtain the same resolution. By switching to quartz pipettes the tip openings could be reduced, and resolution could accordingly be improved.

Measurements by Takahashi on biological samples have employed a more robust approach through a SECM/SICM system for measuring topography and electrochemical imaging [145]. By decoupling these signals the channels can be correlated for a better understanding of sample features. SICM provides the topographic measurement of a glucose



oxidase spot, where the smallest feature is a ridge-like structure formed by microvilli, and it measured as approximately 400 nm in diameter (much larger than the 60 nm CNT features). The holes of the ridges seem to be sloped, which suggests the same type of tip convolution observed in the CD sample measured in this study, confirming that this phenomenon also occurs in other SICM systems. Additionally, the electrochemical image is performed at two heights: 100 and 600 nm. **The signal to noise ratio in the 100 nm measurements is much higher, and the electrochemical features are much more distinct.**  This emphasises the importance of being close to the sample to maximize electrochemical contrast. Turning back to the results of this chapter, the tapping amplitude setpoint was around for 10 nm for most AFM scans. By using AFM in conjunction with electrochemical measurements, the probe may be much closer to the surface than a measurement performed with SICM distance regulation, which will in turn yield more sensitive, higher contrast electrochemical measurements. This is further emphasized by another Takahashi measurement on cilia [146]. By comparison scan lines to theoretical approach curves, the relation between scan height and current sensitivity can be examined. By scanning at a current reduction of 1.0% vs. 0.3% the distance regulation sensitivity can be greatly increased. As will be seen in 4, the AFM distance regulation for an even larger reduction in current.

Another important observation on these probes in their ability to scan in liquid. Topography scans in liquid environments are challenging because viscous damping and an increase in effective mass reduce the Q factor of cantilevers. With lower Q factors, the measurements will be less sensitive to force changes.

These observations indicated that the probes function well as AFM sensors. In the next chapter this ability is used not only a stable force feedback, but to produce high resolution force measurements that can be compared with the progression of electrochemical measurements.

# Chapter 4

## Combined Electrochemical and Force Measurements

### 4.1 Introduction

Once the AFM functionality was demonstrated, the electrochemical functions had to be verified. This is broken down into the following steps:

1. Can current be measured through the probes? The probes had to be shown to pass current, and to produce SICM approach curves in liquid while simultaneously recording accurate force information. This is first done at a single position where approach curves are done in two AFM modes - deflection mode and tapping mode (4.2).
2. What crosstalk do the AFM and SICM channels show? To see how the geometry of the tip affects the combined AFM and SICM, a two-dimensional surface scan was performed (4.3).
3. Can spatially resolved electrochemical measurements be performed reproducibly? To demonstrate surface resolved electrochemical measurements and its reproducibility the electrochemical properties of the surface were measured using a droplet method to perform many CVs at a single point on a gold surface (4.4).
4. What are the abilities and limitations of this scanning droplet technique? To investigate this, two-dimensional scans of point resolved current voltammetry are presented (4.5).

5. Can these probes be used as a microfabrication device or to study local corrosion? Their use in creating holes on a surface by locally electrochemically corroding the surface is examined (4.6).

In the following, each of these important questions will be addressed to verify the functionality and understand the capabilities and limitations of the probes developed in this thesis.

These measurements and their analysis of this chapter were performed by the author. Dr. Yoichi Miyahara provided guidance in operating the AFM system. Dr. Madeline Anthonisen provided assistance in operating the Asylum Research MFP 3D microscope to perform the experiments in section 4.6.

## 4.2 Current Sensing Characteristics

The next step in the process introduces ionic current measurements. This was demonstrated using a standard SICM approach. A surface bathed in electrolyte was approached while a bias was applied between an electrode in the pipette probe and an electrode in the electrolyte bath. The electrolyte consisted of 0.4 M NaCl ( $\geq 99.5\%$  purity, Sigma Aldrich [109]) in water (water of  $> 18\text{M}\Omega\text{cm}$  after filtration through a Millipore Milli-Q Reference Water Purification System, Fisher Scientific [110]). This demonstrated that the expected SICM behaviour could be obtained using the pipette probe developed for the current study. Additionally, it demonstrated that force channel can be recorded, allowing for the examination of the correlations between the current and force channel.

Our initial approach curve occurs in deflection mode as seen in figure 4.1.

In deflection mode a small, nonlinear force is felt by the probe until contact with the surface is made. This force, and the hysteresis between the upward and downward Z position sweeps can be attributed to the electrolyte's adhesion on the probe. The length of the probe which is immersed in liquid will change throughout the measurement, and therefore there will be an extra force contribution that is picked up by the deflection. Once the probe contacts the surface, it is deflected linearly as the probe is long and its angular deflection will be close to  $0^\circ$ .

In the SICM channel the resistance to ionic flow should occur once the probe is within one tip opening of the sample. This seems to happen here, as contact and decrease in SICM

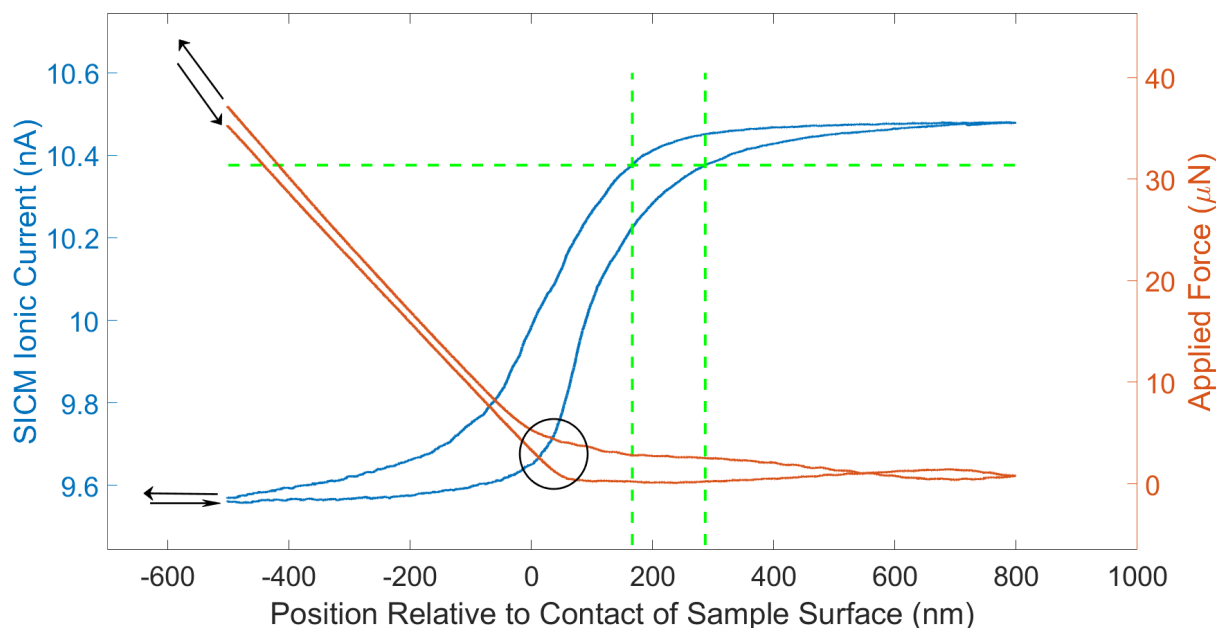


FIGURE 4.1: In this experiment the probe begins in contact with the surface, and is retracted, then it is approached to the surface again. The arrows show where the force curve began and ended. The circle indicates where the probe comes into repulsive contact with the surface, which is defined as 0 tip-sample separation. In typical SICM measurements the feedback is operated at 98-99% of the unapproached signal to avoid tip crashes [147–151], the 99% current level is indicated by the horizontal dashed green line. Over the course of this approach curve the SICM current reduces by 10%. Also, there is a difference between the Z position where the SICM current passes the 99% maximum current threshold on the approach and retraction, shown by the vertical dashed green lines. This was performed on a borosilicate glass sample in 0.4M NaCl in water as electrolyte, with a probe of  $75 \pm 1$  N/m stiffness constant and  $2013 \pm 1$  Hz resonance frequency. The maximum applied force is approximately  $40 \mu\text{N}$  on this approach-retraction cycle.

current occur approximately 200 nm apart. It should be noted that the current did not decrease to zero. As the probe approached the surface, the SICM resistance increased, but due to the orientation and geometry of the tip, there was always a pathway for ions to travel. Larger resistance changes meant larger signal changes, which increased the signal to noise ratio. This is another reason why the probes must be aligned properly during their creation. Note that before the probe contacted the surface, the current change as a function of tip sample separation was very steep. Also, there is a substantial hysteresis in the SICM current, as it crosses the 99% of maximum current threshold at positions separated by over 100 nm. The 99% of maximum current condition is used in SICM scanning to avoid damage through contact of the probe with the surface. While this measurement shows that the surface can be approached much closer without large contact forces, for demonstration purposes nearly 40 nN of force were applied to this probe. It is very probable that this force damaged the probe in a way that lead to

a change in the ionic resistance of the tip. The force channel is less sensitive to this damage, there is a small hysteresis in that channel.

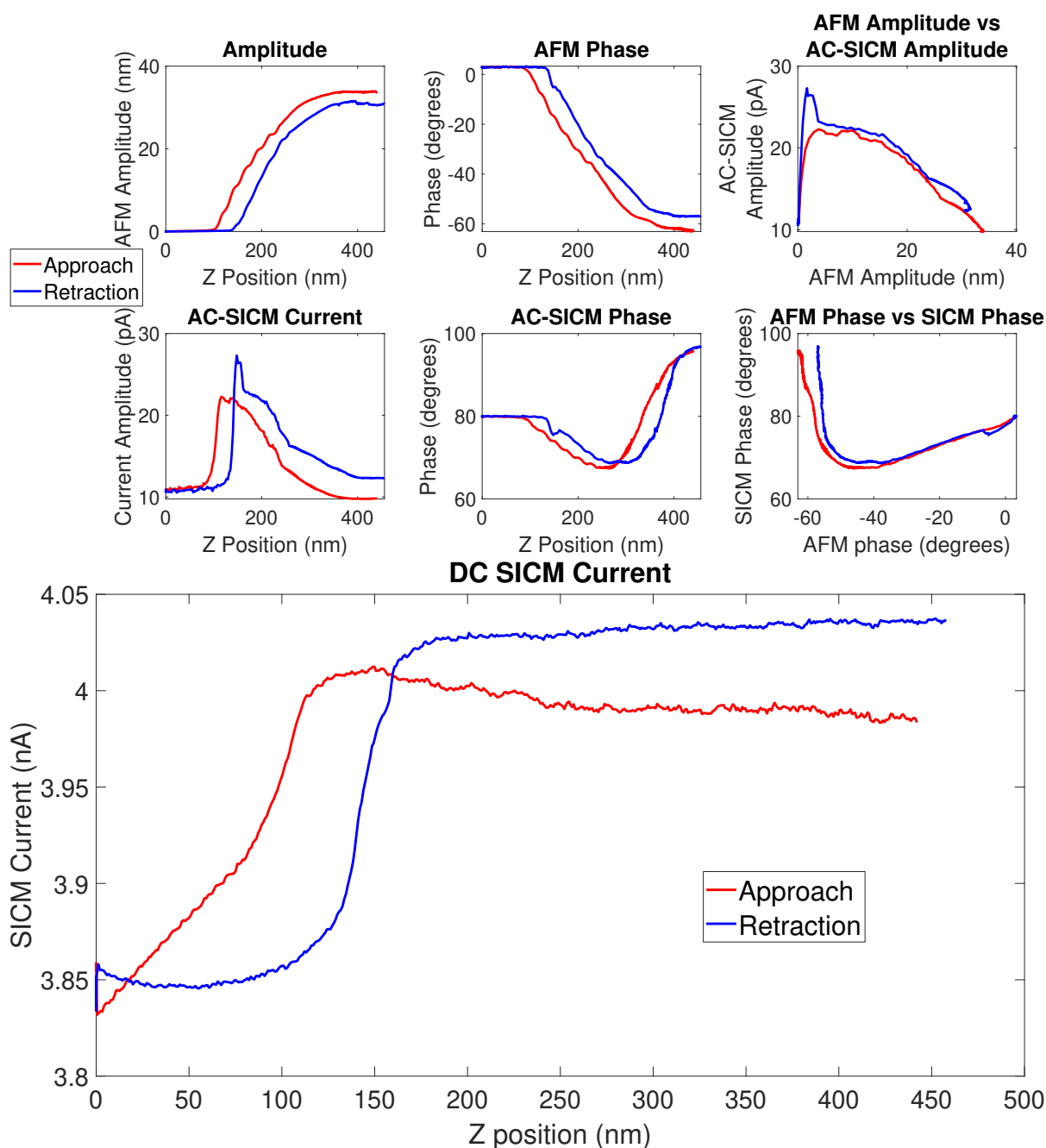


FIGURE 4.2: The tip was oscillated at 2 kHz with an amplitude of  $1 \mu\text{m}$ , and is approached to a borosilicate glass sample at a rate of 100 nm/s. This was performed on a borosilicate glass sample in 0.4 M NaCl in water as electrolyte, with a probe of  $75 \pm 1 \text{ N/m}$  stiffness constant and  $2013 \pm 1 \text{ Hz}$  resonance frequency.

In tapping mode the same phenomena are at play, as seen in figure 4.2. In the measurement above the tip was oscillated at 2.013 kHz with an amplitude of approximately 30 nm, and was approached to a borosilicate glass sample at a rate of 100 nm/s. In this

measurement additional data channels were recorded to examine the correlations between the registered force information and ionic current information.

The DC-SICM channel shows a curve similar to the approach curve seen in the contact mode measurement. There was a significant hysteresis between the approach and retraction. One possible explanation of this could be contamination at the tip of the probe, such as salt crystallization or loose particles such as dust. Contamination at the tip could have increased ionic resistance and contact with the surface could remove this contamination.

The AC-SICM current amplitude was also measured. As the probe oscillates, the measured current depends on the instantaneous position of the probe. Therefore, there should be a small SICM current oscillation at the same frequency as the cantilever oscillation. The amplitude of this oscillating AC-SICM current should be the derivative of SICM approach curve, and this is what is seen if the DC-SICM current and the AC-SICM Current Amplitude are compared. Because the frequency of this oscillatory AC-SICM current is known, the amplitude can be found by using a Lock-In amplifier. This could prove useful as a measurement channel as it provided information about the slope of the approach curve without performing an approach curve. The expected phenomena can be seen in this approach curve. When the probe was far from the surface, and when the probe was approached to the point that the amplitude was 0 nm, the DC-SICM signal was constant. Therefore, the AC-SICM signal should have been zero. However, due to the noise in the SICM channel, one would expect to see a constant value of the AC-SICM current over the regions, which is what was seen in this measurement. As the probe approached, the AC current decreased as the DC current decreased. This reached a maximal AC current value. As the probe continued to approach, the amplitude decreased to 0 nm. The AFM amplitude determined the region over which the numerical differentiation of the DC current occurs. Also, the steep drop in the DC current channel flattened out. These two factors produced a steep drop in the AC-SICM current channel.

The phase information is not as simple to interpret. The AFM phase is the phase delay between the excitation signal applied to the probed, and the measured oscillation signal. This phase can be influenced by visco-elastic properties measured by the probe, which leads to phase contrast between materials, and the usefulness of phase imaging. For the SICM phase, the phase delay is between the excitation signal applied to the probe and the sinusoidal component of the SICM current. This means that if the phase contrast in the SICM channel were only due to the mechanical properties of the probe, then both phase curves should have been the same, with an additional phase offset between them.

This seems to be the case until the probe approached 200 nm away from the surface, where a significant deviation began. This means that the ionic impedance must be a function of Z position for this experiment. Interpretation of what may have occurred is beyond the scope of our measurements and requires further investigation.

Performing these approach curves has confirmed the ionic approach curve characteristics that have been reported elsewhere [152]. Approach curves were performed in liquid, confirming that we can measure ionic currents with these probes as low as  $\sim 100$  fA. Additionally, the force channel demonstrates the linear correlation of the ionic current with the measured force. From this it can be concluded that the ionic current is indeed a good proxy for the force channel, and the method of SICM for performing topography scans is valid; however, the approach curves show a major advantage of a combined AFM-SICM method versus a purely SICM method.

In most SICM measurements the scanning condition is that the ionic current will be equal to 99% of the signal far from the sample surface. Firstly, this means in a purely SICM method, the probe is not necessarily scanning where the derivative of the ionic current by Z position is maximized, so the sensitivity of the measurement is not maximized. Secondly, for example, assuming the current signal noise is 100 fA (which it was in the present study) and the desired signal to noise ratio is 10 to 1, this would mean that the minimum magnitude of the ionic current far from surface would have to be 200 pA. In turn, this places a restriction on the minimum electrolyte concentration and the minimum tip apex diameter. Depending on the sample being measured, this can be limiting. If one increases the size of the tip apex, the larger tip will have a worse lateral resolution. On the other hand, electrolyte concentration changes are not always feasible. For example, if one wishes to look at surface charge effects, the electrolyte concentrations must be low to facilitate ionic current rectification at the pipette tip (see section 1.3.1.1) [50, 51]. Or, if the sample is biological in nature, a change in electrolyte concentration may cause cells to die prematurely. However, with the proposed technique, safely approach the probe to the sample surface based on force feedback. At this position the current is reduced by 10%. If this is applied to the example above, this means one can operate with the same current to noise ratio at 20 pA instead of 200 pA. This is a major step forward towards facilitating surface charge measurements via SICM.

From the data presented in this section, two major conclusions can be drawn:

1. The various AFM and SICM information channels strongly correlate on a homogeneous sample at tip-sample separations exceeding  $\sim 100$  nm. This is the basis of



the common usage of ‘regular’ SICM to image structures with  $\sim 100$  nm resolution by operating at small changes in current (and thus tip-sample separations of  $>100$  nm).

2. These measurements clearly show that these AFM-SICM probes can be used to simultaneously perform regular tapping mode AFM and measure an ionic current. This allows the combined techniques to be used to extract sample-specific information on heterogenous samples.

### 4.3 Dual AFM-SICM Measurements

The measurements described in the previous section demonstrated the use and dynamics of the force feedback in relation to the current channel at a single point. These measurements show that a two-dimensional scan is possible. The surface scan measurement was performed on a CD stamper sample. As in the previous topography surface scans, the CD stamper sample allowed for exploration of how the geometry of the probes influence the scans.

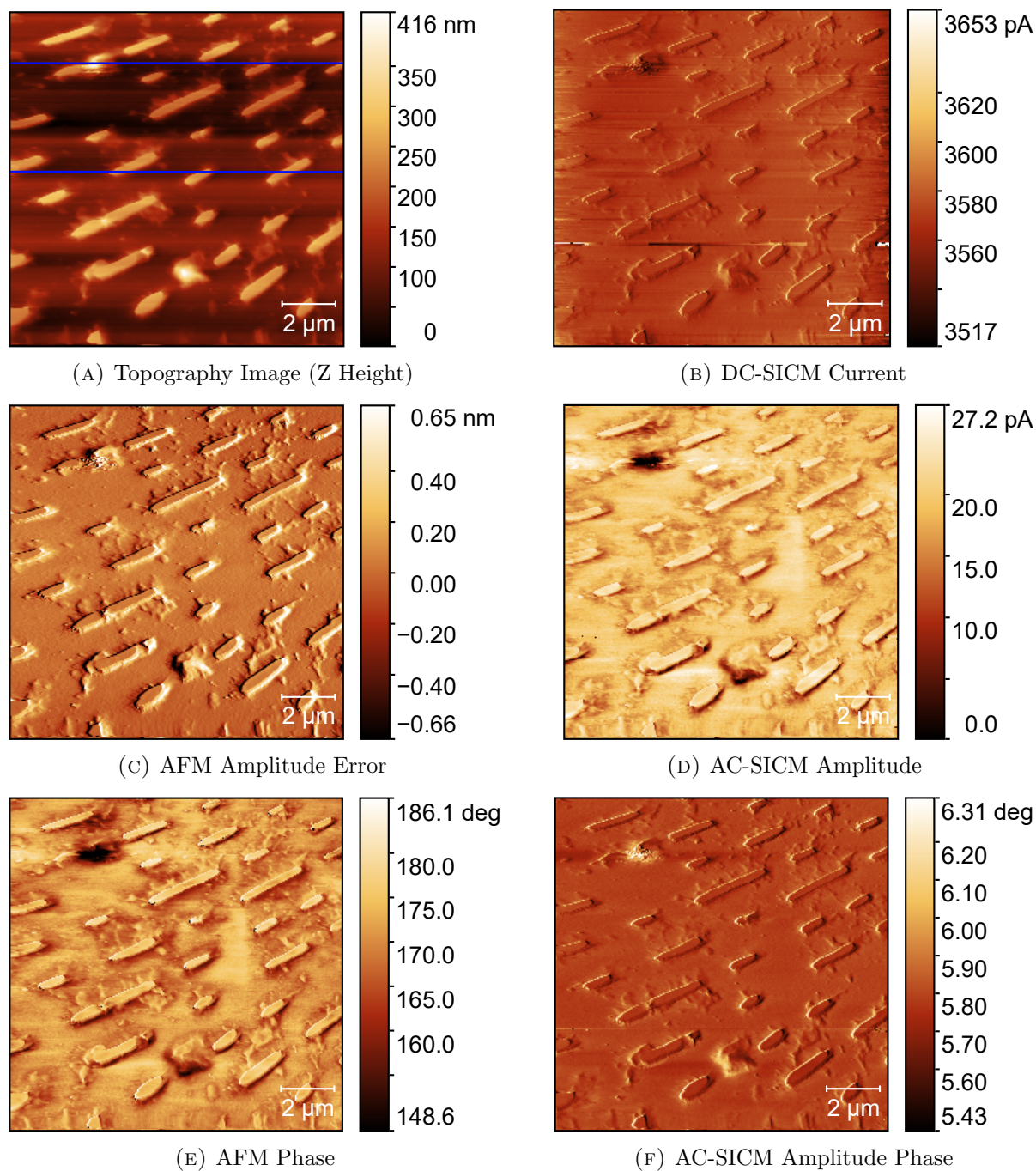


FIGURE 4.3: This data is from an AFM-SICM measurement of a CD stamper surface immersed in an electrolyte of 0.4M NaCl in water. The blue lines in the topography image correspond to the following line scans; the bottom line scan is shown in figure 4.4 and the top horizontal line is shown in figure 4.5.

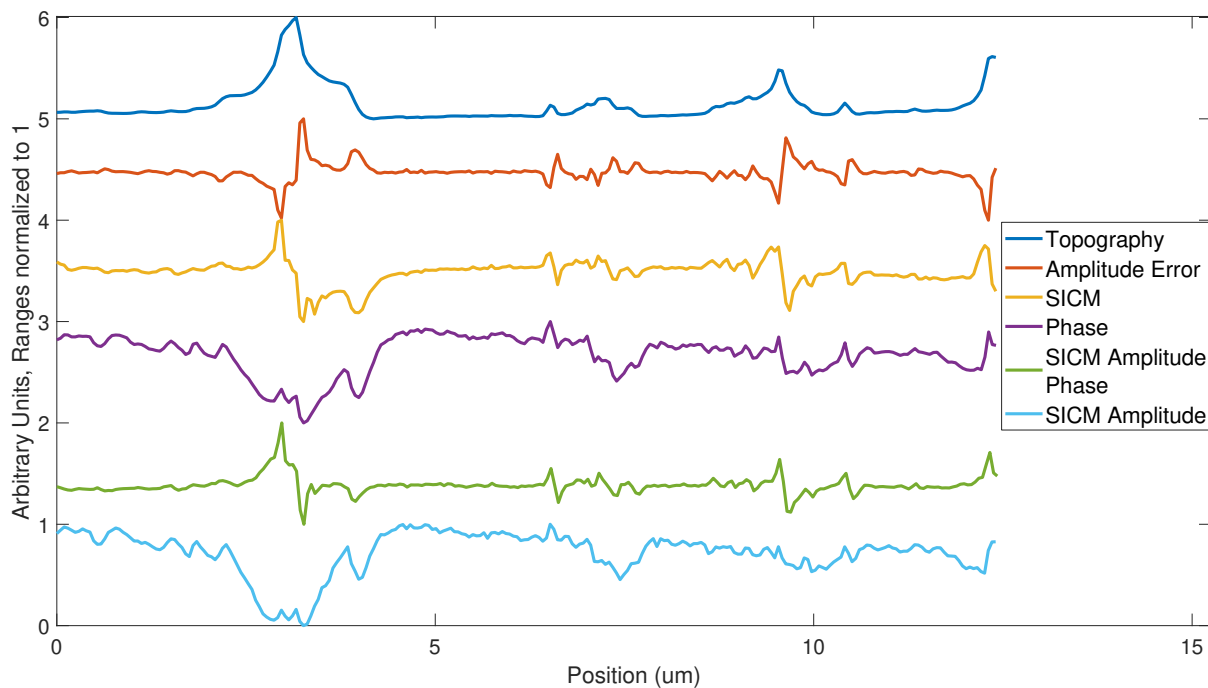


FIGURE 4.4: Line scans extracted from all the data channels from the bottom horizontal line of figure 4.3 demonstrating how the channels coordinate over the regular protrusions of the CD stamper surface. The normalization constants for each channel in the same order as the legend are: 297 nm, 0.484 nm, 29.6°, 61.6 pA, 17.9 pA, 0.767°.

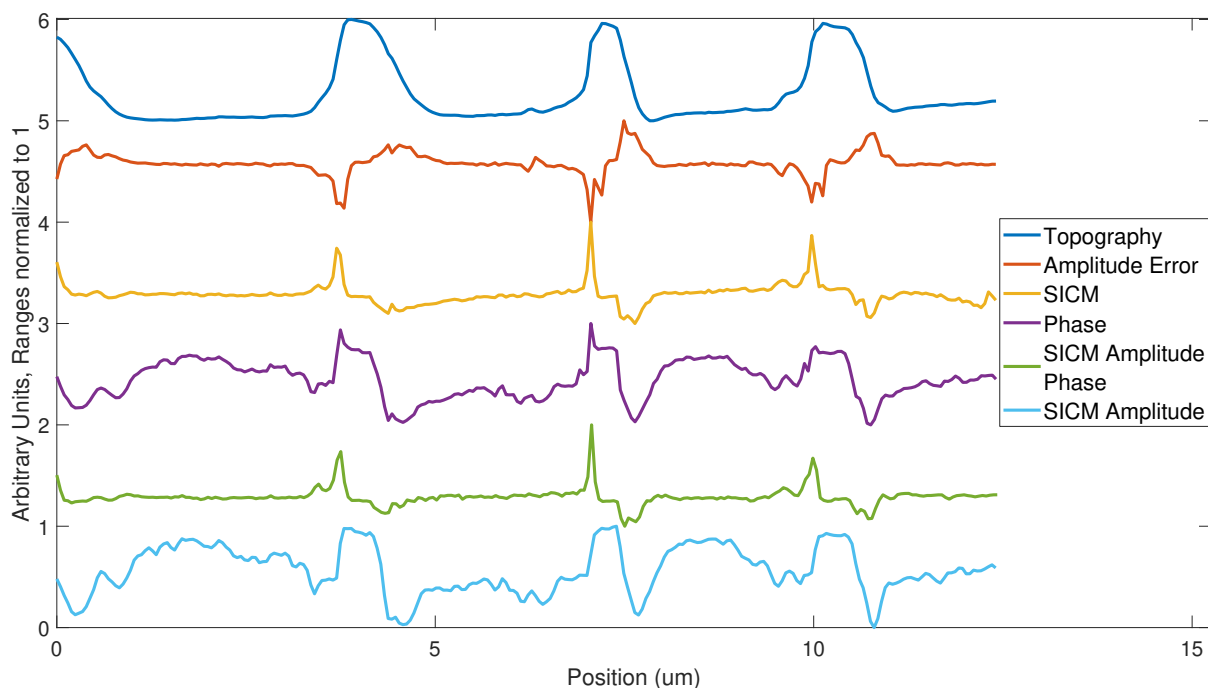


FIGURE 4.5: Line scans extracted from all the data channels from the top horizontal line of figure 4.3 demonstrating how the channels coordinate over the regular protrusions of the CD stamper surface. The normalization constants for each channel in the same order as the legend are: 181 nm, 0.359 nm, 24.6°, 68.3 pA, 12.4 pA, 0.686°.

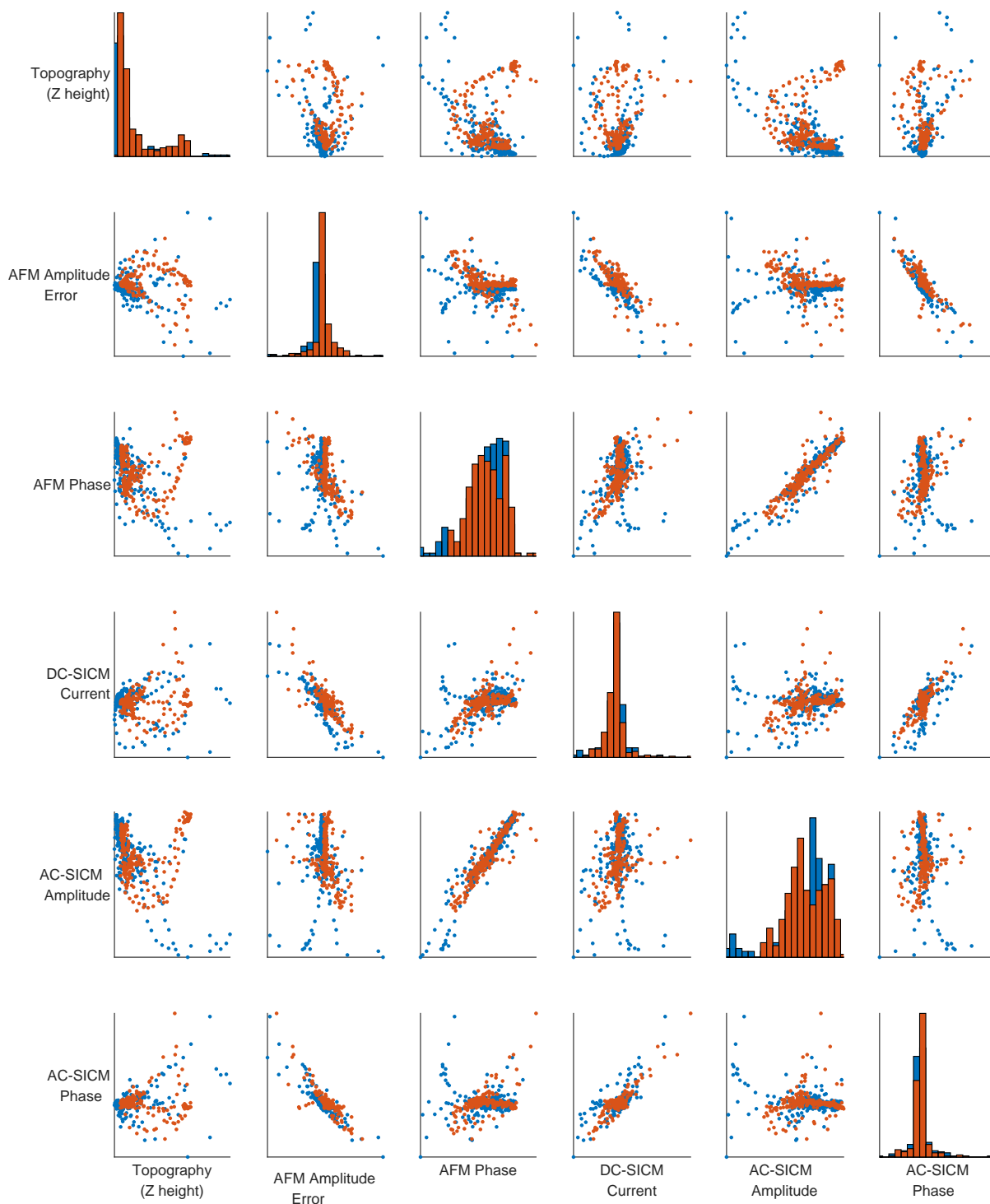


FIGURE 4.6: This pair plot displays the normalized data from figure 4.4 (blue) and figure 4.5 (orange). The histograms display the data from a single channel, with at x-axis being the value of the channel between 0 and 1, while the y-axis is bin counts, where the integrated counts is 256. The scatter plots show the relation between two channels, with x-axis channel label at the bottom of the graph, and the y-axis channel label on the left side of the graph. All axes of the scatter plots have a range of 0 to 1. The plots show the topography generated by tapping mode feedback, AFM Amplitude Error is the difference between the tapping mode amplitude and the setpoint amplitude, AFM Phase is the phase difference between the measured AFM tapping mode signal and signal which modulates the blue laser which oscillates the probe, the DC-SICM signal which is DC component of the ionic current, the AC-SICM Amplitude signal which is the AC component of the ionic current, and the SICM Phase which is the phase difference between AFM Amplitude and the AC-SICM Amplitude.

In figures 4.3, each image corresponds to a separate data channel recorded during the same scan of a CD stamper. Specifically, the plots show the topography generated by tapping mode feedback. AFM Amplitude Error is the difference between the tapping mode amplitude and the setpoint amplitude, while AFM Phase is the phase difference between the measured AFM tapping mode signal and signal which modulates the blue laser which oscillates the probe. The DC-SICM signal is the DC component of the ionic current, while the AC-SICM Amplitude signal is the AC component of the ionic current. Finally, the SICM Phase refers to the phase difference between AFM Amplitude and the AC-SICM Amplitude. Figures 4.4 and 4.5 show information from each of the 6 channels over the same line scans. Finally, in figure 4.6 the data from the two line scans is shown in a pair plot so the correlations between the data channels are easily identifiable.

The topography scan looks appropriate with some tip orientation artifacts, like the effect demonstrated in figure 3.16. The line scan of figure 4.5 shows this most clearly. While the bumps should be symmetric, the slopes on the left side are steeper than those on the right. This indicates that the probe was angled such that it was accurately measuring on the left side, but the right side was affected by the tip geometry. This indicates that the tip was slanted in the same direction as the tip in figure 3.16.

Some features on the surface can also be seen that are not identifiable as the bumps of the CD stamper. One of these areas is shown in figure 4.5. This irregularity leads to an amplitude error due to a feedback error, recorded in the AFM Amplitude error channel. This channel tracks the difference between the setpoint oscillation amplitude of the probe and the actual oscillation amplitude of the probe. The AFM feedback should minimize this error, and figure 4.3d shows that this was, in fact, the case. The amplitude error is small, with the largest deviation being 0.65 nm. Also, the largest errors occur at the steepest slopes of the topography channel. This is consistent with feedback mechanics, as this is where the amplitude signal is changing the fastest. Therefore, the feedback is functioning well, and these unknown features are real. These features are most likely a damaged bump or some unknown contaminant.

The AFM amplitude error image and the DC-SICM channel demonstrate that the channels are anti-correlated. This is clearly shown in the line scans, as well as the pair plot where a linear trend is seen when the channels are graphed together. This relation can be explained by looking back to the approach curves (see figure 4.2). Both the DC-SICM and the AFM amplitude change linearly as the probe is tapped on the surface. In this case, small positive errors in the amplitude error indicate that the probe was closer to the surface, and the DC-SICM current decreased accordingly, and vice versa. Therefore,

when close to the surface, these channels indicate the same information. It should be noted that this is dependant on how far away the probe is from the surface. As can be seen in the approach curve, if a larger setpoint amplitude is used, this correlation can change.

The phase image should relate information about the visco-elastic properties of the surface and can reveal material contrasts. The entirety of this surface should be made of one material, so contrast should not be apparent. Looking to the phase image, we do see some contrast. We see some small changes, which correlate with the amplitude error. Looking to the approach curve, both decrease linearly when approaching the sample surface, so this cross talk makes sense. Also, there is a large dark spot in the phase image, and the line corresponding to figure 4.5 crosses through this area. This phase difference is larger than the cross talk and shows up in the topography channel as previously noted. This indicates that the feature is real and is probably an unknown contaminant and thus a sample heterogeneity.

The AC-SICM amplitude is the AC component of the SICM current. The AC component exists because the probe oscillates near the surface, so the current is greatest when it is furthest away from the surface, and smallest when it is closest to the surface. The difference between the ionic current at these two positions is the amplitude of the AC-SICM current. Because the AFM amplitude is a measure of total distance the probe travels in the Z direction, amplitudes correlate with large AC-SICM current amplitude. Additionally, this current is affected by the access resistance at the pipette apex. The access resistance of the pipette is directly dependant on the mean distance of the probe hole to the closest surface. At a high aspect ratio feature, such as in the second line scan, the access resistance decreases while the force remains the same. This means that the SICM current will increase, and now the AC-SICM amplitude will be a derivative of a different part of the SICM surface approach curve. Specifically, the AC-SICM current amplitude decreases because we are now oscillating over a flat portion of the SICM curve. Due to these competing effects, it is difficult to interpret this AC-SICM amplitude. In this case, there is no correlation in the pair plot of the AC-SICM amplitude channel with the DC-SICM signal or the AFM amplitude error signal. This could be due to the shape of the AC-SICM amplitude approach curve at this AFM amplitude, which may essentially be flat under the scanning conditions. Looking to the pair plot, there is a correlation between the AC-SICM amplitude channel and the AFM phase channel. In fact, at the same position where some type of contamination was previously identified in the phase channel, the AC-SICM amplitude drops to zero. This is difficult to interpret

without further study, but it seems like this AC-SICM amplitude may indicate similar information as the AFM phase channel, which means that it could be used to identify material contrast.

Finally, we can examine the AC-SICM current amplitude phase. This is the phase difference between the AFM excitation signal and the AC component of the SICM current. In the pair plot, this channel is correlated with the DC-SICM channel and AFM amplitude channel. In accordance with the approach curves, one would expect all three of these channels to be linear, so this relation makes empirical sense. Also, the AFM phase and AC-SICM amplitude phase do not correlate, meaning that the AC-SICM amplitude phase measurement must be independent of the visco-elastic forces measured in the phase channel.

These combined AFM-SICM scans demonstrated both that the techniques function and that some interesting correlations exist within the channels of information. The force channel information demonstrates that high aspect ratio feature scan be followed in liquid, with a small amplitude error. This functionality means that surfaces can be scanned without the usual difficulties involved in SICM scans. Specifically, probes can approach the sample surface much closer without the danger of crashing. Therefore, a steeper part of the SICM curve can be used, resulting in a higher signal-to-noise ratio. While the error in the amplitude channel only varies by  $1.3 \pm 0.2$  nm between it's highest and lowest values, the SICM channel varies by  $136 \pm 1$  pA. The relative magnitudes show that the probes' ionic current sensitivity to Z distance changes is very high.

Due to this high signal to noise ratio this system is able to perform higher resolution and high-sensitivity SICM measurements. However, the increased sensitivity and lateral resolution come at the price of more edge effects due to the proximity of the probe to the surface. These edge effects also exist in traditional SICM, but are hard to observe due to the limited sensitivity and lower lateral resolution related to the increased tip-sample separation necessary for safely scanning the probes. These effects can be disentangled by looking at all the channels that have been examined.

Another effect of having such a high signal to noise ratio is our ability to see correlations within the data. The total range of many of these values is small enough that they could easily be drowned out by noise if the AFM was not correctly shielded from electrical and mechanical noise. Such a system provides access to information that would be impossible to measure without AFM feedback.



In terms of correlations, three independent groups can be seen in these measurements: topography, phase information, and amplitude error.

The AFM amplitude error channel and the AC-SICM current amplitude channels correlate well. This shows conclusively that AFM and SICM measurement both provide the topography information on a homogeneous sample, although AFM feedback allows for safer scanning on heterogenous samples (recall that the sign of the SICM current can change as a function of the conductivity of the sample). In the future, by switching to lower concentrations of electrolyte, this fact can be exploited. Surface charges can rectify the current, completely changing the SICM current approach curve dependent on the material being investigated. Therefore, the AFM amplitude channel can be relied upon completely for feedback and while the SICM channel records information on these surface charges. These types of measurements could previously only be performed in a purely SICM system using a constant height mode. Such a mode must remain much further from the surface, so AFM-SICM should be able to perform these measurements with superior signal to noise and lateral resolution.

Phase information comes from the AFM phase and the AC-SICM amplitude. This correlation could lead to some interesting techniques. Firstly, is the material property that is measured in these two channels always the same? Performing scans on more materials may elucidate whether this correlation is always presents. If deviations in other materials are seen, then two separate properties could be measured with each of these channels, but those properties happen to be correlated in the CD stamper. If it is found that the two channels do correlate, then this work could apply to improving SICM microscope scanning procedures. If the phase information provided by AFM measurements could also be recorded via a SICM system, without beam detection mechanics, this could be a powerful and simple method to gain materials contrast.

In summation, this combined AFM-SICM system can perform SICM measurements with force-based distance control, phase information, and a greatly increased sensitivity compared to typical systems. It will thus provide opportunities to validate our theoretical assumptions and push forward into regimes of electrochemical scanning techniques which could not have been inferred from a pure SICM system.

## 4.4 Electrochemical Droplet Measurements at a Point

The measurements of section 4.3 have shown that these AFM-SICM probes function properly as a combined AFM-SICM technique. However, in this electrode configuration, this technique only measures the topography via SICM. The motivation for this project was to perform measurements on electroactive materials and demonstrate electrochemical contrast that is unrelated to topography. To do this, an interesting option is pointwise cyclic voltammetry, with the goal of charging and discharging a small area of battery material directly at the tip of the probe. In this configuration, a potential is applied between the probe and sample. By ramping the voltage and recording the ionic current one can extract the charging characteristics at each point on a surface. The difficulty is that this measurement must be confined to that area under the probe apex. To do this, the resistance to ionic current flow to the rest of the sample must be great enough so that the area being measured is not drowned out.

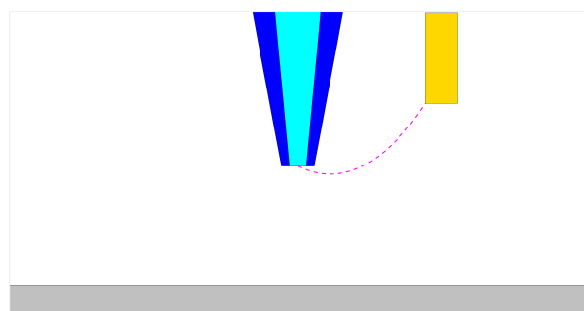
The first step in accomplishing this was introducing a redox mediator, ferrocene methanol ( $\text{FcCH}_2\text{OH}$ ) in the present case. A redox mediator functions as an intermediary between the two electrodes. In this situation the will undergo oxidation to become  $[\text{FcCH}_2\text{OH}]^+$ . The probe is filled with 1 M sodium perchlorate and 0.002 M ferrocene methanol in propylene carbonate electrolyte. The Ag/AgCl electrode functions as a quasi-reference electrode because there are no  $\text{Cl}^-$  in solution. A form of the Nernst equation can be used to determine the standard potential of the Ag/AgCl QRE [153]:

$$E_{\text{QRE}} = E_{\text{Ag/AgCl}}^\circ - \frac{RT}{2F} \ln(K_{\text{sp}}) \quad (4.1)$$

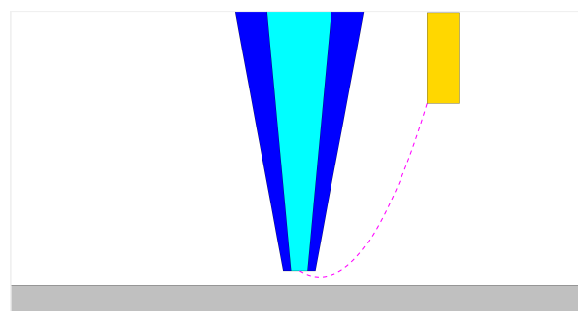
Where  $E_{\text{QRE}}$  is the potential of the quasi-reference electrode (V),  $E_{\text{Ag/AgCl}}^\circ$  is the standard potential of Ag/AgCl (0.2223 V vs. SHE [47]), R is the gas constant ( $8.3145 \text{ J} \cdot \text{mol}^{-1} \cdot \text{K}^{-1}$  [48]), T is temperature (298K), F is the Faraday constant ( $9.65 \cdot 10^4 \text{ C} \cdot \text{mol}^{-1}$  [49]), and  $K_{\text{sp}}$  is the solubility product of AgCl in propylene carbonate ( $\ln(K_{\text{sp}}) = 19.82 \pm .02$  [154]). Evaluating this equation,  $E_{\text{QRE}}$  is 32 mV vs. SHE. The standard potential of ferrocene methanol in propylene carbonate is  $E^\circ = 0.446 \text{ V}$  vs. NHE [155], and acts as an internal reference to the Ag/AgCl QRE.

The second step was to record these cyclic voltammograms within a droplet of electrolyte rather than a bath. In a bath of electrolyte, with a probe far from the sample surface, the ionic resistance is negligible so at every voltage the redox mediator will be able shuttle an

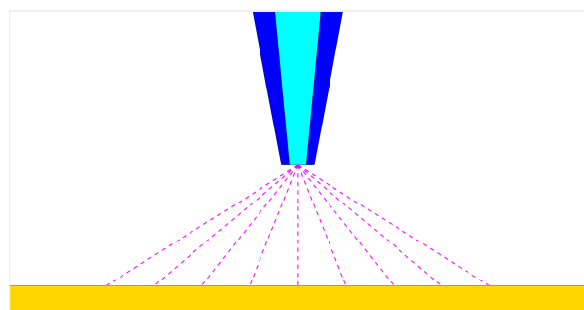
electron between the probe and surface. This will yield a linear CV curve, and this will not change as the probe is moved parallel to the surface. As the probe approaches the surface ionic resistance to the sample that is not directly below the hole of the probe will increase according to the formula give in section 1.3.1. This increase in resistance is what we see in the previous approach curves, although the electrode configuration is different as shown in figure 4.7. In the previous case resistance will only increase with increased proximity to the surface. In this case, the resistance will increase to all the surface that isn't directly under the probe opening, but the resistance between the probe opening and the area directly under the probe opening will decrease.



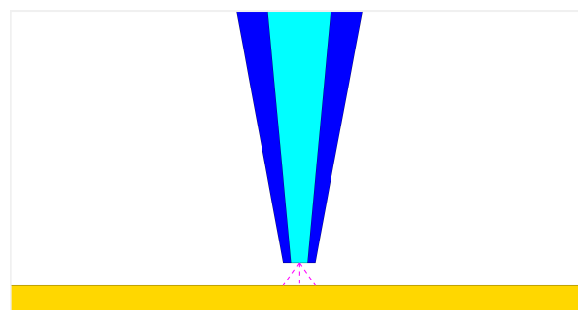
(A) Unapproached SICM measurement, one electrode is inside the probe and the other is somewhere in the bulk liquid.



(B) Approached SICM measurement, one electrode is inside the probe and the other is somewhere in the bulk liquid. The ionic resistance between the electrodes has increased due to the proximity of the probe opening to the sample surface.



(C) Unapproached SICM measurement, one electrode is inside the probe and the other is the sample below the tip.



(D) Approached SICM measurement, one electrode is inside the probe and the other is the sample below the tip. The resistance to the sample directly below the tip opening has decreased, while the resistance to the rest of the sample surface is increased as the ions must pass through the small gap between the tip and surface.

FIGURE 4.7

To perform spatially resolved CV curves, the magnitude of the current must be limited by the area of the sample directly under the tip. To increase this resistance, the tip apex must be very close to the sample. Although AFM force feedback allows the tip to get close

to the surface without crashing and breaking the probe, even this is not enough. From section 1.3.1, angular misalignment of the probe and sample will increase the parasitic conductivity to the rest of the sample dramatically. This means that the probe must be aligned perfectly in terms of angle, and there must not be any protrusion at the apex of the probe that would allow the probe to contact the surface at only the protrusion while the rest of the probe opening is not touching the sample. Due to this potential issue, a droplet approach was attempted. In the droplet approach, the probe is filled with liquid, and it is approached to a dry surface through either deflection force feedback or tapping mode force feedback. Once the probe is approached to the surface, a droplet at the end of the tip will contact the surface. By doing this, we limit the area we are electrochemically measuring to superficially the area within the droplet. An electrical potential is then applied between an electrode in the probe, and the surface.

To test this method, the droplet measurements were performed on template strip gold. This demonstrated how reproducible these droplet CV measurements are, and whether they are viable for performing a surface scan measurement.

To perform this measurement a 75 N/m probe filled with 1 M sodium perchlorate and 0.002 M ferrocene methanol in propylene carbonate electrolyte is in fluidic contact with a template stripped gold surface. Bias is applied between an AgCl electrode in the probe, and the gold surface. The voltage is ramped 10 times between 0 and 1 V, creating repeatable CV curves. The probe is feeding back on the sample surface via deflection.

To interpret what is going on one should first examine the effect of changing voltage. The voltage is a preprogrammed routine set by the user (figure 4.8). As the voltage is ramped, a current is recorded as the SICM mean current. In this graph, the x-axis is time, so that one can look for correlations between the other channels which are also recorded as a function of time. To examine the position of the reduction and oxidation peaks, and to evaluate reproducibility, this current information is plotted as a function of voltage to create a current voltammetry curve (see figure 4.9). The integrated charge graph can then be used to compare one voltammetry cycle to the next (see figure 4.10). CVs can be examined quantitatively by fitting the background of the curve, fitting the reduction-oxidation peaks, and integrating these peaks. The area of the anodic and cathodic peaks are integrated separately so these values may be compared; in a reversible reaction these areas will be the same, but will deviate in an irreversible reaction. Typically, the background is not included as it often dictated by capacitance of the measurement system, which is not relevant to the chemistry being studied. However, it is important to understand how capacitance changes over time, which could be indicative of changes in droplet size.

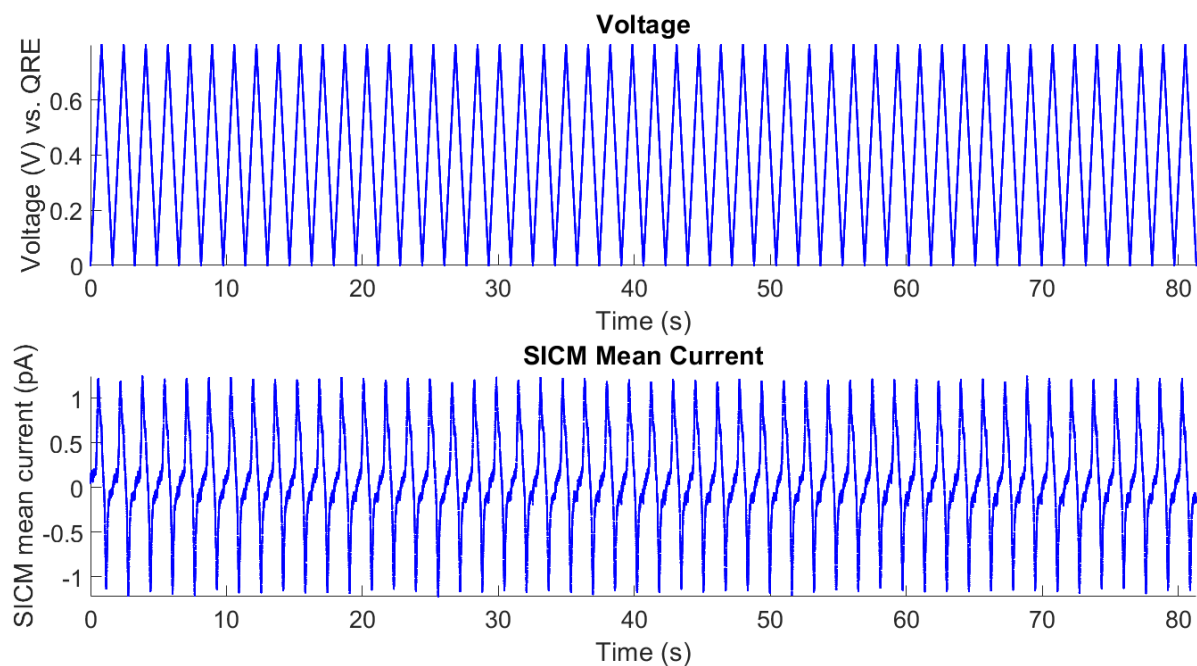


FIGURE 4.8: The time trace of the current and voltage signals of a droplet measurement on gold.

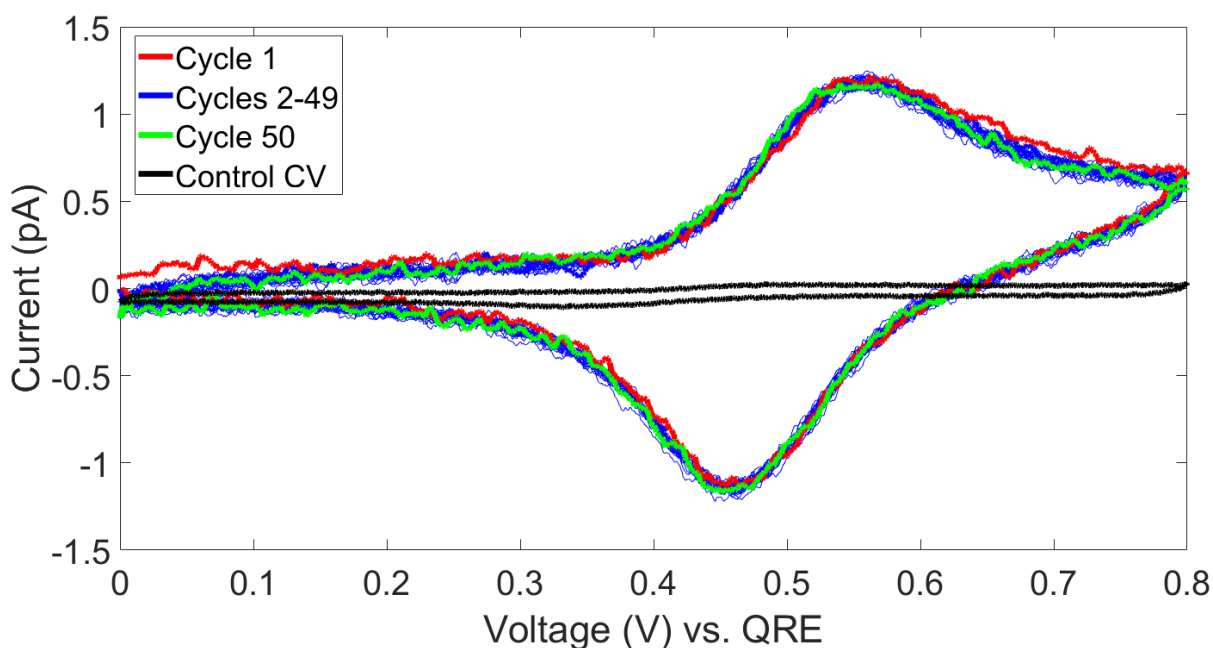


FIGURE 4.9: A cyclic voltammogram of the droplet measurement on gold shown in figure 4.8. Cycles 1-50 are performed in 1 M sodium perchlorate and 0.002 M ferrocene methanol in propylene carbonate electrolyte vs. a Ag/AgCl quasi-reference electrode while the control CV was performed without ferrocene methanol.

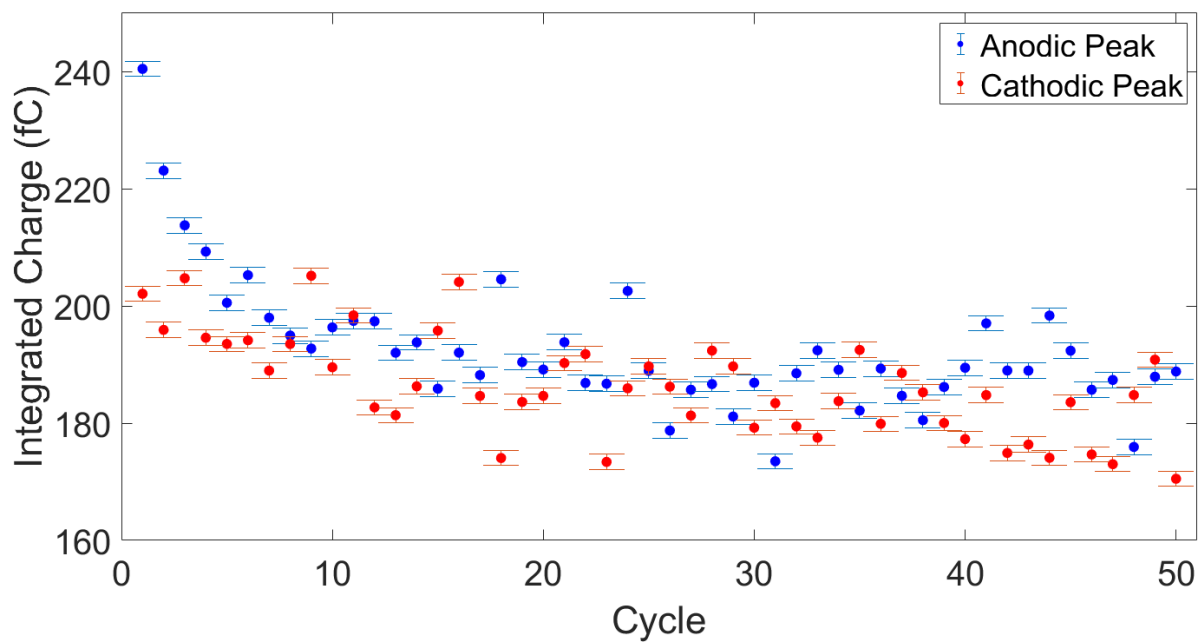


FIGURE 4.10: The integrated charge of the droplet measurement on gold shown in figure 4.8. Error is calculated by propagating the time increment error of the GXSM acquisition software, and the measured current noise.

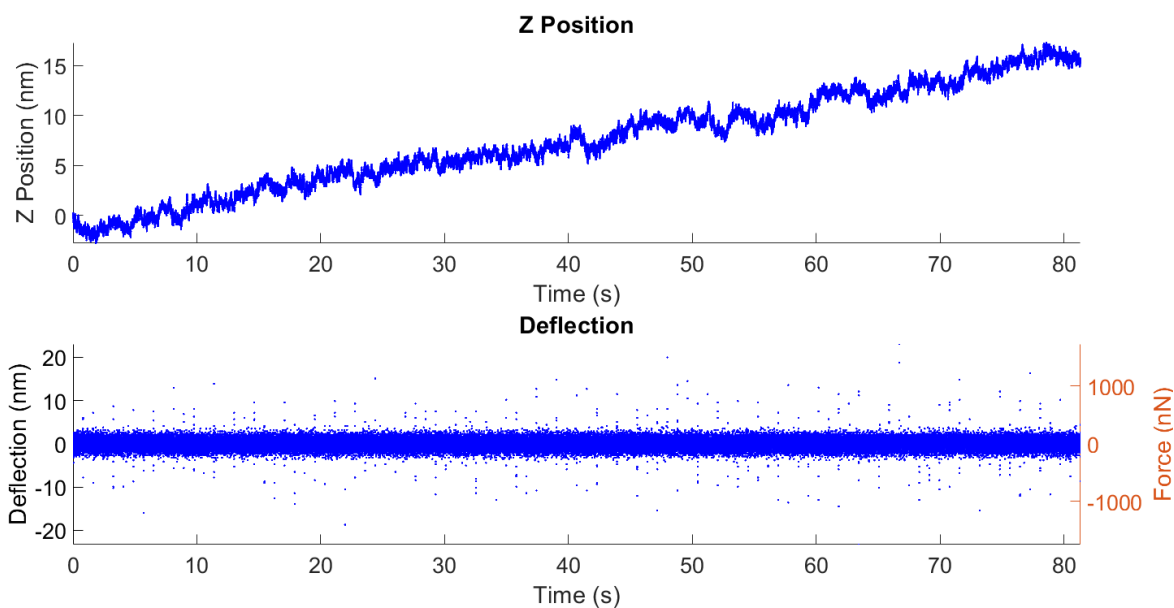


FIGURE 4.11: The AFM feedback data of the droplet measurement on gold shown in figure 4.8

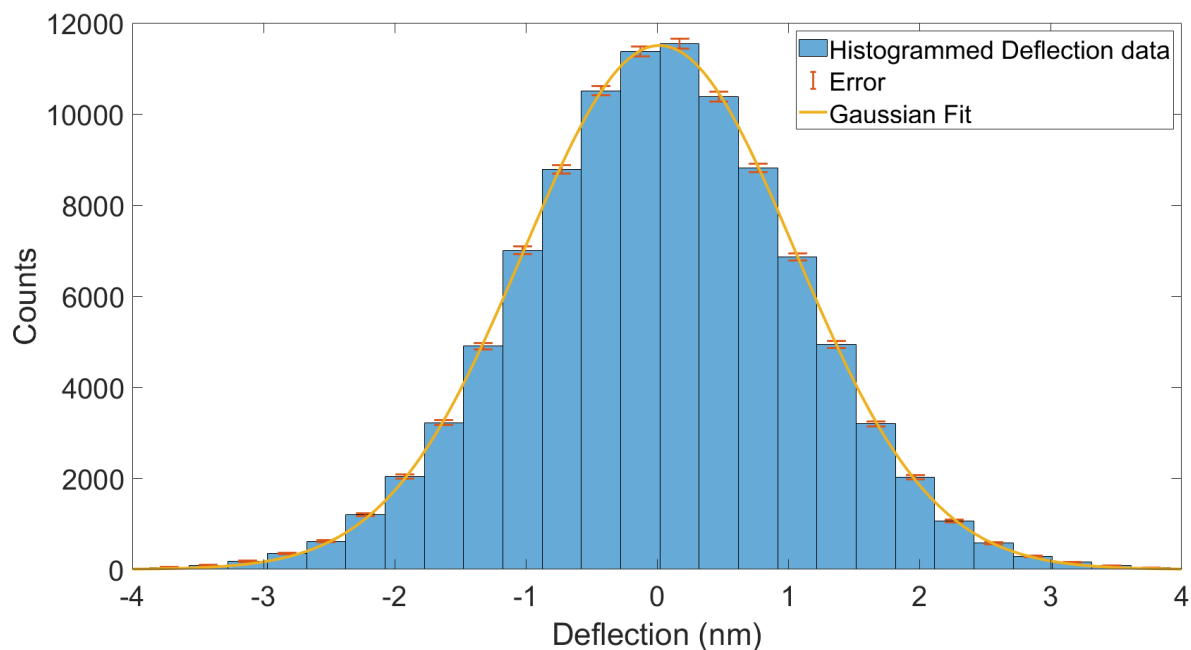


FIGURE 4.12: Deflection data from figure 4.8 is histogrammed. The data is fit to a Gaussian distribution of  $C = a \cdot e^{-\left(\frac{D-b}{c}\right)^2}$  where  $C$  is counts,  $D$  is deflection,  $a = (1.151 \pm 0.003) \cdot 10^4$ ,  $b = 0.019 \pm 0.002$ , and  $c = 1.467 \pm 0.003$ .

This data shows that this system can perform CV measurements and see the characteristic redox peaks with extremely low currents. Here, the measurement is on the order of 1 pA peak amplitude. Even though the probe moves in Z direction during the measurement, the CV curves are identical. This is confirmed by the integrated charge graph, which shows the anodic peak and cathodic peaks charges closely following each other. For some of the cycles the anodic peak is larger than the cathodic peak, which can be attributed to statistical and systematic error. The half wave potential is  $0505 \pm 0.002V$  vs. Ag/AgCl QRE, while this value would be expected to be 412V adjusted to be vs. Ag/AgCl QRE [155]. The Ag/AgCl QRE potential will drift over time as AgCl dissolves in the propylene carbonate, which could partially explain this discrepancy. Additionally, values within literature can vary, such as the use potential of ferrocene in acetonitrile [156].

Additionally, the graph provides information on the force feedback (see figure 4.11). The Z Position graph demonstrates the movement of the probe relative to its initial position. If the force feedback is on, then the sample z position will change to maintain the deflection at a set value and thus maintain a constant tip-sample separation. The feedback must compensate for a drift of 15 nm over 80 seconds. The linearity of the drift suggests that this is most likely due to the thermalization of the microscope, and it indeed a very low amount of drift for a microscope operating in liquid in ambient conditions. This can

be confirmed by examining the deflection, and a histogram of the deflection values. As seen in figure 4.12, the deflection, and thereby the force, is kept constant with a gaussian distributed noise, attributable to thermal fluctuations.

This shows that it is possible to perform sub picocoulomb CV curves while measuring topography with extremely low drift in ambient conditions.

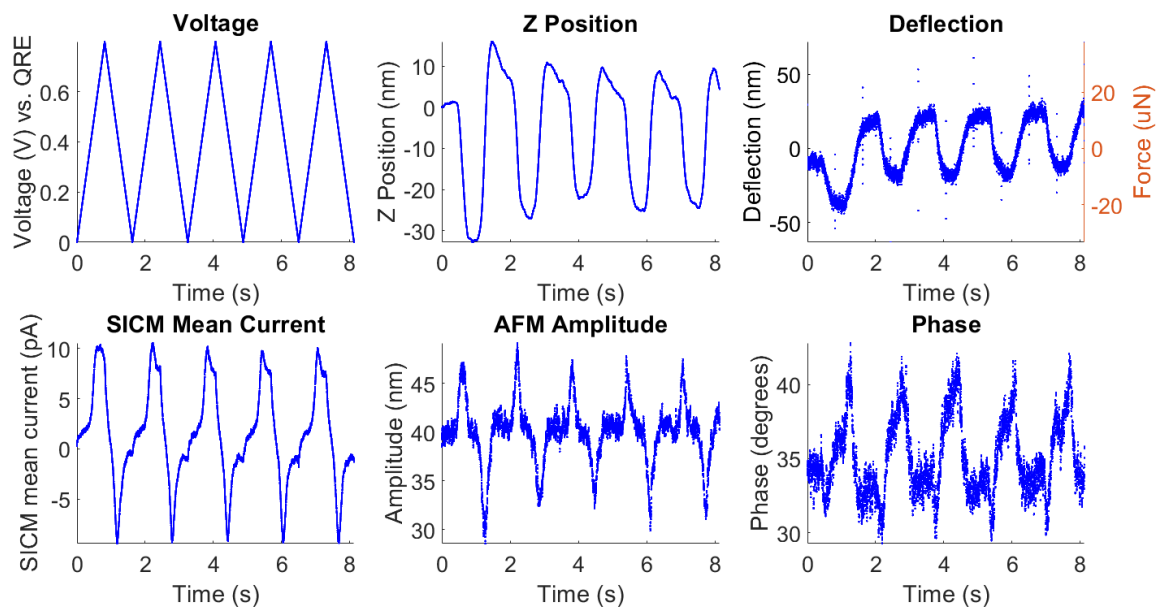


FIGURE 4.13: The experiment begins with probe approached to the surface in tapping mode. The voltage is ramped from 0 to 0.8V while the probe feeds back on the surface via its amplitude signal.

The measurement in figure 4.13 shows a tapping mode version of the previous measurement. Here, the probe is approached to the surface before the measurement begins, then the tapping mode will adjust the position of the tip relative to the surface to maintain a consistent amplitude, and therefore a constant force.

The CV curves in figure 4.14 and integrated charge plot in figure 4.15 show that the first curve is significantly different from the final cycles; however, the last three CV curves vary by less than 2% of total charge. In cyclic voltammetry, it is common practice to eliminate the initial CV curve of an experiment. In the present experiment, the same was done by performing 5 CV curves at each point and eliminating the first two.

The force channels show large variations through the CV measurement. The deflection moves approximately 50 nm per cycle, and the AFM amplitude varies by 15 nm despite the Z feedback changing the sample position by 40 nm per cycle. The potential applied between the surface and the electrode in the probe will create a force between the probe



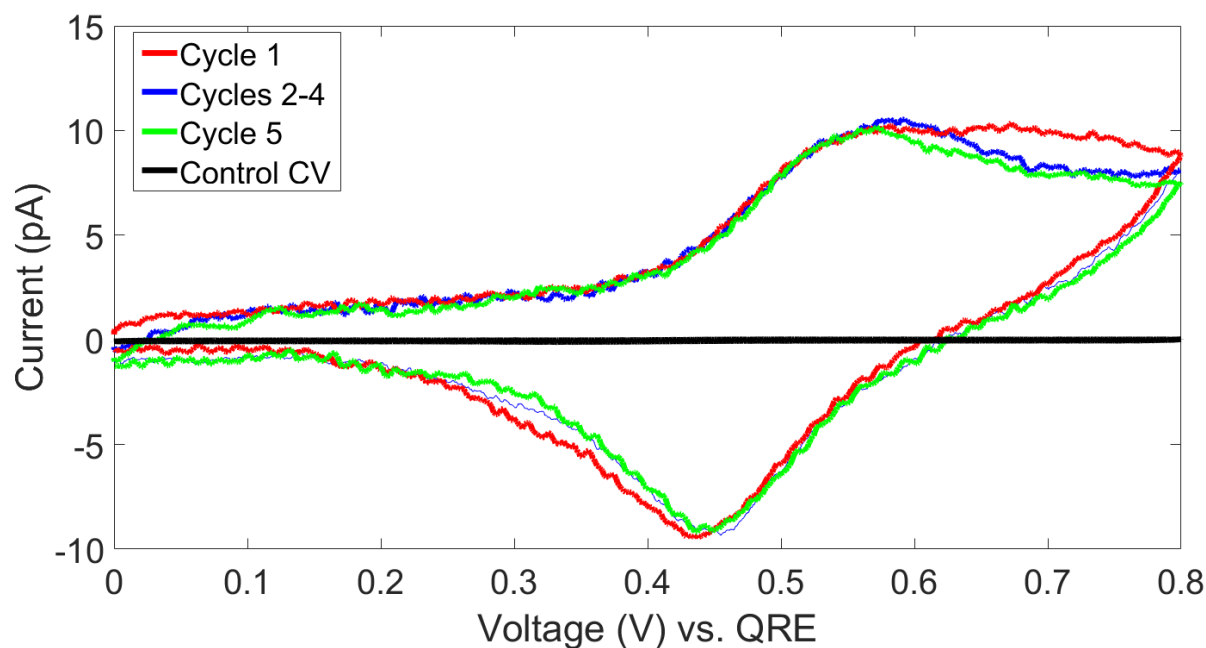


FIGURE 4.14: A cyclic voltammogram depicting information from figure 4.13. Cycles 1-50 are performed in 1 M sodium perchlorate and 0.002 M ferrocene methanol in propylene carbonate electrolyte vs. a Ag/AgCl quasi-reference electrode while the control CV was performed without ferrocene methanol.

and surface proportional to the magnitude of the voltage difference. This deflects the probe, and the ability to see this force via AFM demonstrates the high sensitivity of the technique. However, this variation only occurs while the bias is non-zero. To obtain an accurate measurement of the topography, the sample position can simply be recorded at the beginning and end of the measurement when it is accurate and the variations occurring during the measurement can be ignored. Furthermore, these variations in tip position do not seem to affect the current measurement, so there is no need to compensate for cross talk between the channels. This statement also applies to the phase measurement.

Another influence on the deflection of the probe during the ramping of the voltage could be that liquid is being pulled from the tip, onto the surface. We can study the dynamics of this liquid connection between the tip and surface through other measurement routines. One way is to approach the sample in steps, with interspersed voltage sweeps as in the measurement in figures 4.16 and 4.17.

This experiment demonstrates that the electrochemical connection to this surface occurs at 46 seconds into the run and is maintained as the probe moves towards the surface. Before this time, changes can be seen in the current as the voltage is ramped, but this can be attributed to capacitance in the system.

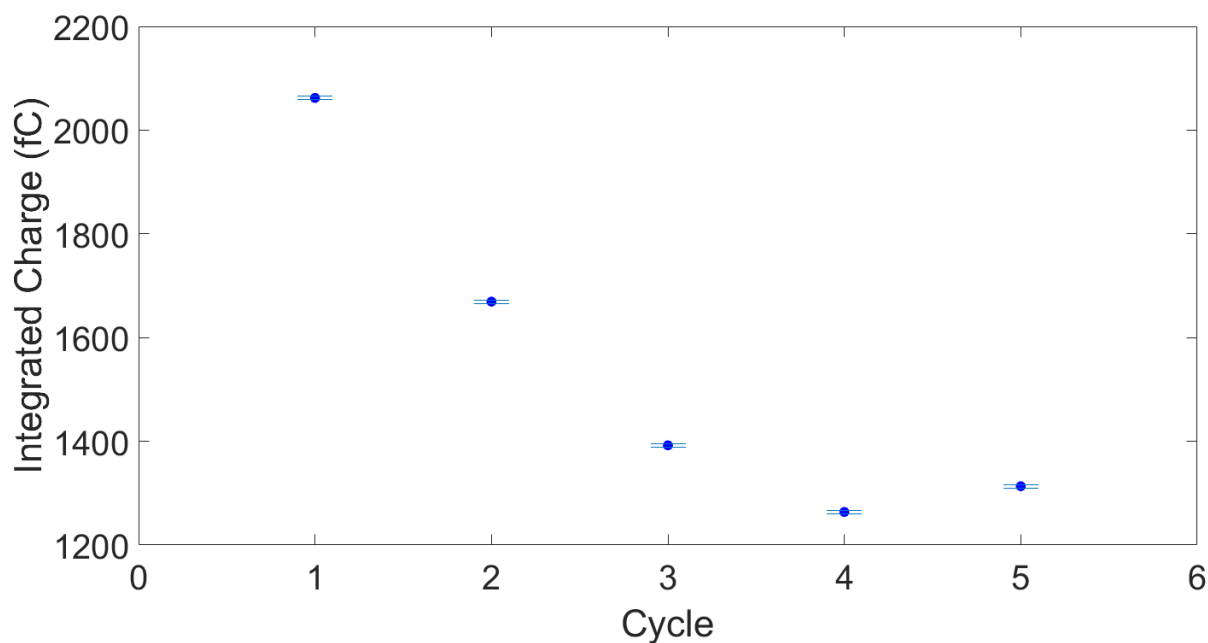


FIGURE 4.15: The integrated charge the anodic peak of each voltammetry cycle from figure 4.13. Error is calculated by propagating the time increment error of the GXSM acquisition software, and the measured current noise.

There is some attractive force between the probe and the surface just as the liquid initially touches down on the surface. This is important for accurate measurements of the surface. If the probe is approached to the surface, then slightly retracted, a regime may be entered where the probe senses the force of the droplet but does sense the force of the surface.

This measurement shows how important it is for the probe to be approached sufficiently. It also shows that the force between the liquid and the probe can be measured. This demonstrates the great degree of sensitivity our measurement has and offers an ability to study this liquid-solid interface.

Specifically, electrophoretic forces were examined to determine how they may have drawn liquid out onto the sample surface, and in turn, pulled the tip toward the surface during the ramping of the voltage. During the CV measurements this may have affected the probe dynamics by applying a time varying force to the probe, and it may have also changed the footprint of the droplet over time. Such effect needed to be characterized to improve the accuracy of the current scanning system.

The force sensing and electrochemical measurement tools inherent to the probe were leveraged in order to see the desired effects. Examining the force channel shows how the changing liquid environment at the tip apex is felt by the probe. Additionally, the

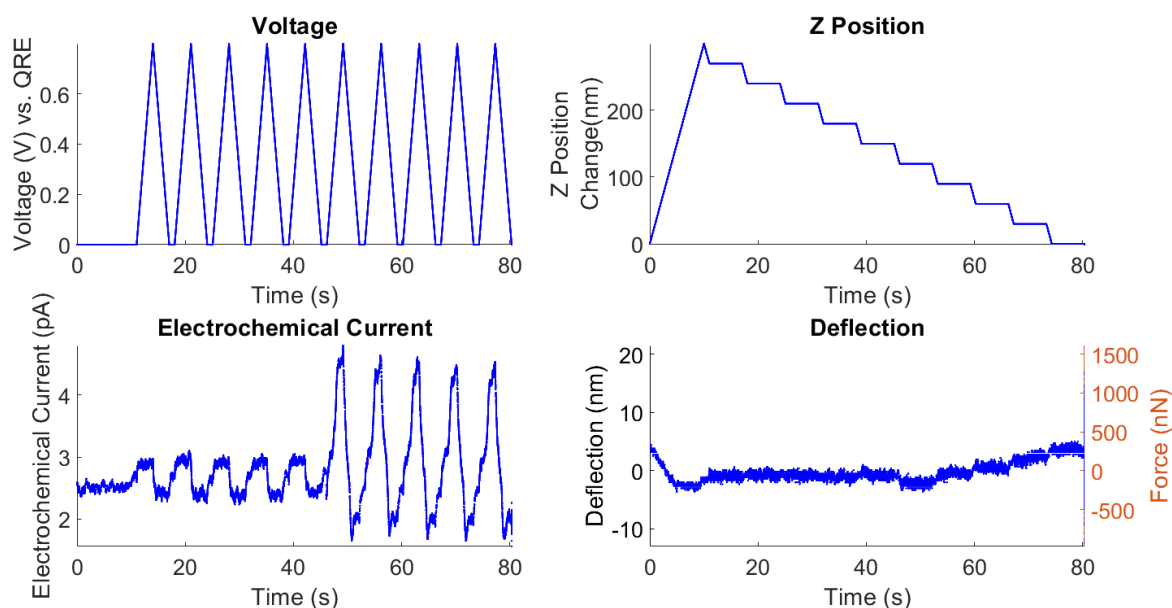


FIGURE 4.16: The probe begins in contact with the surface. The probe is quickly retracted from the surface by 300 nm, then approached to the surface in 30 nm increments. Between each step towards the surface the voltage is swept from 0 to 0.8 V vs. Ag/AgCl QRE.

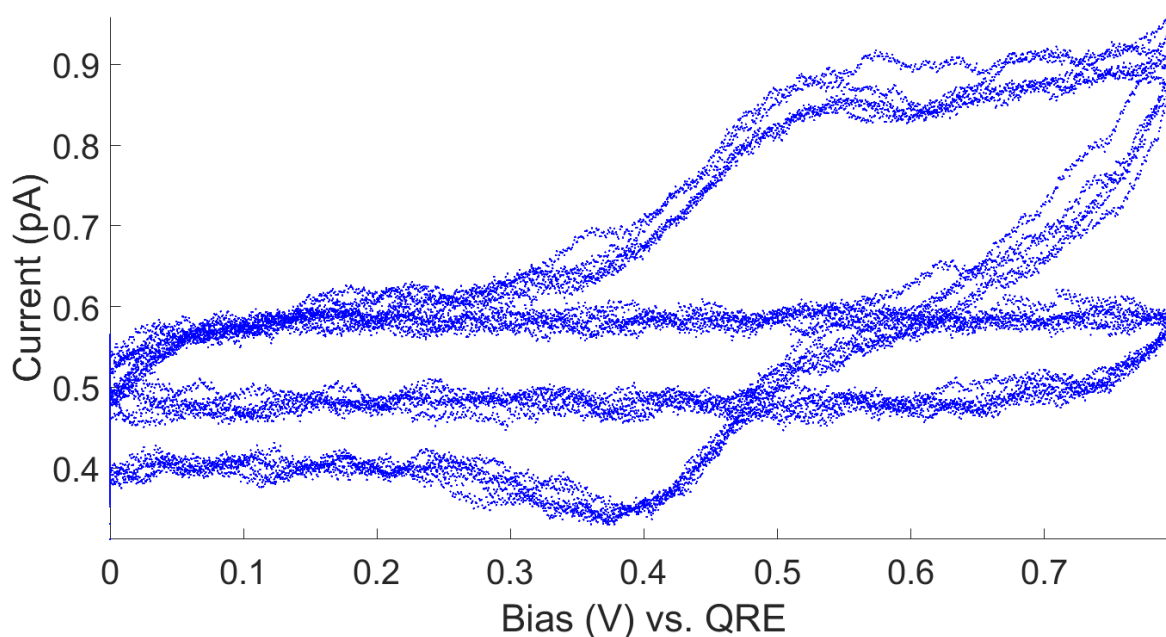


FIGURE 4.17: A cyclic voltammogram depicting information from figure 4.16.

current measured by the probe directly indicates the size of the liquid droplet on the same surface.

A template stripped gold surface was used to perform the following experiment. The probe was brought into force contact with the surface, then a sequence of voltage sweeps

was performed to change and to query the properties of the droplet.

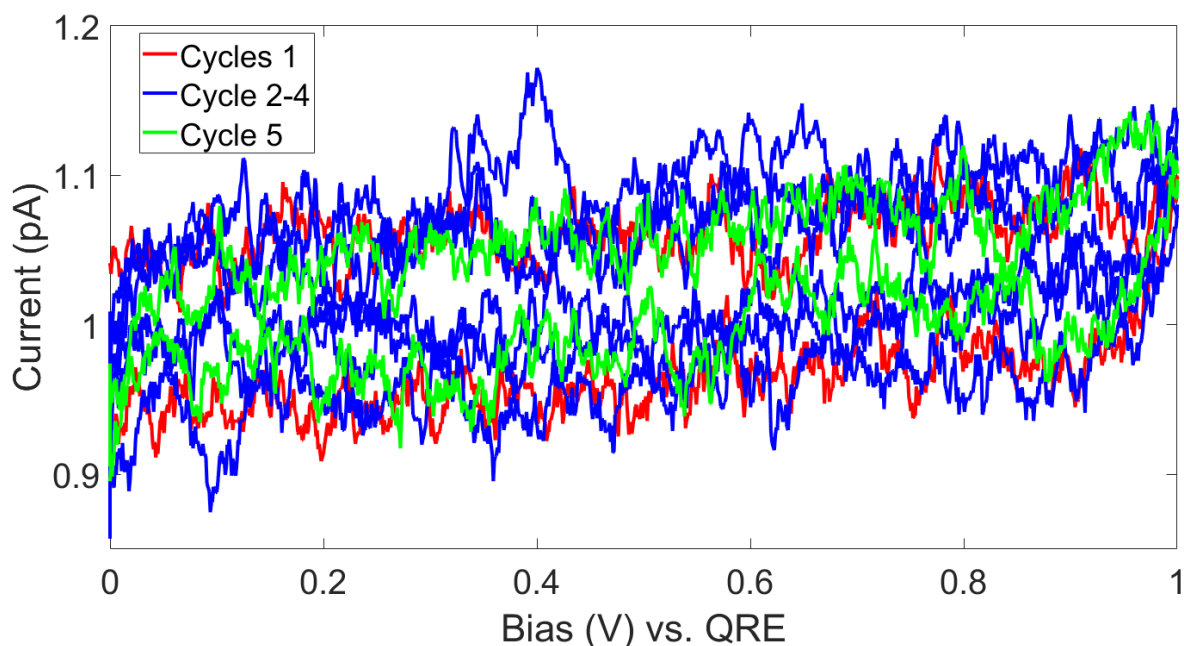


FIGURE 4.18: While the probe is in contact and feeding back on the gold surface, the voltage is ramped between 0 and 1V vs. Ag/AgCl QRE.

Here, the initial approach in figure 4.18 was done via deflection. When the voltage was ramped over 0 to 1V there was no reduction or oxidation peak. There is a non-zero slope to the data which can be attributed to a capacitance. Although the tip may have been in contact with the surface, this doesn't guarantee that the liquid from the tip touched the surface. To establish fluidic contact with the surface, the surface could be approached further in hopes that the bending of the probe establishes fluidic contact; however, increased force can result in damage to the probe or surface. Rather than risk damage to the probe, the voltage range of the ramping was increased, which increased the force on the electrolyte, which should be proportional to the voltage applied.

While the CVs were performed the feedback kept the deflection constant. The characteristic CV curves are not seen in this measurement, which means that there was no pathway from the liquid inside the probe to the surface. This does not preclude liquid from having been on the surface. If there was liquid on the surface, the changing potential may have drawn the liquid towards the probe. Additionally, if liquid coated the outside of the probe, it may have been brought down to the sample, changing the force applied at the tip.

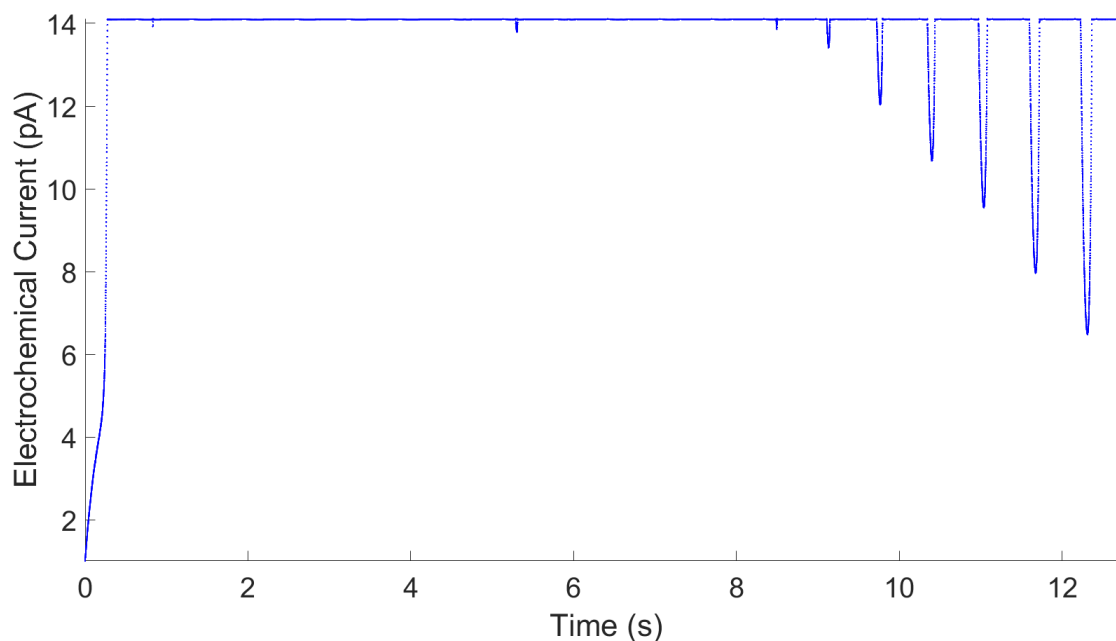


FIGURE 4.19: While the probe was in contact and feeding back on the gold surface, the voltage was ramped between 0 and 3 V vs. Ag/AgCl QRE.

As the current was ramped to 3V in figure 4.19, liquid was driven out of the probe which is shown by the large current increase in the first second of the measurement. In the 0 to 3 V cycles, the current amplifier is saturated at 14 pA and is difficult to interpret. Through this measurement, the deflection was once again held constant as the feedback adjusted the position of the probe. When the current initially turned on, the feedback must have moved the probe by 10 nm away from the sample. As the voltage continued to be ramped, the probe's position varied up and down by another 10 nm.

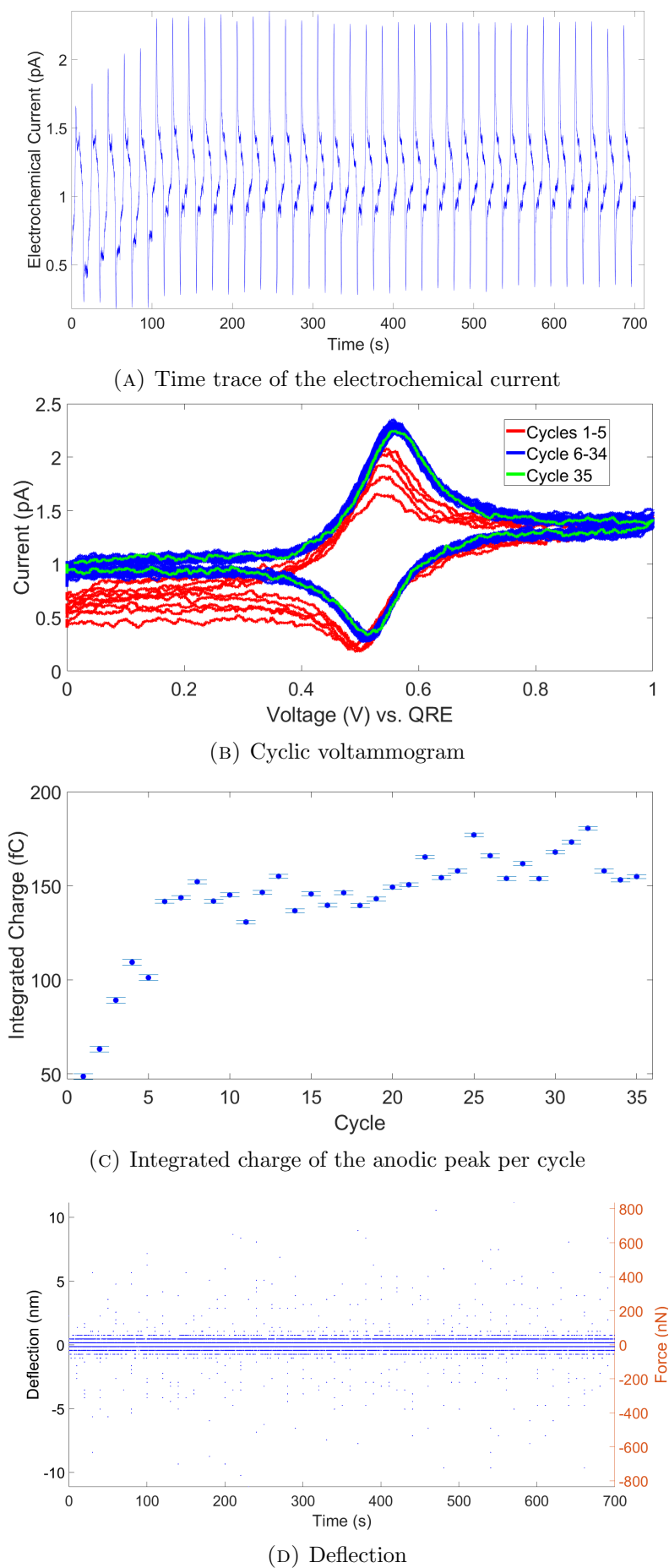


FIGURE 4.20: While the probe is in contact and feeding back on the gold surface, the voltage is ramped between 0 and 1 V vs. Ag/AgCl QRE.

The analysis of figure 4.20 can be divided between the first 5 cycles, and next 30. In the first 5 cycles the voltage ramp changed from 0 to 1V, no liquid was pulled onto the surface, and the existing liquid dispersed. The current amplifier was no longer saturated, and reduction-oxidation peaks can be seen. The SICM current graph shows that the offset of each curve changed, but the integrated charge graph shows that there was not a consistent trend to the variations in total current.

The next 30 cycles of CV curves look very similar, as confirmed by their integrated charge. At this point, the droplet stabilized, and the integrated charge slowly. These measurements demonstrate that performing CVs with this probe can result in electrophoretic effects that may influence the measured electrochemical current. By using force feedback, we can feedback on the surface simultaneously. Doing so means that we can correct for drift, so the chance of tip breakage is minimized. This is a result that could not be established reliably with a technique that only employed electrochemical feedback. With a single electrochemical channel, the probe cannot feedback on the topography while simultaneously performing CV curves. This means that this platform is a much more robust option for performing long, single point CV measurements.

These measurements show that 50 reproducible CV curves can be performed on a gold substrate with sub picoamp current resolution and nanometer scale topography resolution at one point in the XY plane <sup>1</sup>. Additionally, tapping mode feedback can be used as a non-destructive way to measure the topography. The goal is to do this on a grid to create an image of the surface for each of the data channels. To do this, consistent CV curves need to be performed over the surface; however, moving the tip can introduce more challenges. Both the lateral movement of the tip and the Z movement during feedback can act as perturbations to the droplet which can be sources of noise or systematic error in performing CV measurements. Also, topography images of the surface may be influenced by the movement of the droplet. In contact mode AFM, the movements of the droplet affect the topography measurements less as the force applied by the tip is larger compared to tapping mode AFM and noise from the movement of the droplet is smaller in comparison. However, because the contact measurement applies more force, it has the potential to be more destructive to the surface and tip. Damage to the tip can increase the hole size of the probe, which results in changes in electrochemical resolution and degradation of topography resolution. Contact measurements can still be performed without damaging the tip, but the amount of deflection at the tip must be limited to limit

---

<sup>1</sup>It should be noted that the measured current at 0 V varies between 0.5 and 1 pA, where it should settle at 0 pA. This is most likely due to some extraneous source of current, potentially poor grounding and coupling of some stray current from the biasing of the piezo positioner.



the force applied. If small deflections are used, the system becomes susceptible to small thermal drifts, and the probe may come out of contact easily. Alternatively, the scans can be performed in tapping mode, but the distance between sample and probe must be controlled accurately to keep the droplet stable. Large free oscillation amplitudes are required to feedback on the surface while doing stable electrochemical measurements. If the droplet is lost during these measurements, the tip may tap directly on the surface. Without the droplet to “cushion” the probe, this could result in a large amount of force on the tip, leading to tip damage.

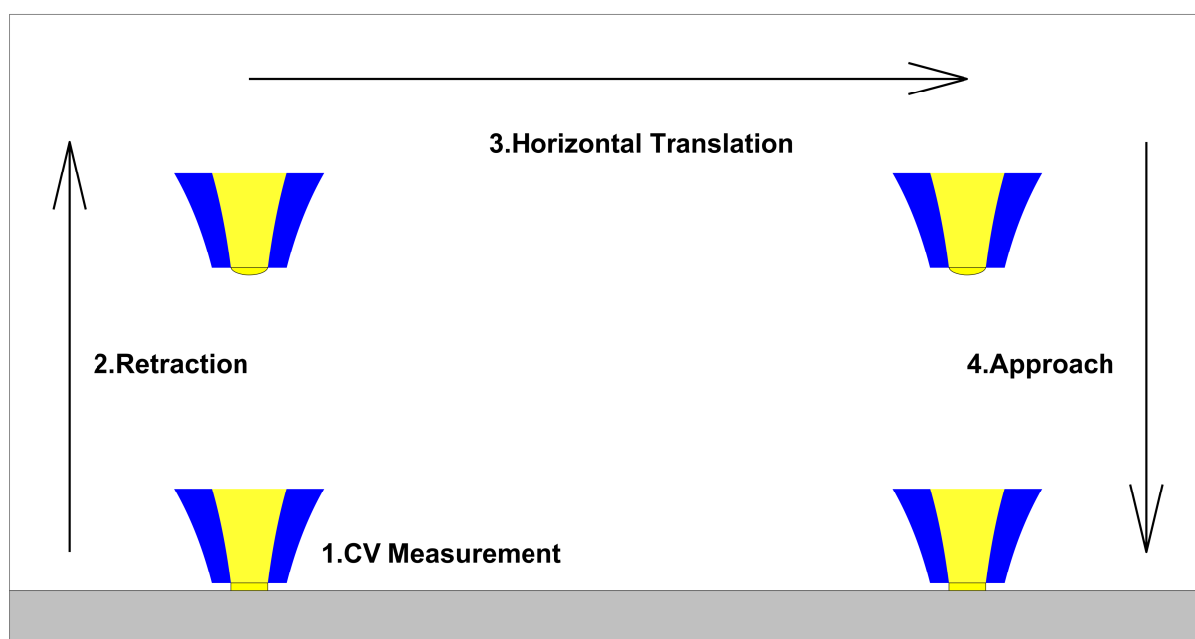


FIGURE 4.21: The measurement proceeds in four steps. (1) A CV measurement is performed while the probe feeds back on the force channel. (2) The probe is retracted to a safe position. (3) The probe is translated horizontally to the next position on the surface. (4) The probe approaches the sample via feedback on the force channel.

We can also perform these measurements in a hopping mode routine [157], which is one of the most commonly used scanning routines in SICM/SECCM along with constant height mode [158], direct current mode [159], and alternating current mode [160]. In hopping mode, the tip performs a measurement at a point, the probe retracts to a safe distance, the probe moves laterally to the next position in the grid of measurements, the probe is approached again, and another CV measurement is performed [157]. In this type of measurement, the tip is protected because it is not laterally dragged across the surface, so there is less force applied to the tip during movements of the tip. This method is time intensive, however, as a substantial amount of time is required to re-approach to



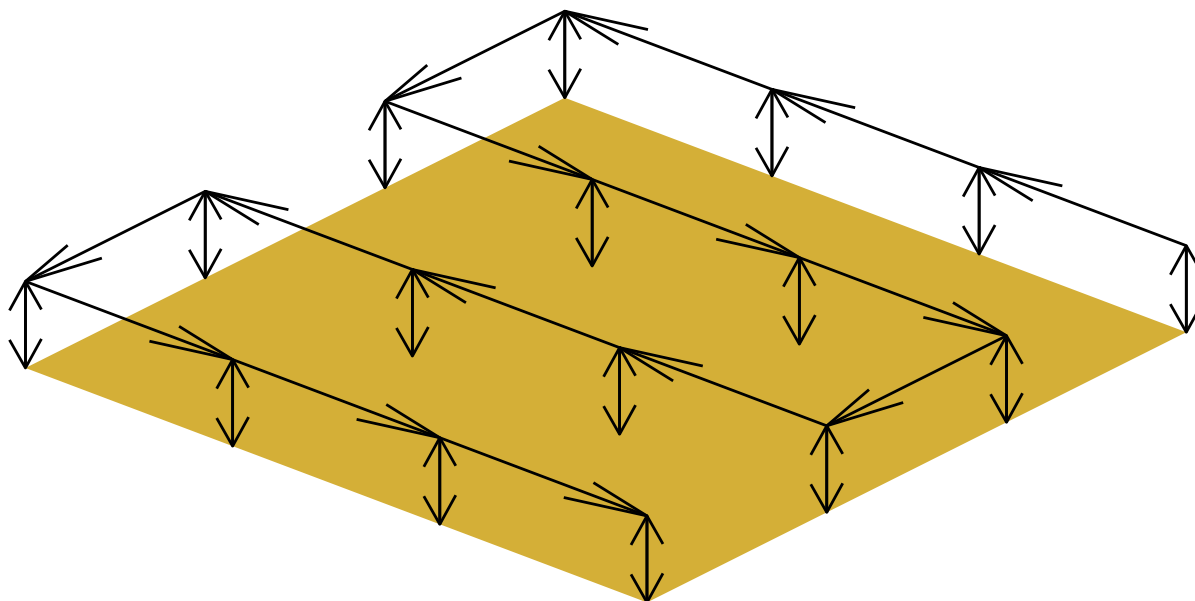


FIGURE 4.22: During the scan the probe follows the sequence outline in figure 4.21. The distance traveled in step 3 depends on the point in the scan and will create a grid of points as shown here.

the sample and perform CV curves. As seen in figure 4.21 and 4.22, each measurement consists of four actions:

1. CV measurement: The electrochemical measurement at the surface can be adjusted dependent on the information required. As the CV measurements have some degree of variation which should be averaged out and eliminated, it's imperative that several CV cycles are performed on each point. The time taken to perform the CV curves depends on how many CVs are performed, what the voltage range is, and how fast the voltage is ramped. Using 10 CVs, a voltage range of 1 V, and a voltage ramp rate of 10 V/s results in a 1-second measurement.
2. Retracting from the surface: This step is performed so that the probe will not crash into the surface when it is moved laterally. 200 nm is a safe distance for all the samples examined. This can be performed as quickly as the microscope's software will permit as the tip moves away from the sample, meaning that it will not crash into anything. The time per retraction will be 10ms.
3. Lateral movement to a new sample position: Since the probe has been retracted from the surface, the chance of crashing into the surface during a lateral movement is negligible. This step will also take 10ms.

4. Surface approach: The approach of the surface depends on the properties of the tip. The maximum available bandwidth of the tapping mode force measurement is:

$$BW = \frac{\omega}{2Q} \quad (4.2)$$

Where  $BW$  is bandwidth,  $\omega$  is frequency, and  $Q$  is the Q factor. If the properties from the frequency sweep in figure 3.6 are used, the resonance frequency is 16279.21 Hz and the Q value yields a time constant of 40ms. For a rough estimate of the maximum approach speed, the feedback will ring if the probe moves from above the setpoint amplitude to zero amplitude within the time constant. If the setpoint is 10 nm, this means the fastest approach speed is 250 nm/s. If the probe needs to approach 200 nm during each approach routine, this will take 0.8 s.

Together, this amounts to 1.82 s per pixel. A typical AFM image consists of a 256 by 256 grid of pixels, which is 65536 pixels and would take 33 hours. In many situations this is prohibitively long, as samples and electrolyte need to be stable and the microscope must have minimal drift on this time scale. This means that the number of pixels measured must be restricted to reduce time, or a tapping mode method must be used to eliminate time-consuming steps.

In summation, these CV measurements suggest that a two-dimensional scan is possible; however, these scans need to be performed to fully understand how the electrochemical measurements are affected by lateral movement, and to correct for them.

In the stepped approach (figures 4.16 - 4.17) and extended voltage range experiments (figures 4.19 - 4.20), there is a clear picture of how electrophoretic effects show up in these droplet measurements. By monitoring both the electrochemical and force channel real phenomena can be seen, described, and directly influenced at a nanoscale. These could have further applications in measuring the forces of charged surfaces in conjunction with polar and non-polar electrolytes. By varying the composition of the electrolyte and the surfaces, the forces can also be varied. This type of measurement could accurately measure these differences in forces.

In the first set of experiments we see how the droplet is spread, and then becomes stable. This shows our capability to eject and perhaps specifically place small volumes of liquid on the surface. If this type of control is combined with further study of hydrophilicity

this could prove to be a powerful tool, quickly “printing” liquid onto surfaces. If so, this could be turned into a unique tool for nano-patterning of surfaces.

These effects are important for the ability to perform surface scans of ionic transport. If the potential is swept over large ranges, these measurements are simply unfeasible. Large swings in voltages mean large changes in electrophoretic forces. To perform measurements where these forces are minimized, the voltage ramping should be minimized, and the electrolyte and surfaces should be engineered to minimize these electrophoretic forces. Additionally, utmost effort needs to be put into protecting the tips from damage. This means using the smallest amount of force possible when feeding back. As the force increases on these probes, the chance of damage increases, and damage to the tips could lead to higher susceptibility to liquid being squirted onto the surface. Additionally, efforts can be made to further delineate electrophoretic effects from physical measurements of the surface. By separating the time at which the topography measurements and the CV measurements occur, the influence of the droplet on the physical measurements can be eliminated. Finally, while this technique seems to be viable, simply switching to a fully immersed technique would side-step these problems. If the probe were completely immersed, then these electrophoretic forces would vary less. This of course would mean that the type of ionic measurements would have to change. Instead, the electrolyte concentration could be drastically reduced, and the surface charging of the probe in the electrolyte would provide an excellent opportunity for measuring surface charge effects in liquid.

In summary, these probes offer us the opportunity to provide a wide range of physio-electrochemical measurements and techniques, and an opportunity to understand the phenomena that allow it to work at a scale of 10-100 nm.

## 4.5 Electrochemical Droplet Measurements of a Surface

Following from the previous section, two-dimensional surface scans were performed while both force and electrochemical information was recorded. This allowed for comparisons to be made between neighbouring points and allowed the probe to scan lines to determine whether real surface features can be distinguished. We were also able to examine how the scanning procedure affects the extracted information.

This measurement was performed on a template stripped gold surface in contact mode. The aim of this experiment was to produce identical CV curves over the surface. For a template-stripped gold surface the topography should be atomically flat. The only topographic features observed should be due to surface contamination.

Contamination here could mean dust, excess electrolyte (any amount that affects the topography measurement), or solute from the electrolyte. There is a high probability of contamination being present as the surface is touched by the liquid from the probe. The CVs performed should also be identical as the composition and topography of the entire surface should be the same at each point.

The probe raster scanned the surface, pausing at each point to perform a CV measurement. Since the CV curves take 10 seconds per point, to perform this 20 by 20 matrix of measurements required over an hour of measurement time. The aim of this measurement was only to confirm that the CVs are identical. Once this was known, the measurement could be performed at a single voltage value to speed up the scan.

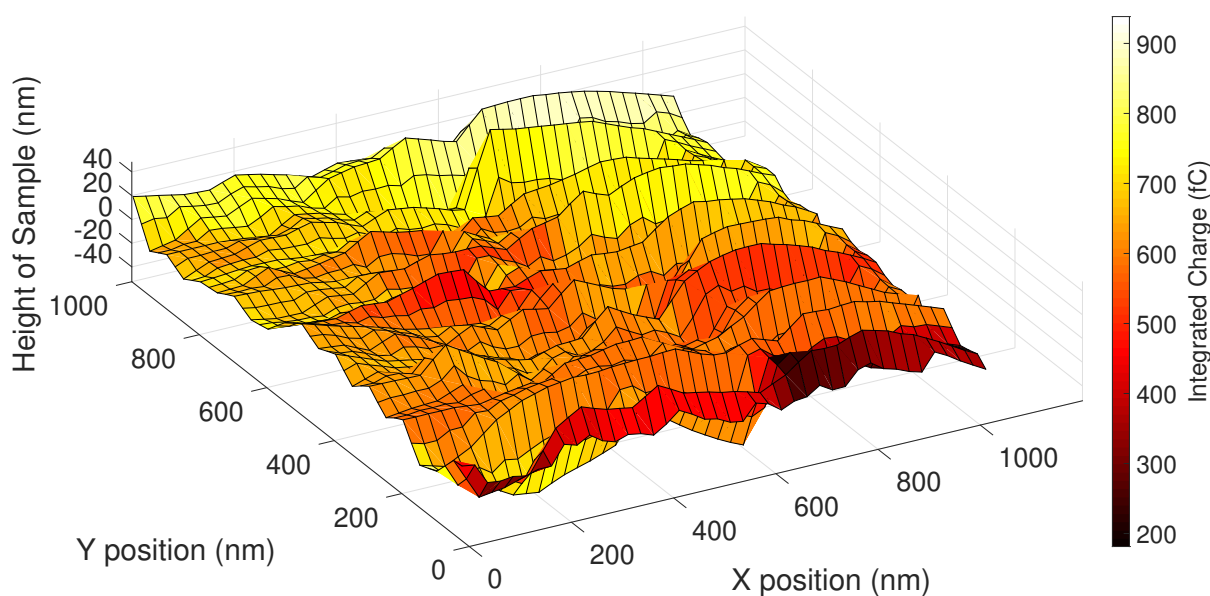


FIGURE 4.23: The contours of this image show the Z topography of the surface, and the colour scale shows the integrated charge measured at each point. The error on the integrated charge measurements is 1 fC.

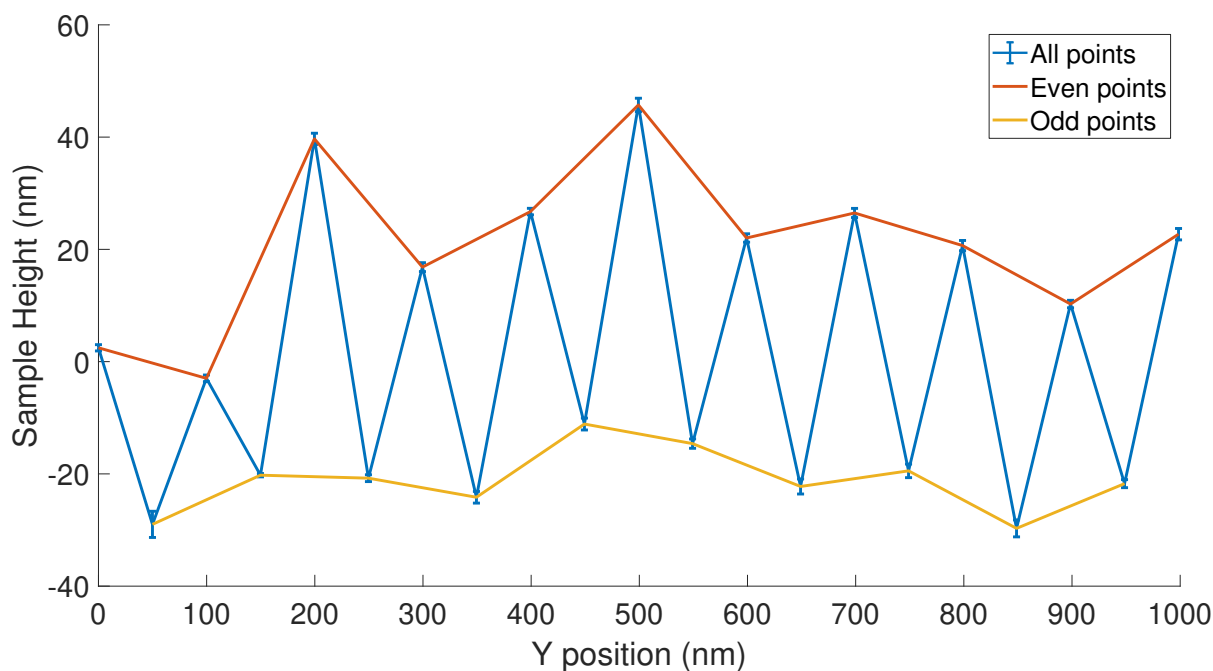


FIGURE 4.24: Recorded sample heights of points at X=1000nm from the data shown in figure 4.23

What can be seen first in the topography channel of figure 4.23 is significant hysteresis. This can be seen by plotting all the points with a X position of 1000 nm, as in figure 4.24. By dividing the points into even and odd, it becomes clear that even points are all higher than the odd points. This is due to the scanning routine. The probe scans from negative x to positive x, moves a step towards negative y, then scans from positive x to negative x. Preventing double-scanning of lines speeds up the scan but results in the hysteresis seen in this graph. The difference between forward and back lines, which may be substantial with these tips, is determined by tip geometry. When the tip switches directions between lines, the probe can be bent in different directions, so different parts of the tip are used to scan the lines afterwards. This can be eliminated by: separating these two directions, using sharper pipette tips—so measurements aren't done with two parts of the probe—, and switching to tapping mode which may not show this hysteresis. The separated scans are shown in figures 4.25 and 4.26.

In the current channel, this hysteresis is not really seen. This makes sense, as this tip bending shouldn't necessarily change the footprint of electrolyte on the gold surface. There are some features in the CV map at the end of the measurements, but it is difficult to say what this was. It could have been a scratch on the surface of the gold, or the electrolyte droplet may not have touched down on the surface properly, increasing the resistance, and decreasing the current.

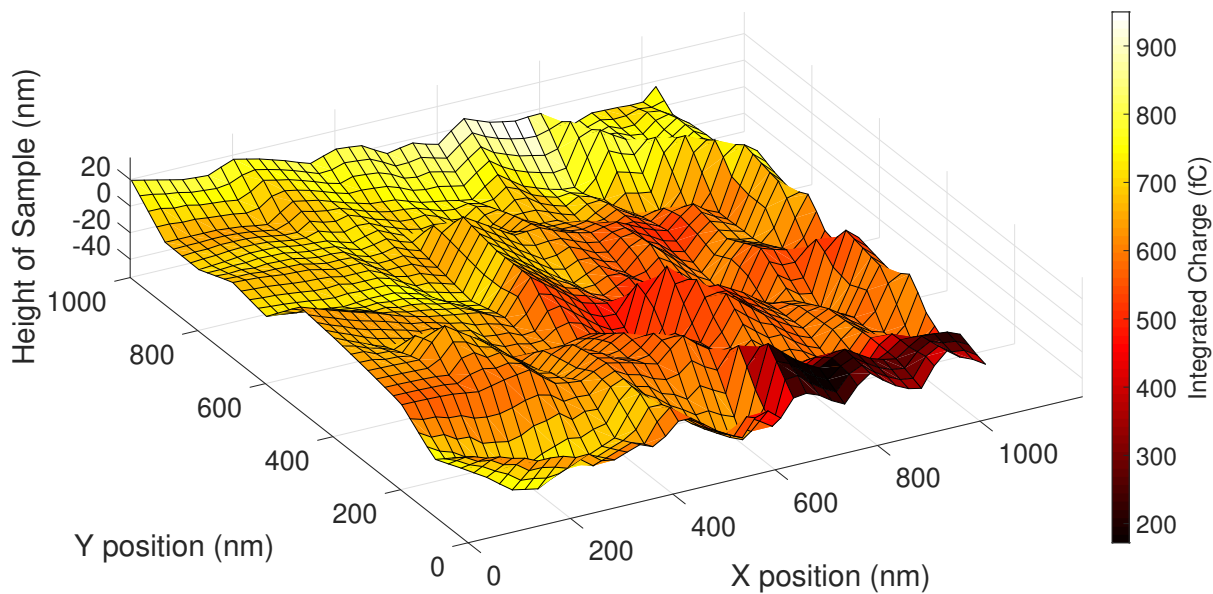


FIGURE 4.25: The even scan lines of figure 4.23.

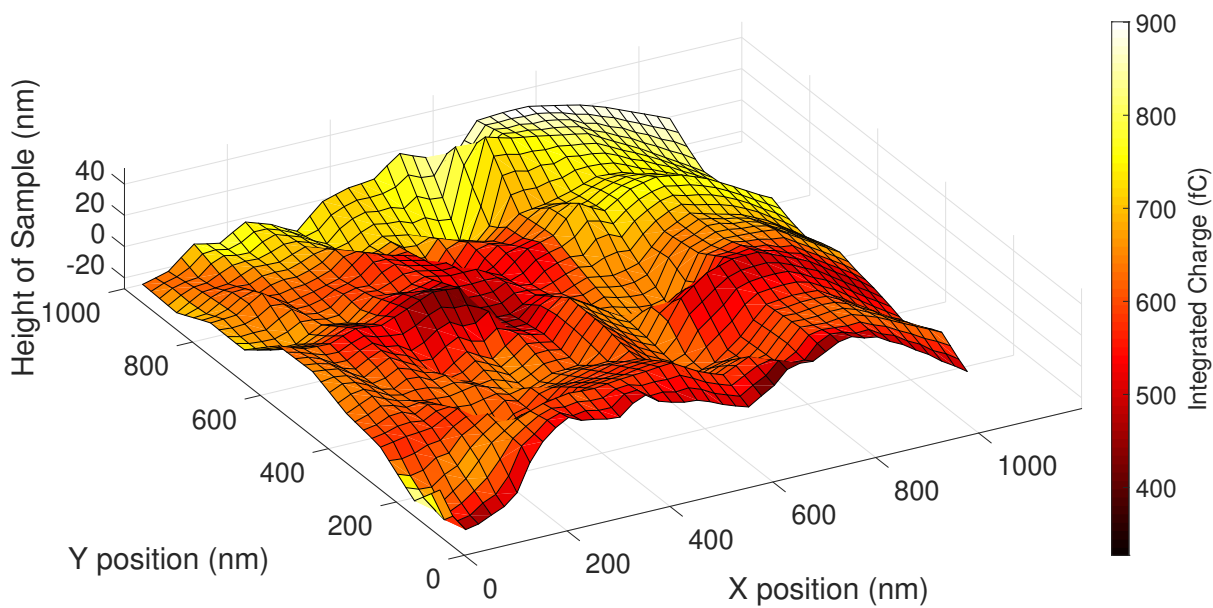


FIGURE 4.26: The odd scan lines of figure 4.23.

A second scan is shown in figures 4.27 and 4.28.

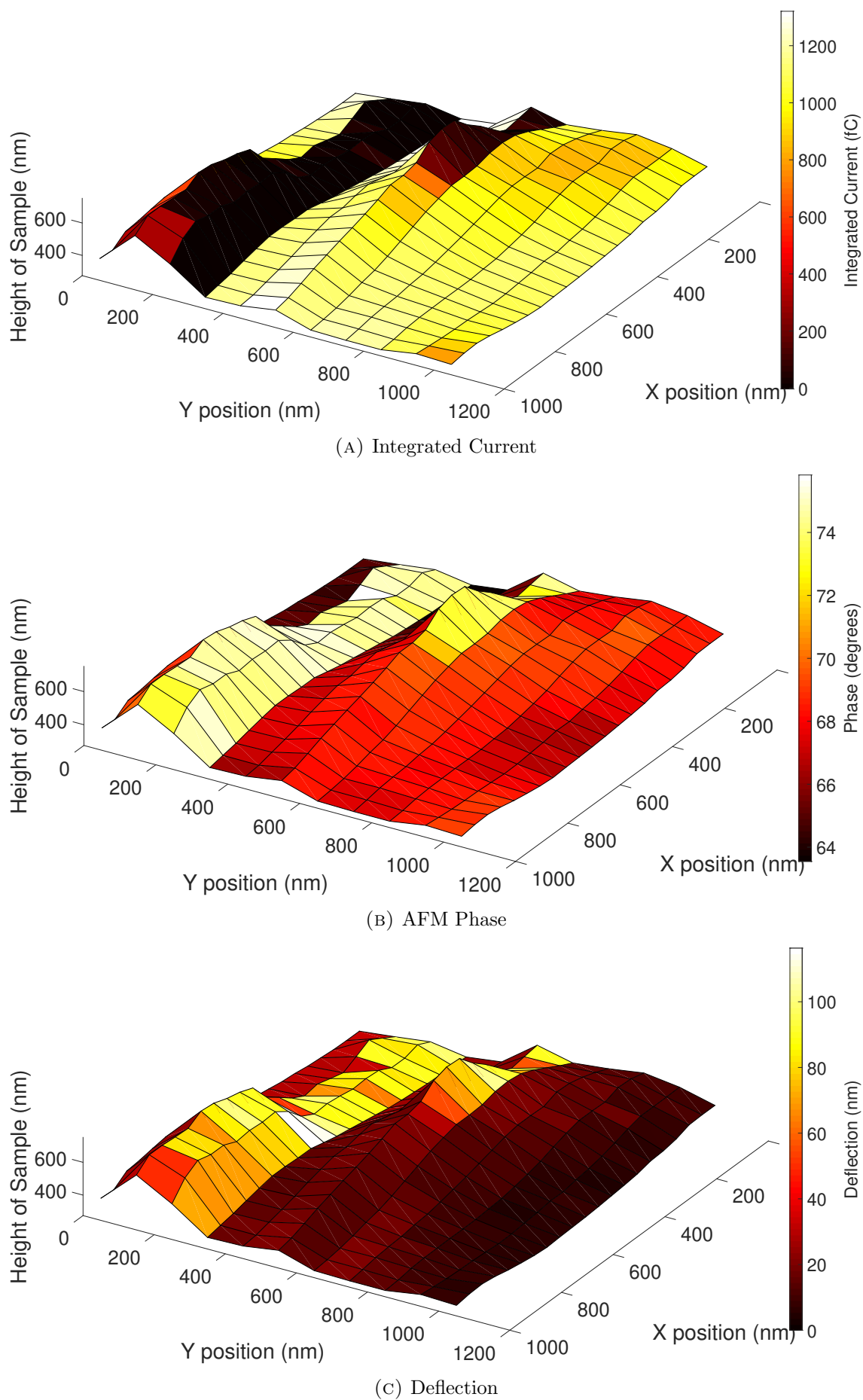


FIGURE 4.27: These are the odd scan lines of a droplet surface scan on gold. The error on the integrated current is 1 fC.



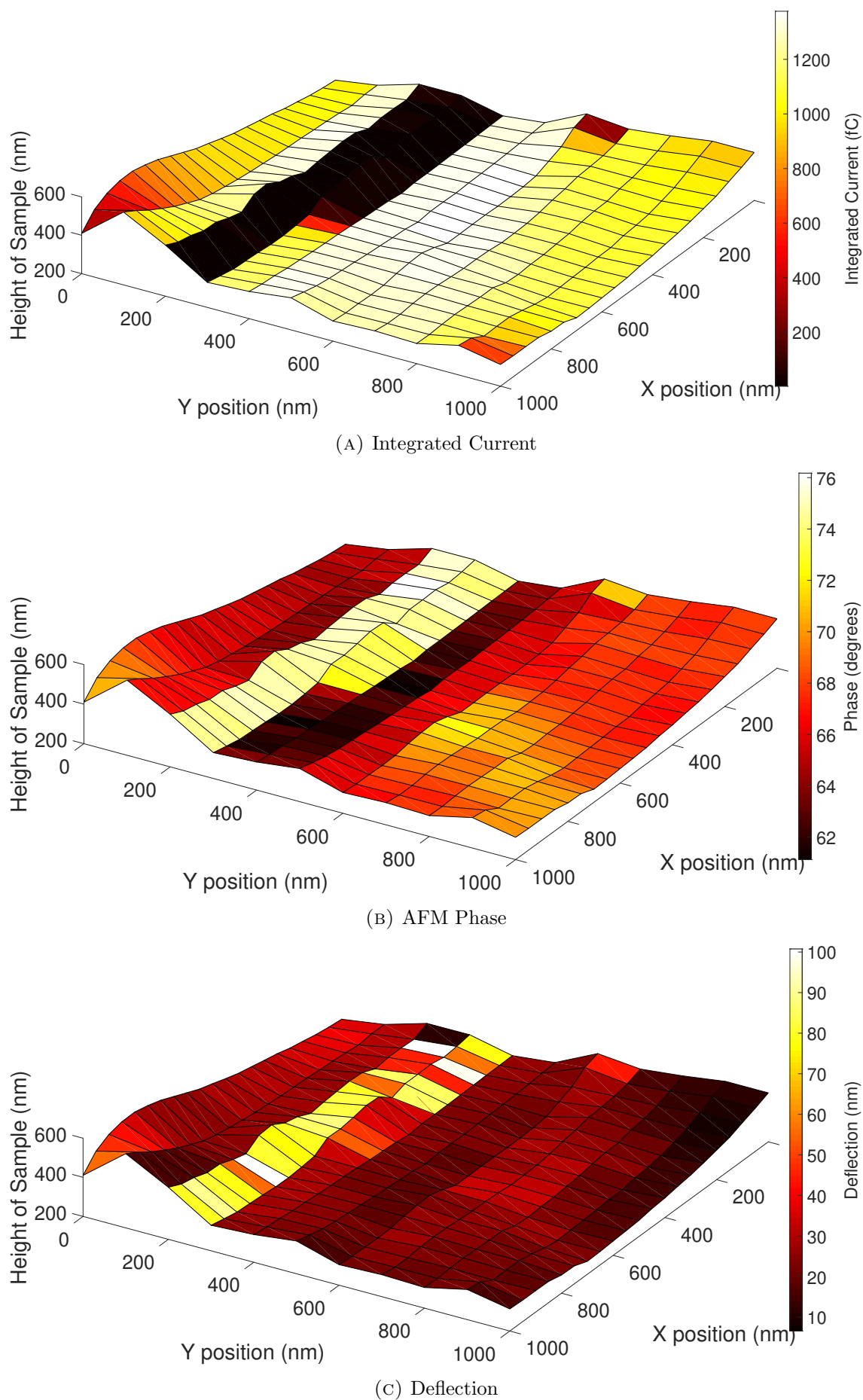


FIGURE 4.28: These are the even scan lines of the droplet surface scan on gold shown in figure 4.27. The error on the integrated current is 1 fC.



In the next measurement the resulting topography is interesting, but it does not resemble the flat surface of template strip gold which was measured. It seems that the topography measured during the trace is very different from the retrace. It could be that the tip is instead measuring the drag caused by some liquid on the surface.

The deflection, phase, and current measurements also tell an interesting story.

In the topography channel of [4.27](#) and [4.28](#) we see an undulating, smooth surface. However, this topography is determined via feedback on the AFM amplitude channel. Previous measurements showed that the liquid at the tip apex can also reduce the oscillation amplitude of the probe. If this is true, the topography seen could be a measure of the liquid at the tip apex. If this is true, the deflection channel of the probe can be examined to see if there is a significant discrepancy. In the deflection image seen above, we see that the probe is deflected by 100 nm for several lines. This could indicate that the probe is deflected by a real physical feature over these lines, and that the deflection is a more accurate depiction of the topography. The integrated charge and phase channels seem to confirm this. Over the exact same pixels that the deflection is increased, there are changes in the phase and integrated charge channels. This could indicate that the probe is passing over an insulating region, so current is restricted and the phase changes due to the change in physical properties of the sample. This may indicate that these measurements are successful, and the probe is able to measure coordinated features in topography and electrochemistry.

We can also look to the pair plot to see the correlations of [figure 4.29](#).

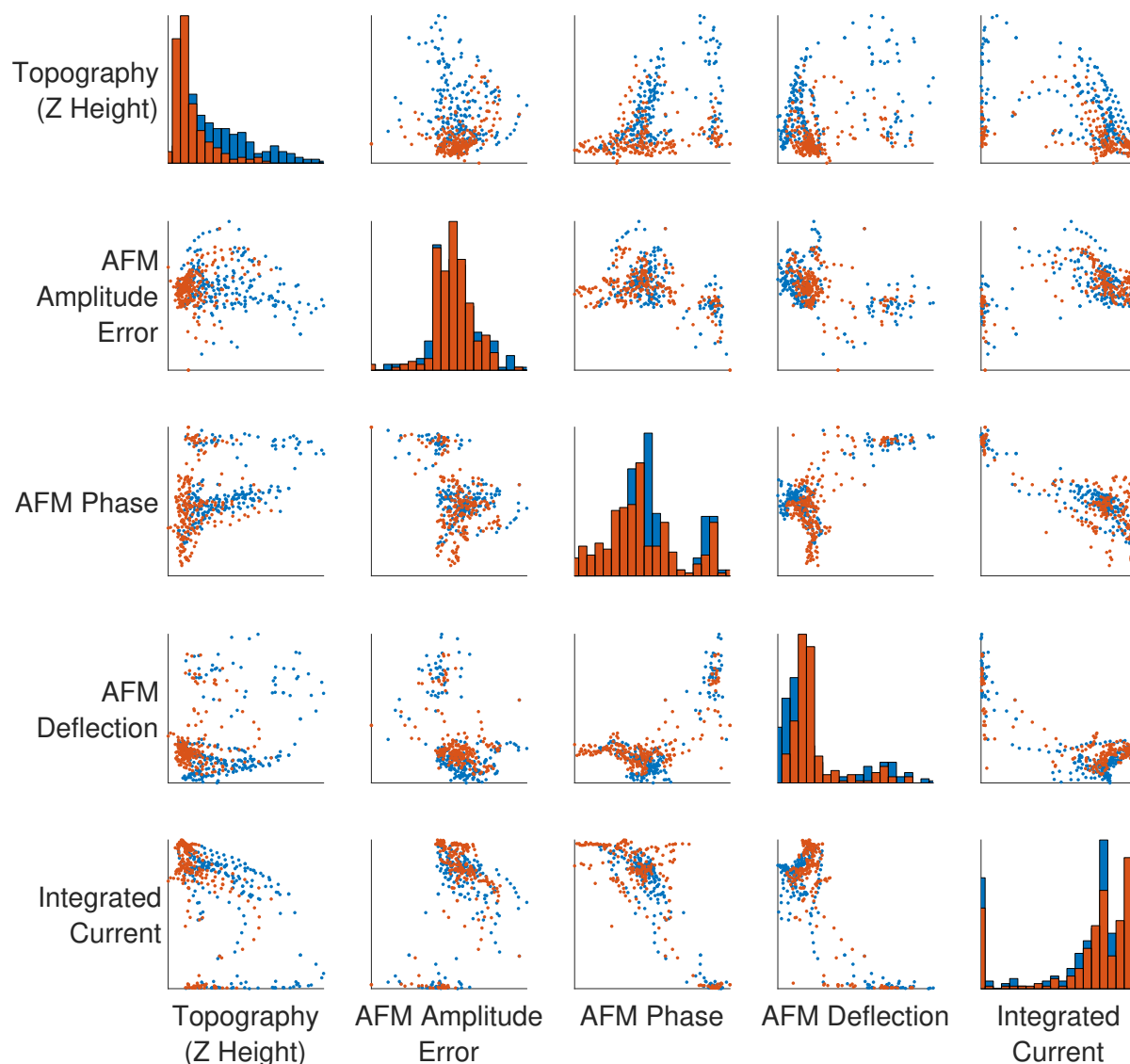


FIGURE 4.29: This pair plot displays the normalized data from the even scan lines of figure 4.27 (blue) and the odd scan lines of figure 4.28 (orange). The histograms display the data from a single channel, with at x-axis being the value of the channel between 0 and 1, while the y-axis is bin counts, where the integrated counts is 256. The scatterplots show the relation between two channels, with x-axis channel label at the bottom of the graph, and the y-axis channel label on the left side of the graph. All axes of the scatterplots have a range of 0 to 1. The plots show the topography generated by tapping mode feedback. AFM Amplitude Error is the difference between the tapping mode amplitude and the setpoint amplitude. AFM Phase is the phase difference between the measured AFM tapping mode signal and signal which modulates the blue laser which oscillates the probe. AFM Deflection is the distance by which the cantilever changes away its initial position. Integrated Current is the cumulative area integrated within the three CV curves performed at each point.

In each of the plots relating phase, deflection, and integrated current we see that there is a cluster of greater deflection, greater phase, and lesser integrated current data points.

The deflection is measuring a real raised area, and this area is a different material in terms of material properties related to phase and electrochemical properties related to the integrated current.

Past this the AFM amplitude error can be examined where the same two group dynamic shows up. The previously described cluster (greater deflection, etc.) has a lower average amplitude error. Changes in noise could be related to liquid layer thickness. Immersing these cantilevers, and AFM cantilevers in general, results in a reduction in the Q factor. So, if the AFM amplitude decreases this could mean that the probe is less immersed in liquid, the Q factor increases, and the relative noise on the amplitude channel reduces.

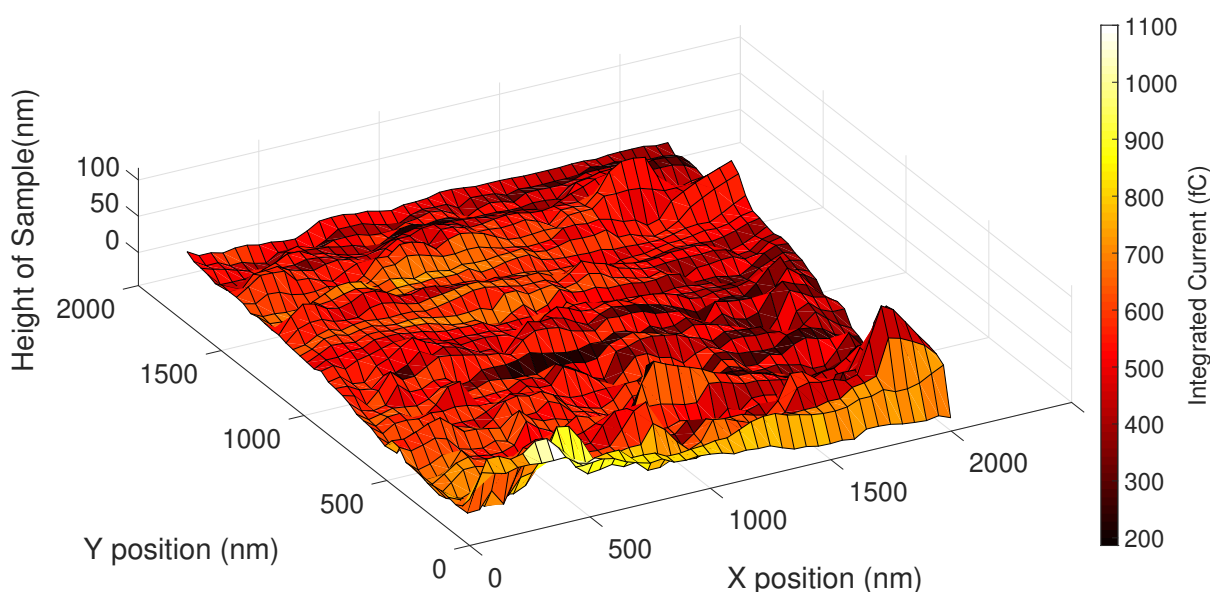


FIGURE 4.30: Topographic and integrated current image of a template stripped gold surface. While the topography is recorded at each point, CV curves are recorded as well. The error on each pixel is 1 fC.

Figure 4.30 shows a larger version of the previous measurement, this shows a grid of 40 by 40 points. Interestingly, the probe stays in electrochemical contact with the sample the entire time. So, we can record CVs over this entire surface. In the topography channel we see a few small features. They seem to be spread through the slow scan direction, so it is possible that these are real features of the surface. In the electrochemical channel the current does show some variation, but there don't seem to be any noticeable features.

The correlations between the two data channels using the current information to color the topographic image. In general, there does not seem to be any correlation between the channels. However, in the first line at  $Y=0$ , the current is elevated. This also happens to be where the tip would first land. When the scans were being set up, the tip was

approached to the surface and left in that XY coordinate while a few preliminary CVs were done to see how the tip was functioning. Then the scan would begin. On this scan, this happened at (X position, Y position)=(2000, 0). This indicates that performing measurements may be driving liquid onto the surface, which may create features in both the electrochemical and topographic channels.

The electrochemical scanning measurements described have demonstrated that this technique can perform a 40x40 pixel scan of a micrometre scan areas with functional AFM feedback while obtaining electrochemical information. Specifically, this project has demonstrated sub pA current resolution, nm topography resolution over 1600 consecutive measurements via droplet contact with the surface. These measurements are an exciting step forward as they offer an opportunity to compare multiple channels of information in one measurement. As can be seen in the above measurements of figure 4.29, phase and integrated current correlated without either observable cross talk from topography channel. This shows that material effects are indeed being measured, and that these effects cannot simply be attributed to topography.

With further development of this functionality these measurements could be performed on other electroactive species such as battery materials [161], active catalytic sites [162], or metal species undergoing corrosion [163]. Corroding materials can be challenging to work with as the corrosion process may create significant variations in topographic height of the samples [164]. This force channel allows scanning techniques to be used that would be slow or destructive in a probe that only had electrochemical sensing. One example is the previously described hopping mode method. By changing the hopping height, this technique can measure samples with very large topographic changes. However, choosing larger hopping distances to prevent crashing reduces the speed at which a new sample position can be found [164]. Additionally, if the signal-to-noise ratio is small, as it is in electrochemical scanning, approach must occur more slowly to avoid feedback crashes due to small jumps in noise, which are significant compared to the electrochemical signal. However, this project has demonstrated that the force feedback is significantly lower noise, meaning that this channel is reliable, and it is possible to vastly increase the speed at which scanning occurs in comparison to the electrochemical method.

This superior control may also lead to questions about other purposes this system can have. Control over the parameters involved including absolute position of the probe to nm, force to tens of nN, and current to sub pA suggest that this high level of control could be useful in the context of surface manipulation. Specifically, control of bias independent

of the position control can be used to perform some distance regulated etching experiments. If possible, this could be used as a tool not only for performing nanolithography, but for characterizing it as well. We explore this concept in the next section.

## 4.6 Destructive Sample Imaging – the Potential for Manipulating Surfaces

In the previous section we demonstrated the great degree of control afforded by force feedback. One possible use of this functionality would be as a tool for performing electrochemical lithography. To be a relevant tool it is important to understand what happens through bias pulses, and whether variations in dwell time and bias magnitude have predictable effects on the surface augmentation. While this type of functionality requires a substantial amount of study, here, an initial exploration of the effects of higher bias experiments is presented.

To perform these experiments, it is important to use a well characterized surface where changes made to the surface can easily be seen. For these measurements a template gold surface was approached with the liquid droplet technique and 10V pulses of various durations were applied.

In this measurement voltage was ramped to 10V, and the bias change resulted in an increase of the size of the droplet on the surface as seen in the droplet footprint in figure 4.31. The anodic limit of  $\text{ClO}_4^-$  salt in propylene carbonate solvent is 6.0 V vs. glassy carbon [165–167] and 4.6 V vs. platinum [165, 168], so at 10V vs. QRE Ag/AgCl electrolyte decomposition must have occurred during these measurements.

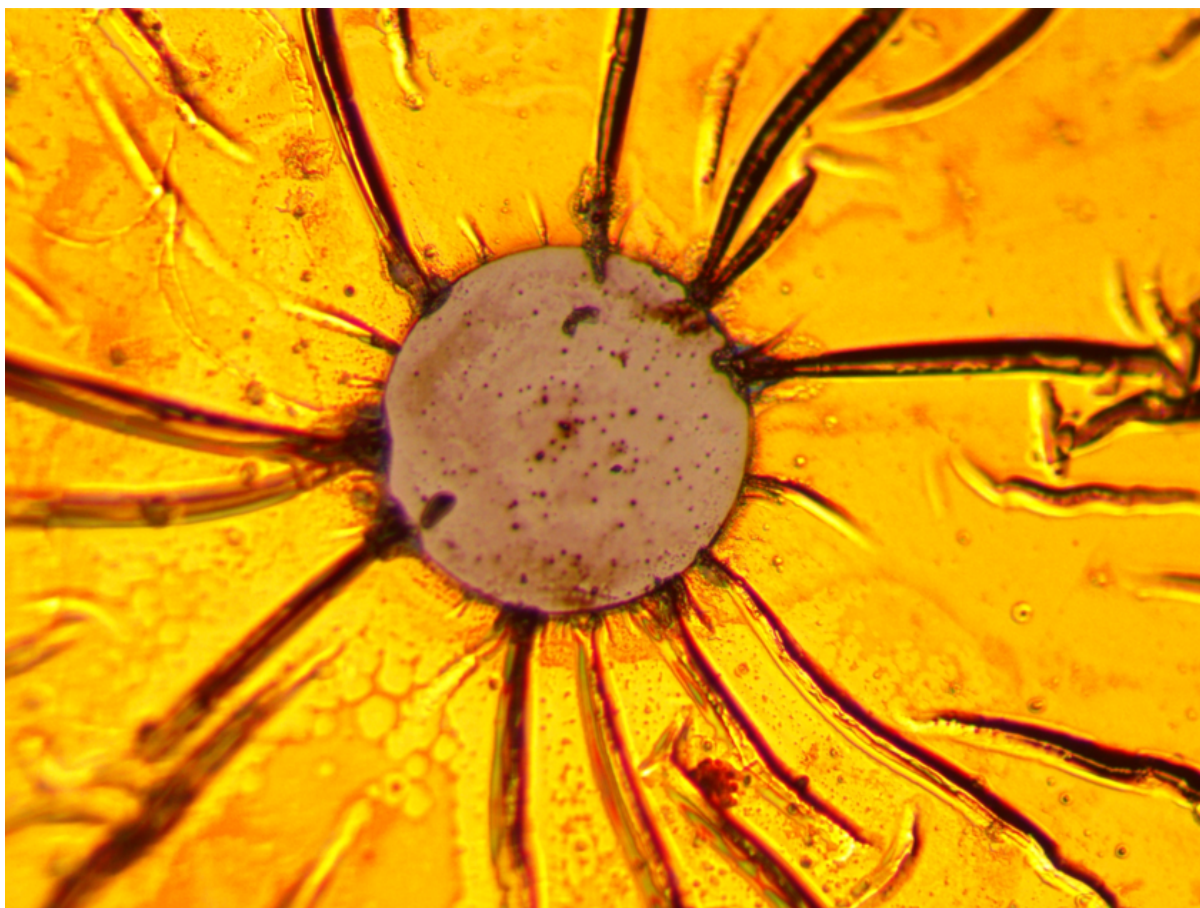


FIGURE 4.31: A circle of gold delamination appears in the middle of the optical image. This was performed by applying a 10 V bias between a silver chloride electrode in the probe and the gold surface shown here. The electrolyte was 0.4 M NaCl in water.

In this experiment, the liquid in the tip was NaCl in water. At this high voltage, it is most likely that electrolysis of  $\text{H}_2\text{O}$  has occurred, so the pH changed drastically, and gas evolution caused the gold film to delaminate. The lines radiating from the center are indicative of bubble formation.

Due to the reaction of the gold with chloride, propylene carbonate with a redox mediator of ferrocene methanol was used instead. Propylene carbonate has an extremely low vapour pressure, meaning that the liquid at the tip apex would not evaporate as it had done with the water electrolyte. This facilitated the droplet connections made during the droplet measurements.

The above experiment raises questions about the use of these probes for microfabrication, or even nanofabrication. If the reaction above was characterized properly, perhaps it could be used as a tool for etching gold. To further characterize this process, the experiment was repeated. However, the electrolyte was switched to propylene carbonate and sodium



perchlorate due to the stability of the droplet. With a stable, small droplet at the probe apex, it was hoped that the smallest features possible could be made.

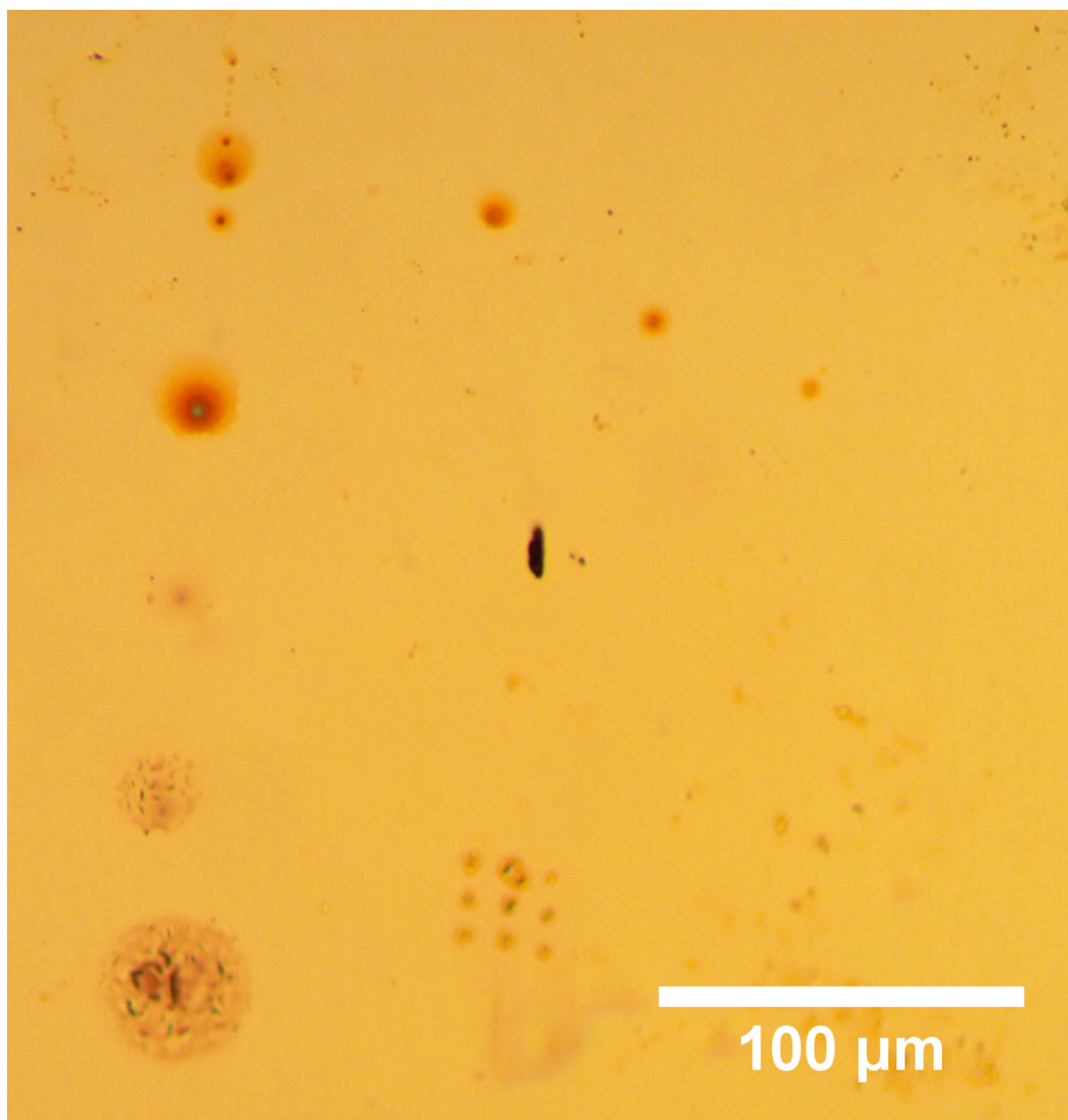


FIGURE 4.32: The results of several experiments where a potential pulse was applied, the probe was moved to a new spot, approached, and another potential pulse was applied. The voltage and length of the pulse were varied for each spot. With new tips this meant applying voltages of 10V for increments of 10 seconds.

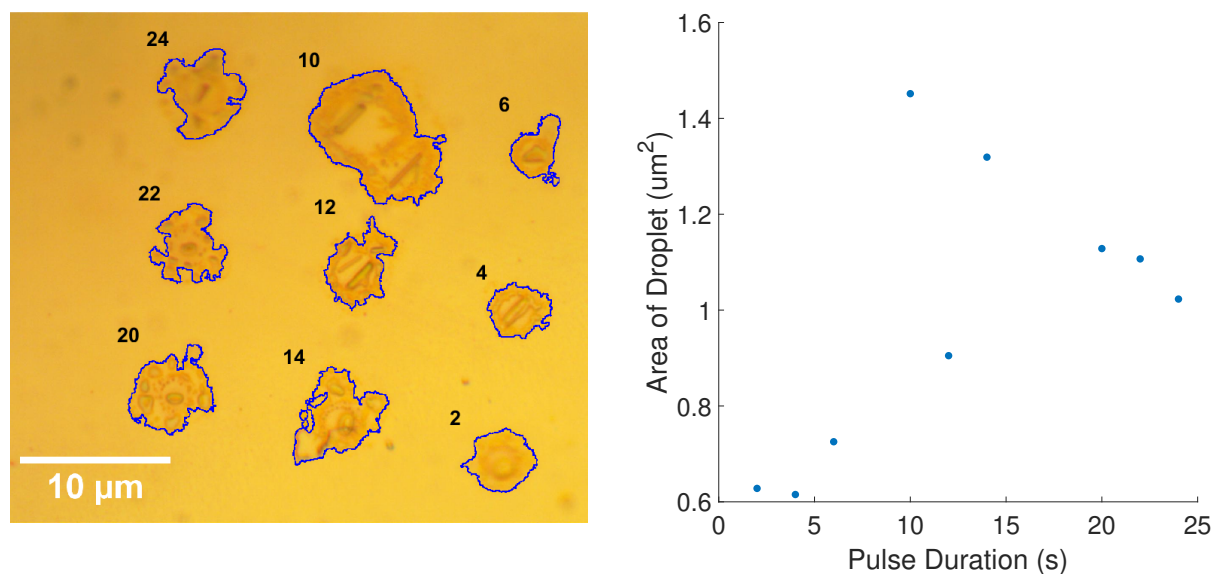


FIGURE 4.33: The bias routine for these measurements consisted of ramping the voltage from 0 to 10 V over 0.01 s, holding the voltage at 10 V for some a variable amount of time, then ramping the voltage from 10 to 0 V over 0.01 s. The time over which the voltage was held for these points is directly labeled on the optical image in seconds. The second graph shows the area of each droplet as a function of the pulse duration.

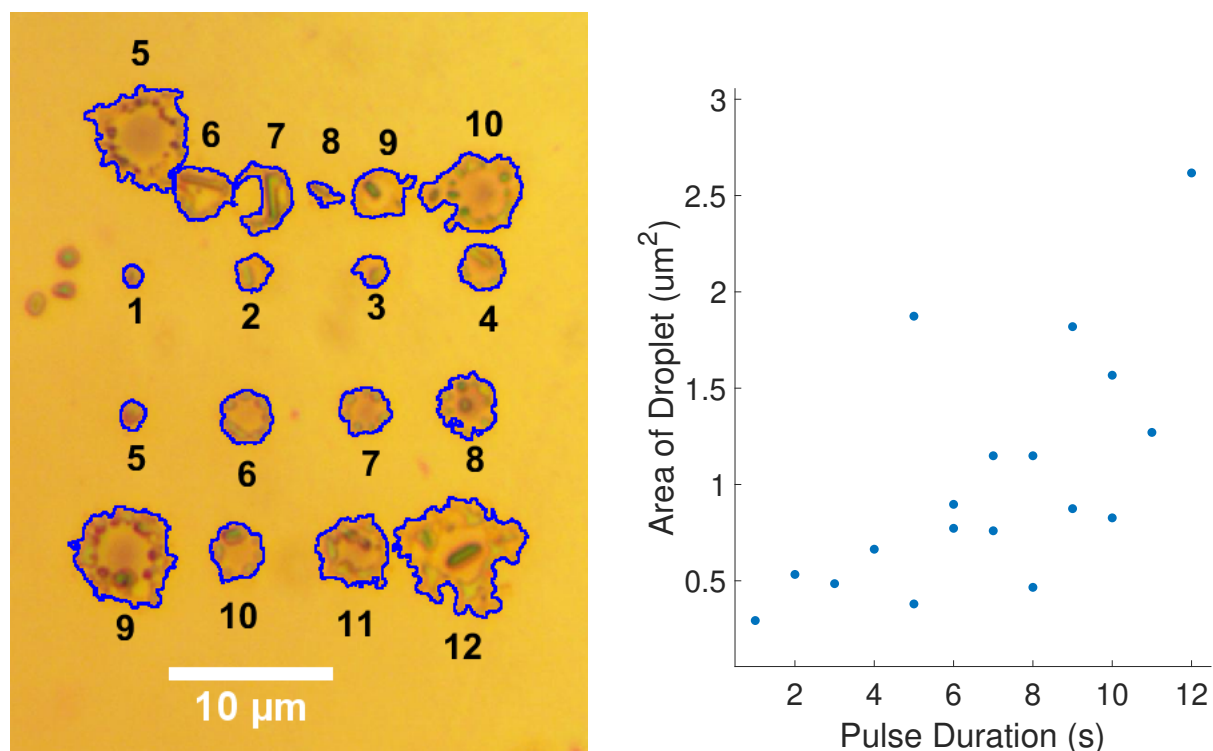


FIGURE 4.34: The bias routine for these measurements consisted of ramping the voltage from 0 to 10 V over 0.01 s, holding the voltage at 10 V for some a variable amount of time, then ramping the voltage from 10 to 0V over 0.01 s. The time over which the voltage was held for these points is directly labeled on the optical image in seconds. The second graph shows the area of each droplet as a function of the pulse duration.



In the measurements seen in figure 4.32, potential pulse was applied, the probe was moved to a new spot, approached, and another potential pulse was applied. The voltage and length of the pulse were varied for each spot. With new tips this meant applying voltages of 10 V for increments of 10 seconds. Several probes were crashed during use. Because of this, the time increment was reduced to 1 second or less due to the reduction in resistance as the probes were damaged through use.

What resulted was liquid being ejected from the surface onto the gold, and crystals of what is presumably sodium perchlorate. Examination of the graphs showing droplet area by pulse duration in figures 4.33 and 4.34 shows an apparent correlation between the two quantities. To determine the nature of this correlation more completely one would need to do many more trials, and employ a method to determine the volume of these droplets rather than the area.

These experiments show liquids can be ejected from inside the probe to the sample surface. Through varying the bias and dwell time it was evident that the amount of liquid that is drawn onto the surface can be increased by using longer pulses of 10 V. However, this is difficult to quantify, and several factors also affected this. The main issue is the condition of the pipette tip. With each approach there is a chance of crashing and damaging the tip. Over many experiments the probe tips were damaged, and this was seen directly in the movement of liquid out of the tip. In some fresh tips, 10 V could be applied for 100 s and a droplet on the order of 1  $\mu\text{m}$  would be produced. Later, the worn tip produced a 10  $\mu\text{m}$  sized droplet from a 10V pulse lasting 1 second. So, while we did see variation due to dwell time, changes due to tip damage were far larger.

Another important factor is separation between droplets. After an experiment was performed on a single point, the probe was retracted from the surface, moved laterally, then approached to the surface. Doing this prevented the probe from mechanically dragging the droplet across the surface. Sometimes, the probe was not moved enough, and the probe would land on the outer edge of the previous droplet. When an experiment was performed at such a location, a single larger droplet would result, rather than two separate droplets. This emphasizes the need for the smallest droplets possible. Smaller droplets are crucial for limiting the footprint of the technique during each bias sweep, and if they spread then it is difficult to create separate patches of electrochemical activity. This suggests that one should carefully engineer the electrolyte and surface. If we increase the contact angle of the liquid droplet, then the droplet will not spread as much, and higher resolution features can be created with this technique.

Another feature that could be better utilized in these experiments is the feedback of the probe. After a droplet is produced, the probe can then be used to scan the area and examine how the surface has been augmented. By doing this our topography resolution can be substantially improved over this optical method, and smaller droplets could be detectable. This would also be a great opportunity for creating and characterizing smaller droplets.


It should be observed that these measurements were performed in a different AFM (Asylum Research MFP 3D) than the rest of the measurements. This microscope has a different geometry than the ECAFM, meaning that these probes were adapted to a new microscope showing the versatility of the technique. Theoretically, this probe could be modified to work in a variety of AFM systems, to varying degrees of functionality.

In summary, by using force feedback and piezo positioning this system is capable of non-destructively approaching a sample surface with a liquid droplet, allowing for the use of the electrochemical system to apply specific bias routines to precise locations on the surface. This could be useful in nano or micro patterning surfaces with whatever substance is contained in the pipette, or for selectively etching surface. Additionally, this platform could be used to probe fluid dynamics at the nano scale.

The physics of the droplets in these measurements also suggests further study.

## 4.7 Conclusion

To assess the results of this Chapter, the initial questions must be considered. The first queried what crosstalk exists between the AFM and SICM channels. To illustrate how the geometry of the tip affects the combined AFM and SICM, a two-dimensional surface scan was performed. These combined AFM-SICM scans demonstrated both that the techniques function and that some interesting correlations exist within the channels of information. The force channel information demonstrates that high aspect ratio features can be followed in liquid, with a small amplitude error. This confirms that the SICM measurements can be operated much closer to the sample surface without the danger of crashing, and a higher signal to noise ratio can be attained. While the error in the amplitude channel only varies by  $1.3 \pm 0.2$  nm between its highest and lowest values, the SICM channel varies by  $136 \pm 1$  pA. The relative magnitudes show that the probes' ionic current sensitivity to Z distance changes is very high. Due to this high signal to noise ratio this system is able to perform higher resolution and high-sensitivity SICM

measurements that would be impossible to measure without AFM feedback. Other combined SICM-AFM systems exist within the literature, one of which is the previously described FluidFM probes used by Zambelli on a calibration grid and hippocampal neurons [169]. The tip diameter will determine the resolution of both the AFM and SICM measurement, and as such the 300 nm top diameter results in lower resolution images. Additionally, these probes are used in contact mode which can damage the surface, which is directly addressed by adding safety retraction conditions to protect the surface. It is specifically stated by the authors that produced worse topography results than the contact mode, which is indicative of the inherent "forest of peaks" challenge. A more recent publication by Zambelli [71] shows that this FluidFM system is suitable for surface charge mapping. This is an indication that by leveraging the strength of this system (high resolution, simultaneous AFM and SICM measurements) this system could prove useful for surface charge measurements. This combined AFM-SICM system can perform SICM measurements with force-based distance control, phase information, and a greatly increased sensitivity compared to typical systems. It will thus provide opportunities to validate our theoretical assumptions and push forward into regimes of electrochemical scanning techniques which could not have been inferred from a pure SICM system.  The next question was whether spatially resolved electrochemical measurements can be performed reproducibly. To examine this, a droplet mode was used to 50 reproducible CV curves can be performed on a gold substrate with sub picoamp current resolution and nanometer scale topography resolution at one point in the XY plane while tapping mode feedback controlled the probe position. These measurements demonstrated that SECCM measurements can be performed at a single point with low enough current and force noise to be the foundation of a reproducible scanning technique. There is a lack of reporting on this type of measurement in the literature as this is really a calibration type measurement. However, just as AFM measurements will often quote transfer functions and drift values over time, this type of long cyclic voltammetry measurement could act as a type of calibration measurement to demonstrate stability of the droplet. Nonetheless, the current level and noise can be compared to other results. Specifically, the work of Mauzeroll/Schougaard [170] shows several low noise measurements. This include a series of galvanostatic measurements which demonstrate the replicability of the measurements, and current voltammetry measurement with peak currents on the order pA to 10s of pA. Additionally, SECCM measurements were performed on spatially distributed LFP particles. Another example is Unwin's voltammetric SECCM study of hydrazine electro-oxidation on platinum electrodes [171]. Therein, the individual spatially resolved CVs are shown, and averaged to depict differences in activity. This averaging works well

to characterize the large current difference between regions, but an interesting avenue of characterization would be to further characterize if these variations were due measurement error or differences in activity spatially resolved within a small region. These current peak current variation are on the order of 10 pA. This is confirmation that the current noise and stability demonstrated in this thesis could be the basis for SECCM measurements.

The third question asked what are the abilities and limitations of this scanning droplet technique. To investigate this, two-dimensional scans of point resolved current voltammetry were performed. These measurements demonstrated that this technique can perform a 40x40 pixel scan of a micrometre scan areas with functional AFM feedback while obtaining electrochemical information. To contrast this to the literature, we can examine the measurements performed by Takahashi on the hydrogen evolution reaction on transition-metal dichalcogenide nanosheets [172]. These measurements show submicrometer spatial resolution, the electrochemical maps show distinct areas of low and high activity. These measurements are then compared to AFM measurements to identify monolayer and bilayer regions. To compare, the SECCM measurement performed in this thesis were performed on sample with fewer sample features, and on a smaller area. This leads to a greater difficulty in clearly identifying sample features and characterizing the spatial and current resolutions. However, one main advantage of using a SICM-AFM probe is the ability to perform AFM simultaneously, and the ability to coordinate those channels of information. In the Takahashi measurement, an additional AFM measurement was performed in contact mode. The process of finding the same area in two scanning probe systems can be challenging, and that challenge increases as the sample features become smaller and less distinct. Additionally, the AFM measurement is performed in contact mode, which is more destructive than the tapping mode used in the gold measurements, and does not yield phase information. This phase information coordinates to material differences, and could perhaps be used to identify the chemical composition of the sheets. These measurements are an exciting step forward as they offer an opportunity to compare multiple channels of information in one measurement. In these measurements phase and integrated current correlated without either observable cross talk from topography channel. This shows that material effects are indeed being measured, and that these effects cannot simply be attributed to topography.

In these measurements, the probe was brought to the surface under AFM force feedback, and specific bias routines were performed. This ejected liquid from the tip onto the sample surface in specification locations. Looking to the literature, there are many recent

examples of SICM-type probes used for electrodeposition. Unwin has created copper nanopillars with 400 to 600 nm diameters [173]. These nanopillars were even with eccentric geometries to showcase their control over the spatial construction in three dimensions. Not only is the probe used to create these structures, but it is further used to characterise them through a hopping mode SICM technique. This result is contrasted with FluidFM nanopillars which are several times larger due to the larger tip diameter [174]. In the FluidFM case however, much more elaborate features were created, demonstrating a higher level of control. It is clear that the measurements presented in this thesis are only the first steps towards the measurements performed by the Unwin and FluidFM systems. However, the small tip pipette opening of the pipette probes presented in this thesis suggests that it would be possible to make pillars double the size of the Unwin project. Additionally, these AFM-SICM probes could perform the scanning of the pillars more accurately. In the Unwin paper, the difficulties of hopping mode are detailed, and it is shown that if the hopping height is not large enough, or the SICM feedback is not sensitive enough, the probe may be bent by the pillar and no change in topography will be measured. While it would be simple to integrate shear force detection into this setup, tapping AFM would be a more sensitive method to record topography. This is especially important for nanopillars. These free standing structures are delicate, and a relatively small lateral force could destroy them. By using tapping mode there will be no lateral force on the pillars, which would be less destructive. In summation, these measurements showcased the potential level of control and customizability that this system offers. This could be useful in nano or micro patterning surfaces with whatever substance is contained in the pipette, or for selectively corroding and etching surface. Additionally, this platform could be used to probe fluid dynamics at the nano scale.

# Chapter 5

## Conclusion

This thesis explored the viability of a combined AFM-SICM system designed to perform combined and simultaneous electrochemical and traditional AFM measurements. To accomplish this, new AFM-SICM probes based on hollow pipettes had to be designed, created, and characterized. Characterization of the probes is an essential prerequisite to their use as a quantitative tool to study structure-property relations in battery materials, neurons or catalytic systems for hydrocarbon conversion. In doing so, not only were the experimental parameters studied and optimized, but systematic artifacts of this system were examined for the refinement of the probes and technique. To assess the novel probes created during this Thesis, the questions set forth in sections 3.1 and 4.1 must be evaluated.

1. Can the probes perform AFM force measurements?

Hollow pipette probes were used to perform AFM deflection and tapping mode measurements. Photothermal actuation was used to oscillate the probe during the tapping mode measurements. This is a novel and unexpected result as these probes are over  $\sim 2$  orders of magnitude larger than microfabricated silicon cantilevers. It is surprising as one might assume that the discrepancy in size between these probes and silicon cantilevers would result in large stiffness constants and an inability to oscillate the pipettes using only an optical drive. However, the process developed in this work allowed for control and modification of the cantilever geometries. A functional probe geometry was determined by exploring the phase space of accessible probe geometries using thermal pulling methods well established in biological patch clamp methods. These probes had stiffness constant

of 80 N/m, and resonance frequencies in the range of kHz. Additionally, the probes could be oscillated at amplitudes of over 1  $\mu\text{m}$ , which is more than sufficient for performing tapping mode measurements.

## 2. Can the probes be used to image a surface using AFM?

These novel AFM-SICM probes were then used to perform topographic scans on multiple sample surfaces, with sample feature sizes ranging from the  $> 100$  nm tall hills on CD stampers to 2 nm tall carbon nanotubes. Through these measurements we studied the role of tip geometry on AFM measurements, which is crucial in reducing systematic artifacts within topographic images.

It was shown that while the geometry of the tip apex can introduce some uncertainty to the topographic images, these effects are predictable and could be eliminated by tip characterization and deconvolution of the topography images. The  $> 100$  nm features of these topographic scans showed some distortion, but these aspect ratios are an order of magnitude larger than the slopes found in many interesting sample materials. Furthermore, predictable systematic errors such as these can be modeled, and those insights can convert the raw image data into a more accurate representation of the true topography.

On the other side of the size spectrum, the carbon nanotube sample demonstrated that the probes are sensitive enough to image and characterize extremely small features. Tip size will ultimately limit the lateral resolution of this technique, however the  $60 \pm 10$  nm tip size shown through measurements on the carbon nanotube sample is enough for many interesting samples.

Another important resultant is that these probes can measure AFM topography in liquid. Scans in liquid environments are challenging as viscous damping and an increase in effective mass reduces the Q factor of cantilevers, thereby lowering force sensitivity. By engineering a long tip for these pipette probes, only the tip entered the liquid environment during the scans.

Having only the tip immersed in liquid (and keeping the cantilever part in air) drastically reduces the viscous damping, and the reduction in Q factor is small. Additionally, the use of photothermal actuation allowed us to avoid the “forest of peaks” problem inherent to piezoelectric actuation. This combination of long-tipped probes and photothermal excitation provides an opportunity for faster, higher signal-to-noise tapping mode AFM measurements in liquid.



Finally, we show that these probes behave like regular AFM cantilevers and tips. In particular, regular tapping mode and phase contrast give rise to AFM data with topographic and chemical information, both in air and liquid.

3. Can current be measured through the probes? Is there cross-talk between the electrochemical techniques and the force channel and vice versa?

Approach curves were performed in liquid, confirming that we can measure ionic currents with these probes as low as  $\sim 100$  fA. The force channel demonstrated the linear correlation of the ionic current with the measured force. This conclusively confirms that ionic current is a good proxy for the force channel. Traditional measurements of SICM topography are thus valid.

These measurements also demonstrated an advantage of a combined AFM-SICM method. The force channel ensured safe approach of the probe to the sample surface based on force feedback. The probe can thus be brought much closer to the sample surface without risk of crashing and damaging the probe tip. Having access to this smaller tip-sample distance regime allows for SICM scanning in a much steeper part of the SICM-distance curve, which will increase the lateral resolution of the technique. This advantage in current to noise ratio can be used to improve the resolution and phase space of structure-property measurements. The maximum current sensitivity is dependent on tip resistance and electrolyte concentration. To attain a sufficient signal to noise ratio, there will be restriction on the minimum electrolyte concentration and the minimum tip apex diameter. Depending on the sample being measured, this can be limiting. If one increases the size of the tip apex, the larger tip will have a worse lateral resolution. On the other hand, electrolyte concentration changes are not always feasible. For example, if one wishes to look at surface charge effects, the electrolyte concentrations must be low to facilitate ionic current rectification at the pipette tip. Or, if the sample is biological in nature, a change in electrolyte concentration may cause cells to die prematurely. However, with the proposed technique, one can approach without worry of damaging the probe or sample. The electrolyte concentration can be reduced by a factor of 10 while obtaining the same current to noise ratio as in a pure SICM measurement. Surface charge measurements require low electrolyte concentration, so this is a major step forward towards facilitating surface charge measurement via SICM.

The measurements presented in this Thesis clearly show that these AFM-SICM probes can be used to simultaneously perform regular tapping mode AFM and measure an

ionic current. This allows the combined techniques to be used to extract sample-specific information on heterogenous samples.

#### 4. What crosstalk do the AFM and SICM channels show?

To see how the geometry of the tip affects the combined AFM and SICM, a two-dimensional surface scan was performed. These combined AFM-SICM scans demonstrated both that the techniques function and that some interesting correlations exist within the channels of information. The force channel information demonstrates that high aspect ratio features can be followed in liquid, with a small amplitude error. This confirms that the SICM measurements can be operated much closer to the sample surface without the danger of crashing, and a higher signal to noise ratio can be attained. While the error in the amplitude channel only varies by  $1.3 \pm 0.2$  nm between it's highest and lowest values, the SICM channel varies by  $136 \pm 1$  pA. The relative magnitudes show that the probes' ionic current sensitivity to Z distance changes is very high. Due to this high signal to noise ratio this system is able to perform higher resolution and high-sensitivity SICM measurements that would be impossible to measure without AFM feedback. However, the increased sensitivity and lateral resolution come at the price of edge effects due to the proximity of the probe to the surface. These edge effects also exist in traditional SICM but are hard to observe due to the limited sensitivity and lower lateral resolution related to the increased tip-sample separation necessary for a safely scanning the probes. These effects can be disentangled by looking at all the channels that have been examined.

Another effect of having such a high signal to noise ratio is our ability to see correlations within the data that would otherwise be washed out by electrical and mechanical noise. In terms of correlations, three independent groups can be seen in these measurements: topography, phase information, and amplitude error.

The AFM amplitude error channel and the AC-SICM current amplitude channels correlate well. This shows conclusively that AFM and SICM measurement both provide the topography information on a homogenous sample, although AFM feedback allows for safer scanning on heterogenous samples (recall that the sign of the SICM current can change as a function of the conductivity of the sample). In the future, by switching to lower concentrations of electrolyte, this fact can be exploited. Surface charges can rectify the current, completely changing the SICM current approach curve dependent on the material being investigated. Therefore, the AFM amplitude channel can be relied upon completely for feedback and while the SICM channel records information on these surface

charges. These types of measurements could previously only be performed in a purely SICM system using a constant height mode. Such a mode must remain much further from the surface, so AFM-SICM should be able to perform these measurements with superior signal to noise and lateral resolution.

Phase information comes from the AFM phase and the AC-SICM amplitude. This correlation could lead to some interesting techniques. Firstly, is the material property that is measured in these two channels always the same? Performing scans on more materials may elucidate whether this correlation is always presents. If deviations in other materials are seen, then two separate properties could be measured with each of these channels, but those properties happen to be correlated in the CD stamper. If it is found that the two channels do correlate, then this work could apply to improving SICM microscope scanning procedures. If the phase information provided by AFM measurements could also be recorded via a SICM system, without beam detection mechanics, this could be a powerful and simple method to gain materials contrast.

This combined AFM-SICM system can perform SICM measurements with force-based distance control, phase information, and a greatly increased sensitivity compared to typical systems. It will thus provide opportunities to validate our theoretical assumptions and push forward into regimes of electrochemical scanning techniques which could not have been inferred from a pure SICM system.

#### 5. Can spatially resolved electrochemical measurements be performed reproducibly?

To demonstrate surface resolved electrochemical measurements and its reproducibility using the newly developed probes the electrochemical properties of the surface were measured using a droplet method to perform many cyclical voltammograms (CV) at a single point on a gold surface. These measurements show that 50 reproducible CV curves can be performed on a gold substrate with sub picoamp current resolution and nanometer scale topography resolution at one point in the XY plane. Additionally, tapping mode feedback can be used as a non-destructive way to measure the topography. These measurements demonstrated that SECCM measurements can be performed at a single point with low enough current and force noise to be the foundation of a reproducible scanning technique.

#### 6. What are the abilities and limitations of this scanning droplet technique?

To investigate this, two-dimensional scans of point resolved current voltammetry are presented. These measurements demonstrated that this technique can perform a 40x40 pixel scan of a micrometre scan areas with functional AFM feedback while obtaining electrochemical information. Specifically, this project has demonstrated sub pA current resolution, nm topography resolution over 1600 consecutive measurements via droplet contact with the surface. These measurements are an exciting step forward as they offer an opportunity to compare multiple channels of information in one measurement. In these measurements phase and integrated current correlated without either observable cross talk from topography channel. This shows that material effects are indeed being measured, and that these effects cannot simply be attributed to topography. These results show that measurements on other electroactive species such as battery materials, active catalytic sites or metal species undergoing corrosion are possible. Corroding materials can be challenging to work with as the corrosion process may create significant variations in topographic height of the samples. This force channel allows scanning techniques to be used that would be slow or destructive in a probe that only had electrochemical sensing. One example is the previously described hopping mode method. By changing the hopping height, this technique can measure samples with very large topographic changes. However, choosing larger hopping distances to prevent crashing reduces the speed at which a new sample position can be found. Additionally, if the signal-to-noise ratio is small, as it is in electrochemical scanning, approach must occur more slowly to avoid feedback crashes due to small jumps in noise, which are significant compared to the electrochemical signal. However, this project has demonstrated that the force feedback is significantly lower noise, meaning that this channel is reliable, and it is possible to vastly increase the speed at which scanning occurs in comparison to the electrochemical method.

#### 7. Can these probes be used as a microfabrication device or to study local corrosion?

By using force feedback and piezo positioning this system is capable of non-destructively approaching a sample surface with a liquid droplet, allowing for the use of the electrochemical system to apply specific bias routines to precise locations on the surface. In one of these experiments the gold was delaminated from the surface, while in the others liquid droplets were ejected onto the surface in specific locations. This showcased the potential level of control and customizability that this system offers. This could be useful in nano or micro patterning surfaces with whatever substance is contained in the pipette, or for selectively corroding and etching surface. Additionally, this platform could be used to probe fluid dynamics at the nano scale.

---

In summary, the methods developed in this Thesis demonstrates the viability of AFM-SICM pipette probes as a powerful and versatile tool in electrochemical scanning probe microscopy. While the technique remains challenging, this developed methodology provides an opportunity for performing more quantitative, and robust measurements of structure and electrochemical properties on a variety of interesting materials.

# Chapter 6

## Outlook

This work established the viability of using pulled pipettes as combined AFM-electrochemical probes. In the future, the possibilities for improvement and implementation are vast. These possibilities can be subdivided into probe creation, electrochemical techniques, and interesting samples.

In terms of probes, the methods developed in this thesis were chosen for rapid prototyping and cost considerations. To this end, the probe bending, positioning, and gluing were all performed by manual operation of micromanipulators, or directly by hand. If these manual operations were automated, then probes could be manufactured much more accurately and faster. This increase in accuracy would lead to more reproducibility, and a smaller spread in the distribution of physical parameters. The effects of small design changes could be more correlated, rather than being drowned out by operator error.

Through a mechanised method the probes could be fixed to the AFM head and placed more precisely. This would allow for smaller reflectors to be fixed to the probes. The reflector is the predominant source of drag when the probe is completely immersed in liquid, so much smaller reflector would limit the Q factor reduction experienced when immersing these probes fully. If it is possible to scan in tapping mode while the reflector of the probe is immersed, then the tip length could be shortened. A shorter tip length would vastly increase the lateral stiffness of the probes, which would reduce measurement hysteresis and tip instabilities.

However, tip bending also placed limits on how short the tip could be. The plasma arc bending employed in this work was cheap, safe, and fast. However, the plasma arc's spatial position varies over time due to small air currents and reactions on the surface of

the electrodes. If this position changes and the plasma arc runs through the tip apex, the probe will be melted shut. This limited the probe length to lengths of 250  $\mu\text{m}$  or greater. If a light source, such a  $\text{CO}_2$  laser were used to soften the probes during bending [175], it might be possible to make shorter probes. This would require a beam profile where the bend area softens, while the tip apex does not. By using a pinhole filter close to the probe, a beam profile of substantially less than 250  $\mu\text{m}$  could be established (the wavelength of a  $\text{CO}_2$  laser is 10.6  $\mu\text{m}$  [176]).

Another effect of more precise probe creation is better angular precision when setting up the probe. This study has shown that we can attain a current reduction of 10%. This is limited by how parallel the probe is to the (flat) surface. The current reduction could be increased, which would increase the current to noise ratio of the measurements, If the probe tip axis could be consistently manufactured more perpendicular to the sample surface.

SICM and AFM measurement are limited by the tip apex geometry, so one could also use a  $\text{CO}_2$  laser to improve this aspect. While  $\text{CO}_2$  laser pullers already exist [177], a customised laser pulling system could offer another level of control over the pipette geometry. By using a mechanically controlled pinhole, the beam profile of the  $\text{CO}_2$  laser could be controlled. This would lead to better heating control, and through a multi-step process probes of smaller diameters could be pulled. Not only this, but probes with shorter, steeper tapers could be produced. The resistance of the probe increases as a function of the inverse of the cross-sectional area of the pipette, integrated over the length (see subsection 1.3.1). Pipettes with small openings and long tapers will have very high resistances, and therefore a poor signal to noise ratio. If the length of the smallest diameter section of the pipette is reduced, then the resistance can be decreased significantly, and signal to noise ratio can be increased. Additionally, this could produce higher stiffness, higher resonance frequency probes.

Another way to limit to increase the current resolution would be to reduce the inner radius of the tip apex by chemical deposition. If the tip apex of the probe is silanized, then a layer of silane will coat the glass surface [178]. If this is controllably done, then the tip apex opening can be reduced in diameter and the spatial current resolution of the technique would increase. This would also increase the total size of the tip apex, which would decrease the AFM spatial resolution. To solve this problem, a focused ion beam could be used to create a pillar of gallium ions [179] at the end of the tip apex. If this gallium pillar is long enough, then it will effectively function as a nanotip where all the force interaction occurs, and it will determine the AFM resolution.



A focused ion beam could be used in other ways. While taking Scanning Electron Microscope images of the probes in this study, it was observed that the energy from the focused electron beam actually softened and distorted the probes. If this were done controllably, the tip apex could be softened and closed. Then, a focused ion beam could be used to create a small hole [180] at the tip apex, and then be used to create a gallium pillar tip. This would produce a much better spatial resolution, while the increase in ionic resistance would be small.

Alternatively, a hollow, pyramidal AFM cantilever could be attached to the tip apex of a pipette probe. Then a focused ion beam could be used to create a hole near the tip of the AFM cantilever [181]. This would result in a pipette tip with the AFM resolution of a normal AFM cantilever, and an extremely high SICM spatial resolution. Also, the pipette tip apex would only have to be  $\sim 10\mu\text{m}$  in diameter to fit the AFM cantilever, so the resistance of the pipette would be primarily determined by the thickness of the AFM cantilever where the hole is created. This could substantially reduce the resistance of the probe. The main challenge is fixing the pipette to the AFM cantilever so that there is a continuous path through the pipette from electrode to AFM cantilever hole. This could again be accomplished via a  $\text{CO}_2$  laser. Optical fiber splicing methods commonly employ a  $\text{CO}_2$  laser to soften and join two optical fibers [182]. If the pipette probe tip apex could be heated precisely, then it could be fused to the AFM cantilever.

These changes would be challenging to implement, but they could result in orders of magnitude increases in resolution and signal to noise ratio. A major challenge when using small, nanometer sized SICM tip openings will be how to fill them with liquid, avoiding bubbles (which are a source of current noise). Engineering surface coatings to modify wettability will be needed.

Using knowledge gained through this work, new electrochemical techniques and measurements are possible. This thesis has shown that the AFM functionality of these probes can control for topography, while the SICM measurement is freed up to other things. This provides the opportunity to perform surface charge mapping in solution. If the concentration of the electrolyte is low enough, ionic current rectification will occur due to the double layer capacitance along the walls of the borosilicate pipette [43]. The current rectification will change in the presence of another charged surface, so the probe can be used to find surface charges. This could then be used on catalytic materials to find and study reaction sites.

Another venue would be related to patch clamp measurements on biological cells. Patch pipettes are commonly used in physiology to measure the ionic currents of cells such as neurons [91]. This is sometimes performed as the cells are stimulated through force application [183]. This is a delicate, challenging process that is made particularly difficult by the need to approach one microscopic cell with two probes. Also, applying too much force to a cell can kill it, so the actual connection process is quite difficult. The probes detailed here could aid in this connection problem as the deflection channel of these probes yields a direct measurement of the force applied to the cell. This could be used to use the minimum amount of necessary force requisite to make patch clamp connection. Additionally, it could be used to study visco-elastic properties of cells via poking the cells while a loose patch clamp connection is used to measure the ionic currents. All of this could be incorporated into a complete patch clamp technique where cells are scanned in tapping mode in liquids while the current channel records any variations in the biological ionic current.

In this Thesis we also examined how the probe can be used to perform droplet measurements. This functionality can be used for micro-cell electrochemical measurements of single molecules. Molecules may be deposited on a surface, and through AFM probe scanning these molecules may be found. Through the current channel current voltammetry can be performed to examine single molecule electrodynamics. This would allow us to measure in detail how the local environment of a molecule or catalytic site) influences its electrochemical properties.

Another application would be the use of these probes in nanofabrication. As examined in section 4.6 the probes can be used to apply localised voltage pulses within small droplets of liquid. This type of measurement could facilitate localised etching of surfaces. It could also be used to eject liquids on surface in a controlled manner, in a type of nano-printing method. The volume of liquid ejected would be limited by the tip apex and applied voltage, so extremely small amounts of liquid could be deposited in this manner.

Finally, and most importantly, this system can be used to examine battery materials. The microscope system would be placed within a glovebox so that air sensitive materials could be used. The sample surface would be a piece of battery material such as  $\text{LiFePO}_4$  immersed in a bath of commercially used battery electrolyte. A potential would be applied between the probe and the surface while the sample topography is recorded via AFM measurements. Using this measurement, one could correlate topographic features from the force feedback, material contrasts from the phase channel, and the SICM current would relate electrochemical information about the sample. For example, the battery material

could be semi-charged before the measurement. A measurement of this surface would show a difference in current magnitude over areas that are completely charge or completely uncharged. This might yield important information on the process of lithiation, such as how homogenous it is as a function of processing parameters, aging or charging rate. Furthermore, the battery electrolyte bath may be removed, and a droplet method can be used on uncharged and charged areas. In this way, full cyclic voltammetry curves could be performed on these areas to investigate if there are differences in these curves. With this completed, the same battery material may then be scanned with complementary techniques to coordinate these properties with more specific information about the chemical composition of the surface, and the ionic conductivity in the bulk of the material beneath the surface. With this platform, many interesting battery phenomena may be studied. This extends from finding ‘hot spots’ to the role of chemical additives on the SEI layer and the resultant electrochemical changes to monitoring battery degradation during charge cycling in situ. In conclusion, it is predicted that the potential benefits of this method are numerous, and could yield substantial, important information for the battery community, and science at large.

# Appendix A

## Plasma Arc Circuit Diagram

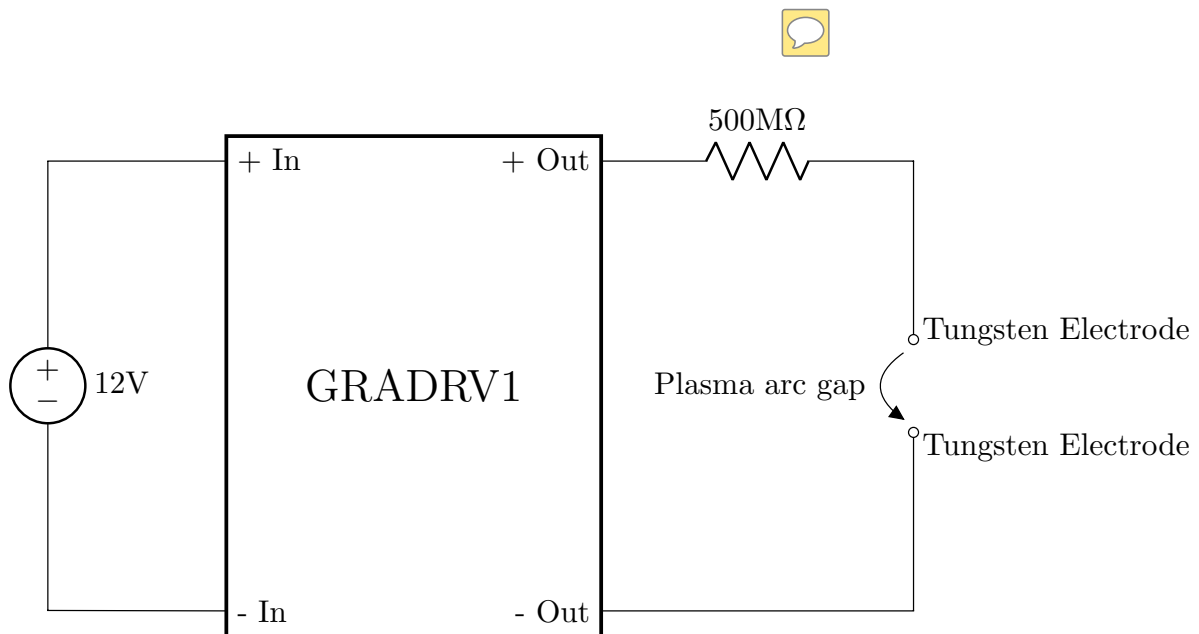


FIGURE A.1: The plasma arc circuit consists of a DC voltage source, the GRADRV1 high voltage/frequency driver module, and a resistor in series with two electrodes. There is an air gap between the two electrodes where the plasma arc forms.

The circuit of figure A.1 was used to produce a plasma arc within the bending apparatus. The GRADRV1 high voltage/frequency driver module (Information Unlimited [103]) is manually controlled by turning a knob connected to a variable resistor. This controls the intensity of the plasma arc.

# Appendix B

## GXSM Python Code

The GXSM controller software includes a python console. This console allows the user to run scripts which may:

- Change variable values in the controller software
- Initiate processes in the controller which are otherwise initiated by pressing execution buttons in the controller's user interface
- Perform Python based actions

This automates any action that a user may perform through the user interface. These programs are structured by:

1. Setting all global variables
2. Setting all routine variables, such as the multiple stored General Vector Probe actions
3. Calling the routines and actions in a loop format
4. Including the `gxsm.sleep` command to pause the Python controller

## B.1 Setting the General Vector Probe Variables for Hopping Mode Scan

```
1 import gxsm
2
3 distx = 500      #separation between points (angstroms)
4 retractionz = 1000  #Z retraction distance (angstroms)
5
6 #to reset the routines, call the empty Vector Probe D, and store this
   information in Vector Probes A, B, and C
7 gxsm.action("DSP_VP_RCL_VPD")
8 gxsm.action("DSP_VP_STO_VPB")
9 gxsm.action("DSP_VP_RCL_VPD")
10 gxsm.action("DSP_VP_STO_VPC")
11 gxsm.action("DSP_VP_RCL_VPD")
12 gxsm.action("DSP_VP_STO_VPA")
13 #specify the Vector Probe values for Vector Probe A
14 #step 0: retract
15 gxsm.set("dsp-gvp-dz00",str(retractionz))  #Change in Z
16 gxsm.set("dsp-gvp-dt00",str(1))  #Change in time
17 gxsm.set("dsp-gvp-n00",str(100))  #Number of measurements
18 #step 1: move right
19 gxsm.set("dsp-gvp-dx01",str(distx))
20 gxsm.set("dsp-gvp-dt01",str(1))
21 gxsm.set("dsp-gvp-n01",str(100))
22 #step 2: wait
23 gxsm.set("dsp-gvp-dt02",str(1))
24 gxsm.set("dsp-gvp-n02",str(100))
25 #step 3: approach surface (the FB must be checkmarked manually before
   using this Vector Probe)
26 gxsm.set("dsp-gvp-dt03",str(5))
27 gxsm.set("dsp-gvp-n03",str(100))
28 #Store as Vector Probe A
29 gxsm.action("DSP_VP_STO_VPA")
30 #Open an empty Vector Probe D
31 gxsm.action("DSP_VP_RCL_VPD")
32
33
34 #Specify the values for Vector Probe B, just as in Vector Probe A
35 #The difference is that the movement is in the opposite direction (-x)
36 gxsm.set("dsp-gvp-dz00",str(retractionz))
37 gxsm.set("dsp-gvp-dt00",str(1))
38 gxsm.set("dsp-gvp-n00",str(100))
```

```
39
40 gxsm.set("dsp-gvp-dx01",str(-(distx)))
41 gxsm.set("dsp-gvp-dt01",str(1))
42 gxsm.set("dsp-gvp-n01",str(100))
43
44 gxsm.set("dsp-gvp-dt02",str(1))
45 gxsm.set("dsp-gvp-n02",str(100))
46
47 gxsm.set("dsp-gvp-dt03",str(5))
48 gxsm.set("dsp-gvp-n03",str(100))
49
50 gxsm.action("DSP_VP_STO_VPB")
51 gxsm.action("DSP_VP_RCL_VPD")
52
53
54 #Specify the values for Vector Probe C, just as in Vector Probe A
55 #The difference is that the movement is in the y direction
56 gxsm.set("dsp-gvp-dz00",str(retractionz))
57 gxsm.set("dsp-gvp-dt00",str(1))
58 gxsm.set("dsp-gvp-n00",str(100))
59
60 gxsm.set("dsp-gvp-dy01",str(distx))
61 gxsm.set("dsp-gvp-dt01",str(1))
62 gxsm.set("dsp-gvp-n01",str(100))
63
64 gxsm.set("dsp-gvp-dt02",str(1))
65 gxsm.set("dsp-gvp-n02",str(100))
66
67 gxsm.set("dsp-gvp-dt03",str(5))
68 gxsm.set("dsp-gvp-n03",str(100))
69
70 gxsm.action("DSP_VP_STO_VPC")
```

## B.2 Setting the General Vector Probe Variables for Tapping Mode Scan

```
1 import gxsm
2
3 distx = 500 #separation between points (angstroms)
4
5 #to reset the routines, call the empty Vector Probe D, and store this
6   information in Vector Probes A, B, and C
7 gxsm.action("DSP_VP_RCL_VPD")
8 gxsm.action("DSP_VP_STO_VPB")
9 gxsm.action("DSP_VP_RCL_VPD")
10 gxsm.action("DSP_VP_STO_VPC")
11 gxsm.action("DSP_VP_RCL_VPD")
12 gxsm.action("DSP_VP_STO_VPA")
13 #specify the Vector Probe values for Vector Probe A
14 #the FB must be checkmarked manually before using this Vector Probe
15 gxsm.set("dsp-gvp-dx00",str(distx))
16 gxsm.set("dsp-gvp-dt00",str(1))
17 gxsm.set("dsp-gvp-n00",str(100))
18 #Store as Vector Probe A
19 gxsm.action("DSP_VP_STO_VPA")
20 #Open an empty Vector Probe D
21 gxsm.action("DSP_VP_RCL_VPD")
22
23 #Specify the values for Vector Probe B, just as in Vector Probe A
24 #The difference is that the movement is in the opposite direction (-x)
25 gxsm.set("dsp-gvp-dx00",str(-(distx)))
26 gxsm.set("dsp-gvp-dt00",str(1))
27 gxsm.set("dsp-gvp-n00",str(100))
28 gxsm.action("DSP_VP_STO_VPB")
29 gxsm.action("DSP_VP_RCL_VPD")
30
31 #Specify the values for Vector Probe C, just as in Vector Probe A
32 #The difference is that the movement is in the y direction
33 gxsm.set("dsp-gvp-dy00",str(-(distx)))
34 gxsm.set("dsp-gvp-dt00",str(1))
35 gxsm.set("dsp-gvp-n00",str(100))
36
37 gxsm.action("DSP_VP_STO_VPC")
```



## B.3 Scanning Routine

This routine can use [B.1](#) to perform a Hopping Mode Scan with a CV performed at each point or it can be used with [B.2](#) to perform a Tapping Mode scan with a CV performed at each point.

```
1 import gxsm
2
3 points = 21    #number of rows/columns in grid
4 N = 1        #number of consecutive runs to do at each point
5 row=1       #switch for routines, switches movement between +x and -x
              direction
6
7 for j in range(0,points):
8     gxsm.action("DSP_VP_IV_EXECUTE") #perform bias sweep
9     gxsm.sleep(80)
10    for k in range(0,points):
11        if row > 0:
12            gxsm.action("DSP_VP_RCL_VPA")    #load vector probe A
13        if row < 0:
14            gxsm.action("DSP_VP_RCL_VPB")    #load vector probe B
15            gxsm.action("DSP_VP_GVP_EXECUTE") #perform vector probe
16            gxsm.sleep(40)
17            for i in range(0,N): # This loop repeats N times at the same point
18                gxsm.action("DSP_VP_IV_EXECUTE")
19                gxsm.sleep(80)
20            gxsm.action("DSP_VP_RCL_VPC")    #load vector probe C
21            gxsm.action("DSP_VP_GVP_EXECUTE") #perform vector probe
22            gxsm.sleep(40)                  # Wait
23            row=row*(-1) #change x direction after finishing row
```

## B.4 Line Scan

The manually entered variables may be queried through the Python console. In this case, the CV measurement parameters and probe movement speed are queried, and those values are used to determine the pause lengths (`gxsm.sleep( $\alpha$ )`) between actions.

```
1 import gxsm
2
3 #the probe begins engaged with the surface
4 dist=100 #separation between points (angstroms)
5 points=10 #number of points in the line
6
7 #determination of gxsm.sleep time during CV measurements
8 IVstart=gxsm.get("DSP_IV-Start-End") #query min voltage of bias sweep
9 IVend=gxsm.get("DSP_IV-End") #query max voltage of bias sweep
10 IVslope=gxsm.get("DSP_IV-Slope") #query bias ramp rate
11 numIVs=gxsm.get("DSP_IV-rep") #query number of CV cycles per point
12 IVtime=2*10*numIVs*(IVend-IVstart)/IVslope #calculate time per CV
    measurement
13 #in case the controller/Python system has some unwanted time lag
    between actions, add 10% extra time, and round up to the next
    nearest integer value
14 IVtimemod=1.1*IVtime
15 IVtimemodint=int(round(IVtimemod)+10)
16 #determination of gxsm.sleep time during General Vector Probe movement
17 movespeed=gxsm.get("DSP_MoveSpd") #query probe movement speed
18 movetime=10*dist/(movespeed/10) #calculate time to move between
    points
19 #in case the controller/Python system has some unwanted time lag
    between actions, add 10% extra time, and round up to the next
    nearest integer value
20 movetimemod=1.1*movetime
21 movetimemodint=int(round(movetimemod)+1)
22
23 for k in range(0,points):
24     gxsm.action("DSP_VP_IV_EXECUTE") #perform a CV measurement
25     gxsm.sleep(IVtimemodint) #wait for the calculated time
26     gxsm.set("ScanX",str(gxsm.get("ScanX")-dist)) #move to the next
    point
27     gxsm.sleep(movetimemodint)
```

## B.5 Retraction Followed by Alternating Approach Steps and CV Measurements

A long list of actions can be written to a General Vector Probe routine. In this circumstance the `gxsm.sleep(alpha)` function is not required as the General Vector Probe will wait for each step to complete before proceeding to the next action.

```

1 import gxsm
2
3 initialretraction = 3000 #initial retraction (angstroms)
4 approachsteps = 300 #step size
5 points=initialretraction/approachsteps #number of steps required to
   span initialretraction with steps of initialsteps
6 #load the empty Vector D and store it as Vector A to clear it
7 gxsm.action("DSP_VP_RCL_VPD")
8 gxsm.action("DSP_VP_STO_VPA")
9 #Retract from surface steps determined by points
10 for h in range(0,points):
11     if h < 10: #adjustment for naming convention of Vector Probe
12         buttondz="dsp-gvp-dz0"
13         buttondt="dsp-gvp-dt0"
14         buttonn="dsp-gvp-n0"
15         buttнду="dsp-gvp-du0"
16     if h > 9: #adjustment for naming convention of Vector Probe
17         buttondz="dsp-gvp-dz"
18         buttondt="dsp-gvp-dt"
19         buttonn="dsp-gvp-n"
20         buttнду="dsp-gvp-du"
21 #Set variables for General Vector Probe
22 buttнду0=buttнду+str(h)
23 buttondz0=buttondz+str(h)
24 buttondt0=buttondt+str(h)
25 buttonn0=buttonn+str(h)
26 #Set General Vector Probe
27 gxsm.set(buttondz0, str(approachsteps))
28 gxsm.set(buttondt0, "1")
29 gxsm.set(buttonn0, "100")
30 #Approach the surface in steps, with a CV measurement at each point
31 for j in range(0,points):
32     if points < 10: #adjustment for naming convention of Vector Probe
33         buttondz="dsp-gvp-dz0"
34         buttondt="dsp-gvp-dt0"
35         buttonn="dsp-gvp-n0"

```

```
36     buttondu="dsp-gvp-du0"
37     if points > 9: #adjustment for naming convention of Vector Probe
38         buttondz="dsp-gvp-dz"
39         buttondt="dsp-gvp-dt"
40         buttonn="dsp-gvp-n"
41         buttondu="dsp-gvp-du"
42 #10 sequences of 3 actions are set
43 #Action 1: Approach surface
44     buttondu1=buttondu+str(3*j+10)
45     buttondz1=buttondz+str(3*j+10)
46     buttondt1=buttondt+str(3*j+10)
47     buttonn1=buttonn+str(3*j+10)
48     gxsm.set(buttondz1, str((-1)*approachsteps))
49     gxsm.set(buttondt1, "1")
50     gxsm.set(buttonn1, "100")
51 #Action 2: Sweep the voltage by +0.8 V
52     buttondu2=buttondu+str(3*j+11)
53     buttondz2=buttondz+str(3*j+11)
54     buttondt2=buttondt+str(3*j+11)
55     buttonn2=buttonn+str(3*j+11)
56     gxsm.set(buttondu2, str(0.8))
57     gxsm.set(buttondt2, "3")
58     gxsm.set(buttonn2, "1000")
59 #Action 3: Sweep the voltage by -0.8V
60     buttondu3=buttondu+str(3*j+12)
61     buttondz3=buttondz+str(3*j+12)
62     buttondt3=buttondt+str(3*j+12)
63     buttonn3=buttonn+str(3*j+12)
64     gxsm.set(buttondu3, str(-0.8))
65     gxsm.set(buttondt3, "3")
66     gxsm.set(buttonn3, "1000")
```

## B.6 Alternating Approach Steps and CV Measurements Retraction Followed by Retraction

```
1 import gxsm
2
3 initialretraction = 3000 #initial retraction (angstroms)
4 approachsteps = 300 #step size
5 points=initialretraction/approachsteps #number of steps required to
   span initialretraction with steps of initialsteps
6 #load the empty Vector D and store it as Vector A to clear it
7 gxsm.action("DSP_VP_RCL_VPD")
8 gxsm.action("DSP_VP_STO_VPA")
9 #Approach the surface in steps, with a CV measurement at each point
10 for j in range(0,points):
11     if points < 10: #adjustment for naming convention of Vector Probe
12         buttondz="dsp-gvp-dz0"
13         buttondt="dsp-gvp-dt0"
14         buttonn="dsp-gvp-n0"
15         buttнду="dsp-gvp-du0"
16     if points > 9: #adjustment for naming convention of Vector Probe
17         buttondz="dsp-gvp-dz"
18         buttondt="dsp-gvp-dt"
19         buttonn="dsp-gvp-n"
20         buttнду="dsp-gvp-du"
21 #10 sequences of 3 actions are set
22 #Action 1: Approach surface
23 buttнду1=buttнду+str(3*j)
24 buttondz1=buttondz+str(3*j)
25 buttondt1=buttondt+str(3*j)
26 buttonn1=buttonn+str(3*j)
27 gxsm.set(buttondz1, str((-1)*approachsteps))
28 gxsm.set(buttondt1, "1")
29 gxsm.set(buttonn1, "100")
30 #Action 2: Sweep the voltage by +0.8 V
31 buttнду2=buttнду+str(3*j+1)
32 buttondz2=buttondz+str(3*j+1)
33 buttondt2=buttondt+str(3*j+1)
34 buttonn2=buttonn+str(3*j+1)
35 gxsm.set(buttнду2, str(0.8))
36 gxsm.set(buttondt2, "3")
37 gxsm.set(buttonn2, "1000")
38 #Action 3: Sweep the voltage by -0.8V
39 buttнду3=buttнду+str(3*j+2)
```

```
40  buttondz3=buttondz+str(3*j+2)
41  buttondt3=buttondt+str(3*j+2)
42  buttonn3=buttonn+str(3*j+2)
43  gxsm.set(buttondu3, str(-0.8))
44  gxsm.set(buttondt3, "3")
45  gxsm.set(buttonn3, "1000")
46 #Retract from surface steps determined by points
47 for h in range(0, points):
48     if h < 10: #adjustment for naming convention of Vector Probe
49         buttondz="dsp-gvp-dz0"
50         buttondt="dsp-gvp-dt0"
51         buttonn="dsp-gvp-n0"
52         buttondu="dsp-gvp-du0"
53     if h > 9: #adjustment for naming convention of Vector Probe
54         buttondz="dsp-gvp-dz"
55         buttondt="dsp-gvp-dt"
56         buttonn="dsp-gvp-n"
57         buttondu="dsp-gvp-du"
58 #Set variables for General Vector Probe
59  buttondu0=buttondu+str(h+30)
60  buttondz0=buttondz+str(h+30)
61  buttondt0=buttondt+str(h+30)
62  buttonn0=buttonn+str(h+30)
63 #Set General Vector Probe
64  gxsm.set(buttondz0, str(approachsteps))
65  gxsm.set(buttontdt0, "1")
66  gxsm.set(buttonn0, "100")
```

# Appendix C

## Stiffness Test Protocol

1. A pipette or pipette probe is mounted into a hole in the wood block.
2. The block is placed on the mass scale (APX-200, Denver Instrument Company [184]), and the scale is tared.
3. The force applicator [185] is moved via the XY translation stage (148-132, Mitsuoyo [186]) into a position where the razor blade is directly above the probe tip. A USB microscope (B005, Supereyes [93]) can be used to facilitate this positioning.
4. The micrometer screw of the force applicator is turned to approach the razor blade to the pipette. The approach is immediately halted as soon as a change in mass is registered by the scale.
5. The micrometer screw is rotated to retract the probe until the recorded mass returns to the tared mass.
6. The position of the micrometer screw is recorded as the  $x_i$  position.
7. The micrometer screw is rotated to apply force on the probe. The micrometer screw is rotated by a set distance (in the case of these pipette probes, 1  $\mu\text{m}$  on the screw scale). This new micrometer position is  $x_f$ .
8. The mass registered by the scale is  $M$ .
9. The micrometer screw is retracted, and the probe is removed from the system.
10. Stiffness is calculated by using  $x_i$ ,  $x_f$ , and  $M$  in equation 3.1.

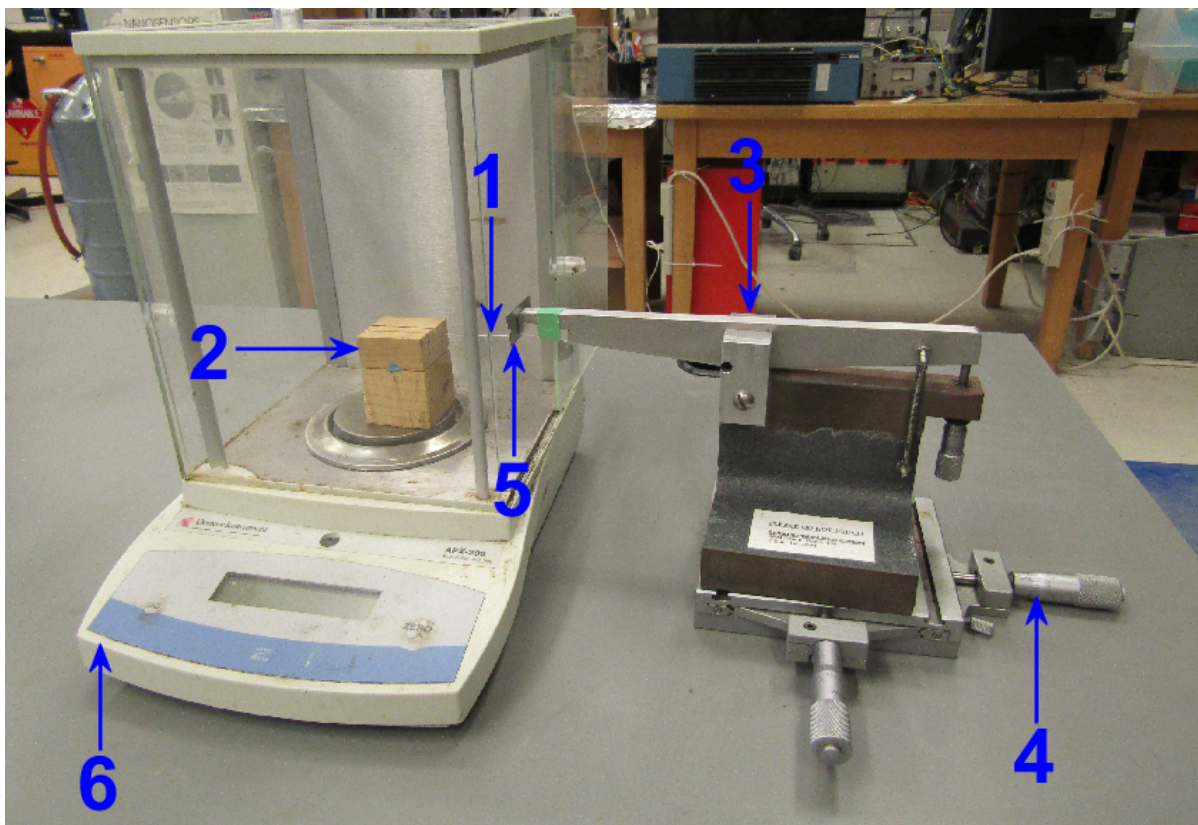


FIGURE C.1: The components of the stiffness testing system are labeled here as (1) pipette (2) wooden block (3) force applicator (4) XY translation stage (5) razor blade (6) scale



# Appendix D

## Tungsten Electrode Protocol

In the Plasma Arc Circuit (Appendix A) the plasma arc forms between the electrodes. Blunt electrodes allow the the end points of the arc to move around slightly on the electrode tip. This movement may result in the arc passing through the pipette tip, and melting the probes closed. Sharp tips confine the position of the arc. The method to make these sharp tips was developed by Anne-Sophie Lucier [187, 188], Till Hagedorn [189], and William Paul [190] and the following excerpt comes from FIM System Instruction Manuals compiled by William Paul.

The tungsten wire used in this work was 0.1 mm in diameter, and 99.95% pure (10404 Tungsten Wire, Alfa Aesar [191]).

### 3. Tip Preparation

---

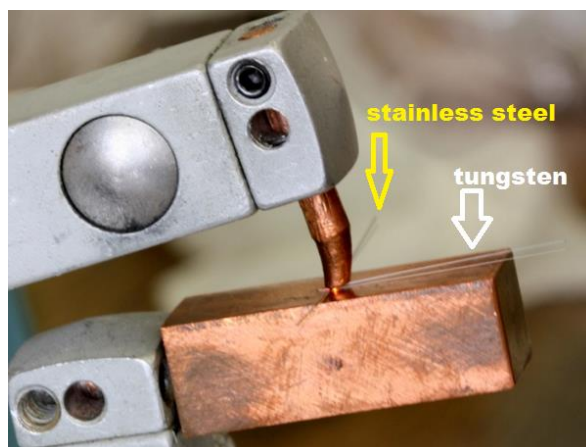
Tips, tip holders and tip transfer holders:



#### 3.1 Spot welding wire cross

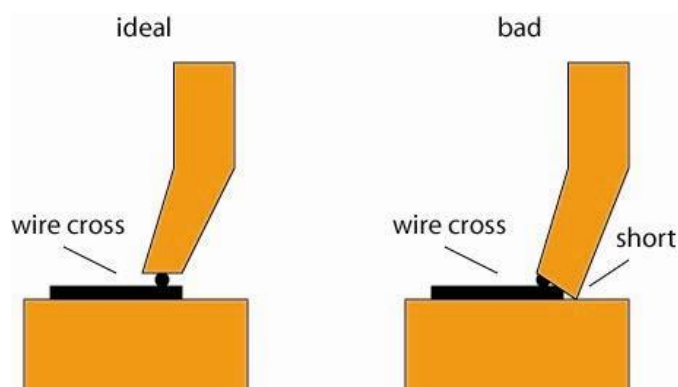
---

- Use Alfa Aesar annealed (more compliant) stainless steel wire for the wire base (diameter 0.25 mm)
- Put the W-wire first (0.1 or 0.125 mm), parallel to the axis of the Cu block. Then, place the stainless-wire on top and adjust the orientation with tweezers.
- Make wire cross with power setting 1. *Wire crosses can be made in advance (in bulk quantities) and stored for later use – especially with inexpensive polycrystalline wire.*



This illustration shows **absurdly long wires**, they should not be this long. First, cut them to the appropriate length, since trimming them after spot welding stresses the weld and can destroy it.

- Spot weld the cross to the tip holder with setting 2
- Correct the orientation of the wire with tweezers to make it perpendicular to the tip holder
- If spot welding doesn't work, try a higher setting (but not too high, as this produces a weak weld). The electrodes can be sanded lightly with a very fine grit while the spot welder is closed (while electrode is pressed against the lower Cu block) so that they become parallel and clean.
  - *Usually not a problem... perhaps necessary every year or so*
- Make sure that the contact is made through the wire ONLY (make the electrode flat with respect to the Cu block see drawing) otherwise you'll get sparks and the cross will be welded to the upper Cu electrode!



- Check for electrical continuity across the spot welds (sometimes one can be slightly loose without obvious visual clues).
- Put the tip holder onto a tip-transfer holder and check electrical continuity. Sometimes the tip-transfer holder magnets do not make great contacts, so the tip may have to be scraped against them, or moved slightly on them.
- Check that the tip holder wobble stick holes are pointing in the correct direction (long axis of the UHV system) before putting it in UHV.
- Put wire cross into UHV and test if the resistive annealing works – see annealing later on for experimental details - (sometimes the wire becomes loose during the annealing or the resistance at the contact points gets reduced and the current shoots up; annoying to ruin a good tip this way)

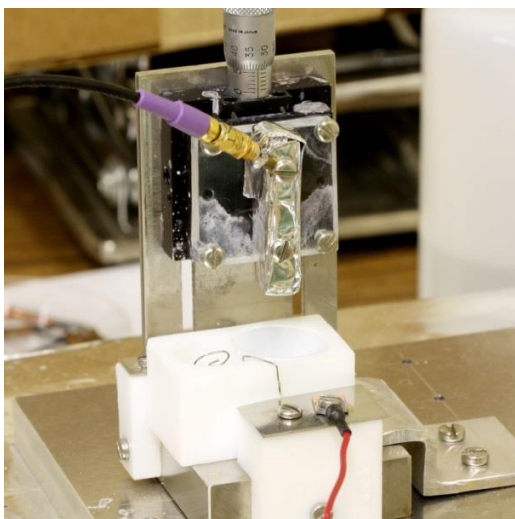
## 3.2 Tip Etching

---

### 3.2.1 KOH Solution & Set-Up

---

- Concentration 9.8 mol/l KOH (11.00 g KOH + water for total volume of 20 ml) – weigh and add the water under fume hood (!nice for lung and respiratory tracts!))
- There is a glass container with etching solution in it which can be made as required (usually make 100 or 200 ml at a time and store it in there). Some people like “fresh” etching solution, but I (WP) think this works fine and is clearly NOT a limiting factor.
- Fill Teflon etching station so that the counter electrode is well inside the solution (but not too low so that bubbles are transported under bubble shield, but not too much at the surface to inhibit conductivity, which seems to lead to poor drop-off behaviour)
- Wrap a fresh piece of Al foil around the brass tip holding piece to provide electrical contact to the tip (has a magnet in the bottom held by epoxy). *Note this is a different tip-holding device than the one used by the ULT-SPM employing qPlus sensors.*



### 3.2.2 Etching Station

---

The “Tip” switch can be set to ON or TEST – this is an essential feature of the tip etching station.

**TEST** mode is used to light up the LED when the tip wire touches the solution. This mode will not etch the tip.

**ON** mode allows etching to begin by pressing the large button. The button will illuminate when etching is active. The light will turn off when etching has been stopped by the drop-off detection circuit. Sometimes the light stays on and the circuit must be re-set in one of several ways:

1. Fake a drop-off by pulling the tip out of the etching solution using the micrometer screw
2. Short the tip and counter-electrode connections using a metal object – removing the metal object will fake a drop-off
3. Cycle power to the tip-etching station

Set up small petri dishes of DI-water, ethanol, and acetone for tip cleaning after etching.

### 3.2.3 Etching Procedure

---

Use a stereo microscope to monitor etching. You will need a gooseneck lamp to illuminate the etching bath. *Lamps with built-in fans are a bad idea because of vibration.*

***Don't touch the table during etching! The meniscus is vibration sensitive!***

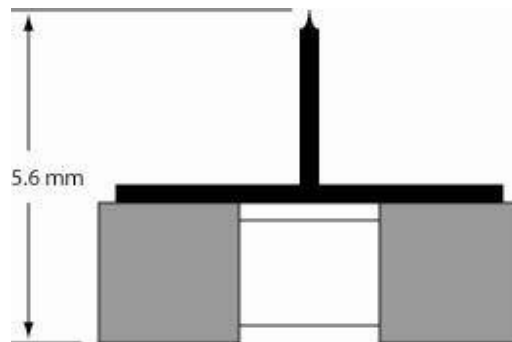
- Pre-etch to smooth wire surface:
  - Polycrystalline wire: 0.8 mm for 5 sec
  - Single crystal wire: no pre-etch necessary
- Clean pre-etched wire (DI-water, ethanol, dry N<sub>2</sub>)
- Dip in wire 0.6 mm (measured from contact point with the liquid – TEST light)
- Start NI board vi to acquire etching current (optional)
- Press and hold start button until current is stable (until it has dropped to ~10 mA)
- Release button
- Wait for switch off (should be between 2-3 mA but higher values work sometimes as well; etching time about 1 min)
- Clean tip with DI-water, ethanol, acetone, ethanol, dry with N<sub>2</sub>
- Stop the vi and save file as wiretypedate-number.ssf
- Inspect the apex with the optical microscope – if you can't see the apex, it's probably sharp.

### Troubleshooting

- Metal flakes from tungsten wire cause trouble!!! Pull out the top layer of etching solution and replace with fresh liquid every several tips.
- Little bubbles formed while dipping in the wire cause trouble during the etching (the will migrate to the surface during the etching process)
- Check for fibers and dust particles – they can make the meniscus drop (vibrations can do this too) and make the following type of double-etched tip shape:



- **Max tip length ~5.6 mm based on STM microscope constraints! (including tip holder – see drawing below)**



**Tips can generally be re-etched once or twice before they become too short to use. Re-etching saves a lot of time!**

#### **Etching Data treatment**

- Check tip shape with optical microscope
- Take image with digital camera
- Use ConvertALLSfiles.m to convert the .ssf file
- Use SSFPlotniceplot.m to plot the etching current vs. time

#### **Notes on Etching**

Inconsistent results are caused by many factors. The following are a few things I noticed while etching:

- Check that the counter-electrode wire is not too low, otherwise the bubbles will get swept under the bubble shield and will disturb the etching.
- If counter electrode is too high at the liquid's surface, the tip will not drop off – it will just disappear. Shaking the bubbles off the counter-electrode wire before etching can be helpful.
- After etching 2-3 tips, it is a good idea to suck out the top layer of etchant to remove particulates. Replace it with an equal amount of new etching solution.

- The voltage display is actually half of the applied voltage on the tip... 3V on the display is actually 6V on the tip. For the 3V recommended voltage, the display will read 1.5V... Though it seems voltage is not make-or-break to good tip making.
- If the screws holding the counter-electrode look corroded, it may be necessary to disassemble these parts and polish them with sandpaper to ensure a good electrical connection.
- A.-S. Lucier thesis is a great reference for tip fabrication.

# Bibliography

- [1] Paris Agreement. *United Nations Treaty Collection*, Dec 2015. URL [https://treaties.un.org/pages/ViewDetails.aspx?src=TREATY&mtdsg\\_no=XXVII-7-d&chapter=27&clang=\\_en](https://treaties.un.org/pages/ViewDetails.aspx?src=TREATY&mtdsg_no=XXVII-7-d&chapter=27&clang=_en).
- [2] Paris Agreement, FCCC/CP/2015/L.9/Rev.1. *UNFCCC secretariat*, Dec 2015. URL <http://unfccc.int/resource/docs/2015/cop21/eng/l09r01.pdf>.
- [3] Climate Change Canada. Progress towards canada's greenhouse gas emissions reduction target. *Government of Canada*, Jan 2020. URL <https://www.canada.ca/en/environment-climate-change/services/environmental-indicators/progress-towards-canada-greenhouse-gas-emissions-reduction-target.html>.
- [4] Rosnazri Ali, Tunku Muhammad Nizar Tunku Mansur, Nor Hanisah Baharudin, and Syed Idris Syed Hassan. 21 - environmental impacts of renewable energy. In Muhammad H. Rashid, editor, *Electric Renewable Energy Systems*, pages 519 – 546. Academic Press, Boston, 2016. ISBN 978-0-12-804448-3. doi: <https://doi.org/10.1016/B978-0-12-804448-3.00021-9>. URL <http://www.sciencedirect.com/science/article/pii/B9780128044483000219>.
- [5] Nana Yaw Amponsah, Mads Troldborg, Bethany Kington, Inge Aalders, and Rupert Lloyd Hough. Greenhouse gas emissions from renewable energy sources: A review of lifecycle considerations. *Renewable and Sustainable Energy Reviews*, 39:461 – 475, 2014. ISSN 1364-0321. doi: <https://doi.org/10.1016/j.rser.2014.07.087>. URL <http://www.sciencedirect.com/science/article/pii/S1364032114005395>.
- [6] L. J. Ricalde, E. Ordoñez, M. Gamez, and E. N. Sanchez. Design of a smart grid management system with renewable energy generation. In *2011 IEEE Symposium on Computational Intelligence Applications In Smart Grid (CIASG)*, pages 1–4, 2011.



- [7] Isidor Buchmann. *Batteries in a portable world: a handbook on rechargeable batteries for non-engineers*. Cadex Electronics, 1997.
- [8] David B. Richardson. Electric vehicles and the electric grid: A review of modeling approaches, impacts, and renewable energy integration. *Renewable and Sustainable Energy Reviews*, 19:247 – 254, 2013. ISSN 1364-0321. doi: <https://doi.org/10.1016/j.rser.2012.11.042>. URL <http://www.sciencedirect.com/science/article/pii/S1364032112006557>.
- [9] Languang Lu, Xuebing Han, Jianqiu Li, Jianfeng Hua, and Minggao Ouyang. A review on the key issues for lithium-ion battery management in electric vehicles. *Journal of Power Sources*, 226:272–288, 2013. ISSN 0378-7753. doi: 10.1016/j.jpowsour.2012.10.060. URL <https://doi.org/10.1016/j.jpowsour.2012.10.060>. 272.
- [10] Ghassan Zubi, Rodolfo Dufo-López, Monica Carvalho, and Guzay Pasaoglu. The lithium-ion battery: State of the art and future perspectives. *Renewable and Sustainable Energy Reviews*, 89:292 – 308, 2018. ISSN 1364-0321. doi: <https://doi.org/10.1016/j.rser.2018.03.002>. URL <http://www.sciencedirect.com/science/article/pii/S1364032118300728>.
- [11] B. Sarlioglu, C. T. Morris, D. Han, and S. Li. Driving toward accessibility: A review of technological improvements for electric machines, power electronics, and batteries for electric and hybrid vehicles. *IEEE Industry Applications Magazine*, 23(1):14–25, 2017.
- [12] Zachary P. Cano, Dustin Banham, Siyu Ye, Andreas Hintennach, Jun Lu, Michael Fowler, and Zhongwei Chen. Batteries and fuel cells for emerging electric vehicle markets. 3:279–289, 2018. doi: 10.1038/s41560-018-0108-1. URL <https://doi.org/10.1038/s41560-018-0108-1>. 4.
- [13] R M Dell and D A J Rand. *Understanding Batteries*. RSC Paperbacks. The Royal Society of Chemistry, 2001. ISBN 978-0-85404-605-8. doi: 10.1039/9781847552228. URL <http://dx.doi.org/10.1039/9781847552228>.
- [14] John B. Goodenough. Nobel lecture. *Nobel Media AB 2020*, 2020. URL <https://www.nobelprize.org/prizes/chemistry/2019/goodenough/lecture/>.
- [15] Venkat Srinivasan and John Newman. Discharge model for the lithium iron-phosphate electrode. *Journal of The Electrochemical Society*, 151(10):A1517, 2004.

- ISSN 0013-4651. doi: 10.1149/1.1785012. URL <https://doi.org/10.1149/1.1785012>. 1517.
- [16] Nurhaswani Alias and Ahmad Azmin Mohamad. Advances of aqueous rechargeable lithium-ion battery: A review. *Journal of Power Sources*, 274:237 – 251, 2015. ISSN 0378-7753. doi: <https://doi.org/10.1016/j.jpowsour.2014.10.009>. URL <http://www.sciencedirect.com/science/article/pii/S0378775314016188>.
- [17] Aiping Wang, Sanket Kadam, Hong Li, Siqi Shi, and Yue Qi. Review on modeling of the anode solid electrolyte interphase (sei) for lithium-ion batteries. *npj Computational Materials*, 4(1):15, Mar 2018. doi: 10.1038/s41524-018-0064-0. URL <https://doi.org/10.1038/s41524-018-0064-0>.
- [18] Maier J. Nanoionics: ion transport and electrochemical storage in confined systems. *Nature materials*, 4(11):805–15, 2005. ISSN 1476-1122. 805.
- [19] Delmas C, Maccario M, Croguennec L, Le Cras F, and Weill F. Lithium deintercalation in lifepo4 nanoparticles via a domino-cascade model. *Nature materials*, 7(8):665–71, 2008. ISSN 1476-1122. doi: 10.1038/nmat2230. URL <https://doi.org/10.1038/nmat2230>. 665.
- [20] C.V. Ramana, A. Mauger, F. Gendron, C.M. Julien, and K. Zaghib. Study of the li-insertion/extraction process in lifepo4/fepo4. *Journal of Power Sources*, 187(2):555 – 564, 2009. ISSN 0378-7753. doi: <https://doi.org/10.1016/j.jpowsour.2008.11.042>. URL <http://www.sciencedirect.com/science/article/pii/S0378775308021794>.
- [21] L. Laffont, C. Delacourt, P. Gibot, M. Yue Wu, P. Kooyman, C. Masquelier, and J. Marie Tarascon. Study of the lifepo4/fepo4 two-phase system by high-resolution electron energy loss spectroscopy. *Chemistry of Materials*, 18(23):5520–5529, 2006. doi: 10.1021/cm0617182. URL <https://doi.org/10.1021/cm0617182>.
- [22] Stephen J. Harris, Adam Timmons, Daniel R. Baker, and Charles Monroe. Direct in situ measurements of li transport in li-ion battery negative electrodes. *Chemical Physics Letters*, 485(4):265 – 274, 2010. ISSN 0009-2614. doi: <https://doi.org/10.1016/j.cplett.2009.12.033>. URL <http://www.sciencedirect.com/science/article/pii/S0009261409015462>.
- [23] Aiping Wang, Sanket Kadam, Hong Li, Siqi Shi, and Yue Qi. Review on modeling of the anode solid electrolyte interphase (sei) for lithium-ion batteries. *npj*

- Computational Materials*, 4(1):15, Mar 2018. ISSN 2057-3960. doi: 10.1038/s41524-018-0064-0. URL <https://doi.org/10.1038/s41524-018-0064-0>.
- [24] Martin Ebner, Federica Marone, Marco Stampanoni, and Vanessa Wood. Visualization and quantification of electrochemical and mechanical degradation in li ion batteries. *Science*, 342(6159):716–720, 2013. doi: 10.1126/science.1241882.
- [25] C. P. Aiken, J. Self, R. Petibon, X. Xia, J. M. Paulsen, and J. R. Dahn. A survey of in situ gas evolution during high voltage formation in li-ion pouch cells. *Journal of The Electrochemical Society*, 162(4):A760–A767, 2015. doi: 10.1149/2.0941504jes. URL <https://doi.org/10.1149/2.0941504jes>.
- [26] Samuel Pelletier, Ola Jabali, Gilbert Laporte, and Marco Veneroni. Battery degradation and behaviour for electric vehicles: Review and numerical analyses of several models. *Transportation Research Part B*, 103:158–187, 2017. ISSN 0191-2615. doi: 10.1016/j.trb.2017.01.020. URL <https://doi.org/10.1016/j.trb.2017.01.020>. 158.
- [27] Chueh WC, El Gabaly F, Sugar JD, Bartelt NC, McDaniel AH, Fenton KR, Zavadil KR, Tyliczszak T, Lai W, and McCarty KF. Intercalation pathway in many-particle lifepo4 electrode revealed by nanoscale state-of-charge mapping. *Nano letters*, 13(3):866–72, 2013. ISSN 1530-6984. doi: 10.1021/nl3031899. URL <https://doi.org/10.1021/nl3031899>. 866.
- [28] Cameron L. Bentley, Minkyung Kang, and Patrick R. Unwin. Scanning electrochemical cell microscopy: New perspectives on electrode processes in action. *Current Opinion in Electrochemistry*, 6(1):23 – 30, 2017. ISSN 2451-9103. doi: <https://doi.org/10.1016/j.coelec.2017.06.011>. URL <http://www.sciencedirect.com/science/article/pii/S2451910317300509>.
- [29] Xuebing Han, Languang Lu, Yuejiu Zheng, Xuning Feng, Zhe Li, Jianqiu Li, and Minggao Ouyang. A review on the key issues of the lithium ion battery degradation among the whole life cycle. *eTransportation*, 1:100005, 2019. ISSN 2590-1168. doi: <https://doi.org/10.1016/j.etrans.2019.100005>. URL <http://www.sciencedirect.com/science/article/pii/S2590116819300050>.
- [30] Nader Jalili and Karthik Laxminarayana. A review of atomic force microscopy imaging systems: application to molecular metrology and biological sciences. *Mechatronics*, 14(8):907 – 945, 2004. ISSN 0957-4158. doi: <https://doi.org/10.1016/j.mechatronics.2004.08.001>.

- org/10.1016/j.mechatronics.2004.04.005. URL <http://www.sciencedirect.com/science/article/pii/S0957415804000455>.
- [31] Aleksander Labuda, William Paul, Brendan Pietrobon, R. Bruce Lennox, Peter H. Grütter, and Roland Bennewitz. High-resolution friction force microscopy under electrochemical control. *Review of Scientific Instruments*, 81(8):083701, 2010. doi: 10.1063/1.3470107. URL <https://doi.org/10.1063/1.3470107>.
- [32] Sascha. Sadewasser and Thilo. Glatzel. *Kelvin probe force microscopy : measuring and compensating electrostatic forces*. Springer-Verlag Berlin Heidelberg, Heidelberg ;, 2012. doi: 10.1007/978-3-642-22566-6. URL <https://doi.org/10.1007/978-3-642-22566-6>.
- [33] Gaoliang Dai, Lena Jung, Frank Pohlenz, Hans-Ulrich Danzebrink, Rolf Krüger-Sehm, Klaus Hasche, and Günter Wilkening. Measurement of micro-roughness using a metrological large range scanning force microscope. *Measurement Science and Technology*, 15(10):2039–2046, aug 2004. doi: 10.1088/0957-0233/15/10/013. URL <https://doi.org/10.1088%2F0957-0233%2F15%2F10%2F013>.
- [34] Joska Broekmaat, Alexander Brinkman, Dave H. A. Blank, and Guus Rijnders. High temperature surface imaging using atomic force microscopy. *Applied Physics Letters*, 92(4):043102, 2008. doi: 10.1063/1.2836943. URL <https://doi.org/10.1063/1.2836943>.
- [35] Xin Zhou, James Hedberg, Yoichi Miyahara, Peter Grutter, and Koji Ishibashi. Scanning gate imaging of two coupled quantum dots in single-walled carbon nanotubes. *Nanotechnology*, 25(49):495703, nov 2014. doi: 10.1088/0957-4484/25/49/495703. URL <https://doi.org/10.1088%2F0957-4484%2F25%2F49%2F495703>.
- [36] Lianqing Liu, Ning Xi, Guangyong Li, and Heping Chen. *Chapter 4 - Atomic Force Microscope-Based Nanorobotic System for Nanoassembly*. Micro and Nano Technologies. William Andrew Publishing, Oxford, 2012. ISBN 978-1-4377-3471-3. doi: <https://doi.org/10.1016/B978-1-4377-3471-3.00004-6>. URL <http://www.sciencedirect.com/science/article/pii/B9781437734713000046>.
- [37] Peter Jonathan Eaton, Paul West, and Oxford University Press. Atomic force microscopy, 2010. URL <https://doi.org/10.1093/acprof:oso/9780199570454.001.0001>.

- [38] F. Z. Fang, Z. W. Xu, and S. Dong. Study on phase images of a carbon nanotube probe in atomic force microscopy. *Measurement Science and Technology*, 19(5), 2008. ISSN 0957-0233. doi: 10.1088/0957-0233/19/5/055501. URL <https://doi.org/10.1088/0957-0233/19/5/055501>.
- [39] T. E. Schäffer, J. P. Cleveland, F. Ohnesorge, D. A. Walters, and P. K. Hansma. Studies of vibrating atomic force microscope cantilevers in liquid. *Journal of Applied Physics*, 80(7):3622–3627, 1996. doi: 10.1063/1.363308. URL <https://doi.org/10.1063/1.363308>.
- [40] Tatsuo Ushiki, Masato Nakajima, MyungHoon Choi, Sang-Joon Cho, and Futoshi Iwata. Scanning ion conductance microscopy for imaging biological samples in liquid: A comparative study with atomic force microscopy and scanning electron microscopy. *Micron*, 43(12):1390–1398, 2012. ISSN 0968-4328. doi: 10.1016/j.micron.2012.01.012. URL <https://doi.org/10.1016/j.micron.2012.01.012>. 1390.
- [41] Thorsten Hugel and Markus Seitz. The study of molecular interactions by afm force spectroscopy. *Macromolecular Rapid Communications*, 22(13):989–1016, 2001. doi: 10.1002/1521-3927(20010901)22:13<989::AID-MARC989>3.0.CO;2-D. URL <https://onlinelibrary.wiley.com/doi/abs/10.1002/1521-3927%2820010901%2922%3A13%3C989%3A%3AAID-MARC989%3E3.0.CO%3B2-D>.
- [42] Greg Haugstad. Atomic force microscopy : understanding basic modes and advanced applications, 2012. URL <https://doi.org/10.1002/9781118360668>.
- [43] Chiao-Chen Chen, Yi Zhou, and Lane A. Baker. Scanning ion conductance microscopy. *Annual Review of Analytical Chemistry*, 5(1):207–228, 2012. ISSN 1936-1327. doi: 10.1146/annurev-anchem-062011-143203. URL <https://doi.org/10.1146/annurev-anchem-062011-143203>. 207.
- [44] M. Pellegrino, P. Orsini, M. Pellegrini, P. Baschieri, F. Dinelli, D. Petracchi, E. Tognoni, and C. Ascoli. Integrated sicm-afm-optical microscope to measure forces due to hydrostatic pressure applied to a pipette. *Micro Nano Letters*, 7(4): 317–320, 2012.
- [45] Albert L. Lipson, Ryan S. Ginder, and Mark C. Hersam. Nanoscale in situ characterization of li-ion battery electrochemistry via scanning ion conductance microscopy. *Advanced Materials*, 23(47):5613–5617, 2011. ISSN 0935-9648. doi: 10.1002/adma.201103094. URL <https://doi.org/10.1002/adma.201103094>. 5613.

- [46] Niya Sa, Wen-Jie Lan, Wenqing Shi, and Lane A. Baker. Rectification of ion current in nanopipettes by external substrates. *ACS Nano*, 7(12):11272–11282, 2013. doi: 10.1021/nm4050485. URL <https://doi.org/10.1021/nm4050485>. PMID: 24200344.
- [47] Allen J. Bard and Larry R. Faulkner. *Electrochemical methods: fundamentals and applications*. Wiley, New York, 1980. ISBN 0471055425. URL [//catalog.hathitrust.org/Record/000707476](http://catalog.hathitrust.org/Record/000707476).
- [48] NIST. molar gas constant, 2020. URL <https://physics.nist.gov/cgi-bin/cuu/Value?r>.
- [49] NIST. Faraday constant, 2020. URL <https://physics.nist.gov/cgi-bin/cuu/Value?f>.
- [50] Ashley Page, David Perry, and Patrick R. Unwin. Multifunctional scanning ion conductance microscopy. *Proceedings of the Royal Society A: Mathematical, Physical and Engineering Sciences*, 473(2200):20160889, 2017. doi: 10.1098/rspa.2016.0889.
- [51] David Perry, Dmitry Momotenko, Robert A. Lazenby, Minkyung Kang, and Patrick R. Unwin. Characterization of nanopipettes. *Analytical Chemistry*, 88(10):5523–5530, 2016. doi: 10.1021/acs.analchem.6b01095. URL <https://doi.org/10.1021/acs.analchem.6b01095>. PMID: 27108872.
- [52] Timothy Plett, Wenqing Shi, Yuhan Zeng, William Mann, Ivan Vlassiouk, Lane A. Baker, and Zuzanna S. Siwy. Rectification of nanopores in aprotic solvents – transport properties of nanopores with surface dipoles. *Nanoscale*, 7:19080–19091, 2015. doi: 10.1039/C5NR06340J. URL <http://dx.doi.org/10.1039/C5NR06340J>.
- [53] Kim McKelvey, Sophie L. Kinnear, David Perry, Dmitry Momotenko, and Patrick R. Unwin. Surface charge mapping with a nanopipette. *Journal of the American Chemical Society*, 136(39):13735–13744, 2014. doi: 10.1021/ja506139u. URL <https://doi.org/10.1021/ja506139u>. PMID: 25181551.
- [54] Neil Ebejer, Aleix G. Güell, Stanley C.S. Lai, Kim McKelvey, Michael E. Snowden, and Patrick R. Unwin. Scanning electrochemical cell microscopy: A versatile technique for nanoscale electrochemistry and functional imaging. *Annual Review of Analytical Chemistry*, 6(1):329–351, 2013. doi: 10.1146/annurev-anchem-062012-092650. URL <https://doi.org/10.1146/annurev-anchem-062012-092650>. PMID: 23560932.

- [55] David Polcari, Philippe Dauphin-Ducharme, and Janine Mauzeroll. Scanning electrochemical microscopy: A comprehensive review of experimental parameters from 1989 to 2015. *Chemical Reviews*, 116(22):13234–13278, 2016. doi: 10.1021/acs.chemrev.6b00067. URL <https://doi.org/10.1021/acs.chemrev.6b00067>. PMID: 27736057.
- [56] Luyao Huang, Ziyu Li, Yuntian Lou, Fahe Cao, Dawei Zhang, and Xiaogang Li. Recent advances in scanning electrochemical microscopy for biological applications. *Materials (1996-1944)*, 11(8):1389, 2018. ISSN 19961944. URL <https://proxy.library.mcgill.ca/login?url=http://search.ebscohost.com/login.aspx?direct=true&db=a9h&AN=131449794&scope=site>.
- [57] Enrico Daviddi, Katerina L. Gonos, Alex W. Colburn, Cameron L. Bentley, and Patrick R. Unwin. Scanning electrochemical cell microscopy (seccm) chronopotentiometry: Development and applications in electroanalysis and electrocatalysis. *Analytical Chemistry*, 91(14):9229–9237, Jul 2019. ISSN 0003-2700. doi: 10.1021/acs.analchem.9b02091. URL <https://doi.org/10.1021/acs.analchem.9b02091>.
- [58] Neil Ebejer, Aleix G. Güell, Stanley C.S. Lai, Kim McKelvey, Michael E. Snowden, and Patrick R. Unwin. Scanning electrochemical cell microscopy: A versatile technique for nanoscale electrochemistry and functional imaging. *Annual Review of Analytical Chemistry*, 6(1):329–351, 2013. doi: 10.1146/annurev-anchem-062012-092650. URL <https://doi.org/10.1146/annurev-anchem-062012-092650>. PMID: 23560932.
- [59] Paolo Bertocello. Advances on scanning electrochemical microscopy (secm) for energy. *Energy Environ. Sci.*, 3:1620–1633, 2010. doi: 10.1039/C0EE00046A. URL <http://dx.doi.org/10.1039/C0EE00046A>.
- [60] Cynthia G. Zoski. Nanoscale scanning electrochemical microscopy: Emerging advances in applications and theory. *Current Opinion in Electrochemistry*, 1(1):46 – 52, 2017. ISSN 2451-9103. doi: <https://doi.org/10.1016/j.coelec.2017.01.002>. URL <http://www.sciencedirect.com/science/article/pii/S2451910316300357>.
- [61] Cynthia G. Zoski. Review—advances in scanning electrochemical microscopy (SECM). *Journal of The Electrochemical Society*, 163(4):H3088–H3100, dec 2015. doi: 10.1149/2.0141604jes. URL <https://doi.org/10.1149%2F2.0141604jes>.
- [62] Zhuangqun Huang, Peter De Wolf, Rakesh Poddar, Chunzeng Li, Andreas Mark, Michael Nellist, Yikai Chen, Jingjing Jiang, Georg Papastavrou, Shannon



- Boettcher, Chengxiang Xiang, and Bruce Brunshwig. Peakforce scanning electrochemical microscopy with nanoelectrode probes. *Microscopy Today*, 24:18–25, 11 2016. doi: 10.1017/S1551929516000882.
- [63] Peng Sun, François O. Laforge, and Michael V. Mirkin. Scanning electrochemical microscopy in the 21st century. *Phys. Chem. Chem. Phys.*, 9:802–823, 2007. doi: 10.1039/B612259K. URL <http://dx.doi.org/10.1039/B612259K>.
- [64] Tatsuo Ushiki, Masato Nakajima, MyungHoon Choi, Sang-Joon Cho, and Futoshi Iwata. Scanning ion conductance microscopy for imaging biological samples in liquid: A comparative study with atomic force microscopy and scanning electron microscopy. *Micron*, 43(12):1390 – 1398, 2012. ISSN 0968-4328. doi: <https://doi.org/10.1016/j.micron.2012.01.012>. URL <http://www.sciencedirect.com/science/article/pii/S0968432812000133>. Special issue on AFM in Biology & Bionanomedicine.
- [65] Bharat Bhushan and H. Fuchs. Applied scanning probe methods ii : scanning probe microscopy techniques, 2006. URL <https://doi.org/10.1007/b139097>.
- [66] Park nx10 - overview: Park atomic force microscope, 2020. URL <https://parksystems.com/products/small-sample-afm/park-nx10/overview>.
- [67] Irmgard D. Dietzel, Patrick Happel, and Denis Thatenhorst. Scanning ion conductance microscopy for studying biological samples. 12:14983–15008, 2012. ISSN 1424-8220. doi: 10.3390/s121114983. URL <https://doi.org/10.3390/s121114983>. 11.
- [68] Mario Pellegrino, Paolo Orsini, Monica Pellegrini, Paolo Baschieri, Franco Dinelli, Donatella Petracchi, Elisabetta Tognoni, and Cesare Ascoli. Weak hydrostatic forces in far-scanning ion conductance microscopy used to guide neuronal growth cones. *Neuroscience Research*, 69(3):234–240, 2011. ISSN 0168-0102. doi: 10.1016/j.neures.2010.11.009. URL <https://doi.org/10.1016/j.neures.2010.11.009>. 234.
- [69] Proksch R, Lal R, Hansma PK, Morse D, and Stucky G. Imaging the internal and external pore structure of membranes in fluid: Tappingmode scanning ion conductance microscopy. *Biophysical journal*, 71(4):2155–7, 1996. ISSN 0006-3495. 2155.
- [70] Tilman E. Schäffer, Cristian Ionescu-Zanetti, Roger Proksch, Monika Fritz, Deron A. Walters, Nils Almqvist, Charlotte M. Zaremba, Angela M. Belcher, Bettye L. Smith, Galen D. Stucky, Daniel E. Morse, and Paul K. Hansma. Does



- abalone nacre form by heteroepitaxial nucleation or by growth through mineral bridges? *Chemistry of Materials*, 9(8):1731–1740, 1997. doi: 10.1021/cm960429i. URL <https://doi.org/10.1021/cm960429i>.
- [71] Livie Dorwling-Carter, Morteza Aramesh, Hana Han, Tomaso Zambelli, and Dmitry Momotenko. Combined ion conductance and atomic force microscope for fast simultaneous topographical and surface charge imaging. *Analytical chemistry*, 90(19):11453–11460, October 2018. ISSN 0003-2700. doi: 10.1021/acs.analchem.8b02569. URL <https://doi.org/10.1021/acs.analchem.8b02569>.
- [72] Ágoston G. Nagy, Judit Kámán, Róbert Horváth, and Attila Bonyár. Spring constant and sensitivity calibration of fluidfm micropipette cantilevers for force spectroscopy measurements. *Scientific Reports*, 9(1):10287, Jul 2019. ISSN 2045-2322. doi: 10.1038/s41598-019-46691-x. URL <https://doi.org/10.1038/s41598-019-46691-x>.
- [73] Tomaso Zambelli, Mathias J. Aebbersold, Pascal Behr, Hana Han, Luca Hirt, Vincent Martinez, Orane Guillaume-Gentil, and János Vörös. *FluidFM: Development of the Instrument as well as Its Applications for 2D and 3D Lithography*, chapter 14, pages 295–323. John Wiley & Sons, Ltd, 2018. ISBN 9783527696789. doi: 10.1002/9783527696789.ch14. URL <https://onlinelibrary.wiley.com/doi/abs/10.1002/9783527696789.ch14>.
- [74] Zhuangqun Huang, Peter De Wolf, Rakesh Poddar, Chunzeng Li, Andreas Mark, Michael R. Nellist, Yikai Chen, Jingjing Jiang, Georg Papastavrou, Shannon W. Boettcher, and et al. Peakforce scanning electrochemical microscopy with nanoelectrode probes. *Microscopy Today*, 24(6):18–25, 2016. doi: 10.1017/S1551929516000882.
- [75] Johannes Rheinlaender, Nicholas A. Geisse, Roger Proksch, and Tilman E. Schäffer. Comparison of scanning ion conductance microscopy with atomic force microscopy for cell imaging. *Langmuir*, 27(2):697–704, 2011. doi: 10.1021/la103275y. URL <https://doi.org/10.1021/la103275y>. PMID: 21158392.
- [76] Aleksander Labuda, William Paul, Brendan Pietrobon, R. Bruce Lennox, Peter H. Grütter, and Roland Bennewitz. High-resolution friction force microscopy under electrochemical control. *Review of Scientific Instruments*, 81(8):083701, 2010. doi: 10.1063/1.3470107. URL <https://doi.org/10.1063/1.3470107>.

- [77] Aleksander Labuda, Kei Kobayashi, Yoichi Miyahara, and Peter Grutter. Retrofitting an atomic force microscope with photothermal excitation for a clean cantilever response in low  $q$  environments. *Review of Scientific Instruments*, 83(5):053703, 2012. doi: 10.1063/1.4712286. URL <https://doi.org/10.1063/1.4712286>.
- [78] Aleksander Labuda. *Adventures in atomic force microscopy towards the study of the solid-liquid interface*. PhD thesis, McGill University, Montreal, 2012. URL <https://central.bac-lac.gc.ca/.item?id=TC-QMM-110355&op=pdf&app=Library>. 1 online resource.
- [79] Stanford Research Instruments. SR570 Low noise current preamplifier, 2020. URL <https://www.thinksrs.com/downloads/pdfs/catalog/SR570c.pdf>.
- [80] Mlct, 2020. URL <https://www.brukerafmprobes.com/p-3444-mlct.aspx>.
- [81] Núria Gavara. A beginner's guide to atomic force microscopy probing for cell mechanics. *Microscopy research and technique*, 80(1):75–84, Jan 2017. ISSN 1097-0029. doi: 10.1002/jemt.22776. URL <https://pubmed.ncbi.nlm.nih.gov/27676584>. 27676584[pmid].
- [82] C. E. Dimas, C. L. Tan, H. S. Djie, and B. S. Ooi. Coherence length characteristics from broadband semiconductor emitters: superluminescent diodes versus broadband laser diodes. In Alexey A. Belyanin and Peter M. Snowton, editors, *Novel In-Plane Semiconductor Lasers VIII*, volume 7230, pages 27 – 34. International Society for Optics and Photonics, SPIE, 2009. doi: 10.1117/12.809118. URL <https://doi.org/10.1117/12.809118>.
- [83] Optical isolator tutorial, 2020. URL <https://www.thorlabs.com/tutorials.cfm?tabID=1B9018F1-1C6F-47AD-A194-F30639F7A6C5>.
- [84] Yoichi Miyahara, Harrisonn Griffin, Antoine Roy-Gobeil, Ron Belyansky, Hadalía Bergeron, José Bustamante, and Peter Grutter. Optical excitation of atomic force microscopy cantilever for accurate spectroscopic measurements. *EPJ Techniques and Instrumentation*, 7(1):2, Feb 2020. ISSN 2195-7045. doi: 10.1140/epjti/s40485-020-0053-9. URL <https://doi.org/10.1140/epjti/s40485-020-0053-9>.

- [85] Percy Zahl, Thorsten Wagner, Rolf Möller, and Andreas Klust. Open source scanning probe microscopy control software package gxsm. *Journal of Vacuum Science & Technology B*, 28(3):C4E39–C4E47, 2010. doi: 10.1116/1.3374719. URL <https://doi.org/10.1116/1.3374719>.
- [86] Nobel prize technologies supporting science and industry!, 2020. URL <https://scientaomicron.com/en>.
- [87] Specs. Nano measurement: Fast; precise: Nanonis, 2020. URL <https://www.specs-group.com/nanonis/products/>.
- [88] János Kokavecz, Zoltán L. Horváth, and Ádám Mechler. Dynamical properties of the q-controlled atomic force microscope. *Applied Physics Letters*, 85(15):3232–3234, 2004. doi: 10.1063/1.1785863. URL <https://doi.org/10.1063/1.1785863>.
- [89] Tomás R. Rodríguez and Ricardo García. Theory of q control in atomic force microscopy. *Applied Physics Letters*, 82(26):4821–4823, 2003. doi: 10.1063/1.1584790. URL <https://doi.org/10.1063/1.1584790>.
- [90] Axon instruments patch-clamp amplifiers, 2020. URL <https://www.moleculardevices.com/products/axon-patch-clamp-system/amplifiers/axon-instruments-patch-clamp-amplifiers#specs>.
- [91] *The Practice of Patch Clamping*, chapter 4, pages 95–114. John Wiley & Sons, Ltd, 2003. ISBN 9780470856529. doi: 10.1002/0470856521.ch4. URL <https://onlinelibrary.wiley.com/doi/abs/10.1002/0470856521.ch4>.
- [92] Axon instruments and accessories, 2020. URL <https://www.moleculardevices.com/products/patch-clamp-system/axon-accessories#Order>.
- [93] Supereyes. Supereyes usb digital microscope camera 200x zoom handheld endoscope portable magnifier otoscope ip67 waterproof for windows, mac and linux, 11mm diameter, b005. 2020. URL <https://www.supereyes-store.com/collections/microscopes/products/supereyes-b005-200x-handheld-digital-microscope-otoscope-magnifier-w-led-tripod>.
- [94] J.M. Ledue, M. Lopez-Ayon, S.A. Burke, Y. Miyahara, and P. Grutter. High q optical fiber tips for nc-afm in liquid. *Nanotechnology*, 20(26):260418–260423, 2009. doi: <https://doi.org/10.1088/0957-4484/20/26/264018>. URL <https://stacks.iop.org/Nano/20/264018>.

- [95] Corning. Pyrex©7740 borosilicate glass 7070 lithia potash borosilicate. *Glass Silicon Constraint Substrates*, 2007. URL <http://valleydesign.com/Datasheets/Corning-Pyrex-7740.pdf>.
- [96] Schott. Glass 8252. 2017. URL <https://www.schott.com/d/tubing/9f6d86c4-aa78-4029-9b28-dc6c84e68180/schott-tubing-datasheet-glass-8252-english.pdf>.
- [97] Heraeus Conamic. Base materials. pages 10–11, 2019. URL [https://www.heraeus.com/media/media/hca/doc\\_hca/products\\_and\\_solutions\\_8/BaseMaterials\\_Image\\_EN.pdf](https://www.heraeus.com/media/media/hca/doc_hca/products_and_solutions_8/BaseMaterials_Image_EN.pdf).
- [98] Sutter Instrument. Capillary glass & filaments. 2018. URL <https://www.sutter.com/MICROPIPETTE/glass.html>.
- [99] Sutter Instrument. Pipette cookbook 2018 p-97 & p-1000 micropipette pullers. Rev. F, 2018. URL [https://www.sutter.com/PDFs/pipette\\_cookbook.pdf](https://www.sutter.com/PDFs/pipette_cookbook.pdf).
- [100] 2020. URL <https://www.wpiinc.com/var-2288-bare-silver-wire>.
- [101] 2020. URL <https://clorox.ca/products/bleach/original-bleach/>.
- [102] 2020. URL <https://www.warneronline.com/sites/default/files/2018-09/Chloriding%20Ag-AgCl%20electrodes%20%28090728%29.pdf>.
- [103] Universal high voltage modular power supply, 2020. URL <https://www.amazing1.com/products/universal-high-voltage-modular-power-supply.html>.
- [104] Mb-pp2, 2020. URL <http://products.narishige-group.com/group2/MB-PP2/accept/english.html>.
- [105] Gn2 small dual-axis goniometer, 1/2" distance to point of rotation, 2 goniometers and base, 2020. URL <https://www.thorlabs.com/thorproduct.cfm?partnumber=GN2>.
- [106] Xyz linear stage, ultralign, 25 mm, crossed-roller, 8-32; 1/4-20, 2020. URL <https://www.newport.com/p/462-XYZ-M>.
- [107] Mpp-13100-w, 2020. URL <https://www.brukerafmprobes.com/Product.aspx?ProductID=3334>.
- [108] Adair Oesterle. What is "filamented" glass & who needs it? Retrieved 2020. URL [https://www.sutter.com/PDFs/technote\\_FilamentGlass.pdf](https://www.sutter.com/PDFs/technote_FilamentGlass.pdf).

- [109] Sodium chloride 31434, 2020. URL <https://www.sigmaaldrich.com/catalog/product/sigald/31434?lang=en>.
- [110] Sodium chloride 31434, 2020. URL <https://www.sigmaaldrich.com/catalog/product/sigald/31434?lang=en>.
- [111] Ferrocenemethanol, 2020. URL <https://www.sigmaaldrich.com/catalog/product/aldrich/335061?lang=en>.
- [112] Propylene carbonate, 2020. URL <https://www.sigmaaldrich.com/catalog/product/sial/310328?lang=en&region=CA>.
- [113] Sodium perchlorate, 2020. URL <https://www.sigmaaldrich.com/catalog/product/sigald/410241?lang=en&region=CA>.
- [114] Microfil, 2020. URL <https://www.wpiinc.com/var-3121-microfil>.
- [115] Art "space saver" polycarbonate vacuum desiccator with white polypropylene bottom; 0.31 cu. ft., 2020. URL <https://www.belart.com/bel-art-f42025-0000-space-saver-polycarbonate-vacuum-desiccator-with-white-pp-b.html>.
- [116] Aleksander Labuda, Sophia Hohlbauch, Marta Kocun, F. Ted Limpoco, Nathan Kirchhofer, Ben Ohler, and Donna Hurley. Tapping mode afm imaging in liquids with blue-drive photothermal excitation. *Microscopy Today*, 26(6):12–17, 2018. doi: 10.1017/S1551929518001050.
- [117] Aleksander Labuda, Yoichi Miyahara, Lynda Cockins, and P. Grutter. Decoupling conservative and dissipative forces in frequency modulation atomic force microscopy. *Physical Review B*, 84:125433, 09 2011. doi: 10.1103/PhysRevB.84.125433.
- [118] A. Labuda, K. Kobayashi, D. Kiracofe, K. Suzuki, P. H. Grütter, and H. Yamada. Comparison of photothermal and piezoacoustic excitation methods for frequency and phase modulation atomic force microscopy in liquid environments. *AIP Advances*, 1(2):022136, 2011. doi: 10.1063/1.3601872. URL <https://aip.scitation.org/doi/abs/10.1063/1.3601872>.
- [119] J. Kokavecz and A. Mechler. Investigation of fluid cell resonances in intermittent contact mode atomic force microscopy. *Applied Physics Letters*, 91(2):023113, 2007. doi: 10.1063/1.2753104. URL <https://doi.org/10.1063/1.2753104>.

- [120] D 263® t eco-friendly thin glass: Schott advanced optics: Schott ag, 2020. URL [https://www.schott.com/advanced\\_optics/english/products/optical-materials/thin-glass/thin-glass-d-263-t-eco/index.html](https://www.schott.com/advanced_optics/english/products/optical-materials/thin-glass/thin-glass-d-263-t-eco/index.html).
- [121] Eccobond® 286 a/b, 2020. URL <http://www.physics.mcgill.ca/msds/SN0600.pdf>.
- [122] NanoAndMore USA. More about afm cantilevers, 2020. URL <https://www.nanoandmore.com/more-about-afm-cantilevers>.
- [123] Christopher P. Green, Hadi Lioe, Jason P. Cleveland, Roger Proksch, Paul Mulvaney, and John E. Sader. Normal and torsional spring constants of atomic force microscope cantilevers. *Review of Scientific Instruments*, 75(6):1988–1996, 2004. doi: 10.1063/1.1753100. URL <https://doi.org/10.1063/1.1753100>.
- [124] J. Grobelny, N. Pradeep, D.-I. Kim, and Z. C. Ying. Quantification of the meniscus effect in adhesion force measurements. *Applied Physics Letters*, 88(9):091906, 2006. doi: 10.1063/1.2181200. URL <https://doi.org/10.1063/1.2181200>.
- [125] Harry Dankowicz. Nonlinear dynamics as an essential tool for non-destructive characterization of soft nanostructures using tapping-mode atomic force microscopy. *Philosophical Transactions of the Royal Society A: Mathematical, Physical and Engineering Sciences*, 364(1849):3505–3520, 2006. doi: 10.1098/rsta.2006.1907. URL <https://royalsocietypublishing.org/doi/abs/10.1098/rsta.2006.1907>.
- [126] Zeno Schumacher, Yoichi Miyahara, Laure Aeschimann, and Peter Grütter. Improved atomic force microscopy cantilever performance by partial reflective coating. *Beilstein journal of nanotechnology*, 6:1450–1456, Jul 2015. ISSN 2190-4286. doi: 10.3762/bjnano.6.150. URL <https://pubmed.ncbi.nlm.nih.gov/26199849>.
- [127] Keith J. Kasunic. Optomechanical systems engineering, 2015. URL <http://www.books24x7.com/marc.asp?bookid=63673>.
- [128] Richard Lehman. The mechanical properties of glass, 2020. URL <http://glassproperties.com/references/MechPropHandouts.pdf>.
- [129] A. Labuda, K. Kobayashi, D. Kiracofe, K. Suzuki, P. H. Grütter, and H. Yamada. Comparison of photothermal and piezoacoustic excitation methods for frequency and phase modulation atomic force microscopy in liquid environments. *AIP Advances*, 1(2):022136, 2011. doi: 10.1063/1.3601872. URL <https://aip.scitation.org/doi/abs/10.1063/1.3601872>.

- [130] Sodium chloride, 2020. URL <https://www.sigmaaldrich.com/catalog/product/sigald/31434?lang=en>.
- [131] The added mass method. URL <http://nanophys.kth.se/nanophys/facilities/nfl/afm/icon/bruker-help/Content/ProbeandSampleGuide/ThermalTune/AddingMass.htm>.
- [132] Borosilikatglas borofloat® - thermische produkteigenschaften: Schott ag, 2020. URL <https://www.schott.com/borofloat/english/attribute/thermic/index.html>.
- [133] D 263 t eco-friendly thin glass: Schott advanced optics: Schott ag, 2020. URL [https://www.schott.com/advanced\\_optics/english/products/optical-materials/thin-glass/thin-glass-d-263-t-eco/index.html](https://www.schott.com/advanced_optics/english/products/optical-materials/thin-glass/thin-glass-d-263-t-eco/index.html).
- [134] Rubens Bernardes-Filho and Odilio Benedito Garrido de Assis. Development of an algorithm for tip-related artifacts identification in AFM biological film imaging. *Brazilian Archives of Biology and Technology*, 48:667 – 674, 07 2005. ISSN 1516-8913. URL [http://www.scielo.br/scielo.php?script=sci\\_arttext&pid=S1516-89132005000500020&nrm=iso](http://www.scielo.br/scielo.php?script=sci_arttext&pid=S1516-89132005000500020&nrm=iso).
- [135] Martin A. Edwards, Cara G. Williams, Anna L. Whitworth, and Patrick R. Unwin. Scanning ion conductance microscopy: a model for experimentally realistic conditions and image interpretation. *Analytical Chemistry*, 81(11):4482–4492, 2009. doi: 10.1021/ac900376w. URL <https://doi.org/10.1021/ac900376w>. PMID: 19405486.
- [136] Antoine H Roy-Gobeil and Peter H Grutter. *Single-electron charging using atomic force microscopy*. PhD thesis, McGill University, 2017. URL <https://escholarship.mcgill.ca/concern/theses/rf55zb410>.
- [137] U. D. SCHWARZ, H. HAEFKE, P. REIMANN, and H.-J. GÜNTHERODT. Tip artefacts in scanning force microscopy. *Journal of Microscopy*, 173(3):183–197, 1994. doi: 10.1111/j.1365-2818.1994.tb03441.x. URL <https://onlinelibrary.wiley.com/doi/abs/10.1111/j.1365-2818.1994.tb03441.x>.
- [138] E. Ukraintsev, A. Kromka, H. Kozak, Z. Remeš, and B. Rezek. Artifacts in atomic force microscopy of biological samples. In Christopher L. Frewin, editor, *Atomic Force Microscopy Investigations into Biology*, chapter 2. IntechOpen, Rijeka, 2012. doi: 10.5772/36203. URL <https://doi.org/10.5772/36203>.



- [139] Claudio Canale, Bruno Torre, Davide Ricci, and Pier Carlo Braga. Recognizing and avoiding artifacts in atomic force microscopy imaging. In *Methods in Molecular Biology*, pages 31–43. Humana Press, 2011. doi: 10.1007/978-1-61779-105-5\_3. URL [https://doi.org/10.1007/978-1-61779-105-5\\_3](https://doi.org/10.1007/978-1-61779-105-5_3).
- [140] Michael J. Allen, Nicholas V. Hud, Mehdi Balooch, Robert J. Tench, Wigbert J. Siekhaus, and Rod Balhorn. Tip-radius-induced artifacts in afm images of protamine-complexed dna fibers. *Ultramicroscopy*, 42-44:1095 – 1100, 1992. ISSN 0304-3991. doi: [https://doi.org/10.1016/0304-3991\(92\)90408-C](https://doi.org/10.1016/0304-3991(92)90408-C). URL <http://www.sciencedirect.com/science/article/pii/030439919290408C>.
- [141] Evaporation from water surface, 2004. URL [https://www.engineeringtoolbox.com/evaporation-water-surface-d\\_690.html](https://www.engineeringtoolbox.com/evaporation-water-surface-d_690.html).
- [142] Humidity ratio of air, 2004. URL [https://www.engineeringtoolbox.com/humidity-ratio-air-d\\_686.html](https://www.engineeringtoolbox.com/humidity-ratio-air-d_686.html).
- [143] Andrew I. Shevchuk, Gregory I. Frolenkov, Daniel Sánchez, Peter S. James, Noah Freedman, Max J. Lab, Roy Jones, David Klenerman, and Yuri E. Korchev. Imaging proteins in membranes of living cells by high-resolution scanning ion conductance microscopy. *Angewandte Chemie International Edition*, 45(14):2212–2216, 2006. doi: 10.1002/anie.200503915. URL <https://onlinelibrary.wiley.com/doi/abs/10.1002/anie.200503915>.
- [144] Chao Li, Nicholas Johnson, Victor Ostanin, Andrew Shevchuk, Liming Ying, Yuri Korchev, and David Klenerman. High resolution imaging using scanning ion conductance microscopy with improved distance feedback control. *Progress in Natural Science*, 18(6):671 – 677, 2008. ISSN 1002-0071. doi: <https://doi.org/10.1016/j.pnsc.2008.01.011>. URL <http://www.sciencedirect.com/science/article/pii/S1002007108000956>.
- [145] Yasufumi Takahashi, Andrew I. Shevchuk, Pavel Novak, Yumi Murakami, Hitoshi Shiku, Yuri E. Korchev, and Tomokazu Matsue. Simultaneous noncontact topography and electrochemical imaging by secm/sicm featuring ion current feedback regulation. *Journal of the American Chemical Society*, 132(29):10118–10126, 2010. doi: 10.1021/ja1029478. URL <https://doi.org/10.1021/ja1029478>. PMID: 20590117.
- [146] Yuanshu Zhou, Masaki Saito, Takafumi Miyamoto, Pavel Novak, Andrew I Shevchuk, Yuri E Korchev, Takeshi Fukuma, and Yasufumi Takahashi. Nanoscale



- imaging of primary cilia with scanning ion conductance microscopy. *Analytical Chemistry*, 90(4):2891–2895, 2018. doi: 10.1021/acs.analchem.7b05112. URL <https://doi.org/10.1021/acs.analchem.7b05112>. PMID: 29345134.
- [147] Lasse Hyldgaard Klausen, Thomas Fuhs, and Mingdong Dong. Mapping surface charge density of lipid bilayers by quantitative surface conductivity microscopy. *Nature communications*, 7:12447–12447, Aug 2016. ISSN 2041-1723. doi: 10.1038/ncomms12447. URL <https://pubmed.ncbi.nlm.nih.gov/27561322>. 27561322[pmid].
- [148] Ankita Gangotra and Geoff R. Willmott. Scanning ion conductance microscopy mapping of tunable nanopore membranes. *Biomicrofluidics*, 11(5):054102–054102, Sep 2017. ISSN 1932-1058. doi: 10.1063/1.4999488. URL <https://pubmed.ncbi.nlm.nih.gov/28966699>. 28966699[pmid].
- [149] Rheinlaender J and Schäffer TE. An accurate model for the ion current-distance behavior in scanning ion conductance microscopy allows for calibration of pipet tip geometry and tip-sample distance. *Analytical chemistry*, 89(21):11875–11880, 2017. ISSN 0003-2700. doi: 10.1021/acs.analchem.7b03871. URL <https://doi.org/10.1021/acs.analchem.7b03871>. 11875.
- [150] Andrew I. Shevchuk, Gregory I. Frolenkov, Daniel Sánchez, Peter S. James, Noah Freedman, Max J. Lab, Roy Jones, David Klenerman, and Yuri E. Korchev. Imaging proteins in membranes of living cells by high-resolution scanning ion conductance microscopy. *Angewandte Chemie International Edition*, 45(14):2212–2216, 2006. ISSN 1433-7851. doi: 10.1002/anie.200503915. URL <https://doi.org/10.1002/anie.200503915>. 2212.
- [151] P. K. Hansma, B. Drake, O. Marti, S. A. C. Gould, and C. B. Prater. The scanning ion-conductance microscope. *Science*, 243(4891):641–643, 1989. ISSN 0036-8075. 641.
- [152] Alex Zhukov, Owen Richards, Victor Ostanin, Yuri Korchev, and David Klenerman. A hybrid scanning mode for fast scanning ion conductance microscopy (sicm) imaging. *Ultramicroscopy*, 121:1 – 7, 2012. ISSN 0304-3991. doi: <https://doi.org/10.1016/j.ultramicroscopy.2012.06.015>. URL <http://www.sciencedirect.com/science/article/pii/S0304399112001489>.

- [153] Cameron L. Bentley, David Perry, and Patrick R. Unwin. Stability and placement of ag/agcl quasi-reference counter electrodes in confined electrochemical cells. *Analytical Chemistry*, 90(12):7700–7707, 2018. doi: 10.1021/acs.analchem.8b01588. URL <https://doi.org/10.1021/acs.analchem.8b01588>. PMID: 29808685.
- [154] James Newton. Butler. Solubility and complex formation equilibria of silver chloride in propylene carbonate. *Analytical Chemistry*, 39(14):1799–1804, 1967. doi: 10.1021/ac50157a050. URL <https://doi.org/10.1021/ac50157a050>.
- [155] John W. Diggle and A.J. Parker. Solvation of ions—xx. the ferrocene—ferricinium couple and its role in the estimation of free energies of transfer of single ions. *Electrochimica Acta*, 18(12):975–979, 1973. ISSN 0013-4686. doi: [https://doi.org/10.1016/0013-4686\(73\)87030-6](https://doi.org/10.1016/0013-4686(73)87030-6). URL <http://www.sciencedirect.com/science/article/pii/0013468673870306>.
- [156] Vitaly V Pavlishchuk and Anthony W Addison. Conversion constants for redox potentials measured versus different reference electrodes in acetonitrile solutions at 25°C. *Inorganica Chimica Acta*, 298(1):97–102, 2000. ISSN 0020-1693. doi: [https://doi.org/10.1016/S0020-1693\(99\)00407-7](https://doi.org/10.1016/S0020-1693(99)00407-7). URL <http://www.sciencedirect.com/science/article/pii/S0020169399004077>.
- [157] Pavel Novak, Chao Li, Andrew I. Shevchuk, Ruben Stepanyan, Matthew Caldwell, Simon Hughes, Trevor G. Smart, Julia Gorelik, Victor P. Ostanin, Max J. Lab, Guy W. J. Moss, Gregory I. Frolenkov, David Klenerman, and Yuri E. Korchev. Nanoscale live-cell imaging using hopping probe ion conductance microscopy. *Nature Methods*, 6(4):279–281, Apr 2009. ISSN 1548-7105. doi: 10.1038/nmeth.1306. URL <https://doi.org/10.1038/nmeth.1306>.
- [158] O. MARTI, V. Elings, M. Haugan, C. E. Bracker, J. Schneir, B. Drake, S. A. C. Gould, J. Gurley, L. Hellemans, K. Shaw, A. L. Weisenhorn, J. Zasadzinski, and P. K. Hansma. Scanning probe microscopy of biological samples and other surfaces. *Journal of Microscopy*, 152(3):803–809, 1988. doi: 10.1111/j.1365-2818.1988.tb01452.x. URL <https://onlinelibrary.wiley.com/doi/abs/10.1111/j.1365-2818.1988.tb01452.x>.
- [159] Bing-Chen Liu, Xiao-Yu Lu, Xiang Song, Ke-Yu Lei, Abdel Alli, Hui-Fang Bao, Douglas Eaton, and He-Ping Ma. Scanning ion conductance microscopy: a nanotechnology for biological studies in live cells. *Frontiers in Physiology*, 3:483, 2013. ISSN 1664-042X. doi: 10.3389/fphys.2012.00483. URL <https://www.frontiersin.org/article/10.3389/fphys.2012.00483>.

- [160] Julia Gorelik, Yanjun Zhang, Andrew I Shevchuk, Gregory I Frolenkov, Daniel Sánchez, Max J Lab, Igor Vodyanoy, Christopher R.W Edwards, David Klenerman, and Yuri E Korchev. The use of scanning ion conductance microscopy to image a6 cells. *Molecular and Cellular Endocrinology*, 217(1):101 – 108, 2004. ISSN 0303-7207. doi: <https://doi.org/10.1016/j.mce.2003.10.015>. URL <http://www.sciencedirect.com/science/article/pii/S0303720703003861>. International Symposium on Aldosterone.
- [161] E. Ventosa and W. Schuhmann. Scanning electrochemical microscopy of li-ion batteries. *Phys. Chem. Chem. Phys.*, 17:28441–28450, 2015. doi: 10.1039/C5CP02268A. URL <http://dx.doi.org/10.1039/C5CP02268A>.
- [162] Jiyeon Kim, Christophe Renault, Nikoloz Nioradze, Netzahualcóyotl Arroyo-Currás, Kevin C. Leonard, and Allen J. Bard. Electrocatalytic activity of individual pt nanoparticles studied by nanoscale scanning electrochemical microscopy. *Journal of the American Chemical Society*, 138(27):8560–8568, 2016. doi: 10.1021/jacs.6b03980. URL <https://doi.org/10.1021/jacs.6b03980>. PMID: 27315941.
- [163] Marco Hampel, Matthias Schenderlein, Christian Schary, Matthias Dimper, and Ozlem Ozcan. Efficient detection of localized corrosion processes on stainless steel by means of scanning electrochemical microscopy (secm) using a multi-electrode approach. *Electrochemistry Communications*, 101:52 – 55, 2019. ISSN 1388-2481. doi: <https://doi.org/10.1016/j.elecom.2019.02.019>. URL <http://www.sciencedirect.com/science/article/pii/S1388248119300554>.
- [164] F A Martin, J Cousty, J-L Masson, and C Bataillon. In situ afm study of pitting corrosion and corrosion under strain on a 304l stainless steel, Jul 2004.
- [165] Kang Xu. Nonaqueous liquid electrolytes for lithium-based rechargeable batteries. *Chemical Reviews*, 104(10):4303–4418, 2004. doi: 10.1021/cr030203g. URL <https://doi.org/10.1021/cr030203g>. PMID: 15669157.
- [166] Makoto Ue, Masayuki Takeda, Masahiro Takehara, and Shoichiro Mori. Electrochemical properties of quaternary ammonium salts for electrochemical capacitors. *Journal of The Electrochemical Society*, 144(8):2684–2688, dec 2019. doi: 10.1149/1.1837882. URL <https://doi.org/10.1149%2F1.1837882>.
- [167] Makoto Ue, Akinori Murakami, and Shinichiro Nakamura. Anodic stability of several anions examined by ab initio molecular orbital and density functional

- theories. *Journal of The Electrochemical Society*, 149(12):A1572, 2002. doi: 10.1149/1.1517579. URL <https://doi.org/10.1149%2F1.1517579>.
- [168] G. Eggert and J. Heitbaum. Electrochemical reactions of propylenecarbonate and electrolytes solved therein—a dems study. *Electrochimica Acta*, 31(11):1443 – 1448, 1986. ISSN 0013-4686. doi: [https://doi.org/10.1016/0013-4686\(86\)87057-8](https://doi.org/10.1016/0013-4686(86)87057-8). URL <http://www.sciencedirect.com/science/article/pii/0013468686870578>.
- [169] Dario Ossola, Livie Dorwling-Carter, Harald Dermutz, Pascal Behr, János Vörös, and Tomaso Zambelli. Simultaneous scanning ion conductance microscopy and atomic force microscopy with microchanneled cantilevers. *Phys. Rev. Lett.*, 115: 238103, Dec 2015. doi: 10.1103/PhysRevLett.115.238103. URL <https://link.aps.org/doi/10.1103/PhysRevLett.115.238103>.
- [170] Michael E. Snowden, Malak Dayeh, Nicholas A. Payne, Simon Gervais, Janine Mauzeroll, and Steen B. Schougaard. Measurement on isolated lithium iron phosphate particles reveals heterogeneity in material properties distribution. *Journal of Power Sources*, 325:682 – 689, 2016. ISSN 0378-7753. doi: <https://doi.org/10.1016/j.jpowsour.2016.06.081>. URL <http://www.sciencedirect.com/science/article/pii/S0378775316307832>.
- [171] Chang-Hui Chen, Leon Jacobse, Kim McKelvey, Stanley C. S. Lai, Marc T. M. Koper, and Patrick R. Unwin. Voltammetric scanning electrochemical cell microscopy: Dynamic imaging of hydrazine electro-oxidation on platinum electrodes. *Analytical Chemistry*, 87(11):5782–5789, 2015. doi: 10.1021/acs.analchem.5b00988. URL <https://doi.org/10.1021/acs.analchem.5b00988>. PMID: 25942527.
- [172] Yasufumi Takahashi, Yu Kobayashi, Ziqian Wang, Yoshikazu Ito, Masato Ota, Hiroki Ida, Akichika Kumatani, Keisuke Miyazawa, Takeshi Fujita, Hitoshi Shiku, Yuri E. Korchev, Yasumitsu Miyata, Takeshi Fukuma, Mingwei Chen, and Tomokazu Matsue. High-resolution electrochemical mapping of the hydrogen evolution reaction on transition-metal dichalcogenide nanosheets. *Angewandte Chemie International Edition*, 59(9):3601–3608, 2020. doi: 10.1002/anie.201912863. URL <https://onlinelibrary.wiley.com/doi/abs/10.1002/anie.201912863>.
- [173] Dmitry Momotenko, Ashley Page, Maria Adobes-Vidal, and Patrick R. Unwin. Write-read 3d patterning with a dual-channel nanopipette. *ACS Nano*, 10(9): 8871–8878, 2016. doi: 10.1021/acsnano.6b04761. URL <https://doi.org/10.1021/acsnano.6b04761>. PMID: 27569272.

- [174] Luca Hirt, Stephan Ihle, Zhijian Pan, Livie Dorwling-Carter, Alain Reiser, Jeffrey M. Wheeler, Ralph Spolenak, János Vörös, and Tomaso Zambelli. Template-free 3d microprinting of metals using a force-controlled nanopipette for layer-by-layer electrodeposition. *Advanced Materials*, 28(12):2311–2315, 2016. doi: 10.1002/adma.201504967. URL <https://onlinelibrary.wiley.com/doi/abs/10.1002/adma.201504967>.
- [175] Jian Zhao, James Sullivan, John Zayac, and Ted D. Bennett. Structural modification of silica glass by laser scanning. *Journal of Applied Physics*, 95(10):5475–5482, 2004. doi: 10.1063/1.1703832. URL <https://doi.org/10.1063/1.1703832>.
- [176] Todd J. Sawisch, George R. Deeb, and Robert A. Strauss. 8 - use of lasers for minor oral surgery in general practice. In Robert A. Convissar, editor, *Principles and Practice of Laser Dentistry (Second Edition)*, pages 131 – 151. Mosby, St. Louis, second edition edition, 2016. ISBN 978-0-323-29762-2. doi: <https://doi.org/10.1016/B978-0-323-29762-2.00008-5>. URL <http://www.sciencedirect.com/science/article/pii/B9780323297622000085>.
- [177] P-2000 laser base micropipette puller system operation manual, Jun 2010. URL [https://wpi-europe.com/downloads/content/P-2000\\_OpMan.pdf](https://wpi-europe.com/downloads/content/P-2000_OpMan.pdf).
- [178] Xiaolong Xu, Chuanping Li, Ya Zhou, and Yongdong Jin. Controllable shrinking of glass capillary nanopores down to sub-10 nm by wet-chemical silanization for signal-enhanced dna translocation. *ACS Sensors*, 2(10):1452–1457, 2017. doi: 10.1021/acssensors.7b00385. URL <https://doi.org/10.1021/acssensors.7b00385>. PMID: 28971672.
- [179] B.R. Jany, K. Szajna, M. Nikiel, D. Wrana, E. Trynkiewicz, R. Pedrys, and F. Krok. Energy dependence of nanopillars formation on insb semiconductor surfaces under gallium fib and noble gas ions beam irradiation. *Applied Surface Science*, 327:86 – 92, 2015. ISSN 0169-4332. doi: <https://doi.org/10.1016/j.apsusc.2014.11.140>. URL <http://www.sciencedirect.com/science/article/pii/S0169433214026385>.
- [180] K.A. UNOCIC, M.J. MILLS, and G.S. DAEHN. Effect of gallium focused ion beam milling on preparation of aluminium thin foils k.a. unocic, m.j. mills and g.s. daehn effect of gallium fib milling on preparation of aluminium thin foils. *Journal of Microscopy*, 240(3):227 – 238, 2010. ISSN 00222720. URL <https://proxy.library.mcgill.ca/login?url=http://search.ebscohost.com/login.aspx?direct=true&db=a9h&AN=55203418&scope=site>.

- [181] J. Meijer, Sébastien Pezzagna, T. Vogel, Bernd Burchard, H.H. Bukow, Ivo Rangelow, Y. Sarov, Hartmut Wiggers, I. Plümel, F. Jelezko, Ferdinand Schmidt-Kaler, W. Schnitzler, and K. Singer. Towards the implanting of ions and positioning of nanoparticles with nm spatial resolution. *Applied Physics A*, 91:567–571, 06 2008. doi: 10.1007/s00339-008-4515-1.
- [182] Wenxin Zheng, Hiroshi Sugawara, Toshiro Mizushima, and William Klimowych. Heating power feedback control for CO<sub>2</sub> laser fusion splicers. In Sami T. Hendow, editor, *Fiber Lasers X: Technology, Systems, and Applications*, volume 8601, pages 301 – 307. International Society for Optics and Photonics, SPIE, 2013. doi: 10.1117/12.2002648. URL <https://doi.org/10.1117/12.2002648>.
- [183] J. Mosbacher, M. Langer, J.K.H. Hörber, and F. Sachs. Voltage-dependent Membrane Displacements Measured by Atomic Force Microscopy . *Journal of General Physiology*, 111(1):65–74, 01 1998. ISSN 0022-1295. doi: 10.1085/jgp.111.1.65. URL <https://doi.org/10.1085/jgp.111.1.65>.
- [184] Denver Instrument Company, 2020. URL [http://www.denverinstrument.com/denverusa/media/pdf/archive\\_manuals/OpMan\\_AC-Series.pdf](http://www.denverinstrument.com/denverusa/media/pdf/archive_manuals/OpMan_AC-Series.pdf).
- [185] Yan Sun. *Study of interactions at the atomic scale*. PhD thesis, McGill University, [Montreal], 2004. URL <https://central.bac-lac.gc.ca/.item?id=TC-QMM-85652&op=pdf&app=Library>. 1 online resource.
- [186] Mitutoyo. Microm. head, spindle feed 0,25mm/rev. 0-13mm, spherical spindle, 2020. URL <https://shop.mitutoyo.eu/web/mitutoyo/en/index.xhtml?reset=1>.
- [187] Anne-Sophie Lucier. *Preparation and characterization of Tungsten tips suitable for molecular electronics studies*. PhD thesis, McGill University, [Montreal], 2004. URL <https://central.bac-lac.gc.ca/.item?id=TC-QMM-80323&op=pdf&app=Library>. 1 online resource.
- [188] Anne-Sophie Lucier, Henrik Mortensen, Yan Sun, and Peter Grötter. Determination of the atomic structure of scanning probe microscopy tungsten tips by field ion microscopy, 2005. URL [http://digitool.Library.McGill.CA:80/R/?func=dbin-jump-full&object\\_id=95699](http://digitool.Library.McGill.CA:80/R/?func=dbin-jump-full&object_id=95699).
- [189] Till. Hagedorn. *Atomic contacts characterized by force and current*. PhD thesis, McGill University, Montreal, 2010. URL [http://digitool.Library.McGill.CA:8881/R/?func=dbin-jump-full&object\\_id=96938](http://digitool.Library.McGill.CA:8881/R/?func=dbin-jump-full&object_id=96938).

- 
- [190] William Paul. *Atomically defined tips in scanning probe microscopy*. PhD thesis, McGill University, [Montreal], 2013. URL <https://central.bac-lac.gc.ca/.item?id=TC-QMM-119374&op=pdf&app=Library>. 1 online resource.
- [191] Alfa Aesar. 10404 tungsten wire, 0.1mm (0.004in) dia, 99.95% (metals basis), 2020. URL <https://www.alfa.com/en/catalog/010404/>.